UNIVERSITY OF CALIFORNIA SAN DIEGO

Multifunctional Nanocomposite-Enabled Tomographic Imaging for Structural and Human Health Monitoring

A dissertation submitted in partial satisfaction of the requirements for the degree Doctor of Philosophy

in

Structural Engineering

by

Sumit Gupta

Committee in charge:

Professor Kenneth J. Loh, Chair
Professor Yuri Bazilevs
Professor William Hodgkiss
Professor Francesco Lanza Di Scalea
Professor Michael D. Todd

2020

The Dissertation of Sumit Gupta is approved, and it is acceptable in quality and form for publication on microfilm and electronically:

_____

_____

_____

_____

_____

Chair

University of California San Diego

2020

DEDICATIONS

To my friend, philosopher, and guide

"If we knew what it was we were doing,
it would not be called research, would it?"
– Albert Einstein

TABLE OF CONTENTS

LIST OF FIGURES

LIST OF TABLES

LIST OF ABBREVIATIONS AND ACRONYMS

2D	Two-Dimensional
3D	Three-Dimensional
AC	Alternating Current
AFM	Atomic Force Microscope
AI	Analog Input
AR	Area Ratio
CEM	Complete Electrode Model
CFRP	Carbon Fiber-Reinforced Polymer
CG	Center of Gravity
CNF	Carbon Nano-Fibers
CNT	Carbon Nanotube
CT	Computed Tomography
DC	Direct Current
DI	Deionized
DMM	Digital Multimeter
ECT	Electrical Capacitance Tomography
EIT	Electrical Impedance Tomography
EM	Electromagnetic
FAA	Federal Aviation Administration
FD	Finite Difference
FE	Finite Element
FET	Field-Effect Transistor
FRT	Full Region Tomography
GFRP	Glass Fiber-Reinforced Polymer
GGBFS	Ground Granulated Blast Furnace Slag
GN	Gauss-Newton
GNS	Graphene nanosheet

LBE	Load-Bearing Exercises
LbL	Layer-by-Layer
LRT	Limited region tomography
LVDT	Linear Voltage Displacement Transducers
MEMS	Micro Electro Mechanical Systems
MRI	Magnetic Resonance Imaging
MWCNT	Multi-Walled Carbon Nanotubes
NCREE	National Center for Research on Earthquake Engineering
NDE	Nondestructive Evaluation
NI	National Instruments
OIP	Osseointegrated Prosthesis
PE	Polyelectrolyte
PE	Position Error
PET	Positron Emission Tomography
PLA	Polylactic Acid
PVC	Polyvinyl chloride
PZT	Lead Zirconate Titanate
RC	Reinforced concrete
RECT	Rotational Electrical Capacitance Tomography
RES	Resolution
RFID	Radio Frequency Identification
SD	Shape Deformation
SEM	Scanning Electron Microscope
SHM	Structural Health Monitoring
SMU	Source Measuring Unit
SNR	Signal-to-Noise Ratio
SPL	Superplasticizer
SWCNT	Single-Walled Carbon Nanotube
VLSI	Very Large-Scale Integration
W/C	Water-to-Cement Ratio

GLOSSARY

DMF	N-N dimethyl formaldehyde
NMP	N-methyl-2-pyrrolidinone
PANI	Polyaniline
PET	Polyethylene Terephthalate
PSS	Poly(sodium 4-styrene-sulfonate)
PVA	Polyvinyl alcohol

ACKNOWLEDGEMENTS

I would like to thank my Ph.D. advisor, Professor Kenneth J. Loh, for supporting me during these last five and a half years. This journey would not even have started if I did not receive the email from him on a chilly morning in my hometown in India. Every word of that email is encrypted in my memory, and I always relish them whenever I have time. Professor Loh is someone who I trust more than myself. He is the smartest person that I know. I am just astounded by his thinking process, way of writing, scientific and critical thoughts, presentation skills, among many. I wish I can learn more from him and perform a little fraction of what he does. Under his supervision, I learned how to define a research problem and to find its most scientific solution, and finally, how to summarize the findings in the form of a scientific manuscript. He has always been supportive and given me the freedom to work on different projects without any objections. He is always ready to provide critical comments and feedback on my research. He introduced me to the beautiful world of nanotechnology and showed me the path of how to use it as a tool to solve real-world problems. On a personal level, Professor Loh will always be the source of my inspiration because of his hardworking and passionate attitude. His guidance will be the best treasure to me to become a successful researcher.

It was not possible to reach this important milestone of my life without the unconditional love, affection, and support that I got from my family members and friends. First, I would like to thank my parents (Sukriti Gupta and Kalyan Gupta) for their continuous encouragement, endless patience, and unlimited trust throughout all the steps of my life. All my achievements are the signs of the sacrifices that they made to educate me properly. My brother's never-ending support and his faith in me are also the reasons behind all my accomplishments.

The research presented in this dissertation was not possible to accomplish without the assistance, help, and support of my committee members, including Professor Yuri Bazilevs, Professor William Hodgkiss, Professor Francesco Lanza di Scalea, and Professor Michael Todd. Their constructive comments and feedback have helped me a lot to improve the quality of my research.

I would like to express my gratitude to Professor Hyonny Kim for letting me use all his laboratory equipment and supplies during various phases of multiple projects. Professor Kim's wealth of knowledge has tremendously helped me to broaden the horizon of my experience on how to convert a table-top laboratory experiment into a successful large-scale validation test. I would also like to commend Professor Wei-Hung Chiang (National Taiwan University of Science and Technology) for synthesizing the graphene nanosheets that I have extensively used for making nanocomposite sensors. I would also like to thank Professor Chin-Hsiung Loh (National Taiwan University) for allowing me to install my sensors on the seven-story concrete structure that his team tested under earthquake ground motion. Furthermore, my collaboration with Dr. Drew Barnet and Dr. Joey Reed (Elintrix Inc.) has provided me the opportunity to familiarize myself with the industrial work environment.

I think that the ARMOR lab was my second home away from my original home. Besides helping me to fabricate sensors, run tomography experiments, or to analyze the results - all the members of the lab are my real friends who are always ready to extend their helping hands whenever needed. I would especially like to thank Bo Mi Lee and Han-Joo Lee for always being kind and patient with me. They were always there to listen to me with care and giving me feedback and counter my thoughts with a positive and constructive attitude.

During my studies at UC San Diego, I had the privilege to collaborate and work with leading researchers in the different fields of engineering. I would like to thank Konstantinos (Kostas) Anagnostopoulos for his unconstrained help and support. He has always enlightened me with his profound knowledge of mechanical testing and image processing. I would also like to express my sincere gratitude to Hyungsuk (Eric) Kim for always being up to fabricate composite specimens and run the C-scans. He taught me how to always be positive in a very negative situation. In the future, I will love to work with Kostas and Eric in collaboration.

During my undergraduate studies, I was honored to get the opportunity to work under the supervision of Professor Debasish Bandyopadhyay (Jadavpur University). He was the first person to acquaint me with the world of structural health monitoring. I am forever grateful to him for keeping his faith in my abilities and giving me the platform to go to the next step. I am also thankful to my undergraduate intern advisor Professor Anjan Datta (Indian Institute of Technology, Guwahati, India), for offering me the early exposure to research in the area of structural health monitoring.

Behind the scene, my childhood friends have always kept me cheered up during my Ph.D. years. I would like to thank Baitan Chakraborty, Soumendu Bagchi, Soumyajyoti Banerjee, Aranya Lahiri, and Nilay Chatterjee for always keeping faith in my ability to become a successful researcher. They always served as my mirror to point out my shortcomings and mistakes so that I can turn them into my strength for my future battles. I would also like to acknowledge my Davis friends Abhishek Roy, Paromita Dubey, Partha Bhaumik, Shenjuti Gupta, Sanchita Dey, and Pulak Chowdhury for being my friends. I will cherish my Davis memories, especially the late-night parties, cooking, and road trips.

My time at the UC San Diego would not have been so colorful without my San Diego friends - Siddhartha Sengupta, Brato Chakrabarti, Bodhisattwa Majumder, Ahanjit Bhattacharya, Shouvik Ganguly, and Sridip Pal. Some of my memorable moments in San Diego have been spent with them at 9226A and Netai Mama's house. I would also like to thank Netai Singha and Anindita Bhowmik for becoming a part of my family and make me a part of their family as well.

My research was supported by the Federal Aviation Administration (cooperative agreement number: 13-G-017: program manager: Dr. Navneet Garg), Office of Naval Research (grant number: N00014-17-1-2550: program manager: Dr. Liming Salvino), and U.S. Army Corp of Engineers (cooperative agreement number W912HZ-17-2-0024: program manager: Dr. Matt Smith). Additional support was also provided by UC Davis College of Engineering, UC San Diego Jacobs School of Engineering, Center for Information Technology Research in the Interest of Society Seed Grant, Department of Structural Engineering of UC San Diego, SPIE, and Graduate Student Association of UC san Diego.

Chapter 3, in part, is a reprint of the materials as it appeared in Multifunctional Cement Composites Enhanced with Carbon Nanotube Thin Film Interfaces, J. G. Gonzalez, S. Gupta, and K. J. Loh, 2016; Self-Sensing Concrete Enabled by Nano-Engineered Cement Aggregate Interfaces, S. Gupta, J. Gonzalez, and K. J. Loh, 2016; and Damage Detection using Smart Concrete Engineered with Nanocomposite Cement-Aggregate Interfaces, S. Gupta, J. Gonzalez, and K. J. Loh, 2015.

Chapter 4 is a reprint of the materials as appeared in Graphene Sensing Meshes for Densely Distributed Strain Field Monitoring, S. Gupta, G. Vella, I-N Yu, C-H Loh, W-H Chiang, and K. J. Loh, 2019.

Chapter 5 is a partial reprint of the materials as it appeared in Noncontact Electrical Permittivity Mapping and pH-Sensitive Thin Films for Osseointegrated Prosthesis and Infection Monitoring, S. Gupta and K. J. Loh, 2017; Monitoring Osseointegrated Prosthesis Loosening and Fracture using Electrical Capacitance Tomography, S. Gupta and K. J. Loh, 2018; Noncontact Strain Monitoring of Osseointegrated Prostheses, S. Gupta, H-J. Lee, K. J. Loh, M. D. Todd, J. Reed, and A. D. Barnett, 2018; and Enhancing the Imaging Performance of Electrical Capacitance Tomography for Monitoring Osseointegrated Prostheses, S. Gupta, T. Zhang, and K. J. Loh, 2019.

Chapter 6 is partially reprinted from Planar Array Capacitive Imaging for Subsurface Composite Damage Detection, S. Gupta, H. (Eric) Kim, H-J. Lee, H. Kim, and K. J. Loh, 2019; and A Planar Array Capacitive Imaging System for Detecting Damage in Composite Structures, S. Gupta and K. J. Loh, 2018.

ABSTRACT OF THE DISSERTATION

Multifunctional Nanocomposite-Enabled Tomographic Imaging for Structural and Human Health Monitoring

by

Sumit Gupta

Doctor of Philosophy in Structural Engineering

University of California San Diego, 2020

Professor Kenneth J. Loh, Chair

The performance of structural and human health systems deteriorates during their service life. If left unaddressed, catastrophic failures can occur. As a result, the field of structural and human health monitoring is seeking new sensing technologies for condition assessment. Most of the sensors available for structural response measurements are point-sensors and not suitable for spatial sensing. The complex geometries, complicated damage modes, and diverse operational conditions of the structural systems make the damage identification process more challenging.

Earlier works on materials-based sensing have demonstrated its potential to solve the aforementioned challenges. However, time-, labor-, and cost-intensive materials fabrication process, contact-based measurement strategies, and surface-level inspections, among others, limit its practical applications.

This research aims to solve these engineering bottlenecks by integrating new generation *multifunctional materials* with structural systems and combining them with advanced *soft-field tomographic imaging* techniques. In particular, a piezoresistive multi-walled carbon nanotube (MWCNT)-based nanocomposite was fabricated through a scalable, and low-cost *spray fabrication* technique. This nanocomposite was used to engineer the cement-aggregate interface for encoding *self-sensing* property in the cementitious composites. An electrical impedance tomography (EIT) algorithm and measurement strategy were developed and implemented to capture spatially distributed damage in the *self-sensing* concrete. Furthermore, distributed strain filed monitoring was accomplished by combining an updated EIT algorithm with a highly piezoresistive graphene-based *sensing mesh*.

This dissertation also explored a noncontact, radiation-free, electrical permittivity mapping technique for osseointegrated prosthesis (OIP) monitoring. The design of the MWCNT-based thin film was modified in such a way that their electrical permittivity is sensitive to external stimuli. The imaging system was coupled with these nanocomposites for subcutaneous infection and strain sensing at the tissue-OIP interface. The imaging system was also employed for prosthesis loosening and bone-fracture monitoring. As a step forward, the geometry of the imaging system was conformed into a planar array to use it as a scanning tool for rapid assessment of the subsurface condition of composite structures. Unlike traditional sensors, the proposed sensing systems (*i.e.*,

nanocomposite sensors coupled with tomographic imaging) can directly detect spatially distributed damage in structural and human systems hence improving their safety and reliability.

CHAPTER 1 INTRODUCTION

1.1 Damage in Structural Systems

"Structures" can be defined as any physical system with a purposely designed functionality [1]. In essence, the human body is analogous to civil, mechanical, and aerospace structures. Typically, structures are made of materials with particular shapes and geometries to bear loads and operate safely over their expected life spans. Unfortunately, deterioration and damage can occur to the structural systems due to their repeated exposure to operational load and harsh environment. Damage in civil, mechanical, and aerospace structures and as well as in human systems, are described in the following sections.

1.1.1 Damage in Civil, Mechanical, and Aerospace Structures

Normal wear and tear, fatigue, corrosions, as well as extreme events (*e.g*., earthquakes, blasts, impact, to name a few) are some of the main reasons for structural damage. For example, metal corrosion and fatigue with deferred maintenance caused a total failure of a 30-m-long section of the northbound lanes of Mianus river bridge (Greenwich, CT, U.S.) resulting in three casualties [2]. Milwaukee Hoan bridge [3] and Minneapolis I-35 bridge collapse [4] are the two examples of catastrophic structural failures evoked due to excessive loading. More recently, the collapse of the Ponte Morandi motorway bridge in Genoa, Italy, engendered 43 casualties, raising concerns about the aging infrastructures [5]. Furthermore, seismic events in recent past (*e.g*., Chile (2010), New Zeland (2011), and Nepal (2016), among others) have also proved that advanced designing of structures is still insufficient to avoid their damage and failure during natural disasters [6-8].

In addition to the socio-economic losses caused by such failures, millions of dollars are invested each year for the repair and maintenance of the infrastructures. Between 2007 to 2019, spending on operation and maintenance of the infrastructures in the U.S. jumped from $243.3 billion to $266.5 billion [9]. Besides, at least an additional $128 billion is required to upgrade existing structures just to meet current standards [10]. Performance evaluation and health monitoring of the infrastructural systems can significantly reduce this amount.

Similar damage events are observed in other fields of engineering (*e.g.*, aerospace and mechanical engineering). For instance, carbon fiber-reinforced polymer (CFRP) composites are seeing increasing usage in the aerospace and automotive sectors, primarily due to their superior strength-to-weight ratio and excellent corrosion resistance as compared to metals [11, 12]. Half of the fuselage and the wings of Boeing 787 Dreamliner are made of CFRP composites. On the other hand, Airbus 350 XBW utilizes 100% CFRP composites to fabricate its wings and fuselage [13]. However, CFRP's complex internal structure and anisotropic nature cause them to suffer from different damage modes (*e.g.*, delamination).

Delamination can occur in service or during the manufacturing of CFRP. Low-velocity impact and service loads (*e.g.*, tool drop, debris impact, and hail storms, to name a few) can induce such non-visible internal damage in CFRPs [14]. The result is a significant reduction in their mechanical strength, reduced load-carrying capacity, and compromised safety [15]. Therefore, routine maintenance and inspections are required to ensure structural integrity and safety. From 2002 through 2010, ~ $340.2 billion has been spent on an average for maintenance, repair, and overhaul of the aircraft [16]. Like the civil infrastructure systems, this cost can also be significantly reduced through regular structural inspection and maintenance.

1.1.2 Damage in Human Health Systems

The problems encountered in civil, mechanical, and aerospace structures are not unique; similar problems are typically experienced in the medical domain, especially to the patients suffering from limb loss. According to a report published in Archives of Physical Medicine and Rehabilitation in 2008 [17], more than 2 million people in the U.S. have suffered from limb loss, and approximately 185,000 amputations occur every year (in the U.S.) [18]. It has been estimated that 54% of these amputations were necessary due to vascular diseases (such as diabetes and peripheral arterial diseases), while 45% were due to trauma [17]. In 2010, more than 950 U.S. soldiers lost their limbs due to combat-related amputations [19], and that number increased by almost 26% in 2012 due to recent conflicts, as reported by Fischer *et al.* [20]. On the other hand, children can be born with missing limbs, and many teenagers suffer from amputations due to accidents [21]. Overall, hospital costs associated with amputations totaled to more than $8.3 billion, as was reported by the Agency for Healthcare Research and Quality [22]. Despite all of this, amputations are performed because of medical necessity. The main concern thereafter is how the patient can regain functionality after limb loss and to preserve their quality of life.

Recent advancements in medical devices have brought forth tremendous improvements in prosthesis technologies and implants that can help patients resume their daily activities before limb loss and enhance the quality of their lives. Osseointegrated prosthesis (OIP) is gaining popularity since it eliminates the dermatological issues of socket-based systems. Osseointegration, whose application is well-established in dentistry [23], involves anchoring a portion of the entire prosthesis system to the human bone and consists of a percutaneous element that is attached to the artificial limb. In this method, the structural connection between the metallic fixture and bone is generally achieved either by screw fixation [24] or press-fit implantation [25]. Although OIPs

undoubtedly provide benefits by helping amputees improve their quality of life (*e.g.*, hip motion range, sitting comfort, the ability to walk [26], among others), amputees could suffer from various issues at the tissue-prosthesis interface.

Acute infection, which generally occurs within the first three months post-surgery, is frequently caused by a vitriolic bacterial attack by *S. aureus*. Infection due to less malicious bacteria (*e.g.*, *P. acnes*) causes serious issues after several months of osseointegration. Symptoms of an infection are severe pain, swelling, and erythema at the skin-abutment interface with mild to high fever, followed by prosthesis loosening and discharge with sinus tract formation. Purulent discharging fistula can develop at the prosthesis interfaces with the formation of cellulitis or tissue necrosis, which can impair mobility and prosthesis function [26]. Infection can also lead to gradual loosening and implant malposition with dislocation instability [27]. Thus, monitoring signs of infections and identifying regions of infection for early treatment is critical.

It should be mentioned that the osseointegration involves a two-stage surgical process, and the patients need to undergo prolong rehabilitation after the final surgery [28]. The rehabilitation program comprises of a combination of dynamic and static load-bearing exercises (LBE), where it is hypothesized that the timely application of a suitable amount of strain on the implant would help to stimulate bone formation around the prosthesis and prepare the implant to withstand mechanical loading likely to occur during daily activities. In general, patients load the prosthesis twice a day for ~ 30 min [29]. It was reported by several researchers that different mechanical loads, rates of applied strain, strain distributions, and the number of strain cycles, to name a few, are important to influence the rate of bone growth around the tissue-prosthesis interface [30, 31]. At the same time, while a minimum effective strain is required to activate the bone adaptation process, overloading may place the bone-implant interface at risk [32]. Hence, the ability to

accurately measure implant strains and stresses would help doctors, and clinicians better understand the effects of different strain-states on bone-remodeling, ascertain the degree of osseointegration, and design a more efficient rehabilitation process for the patient. The ability to monitor strains also means that clinicians and patients can determine whether suitable amounts of strains are applied to the implant during LBEs [31]. In addition to monitoring uniaxial strains on the OIP, bending or flexural strains are also of interest. Excessive bending during extreme events (*e.g.*, a fall) would result in prosthesis loosening and bone fracture, especially during rehabilitation [33].

Despite these aforementioned reasons, prosthesis loosening can occur due to excessive motion and physical stress during rehabilitation or thereafter, increased shear force at the tissue-prosthesis interface due to misalignment, stress-shielding-related peri-prosthetic bone loss, mineralization defect, and infections, to name a few [34]. Failure of early assessment of prosthesis loosening can result in further complications, such as complete disbonding and bone fracture, which necessitates revision surgery and implant replacement. Hence, OIP monitoring is critical to ensure the safety of the amputees.

1.2 Current-State-of-Practice of Structural Monitoring

1.2.1 Monitoring Civil, Mechanical, and Aerospace Structures

The monitoring of civil, mechanical, and aerospace structural systems heavily relies on visual inspection. Bridges, buildings, railroads, aircraft, among others, are inspected by trained technicians in a regular and timely manner [35]. While visual inspection is a proven technique for damage detection in structures, innumerable disadvantages also exist:

- Visual inspection is qualitative. The method is also highly subjective as it relies on the interpretation of the technicians.
- Only the accessible locations can be inspected through visual inspection.
- Most of the time, structural damage occur at a subsurface level, and visual inspection is unable to detect such damage.
- Finally, being a time-, labor-, and cost-intensive method, the visual inspection cannot be performed frequently on large structures.

Recent advancement in robotic systems has transformed the traditional labor-intensive visual inspection into a fully autonomous process [36]. Critical locations of the structures, which are inaccessible to the technicians for visual inspection, can now be monitored by the unmanned robotic systems [37]. Additionally, being a fully autonomous method, the process is less expensive and does not require much time to complete the inspection. However, as the damage is inferred from the pictures taken by the robotic systems, the method is still limited to detect damage those are visible from the surface of the structures [38].

In order to enhance the objectivity of the visual inspection, sensing technologies and analytical methods are combined to facilitate structural health monitoring (SHM) [39]. Typically, discrete point sensors (*e.g.*, strain gages, accelerometer, linear voltage displacement transducers (LVDT), among others), are installed at the critical locations of the structures where large structural responses (*e.g.*, strain, displacement, accelerations) are expected. These discrete sensors are connected to a central data repository through coaxial cables for power supply and data storage [40]. The measured structural responses are fed into the model updating algorithm where the difference in measurements between the computationally obtained and the experimentally

measured responses is optimized while updating the structural parameters of a physics-based model of the structure [41-44]. From this discussion, it is clear that the accuracy of the model updating-based SHM technique can be significantly enhanced by deploying high-performance sensors in a densely distributed arrangement for structural response measurements.

1.2.2 Monitoring OIPs

Like structural monitoring, OIP monitoring also relies on visual inspection. For example, daily skin inspections can help to detect anomalies that suggest infection at the tissue-prosthesis interface. However, like in the case of structural monitoring, the early subcutaneous sign of infection at the tissue-OIP interface is often hard to detect by visual inspection. In critical circumstances, a more detailed clinical assessment is required. Different types of biosensors are used as a rapid and cost-effective method of bacterial infection detection [45, 46]. Biosensors-based infection monitoring can be performed at the point of care without the need for an expert's clinical assessment [47]. Such sensors generally have a biorecognition element that is connected to some transducer to convert specific bacterial analyte into a measurable quantity. Blood test [48], histopathological examination of periprosthetic tissues [49], intraoperative microbiological testing [50], synovial-fluid test [51] are some other most commonly used methods for infection detection at the tissue-prosthesis interface.

Besides infection monitoring, the stress-strain response of OIP has been studied by various researchers to explore the interaction of the prosthesis with the human body, especially during the rehabilitation. Like the SHM system described in Section 1.1.2, discrete sensors (*e.g.*, strain gage, accelerometer, load cells, among others) are directly attached to the prosthesis for strain, vibration, and load measurements [52]. Similar to the SHM of traditional structural systems, as the OIP

monitoring mostly performed through discrete sensor measurements, their objectivity also relies on the accuracy and robustness of the sensors.

1.3 Fundamental Limitations of the Current-State-of-The-Art

As mentioned earlier, the current SHM techniques mostly rely on the structural response measurements collected at discrete points. Hence, structural response measurements are only possible at the point of the installations of discrete sensors. Densely distributed networks of point sensors tethered with central data repository are required to achieve spatial sensing over a large area. However, the installation and maintenance of the coaxial cables are expensive. Additionally, direct damage detection is not possible from the sensor measurements. Measured sets of structural responses need to be processed through some model updating algorithm to extract the damage features. More research effort is required to achieve an accurate, robust, and computationally efficient model updating algorithm.

In the case of infection sensing at the OIP-tissue interface, one of the major limitations of the biosensors is their requirement for sample processing that increases the time and cost of these tests. In the case of strain, vibration, and load monitoring at the tissue-OIP interface, the installation of strain gages, accelerometers, and load cells on the OIP prosthesis is challenging. Sometimes, the stiff sensors attached to the prosthesis cause discomfort to the patients [53]. Additionally, some of the measured quantities (*e.g.*, vibration response measured by accelerometer) do not provide sufficient clinical information about prosthesis-residual limb interactions [54]. Strain gage-based devices generally consume more power than an accelerometer. Hence, perpetual data collection can only be performed when the devices are tethered to a power supply prohibiting their long-term

usage [55]. Poor resolution, crosstalk, and long-term fatigue of strain gages also limit their ability to measure high-frequency events [52].

1.4 Emerging Technologies for Structural Monitoring

From the above discussion, it is clear that new sensors need to be developed to address the limitations of the current-state-of-the-art. Researchers in the past three decades have proposed different types of sensors for structural response measurements. For example, wireless sensors have been developed and implemented as a cost-effective solution of SHM for both structural [56] and human health systems [57]. A typical wireless sensor node comprises a microcontroller, sensor, and radio [58]. Lynch and Loh [56] described wireless sensors as an interfacing point between the traditional sensors (*e.g*., strain gages, accelerometers, to name a few), mobile computing, and wireless communication elements. As the wireless sensors do not need to be tethered with the central data repository, the cost involved in setting up the coaxial cable connections can be eradicated. The densely distributed sensor network can be achieved by installing a series of wireless sensors at the critical locations of the structures. Such a system can provide more accurate and complete structural response measurements for damage detection through model updating. For instance, a densely distributed wireless sensor network for SHM of large structural systems was proposed by Kim *et al*. [59]. The designed system was implemented on a 4200-ft-long main span and the south tower of the Golden Gate Bridge. It was shown that ambient structural responses could be reliably measured without hindering the operation of the bridge. Cho *et al*. [40] prosed a smart wireless platform for modal identification of structural systems, which was implemented for the modal characteristic study of a balcony structure in a historic theatre in metropolitan Detroit. The measured vibration response was processed through the embedded algorithm to extract the modal features of the structure, and a good agreement was

found with the traditional offline methods. Lynch *et al*. [60] installed a total of 14 high-resolution wireless sensors in the concrete box girder of the Geumdang Bridge, Korea, to measure the acceleration response of the structure subjected to forced vibrations by a calibrated truck. The performance of the wireless system was found comparable with the traditional tethered SHM systems. More applications of wireless sensors for structural health monitoring can be found in [56, 61].

However, wireless sensors need to be powered through portable power supplies (*e.g*., batteries). As the batteries have a finite lifetime, they need to be replaced in a regular time interval. Usage of batteries in large volume also pose a long-term environmental risk with their disposal [62]. On-chip energy harvesting system has been reported as a potential solution to the power-related issue of the wireless sensors [63]. Nonetheless, extensive research needs to be performed to better understand its long-term behavior.

To overcome the power-related issues of the wireless sensors, radio frequency identification (RFID) sensors are developed and implemented for structural sensing [64]. Unlike traditional wireless sensors, RFID-based sensors do not need a constant power source. RFID sensors generally comprise a portable RFID reader and an RFID tag. The RFID tag consumes power from the reader through an inductive coupling action and stores the energy in its capacitive component. Upon finishing the sensor's interrogation, the remaining power is utilized to convert the measurement into a radiofrequency signal and transmitted to the reader [65]. Some key advantages of RFID-based sensors are listed below.

- RFID sensors do not require an active power source (*e.g*., battery).
- They are generally low-cost.

- RFID sensors are lightweight and have a reduced form factor.

Significant research efforts have been conducted in the past on RFID sensors for structural and human health monitoring. Yi *et al*. [66] developed an RFID-based sensor for strain and crack sensing. When the RFID tag is subjected to strain and deformation, its shape changes, resulting in a shift in the electromagnetic (EM) resonance frequency. They have demonstrated that such an RFID sensor has a resolution of 20 με and can operate over a large bandwidth (20 - 10,000 με). A high-gain reader was employed to achieve an interrogation distance of up to 2.1m. More applications of RFID sensors for SHM can be found in [67-69]. Besides mechanical response measurements, RFID sensors are also used for monitoring chemical actions (*e.g*., moisture [70, 71], gas [72, 73], temperature [74, 75], among others).

Apart from structural and chemical sensing, RFID sensors are also implemented for *in vivo* strain monitoring in implants. For example, Burny *et al.* [76] proposed an RFID sensor for strain sensing in implants. The device is capable of delivering energy and reading data from an implanted sensor. A miniaturized RFID sensor was developed by Korduba *et al*. [77] that can be embedded into a glass package for *in vivo* strain sensing in implants. More recently, an RFID-based passive wireless strain-sensing system is proposed by Burton *et al*. [78] for measuring low-level bone strain and high-level hoop strain associated with bone growth at the bone-OIP interface. The system is validated for low-level strain measurement (within −3000 to 3000 με) with a sensitivity of 4.555 Hz/με. More health-care-related applications of RFID-based sensing technology can be found in the comprehensive review article [79]. Apart from their huge potential as a cheap and reliable device for structural and human health monitoring, wireless and RFID sensors are discrete point senor, and they cannot measure damage directly. Furthermore, the installation of such sensors at the critical locations of the structures always remains challenging. RFID measurement

is sensitive to ambient conditions and influenced by the presence of metals and liquids in its vicinity. Additionally, the high market price of RFID reader prohibits their widespread applications.

The location and severity of damage within structural components can be detected through ultrasonic inspection. For example, guided wave-based damage detection is popular in the aerospace industry as the process is suitable to be implemented in complex-shaped structural components. Senyurek [80] utilized a lamb wave-based technique for damage detection in actual wing slats of Boeing 737 aircraft. Four lead zirconate titanate (PZT) transducers were installed to the slats to create surface waves and to monitor their propagation. The study indicated that the defects of over 3-m-long slats could be detected if the traducers are accurately installed. An and Shon [81] employed surface-mounted PZT-generated guided wave signals for detecting bolt loosening, notch, and delamination in structures. The technique was found suitable for damage detection in varying temperature conditions. More application of guided-wave technology for damage detection in structural systems can be found in [82-85].

Apart from structural applications, the guided wave method is also explored for implant monitoring. For instance, Vayron *et al*. [86] proposed the ultrasonic method for *in vivo* dental implant monitoring. They have shown through extensive numerical simulation that ultrasonic response changes significantly when a semi-solid to liquid layer is present at the tissue-implant interface compared to the case of a fully boned implant. This finding suggests that the proposed method can be used for monitoring the osseointegration process at the tissue-OIP interface. The same group of researchers also investigated the ultrasound method to assess the amount of bone in contact with implants [87]. Experimental results presented in this article demonstrate the potential of the method for *in vitro* stability assessment of the implants. More recently, Wang and Lynch

[88] implemented a guided wave to monitor prosthesis loosening and osseointegration. Piezoelectric transducers were mounted on OIP surrogate to generate a guided wave that can propagate along the length of OIP. It was hypothesized that protheses loosening or post-surgical healing could influence the propagation of the guided wave, thereby facilitating OIP monitoring. Through numerical modeling of guided wave propagation and corresponding experimental study, it was validated that the energy of the longitudinal wave mode decreases during the healing of the wound in a post-surgical state. On the contrary, it was also shown that wave energy increases during prostheses loosening. Besides the vast potential of the guided wave method for structural and human health monitoring applications, the linear assumption about the wave response and damage indices diminish the sensitivity of the guided wave methods to identify smaller damage in the structures hence limiting its applications as an early damage detection system [89]. Additionally, damage cannot be directly measured from the wave propagation model-based damage identification techniques.

Rapid advances in fabrication technology have facilitated the development of a new class of sensors called microelectromechanical (MEMS) sensors. MEMS devices can be found in a wide range of applications from mechanical sensors to electronic particle detector that helps for nuclear, biological, and chemical inspection, among others [90]. Their reduced size helps their installation, especially within a small area in a densely-distributed arrangement. Their lightweight structure facilitates densely distributed installation in aerospace systems (*e.g.*, aircraft, space shuttles, among others), causing a negligible increment to the total weight of the structures.

MEMS devices are manufactured using very large-scale integration (VLSI) technology and can embody both mechanical and electrical functions. Bedon *et al*. [91] prototyped a MEMS-based accelerometer and deployed for a cable-stayed bridge monitoring in Pietratagliata (Italy). The

measured vibration responses were used for experimental modal analysis. It was shown that *in situ* vibration response measurements can be reliably achieved by the developed MEMS accelerometers, and the collected measurements were used for modal parameter identification. MEMS sensors are also successfully used as strain gage [92], pressure [93], and corrosion sensors [94], among others.

Besides structural response measurements, MEMS sensors are also extensively used for prosthesis monitoring. For example, Weinberg *et al*. [95] proposed a MEMS-based gyroscope that can be attached to the prosthesis devices for real-time tilt measurements. A polyimide-based MEMS strain-sensing device has been proposed by Hasenkamp *et al*. [96] for monitoring strain-states in artificial knee implants. They demonstrated the sensor is capable of measuring axial strain caused by vertical loading with good sensitivity. More works related to MEMS sensors in the biomedical domain can be found in [97]. However, MEMS sensors generally suffer from large drift over temperature necessitating deployment of a sperate temperature compensation unit or heating arrangements along with the sensor. In addition, MEMS sensors typically have lower precision relative to other traditional sensors.

1.5 Need for New Sensing Technologies

From Section 1.4, it is clear that the SHM field is undergoing a paradigm shift with the development of new sensing technologies (*e.g.*, wireless sensors, guided wave method, MEMS, among others). However, some limitations still exist.

- They are point sensors. As a result, hundreds of sensors are required to achieve spatial sensing.

- Damage can even occur between two sensing nodes. In such a case, damage localization is challenging.
- Sophisticated fabrication process is required for sensor fabrication (*e.g.*, MEMS).
- Damage cannot be directly inferred from the measurements. Recorded measurements need to be processed through some model updating algorithms to extract damage features.
- The method like guided wave can perform spatial sensing; however, advanced signal processing algorithms are required for data processing and subsequent reliable damage detection.

This dissertation aims to take advantage of nanotechnology to develop new materials-based sensor and coupled them with tomographic imaging to achieve distributed spatial sensing for structural and human health monitoring.

1.6 Materials-Based Sensing

Recent advancements in nanotechnology have opened up a new horizon of research on the development of advanced materials with enhanced engineering properties. Among a plethora of nanomaterials, quantum dots, nanoparticles, fullerenes, nanotubes, and nanowires received significant research attention because of their impressive material properties [98]. Nanotechnology also offers new ways for isolating, controlling, and assembling nanomaterials for attaining high-performance functional systems [99]. Nanotechnology-based state-of-the-art fabrication and characterization tools can be leveraged to design a new class of materials-based sensors that can potentially overcome the limitations of current sensors technology. For example, materials with unique electromechanical properties, can be fabricated starting at a molecular-length scale and

thereafter scaled up to macro-level with precise bulk sensing properties following the "bottom-up" fabrication process.

Among various nanomaterials, carbon nanotube (CNT) and graphene have drawn significant attention as sensing materials due to their superior electromechanical properties. Since their discoveries, many researchers have used them as sensing elements. For instance, an attempt was made to characterize the piezoresistive response of individual single-walled carbon nanotube (SWCNT) under mechanical loading [100]. Individual SWCNT was subjected to a three-point bending test while its electrical resistance was simultaneously measured. Force was applied by an atomic force microscope (AFM) tip. This experiment revealed that conductance of the SWCNT is sensitive to deformation, and it decreases by two orders of magnitude when subjected to deformation confirming the superior electromechanical property. Similar research was performed by Smith *et al.* [101] to characterize the piezoresistive response of graphene. In this study, the graphene sheet was suspended over a cavity of a silicon wafer and subjected to pressure while its electrical property was measured. It was found that the pressure sensitivity exhibited by graphene was about 20 to 100 times higher than the other pressure sensors. However, more technological development is required to transfer such impressive sensing properties of the nanomaterials from the nanoscale to a tangible length scale for structural sensing.

As a solution, nanomaterials have been investigated for creating multifunctional coatings or thin films that can be deposited onto the structural surface to achieve sensing. Nanomaterials can be dispersed in a polymeric solution, and thereby, using a bottom-up fabrication technique, they can be scaled up to a macro level for large-scale applications. Numerous thin film fabrication techniques are available and have been employed for assembling nanomaterials within a polymer matrix. For example, extensive work has been conducted to fabricate CNT-based "buckypaper"

by vacuum filtering the polymeric solution of CNT [102]. Besides vacuum filtration, examples of other fabrication methods include polymer casting [103], epoxy molding [104], spin coating [105], layer-by-layer (LbL) [106], shear mixing [107], among many others [108]. Some advantages of such materials-based sensors are listed below.

- Materials have unprecedented functionalities. Multiple sensing properties can be encoded in one material.
- Materials-based sensors are densely distributed by nature.
- The sensor fabrication procedures are scalable and low-cost.
- Such materials-based sensors can be easily integrated with the host structure or combined with structural materials to achieve distributed sensing.
- Direct damage detection is possible from the measured electrical responses.

The idea of fabricating nanocomposite-based thin film sensors is not new. The First CNT-based thin film for strain sensing was developed by Dharap *et al*. [109] through vacuum filtration. It was demonstrated that voltage across the film linearly varies in tandem with the applied tensile and compressive stresses. Shortly thereafter, Loh *et al*. [105] developed a multifunctional SWCNT-based thin film with enhanced electromechanical properties by LbL fabrication process. The superior mechanical property of the LbL thin film makes them appropriate for *in situ* applications where extreme loading is expected. It has been shown that the desired sensing property can be encoded in the LbL thin film by using a suitable polyelectrolyte (PE). First, a piezoresistive thin film (strain sensitivity ~ 4.5) was fabricated by dispersing SWCNTs in poly(sodium 4-styrene-sulfonate) (PSS) and polyvinyl alcohol (PVA) solution. Second, an SWCNT-PSS-polyaniline (PANI)-based thin film was fabricated by LbL method for pH sensing

(pH sensitivity up to 20.66 kΩ cm^{-2}/pH). As pH can be monitored as an indicator of corrosion in structures, this thin film can be used for corrosion monitoring.

Instead of measuring the electrical response of the thin film at every point, an electrical impedance tomography (EIT) algorithm and measurement strategy were implemented for the spatial conductivity reconstruction of the entire thin film [110]. EIT is a soft-field imaging technique where spatial conductivity distribution of a predefined region can be reconstructed from boundary electrical measurements [111]. The location and severity of the damage induced by excessive strain/ corrosion can be directly inferred from the reconstructed conductivity maps of the thin films. Although such materials-based sensors have the potentials to solve some of the present challenges in the SHM domain, some limitations still exist.

- LbL fabrication process is time- and labor-intensive. For example, it requires more than a day to fabricate a 20 × 10 mm^2 thin film. Therefore, it may not be an economical solution to manufacture thin films for large-area applications.
- As the thin film is integrated with the structure as a surface coating, structural responses can only be measured at surface level. Hence, subsurface damage cannot be detected by this method.
- EIT is unable to measure the induced strain in the different directions over a structural surface.
- Spatial sensing was performed on small-sized thin film in the laboratory environment. Large-scale *in situ* applications of the proposed technique remains unexplored.
- EIT still needs the instrumentation of a series of boundary electrodes for interrogation and measurements. Hence, the process is contact-based.

1.7 Research Objective and Dissertation Outline

This dissertation aims to solve these technology gaps by combining the new generation nanomaterials-based thin film sensors with advanced soft-field tomographic imaging techniques, which serve as the primary foundations for damage detection in structural and human health systems. In particular, multi-walled carbon nanotubes (MWCNT) and graphene nanosheets (GNS) were used to develop thin film sensors. These nanomaterials were self-assemble in polymeric solutions to form homogeneous nanocomposites. The spray fabrication method is extensively used as a scalable, low cost, and time-efficient process to fabricate the nanocomposite thin film sensors for large-scale applications. Instead of using the nanocomposite as a structural coating, this dissertation shows how these thin films can be integrated with structural materials to encode self-sensing property and thereby interrogated with EIT for distributed sensing. In addition, this also demonstrates how these nanocomposites can be combined with a noncontact tomographic mapping algorithm and measurement strategy to achieve structural monitoring at a subsurface level.

Chapter 2 describes the mathematical formulation of EIT. In addition to EIT, electrical capacitance tomography (ECT) is introduced as a noncontact, subsurface, radiation-free imaging tool. Upon initial validation of the proposed algorithms, they were implemented in subsequent chapters for structural and human health monitoring.

An MWCNT-PSS nanocomposite was designed in Chapter 3, whose electrical conductivity is sensitive to strain and deformation. A scalable, efficient, and low-cost spray fabrication technique was employed to deposit the nanocomposite thin film over large structural areas. Instead of using the thin film as a structural coating, it was integrated with cementitious composites so that the entire structure can serve as a sensor. This was achieved by nanoengineering

the cement-aggregate interface prior to cementitious composite casting. As every point in the cementitious composites became sensitive to damage, the EIT algorithm described in Chapter 2, was employed to produce electrical maps that indicated the locations and severities of spatially distributed damage in self-sensing cementitious composites. However, the main limitation of this technique is the low strain sensitivity of the thin film as well as the inability of EIT to measure induced strain in different directions.

These issues were addressed in Chapter 4 by patterning a highly piezoresistive graphene-based thin in the form of a "sensing mesh." GNS-PVA-based nanocomposite was fabricated and deposited into a "mesh"-like pattern by spray fabrication. Each strut of the sensing mesh with a high aspect ratio act as a linear strain sensor that is capable of measuring strain components along their lengths. EIT algorithm was also updated to capture such uniaxial change in conductivity of each strut in the sensing mesh. The estimated change in the conductivity at each strut was directly correlated with the strain induced in along their axial length. The sensing mesh was also employed to capture spatially distributed damage in a seven-story reinforced-concrete (RC) building subjected to earthquake ground motion. However, the employment of sensing mesh on the structural surface does not facilitate subsurface strain/ damage measurements. In addition, EIT requires a series of boundary electrodes to be instrumented at the boundary of the sensing region, which may not be a feasible option for human health monitoring (*e.g.*, monitoring OIPs).

To overcome these issues, Chapter 5 implements ECT and stimuli-responsive nanocomposites, particularly for monitoring OIPs. The design of the MWCNT-based thin film was modified in such a way that their electrical permittivity is sensitive to various external stimuli (*e.g.*, pH and strain). The developed nanocomposite thin films and the noncontact imaging technique was implemented for infection and strain monitoring in OIPs. It is hypothesized that the

nanocomposite thin film can be deposited onto prosthesis before surgery. As subcutaneous infection causes a local pH change in the infected cells, the thin film would experience an electrical permittivity change that can be captured through ECT in a noncontact fashion. Similarly, strain-sensitive nanocomposite can be deposited on prothesis and interrogated by ECT to realize noncontact strain monitoring. In addition to nanocomposite-enabled infection and strain monitoring in OIPs, ECT, being a noncontact, radiation-free imaging tool, was applied for prosthesis loosening and bone fracture monitoring.

Although ECT has the potential to be a subsurface damage identification tool, the circular geometry of the ECT electrode array may not be suitable for the inspection of large composite structures. In Chapter 6, the geometry of the traditional circular ECT electrode array was modified into a planar system so that it can be used by the technicians as a handheld instrument to rapidly assess the subsurface condition of the large composite structures. Computational and experimental studies were performed to demonstrate the potential of the proposed system for subsurface damage detection in composite structures. Finally, Chapter 7 summarizes the significant findings and concludes the dissertation by identifying the potential future direction of the research.

CHAPTER 2 SOFT-FIELD TOMOGRAPHIC IMAGE RECONSTRUCTION

2.1 Introduction

The primary objective of this chapter is to establish the mathematical foundations of the tomographic imaging techniques, which will be used in conjunction with the nanocomposite thin film sensors to achieve spatial sensing. As discussed in Chapter 1, every point on the nanocomposite thin film sensors is sensitive to external stimuli. Hence, electrical measurements can be taken at each point over the entire thin film's surface to obtain the film's electrical map. As the electrical properties of the thin films are sensitive to external stimuli, the electrical maps obtained from point measurements will represent the damage state of the entire structure. However, point measurement is time-, labor-, and cost-intensive. The tomographic imaging techniques proposed in this chapter can estimate the spatial distribution of electrical properties over a large area from a limited number of electrical measurements obtained at the boundary.

In general, tomographic imaging is a method to generate cross-sectional images of an object using non-ionizing radiation. In the case of hard-field imaging (*e.g.*, X-ray), the radiation wave is generated and allowed to propagate through the area to be imaged. The property of the medium, which directly interacts with the propagating radiation beam, influences some measurements. In that essence, such hard-field imaging techniques are known as "local imaging." However, at a lower frequency, a local change in material property affects all the measurements. Due to such nonlocal effects, imaging of electrical parameters through low-frequency excitations are difficult. To estimate the electrical property distributions within a specified domain, first, one needs to derive a set of simultaneous equations correlating each measurement with every possible point inside the interrogation region. Second, the electrical property of the interrogated region

needs to reconstructed from the boundary measurements. In this chapter, the mathematical formulations of two different tomographic imaging techniques are described in detail. They are:

- EIT
- ECT

In EIT, the spatial conductivity distribution of a predefined sensing domain is reconstructed from the limited number of boundary voltage measurements [111]. EIT was successfully used in biology and biomedical fields of study for obtaining electrical images and for revealing anomalies inside the bodies of humans or animals. For example, the rate of gastric emptying was studied with the aid of EIT by Barber [112], in which the spatial resistivity distribution of the stomach was evaluated as a function of time so as to obtain an emptying curve. More applications of EIT on gastric imaging can be found in Dijkstra *et al*. [113] and Smallwood *et al*. [114]. Other applications of EIT include the assessment of pulmonary and cardiac parameters, [115-118] detection of internal intraventricular hemorrhages in newborns [119], and the diagnosis of intrathoracic fluid volume, [120] among others.

Although EIT has been successfully demonstrated in bio-related disciplines, its applications for SHM remain fairly new and require further development. As mentioned in Chapter 1, early work by Hou *et al*. [110] showed that EIT could be coupled with LbL CNT-based thin films for monitoring spatially distributed strain and corrosion monitoring. Zhang *et al*. [121] demonstrated the SHM potential of EIT in glass fiber-reinforced polymer (GFRP) composites, where glass fibers were laminated with an epoxy resin containing carbon black. This process enhanced the electrical conductivity of GFRP, and the damage was detected within the composite by calculating the in-plane and through-thickness conductivity changes with the aid of electrical

resistance tomography. Tallman *et al*. [122] also showed that epoxy composites could be filled with carbon nano-fibers (CNFs) for encoding self-sensing characteristics. Local changes in conductivity due to damage in CNF-enhanced epoxy composites were also captured using EIT. Instead of CNT- or CNF-based materials, Hallaji *et al*. [123] employed colloidal silver paints applied directly onto concrete surfaces, and localized changes in electrical conductivity due to cracking or surface damage were subsequently detected by EIT analysis. On the other hand, Hou and Lynch [124] applied EIT for directly mapping the spatial conductivity distributions of engineered cementitious composites and detected regions in which micro-cracking occurred during load testing. Besides all these wide-spread applications of EIT, it should be mentioned that a series of boundary electrodes needs to be attached at the boundary of the sensing region for EIT interrogation and measurements. It could be difficult for some applications to achieve so many electrical connections at the boundary.

On the other hand, ECT seeks electrical permittivity reconstruction from noncontact boundary capacitance measurements [125]. A series of boundary electrodes are equidistantly arranged in a circular array for electrical excitation and measurements. Each electrode is excited with alternating current (AC) signal, and the resulting mutual capacitance between boundary electrode pairs are measured. Spatial electrical permittivity distribution within the region circumscribed by the electrode array is reconstructed from the boundary capacitance measurements. In contrast to EIT, ECT does not require the electrodes to be physically attached to the object to be imaged.

Since the development of ECT in the 1980s [126], it has mainly been used for flow monitoring in applications such as gas separation [127]; pneumatic conveyors [128]; and, more recently, fluidized bed dryers [129]. ECT has also been used for monitoring other industrial

processes (*e.g.*, visualization of flame during combustion [130], nylon-polymerization reaction monitoring [131], and curing monitoring of epoxy resins [132], among others). In addition, ECT was recently used as a nondestructive evaluation (NDE) tool to assess the subsurface condition of structures [133, 134].

Apart from the above-mentioned industrial applications, ECT is also used in biomedical imaging. A dual-modality imaging technique, using EIT and ECT, was proposed by Ren *et al*. [135] to provide real-time 3D images to navigate surgery tools in the femoral bone during total hip replacement. Taruno *et al*. [136] suggested a real-time, volumetric, capacitance-based imaging technique for monitoring brain activities related to human motoric and lung functions.

In general, the mathematical formulation of tomographic imaging techniques can be described into two parts: **a.** forward problem, and **b.** inverse problem. The forward problem aims to predict the boundary electrical responses for an explicitly known electrical property distribution. On the other hand, the inverse problem needs to be solved to reconstruct the distribution of electrical properties from the measured set of boundary responses. In this chapter, forward problems of EIT and ECT are presented. While the forward problem models of EIT and ECT are different, the same inverse problem can be applied for both EIT and ECT image reconstruction.

2.2 Forward Problems

As mentioned earlier, the tomographic forward problem is a computational platform to predict the electrical responses of the system, while the distributions of electrical properties are known. EIT and ECT forward problems are discussed in the following sections.

2.2.1 EIT Forward Problem

EIT forward problem estimates the boundary voltage measurements while the conductivity distribution of a predefined area is known. In general, a series of boundary electrodes are equidistantly arranged at the boundary of a conductive object. An electrical current is injected in the conductive object through a specified pair of boundary electrodes. The resulting voltage differences between the remaining adjacent pairs of boundary electrodes are measured. In this study, "adjacent" and "across" injection patterns are used for EIT interrogation [137]. For adjacent injection, the adjacent pairs of boundary electrodes are used at a time for current injection and grounding purposes, and the resulting voltage differences are measured between the remaining pairs of boundary electrodes. In the case of N electrode EIT system, a total $N\cdot(N-3)$ number of voltage measurements can be obtained through the adjacent injection pattern. In the case of the across injection, opposite electrode pairs are employed for electrical excitation and grounding purpose. The resulting voltage differences between the remaining adjacent electrode pairs are measured. In the case of across injection, a total $N\cdot(N-4)$ voltage measurements can be collected and used for image reconstruction. The excitation and measurement procedures for adjacent and across injection patterns are schematically shown in Figures 2.1a and 2.1b, respectively.

2.2.1.1 Physical Model

The first step of the EIT forward problem is to create a physical model that correlates the input, output, and electrical conductivity. The physical model of EIT can be derived from Maxwell's equations:

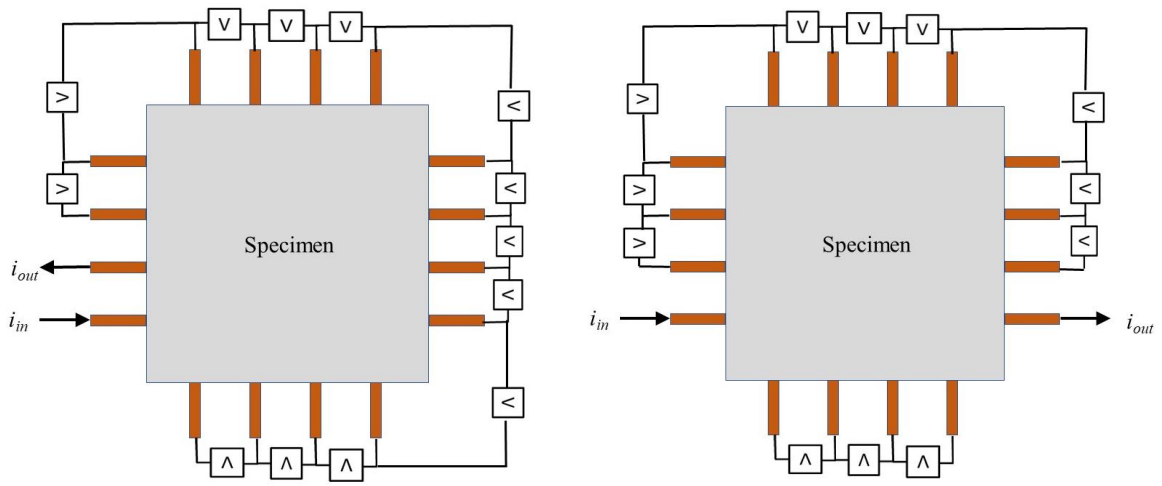

(a) (b)

Figure 2.1 EIT (a) adjacent and (b) across injection patterns and measurement strategies are schematically shown.

$$\nabla \times E = -\frac{\partial B}{\partial t} \tag{2.1}$$

$$\nabla \times H = J + \frac{\partial D}{\partial t} \tag{2.2}$$

where E is the electric field, B is the magnetic induction, H is the magnetic field, D is the electric displacement, and J is the electrical current density. In general, low-frequency alternating current (AC) is used for EIT interrogation. In that case, E and B can be represented as a time-harmonic function of the circular frequency (ω) of excitation current:

$$E = \tilde{E} e^{i\omega t} \tag{2.3}$$

$$B = \tilde{B} e^{i\omega t} \tag{2.4}$$

where $\tilde{E}$ and $\tilde{B}$ are the magnitudes of the oscillating electrical and magnetic induction, respectively. For isotropic conductive materials, *D*, *B*, and *J* can be written in the forms shown in equations 2.5 to 2.7:

$$D = \varepsilon E \tag{2.5}$$

$$B = \mu H \tag{2.6}$$

$$J = \sigma E \tag{2.7}$$

where ε, μ, and σ are the electrical permittivity, magnetic permeability, and electrical conductivity, respectively. Equations 2.3 and 2.4 can be expressed in the form of equations 2.8 and 2.9, respectively, with the assumption of time-harmonic electrical excitation.

$$\nabla \times E = -i\omega\mu H \tag{2.8}$$

$$\nabla \times H = J + i\omega\varepsilon E \tag{2.9}$$

In EIT, *J* can be modeled as an integral of the source density (J^s) and ohmic-current density (J^o) as shown in equation 2.10.

$$J = J^o + J^s \tag{2.10}$$

J^o can be expressed as a product of σ and *E*, as shown in equation 2.11.

$$J^o = \sigma E \tag{2.11}$$

Equation 2.9 can be written as equation 2.12 by replacing *J* in equation 2.9 with the expression obtained from equations 2.10 and 2.11.

$$\nabla \times H = \left(\sigma + i\omega\varepsilon\right)E + J^s \tag{2.12}$$

To further simplify equation 2.12, *E* can be expressed in the form of equation 2.13:

$$E = -\nabla u - \frac{\partial A}{\partial t} \tag{2.13}$$

where *u* and *A* are the electric potentials and magnetic vector potential, respectively. For low-frequency excitation, the effect of magnetic vector potential on *E* can be neglected, and the equation 2.13 can be rewritten as equation 2.14.

$$E = -\nabla u \tag{2.14}$$

In EIT, the capacitive effect (*i.e.*, $i\omega\varepsilon E$) is often neglected. However, this assumption may not be valid for high-frequency excitation and a lower value of σ. This will be explained in Section 2.2.2.

With the above assumptions, equation 2.12 can be written in the form of equation 2.15.

$$\nabla \times H = \sigma E + J^s \tag{2.15}$$

If we take divergence on both sides of equation 2.15, the governing equation for EIT inside a conductive body is obtained:

$$\nabla \cdot \left(\sigma \nabla u\right) = 0 \tag{2.16}$$

Equation 2.16 is valid for the steady-state electrical condition when there is no accumulation of electrical charge inside the conductive object (Ω). In order to achieve the most accurate solution of equation 2.16, proper boundary conditions need to be implemented to obtain the most accurate

solution of the EIT forward problem. The boundary conditions for EIT are discussed in Section 2.2.1.2.

2.2.1.2 Boundary Conditions

By applying the conservation of total electrical charge inside and outside of the Ω, the expression for current density at the boundary can be obtained:

$$\sigma \frac{\partial u}{\partial n} = -J^s \cdot n \equiv J^s \cdot n \equiv j \tag{2.17}$$

where n is the unit outward normal on the boundary of Ω at the point of current injection, and j is the negative normal component of J^s.

In the theoretical formulation of the EIT forward problem, applied electrical current and boundary voltage distributions are taken into account as continuous functions along the entire boundary. Previous research showed that the representation of boundary excitations and voltage measurements in a continuum sense overestimates the resistivity [138]. In this study, discrete boundary electrodes are employed and distributed throughout the entire boundary (Γ) of Ω, and electrical current injection and voltage measurements are only considered at these electrodes. Typically, the "complete electrode model" (CEM) (equations 2.18 and 2.19) is used as the boundary conditions in EIT forward model [111, 125] CEM allows to model the shunting effect and contact impedance between the electrode and the body without any overestimation.

$$\int_{e_l} \sigma \nabla u \cdot n = I_l \quad \text{on } \Gamma_1 \tag{2.18}$$

$$\sigma \nabla u \cdot n = 0 \quad \text{on } \Gamma_2 \tag{2.19}$$

Here, e_l is the area of l^{th} electrode, and I_l is the current in the l^{th} electrode on the surface as defined by a normal vector, n, perpendicular to that surface. Γ_1 is the region of the boundary associated with all the electrodes, and Γ_2 is the remainder of the boundary. Contact impedance between electrodes and the body is taken into account in equation 2.20, which is used to calculate the boundary electrode voltages.

$$u + z_l \sigma \nabla u \cdot n = V_l \text{ on } \Gamma_1 \tag{2.20}$$

where z_l is the contact impedance at the l^{th} electrode, and V_l is the measured voltage at the l^{th} electrode.

2.2.1.3 Finite Element (FE) Formulation of EIT Forward Problem

The second-order partial differential equation shown in equation 2.16 needs to be solved with boundary conditions specified in equations 2.18 to 2.20 to get the boundary voltage distribution. Several numerical methods have been implemented for solving this elliptic partial differential equation. Sherina *et al.* [139] used the finite volume method for an unstructured grid. Lazarovitch *et al.* [140] employed the finite difference (FD) method for solving equation 2.16. Besides these, the FE method remains to be one of the most widely used numerical tools for obtaining robust and accurate solutions [111, 125].

The subsequent weak-form of the EIT problem has been derived by multiplying equation 2.16 with a sufficiently smooth arbitrary test function (v) and integrating over the entire Ω:

$$\int_{\Omega} v \nabla \cdot (\sigma \nabla u) = 0 \tag{2.21}$$

Integrating equation 2.21 using integration by parts results in boundary expressions as follows:

$$\int_{\Omega} \sigma \nabla u \cdot \nabla v dx^2 = \int_{\Gamma} \sigma \nabla u \cdot n v dx \tag{2.22}$$

The right-hand-side of equation 2.22 can be rewritten as equation 2.23.

$$\int_{\Omega} \sigma \nabla u \cdot \nabla v dx^2 = \int_{\Gamma_1} \sigma \nabla u \cdot n v dx + \int_{\Gamma_2} \sigma \nabla u \cdot n v dx \tag{2.23}$$

Substituting equations 2.18 and 2.20 into equation 2.23 yields:

$$\int_{\Omega} \sigma \nabla u \cdot \nabla v dx^2 + \sum_{l=1}^{L} \frac{1}{z_l} \int_{e_l} u v dx = \sum_{l=1}^{L} \frac{1}{z_l} \int_{e_l} V_l v dx \tag{2.24}$$

where L is the total number of boundary electrodes. According to FE theory, the electric potential, u, is approximated (u^h) as a linear combination of nodal voltage (u_i) and the nodal shape function (ϕ_i).

$$u^h = \sum_{i=1}^{n} u_i \phi_i \tag{2.25}$$

Four-node bi-linear quadrilateral elements can be used to discretize the entire domain, as shown in Figure 2.2a. The properties of the shape functions are shown in Figure 2.2b. All the calculations have been carried out in the regular bi-unit square domain and thereafter transferred into the real domain using iso-parametric formulation [141].

Galerkin's approximation states that the test function can be chosen to be the same as the nodal shape function, which turns equation 2.24 to the following form:

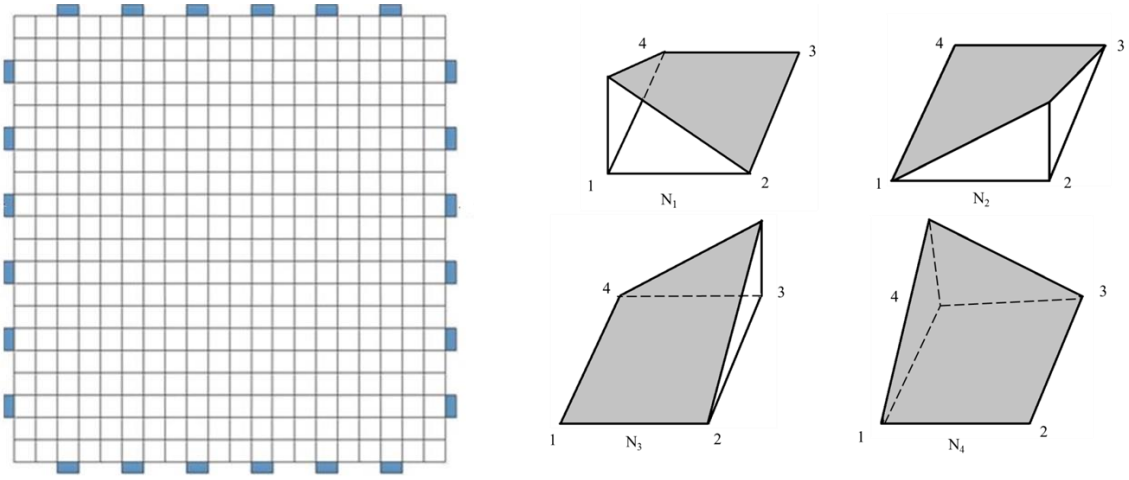

(a) (b)

Figure 2.2 (a) A two-dimensional finite element model of the EIT specimen was generated using quadrilateral elements with bi-linear basis functions. (b) Four shape functions and their values at each node of a four-node quadrilateral element are shown. The values of the shape function corresponding to the i^{th} node is 1 at that node and 0 at all other nodes in accordance with the compacted support property.

$$\sum_{i=1}^{n} u_i \left(u_i \nabla \phi_i \cdot \nabla \phi_j dx^2 + \sum_{l=1}^{L} \frac{1}{z_l} \int_{e_l} \phi_i \phi_j dx \right) = \sum_{i=1}^{n} \frac{1}{z_l} \int_{e_l} V_l \phi_j dx \tag{2.26}$$

The boundary condition mentioned in equation 2.18, when applied on u^h and combined with equation 2.20, results into L number of additional linear equations:

$$\frac{1}{z_l} V_l \mid e_l \mid - \sum_{i=1}^{n} \left(\int_{e_l} \frac{1}{z_l} \phi_i dx \right) u_i = I_l \tag{2.27}$$

Assembling all these expressions finally leads into a matrix equation of the following form:

$$Au = I \tag{2.28}$$

where A, u, and I are the global conductivity matrix, a vector containing the nodal values of potential distribution, and generalized current vector, respectively. A is composed of four elementary matrices A_M, A_Z, A_V, and A_D:

$$A = \begin{bmatrix} A_M + A_Z & A_V \\ A_V^T & A_D \end{bmatrix} \tag{2.29}$$

where,

$$A_M(i,j) = \iint_{\Omega} \sigma \nabla \phi_i \cdot \nabla \phi_j dx^2 \tag{2.30}$$

$$A_Z(i,j) = \sum_{l=1}^{L} \frac{1}{z_l} \int_{e_l} \phi_i \phi_j dx^2 \tag{2.31}$$

$$A_V(i,l) = -\frac{1}{z_l} \int_{e_l} \phi_i dx \ (i=1{:}n \text{ and } l=1{:}L) \tag{2.32}$$

$$A_D(k,l) = \frac{1}{z_l} |\, e_l \,| \ (\text{for } l=k) \tag{2.33}$$

$$A_D(k,l) = 0 \ (\text{for } l \neq k) \tag{2.34}$$

Figure 2.3 shows the electrical potential distribution over the entire EIT specimen when two diametrically opposite electrodes were employed for current injection and grounding purposes. It can be observed that the magnitude of electrical potential is comparatively higher near the excitation electrodes, and it gradually decreases toward the grounding electrodes.

2.2.1.4 Jacobian Calculation

It is evident from equation 2.16 that *V* is a nonlinear function of σ. In order to recover σ from measured *V*, some nonlinear optimization strategies should be implemented for conductivity reconstruction. However, nonlinear optimization algorithms are computationally expensive and time-consuming. As a result, they are avoided for EIT-based image reconstruction. In general,

there are mainly two approaches to tackle this problem. For both cases, the EIT forward model is linearized at some background conductivity (σ_o). In the first approach, Gauss-Newton (GN) iterative algorithm is used to reconstruct the absolute conductivity distribution by minimizing the L^2 norm of the difference between the experimentally (V_m) and numerically obtained (V_c) voltage sets. In the case of the second approach, the change in boundary electrical voltages (δV) is recorded before and after an event (*e.g.*, damage). This δV is used to estimate the change in electrical conductivity due to the occurrence of the event. Although the absolute conductivity distribution is not reconstructed, the second approach is faster than the iterative absolute reconstruction process. For both cases, the jacobian (J_{EIT}) of the discrete conductivity maps needs to be calculated. J_{EIT} can be expressed in the form shown in equation 2.35:

$$J_{EIT} = \begin{pmatrix} \frac{\partial V_1^1}{\partial \sigma_1} & \cdot & \frac{\partial V_1^1}{\partial \sigma_N} \\ \cdot & \cdot & \cdot \\ \frac{\partial V_1^K}{\partial \sigma_1} & \cdot & \frac{\partial V_1^K}{\partial \sigma_N} \\ \cdot & \cdot & \cdot \\ \frac{\partial V_L^K}{\partial \sigma_1} & \cdot & \frac{\partial V_L^K}{\partial \sigma_N} \end{pmatrix} \tag{2.35}$$

where V_j^i is the j^{th} voltage measurements corresponding to the i^{th} current injection pattern, and σ_i is the conductivity of i^{th} element in the FE mesh. From equation 2.35, it is clear that J_{EIT} is basically the set of data that correlates the change in each boundary voltage in response to a small perturbation of the conductivity of each element.

The most straightforward way to calculate the jacobian is to estimate the change in boundary voltage in response to a small change in conductivity of each element in the finite

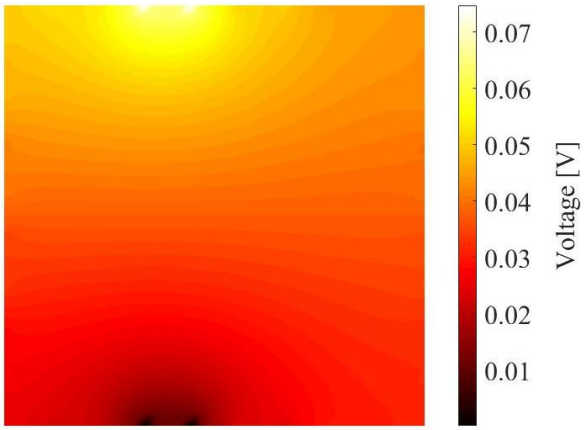

Figure 2.3 Voltage distribution over the finite element domain of the EIT model is shown when DC current was injected through opposite electrode pairs.

element mesh. However, the process is time-consuming and computationally expensive as the forward problem needs to be solved for each FE voxel. A computationally efficient method to calculate J_{EIT} was proposed by Yorkey and Webster [142]. It was shown that the i^{th} column of J_{EIT} could be obtained from the set of linear equations expressed in matrix form (equation 2.28), as shown in equation 2.36:

$$\frac{\partial u}{\partial \sigma_n} = \frac{\partial (A^{-1} I)}{\partial \sigma_n} \tag{2.36}$$

Equation 2.36 can be further simplified in the form shown in equation 2.37:

$$\frac{\partial u}{\partial \sigma_n} = -A^{-1} \frac{\partial A}{\partial \sigma_n} A^{-1} I = -A^{-1} \frac{\partial A}{\partial \sigma_j} u \tag{2.37}$$

$\partial A / \partial \sigma_n$ can be evaluated using equation 2.38:

$$\frac{\partial A}{\partial \sigma_n} = \begin{bmatrix} \frac{\partial A_M}{\partial \sigma_n} & 0 \\ 0 & 0 \end{bmatrix} \tag{2.38}$$

$\partial A_M / \partial \sigma_n$ in equation 2.38 is calculated using equation 2.39:

$$\frac{\partial A(i, j)}{\partial \sigma_n} = \int_{\Delta_n} \nabla \varphi_i \cdot \nabla \varphi_j dA \tag{2.39}$$

where Δ_n is the area of n^{th} finite element. The formulated J_{EIT} has been used for conductivity reconstruction from the experimentally obtained voltage measurements.

2.2.2 ECT Forward Problem

In contrast to EIT, ECT seeks electrical permittivity distribution of a predefined sensing region from the limited number of boundary capacitance measurements obtained in a noncontact fashion. A series of boundary electrodes are equidistantly arranged at the periphery of a circular region, as shown in Figure 2.4a. Each electrode is excited with an AC signal while the remaining electrodes remain grounded. The excitation-measurement pattern is schematically illustrated in Figure 2.4b. This excitation pattern allows the propagation of an electric field through the entire domain (Ω) circumscribed by the boundary electrodes. The mutual capacitance between the excitation and the remaining electrodes are measured. Any change in electrical permittivity distribution results in a change in boundary capacitance responses. The spatial electrical permittivity distribution within Ω is reconstructed from the measured set of boundary capacitance responses by solving the ECT inverse problem. Like EIT, a physical model should be derived for ECT to predict the boundary capacitance responses while the electrical permittivity distribution is known.

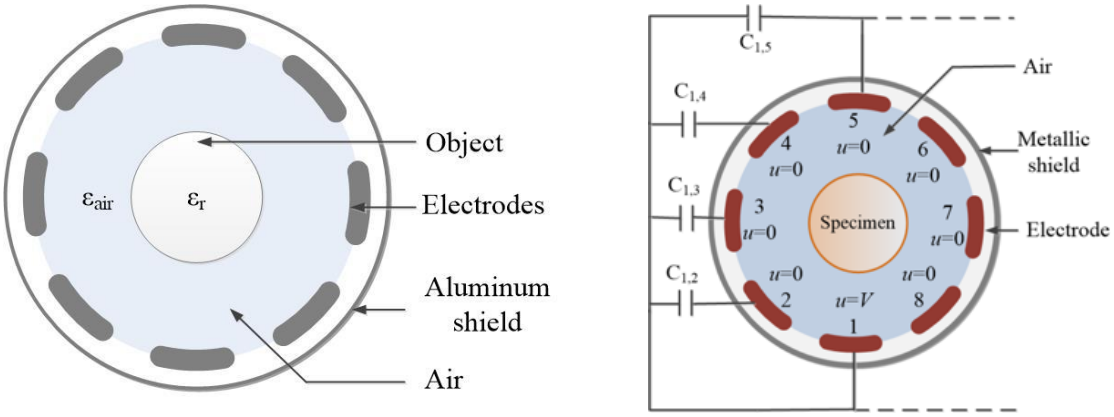

(a) (b)

Figure 2.4 (a) An eight-electrode ECT system is illustrated. (b) The electrodes are numbered consecutively in a clockwise fashion starting from the 3 o'clock position. An AC signal of magnitude V is applied at electrode-1 while all other electrodes are grounded.

2.2.2.1 Physical Model of ECT

The physical model for ECT is also be obtained from Maxwell's equations as described in equations 2.1 and 2.2. For low conductivity and high-frequency excitations, the effect of ε on the rotational component of the magnetic field can not be neglected. In that case, equation 2.12 can be written in the form of equation 2.40:

$$\nabla \times H \approx i\omega E + J^s \tag{2.40}$$

Taking the divergence on both sides of the equation 2.40 and replacing E with ∇u (equation 2.14), the governing equation for ECT is obtained:

$$\nabla \cdot \left(\varepsilon \nabla u \right) = 0 \tag{2.41}$$

2.2.2.2 Boundary Conditions

In order to predict the mutual capacitance responses between the boundary electrode pairs for a known permittivity distribution, equation 2.41 needs to be solved with the appropriate

boundary conditions. This second-order partial differential equation is solved to obtain u with appropriate boundary conditions, in which electric potential is assumed to be constant at each electrode, as shown in equation 2.42:

$$u = V_l \text{ at } E_l \tag{2.42}$$

where E_l is the l^{th} electrode, and V_l is some constant positive voltage at the excitation electrode and zero for the other electrodes. Zero Neumann boundary condition is imposed between two electrodes to decouple the external and internal field from each other, as proposed by Brandstätter *et al.* [143].

2.2.2.3 ECT Forward Problem

Like EIT, the governing equation of ECT forward problem is also solved using FE modeling. The weak form of equation 2.41 is obtained by multiplying it with a sufficiently smooth test function (v) and integrating over the entire domain Ω:

$$\int_{\Omega} v\nabla \cdot (\varepsilon \nabla u) = 0 \tag{2.43}$$

Evaluating the integration described in equation 2.43 and putting the zero Neumann boundary condition in the natural boundary terms results in equation 2.44:

$$\int_{\Omega} \varepsilon \nabla u \cdot \nabla v dx^2 = \int_{\Gamma} \nabla u \cdot n v dx^2 = 0 \tag{2.44}$$

where Γ and n are the boundary of Ω and unit inward normal on the boundary, respectively. Similar to EIT, the electric field is approximated as u^h as a linear combination of nodal shape function (φ_i) and nodal voltage (u_i):

$$u^h = \sum_{i=1}^{n} u_i \varphi_i \tag{2.45}$$

A system of linear equations can be obtained from equation 2.44 after replacing u with u^h and enforcing Dirichlet boundary conditions to obtain:

$$KU = F \tag{2.46}$$

where K is the system stiffness matrix, U is the nodal voltage vector, and F is the force vector arising from the essential boundary condition terms. Linear triangular element has been used for discretizing the entire region. A typical finite element mesh of the numerical model is shown in Figure 2.5a. Figure 2.5b shows the distribution of electric potential over the entire FE domain when electrode-3 was excited; the relative permittivity of the entire sensing region was 1.

Once nodal voltages are obtained by solving the forward problem, the capacitance between excitation and sensing electrodes can be calculated as follows:

$$C_{k,l} = \frac{1}{V} \int_{E_l} \varepsilon \frac{\partial u}{\partial n} dx \tag{2.47}$$

where $C_{k,l}$ is the capacitance between the k^{th} and l^{th} electrode pair, assuming that k is the excitation electrode, and l is the sensing electrode. Here, n is the inward normal at E_l. FD is applied to evaluate equation 2.47. Two parallel layers are considered near the electrode plane, as shown in Figure 2.6. The perpendicular distance between the two planes is Δ. If the values of u at j^{th}, $j+1^{\text{th}}$, and $j+2^{\text{th}}$ node obtained from the FE solution of the forward problem are u_j, u_{j+1}, and $u_{j+2,}$ respectively. From Taylor's series, u_{j+1} and u_{j+2} can be approximated, as shown in equations 2.48 and 2.49.

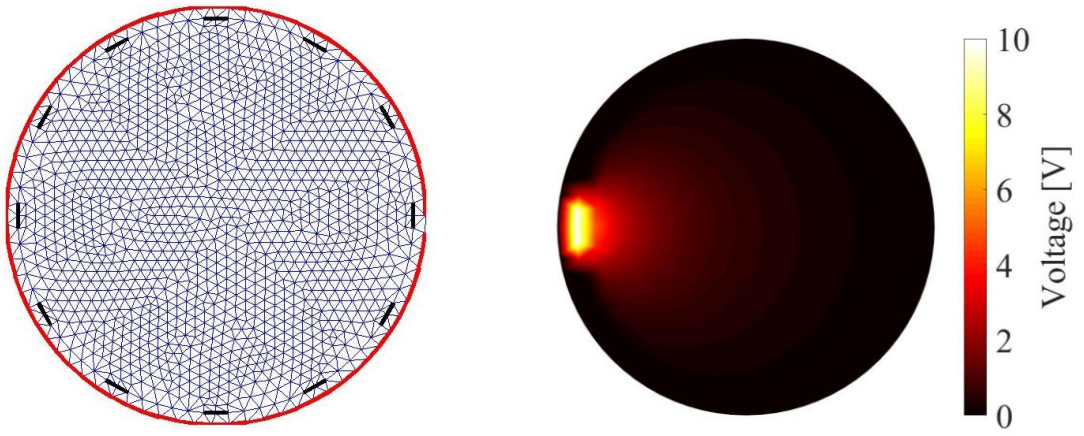

(a) (b)

Figure 2.5 (a) The entire domain has been discretized using linear triangular elements. External shield and the electrodes are highlighted with thick red and black lines respectively. (b) The potential distribution inside the sensing domain was computed by solving the forward problem, in this case, with a 10 V excitation signal.

$$u_{j+1} = u_j + \left.\frac{\partial u}{\partial n}\right|_j 2\Delta + \left.\frac{\partial^2 u}{\partial n^2}\right|_{j+1} \frac{\Delta^2}{2} \tag{2.48}$$

$$u_{j+2} = u_j + \left.\frac{\partial u}{\partial n}\right|_j 2\Delta + \left.\frac{\partial^2 u}{\partial n^2}\right|_{j+2} 2\Delta^2 \tag{2.49}$$

Equation 2.50 can be obtained by multiplying equation 2.48 by 4 and subtracting equation 2.49 from it:

$$4u_{j+1} - u_{j+2} = 3u_j + 2\Delta \left.\frac{\partial u}{\partial n}\right|_j + O(\eta^3) \tag{2.50}$$

where $O(\eta^3)$ is the higher-order error terms. $\partial u/\partial n$ can be obtained from equation 2.50, as shown in equation 2.51:

$$\left.\frac{\partial u}{\partial n}\right|_j = \frac{4u_{j+1} - u_{j+2} - 3u_j}{2\Delta} + O(\eta^3) \tag{2.51}$$

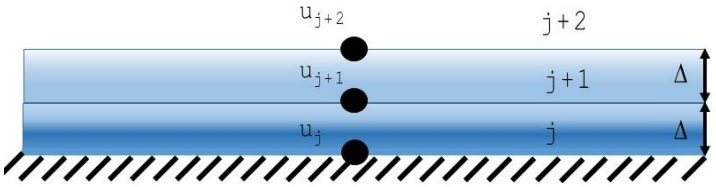

Figure 2.6 Finite difference schematic.

Neglecting the error term in equation 2.51, $\partial u/\partial n$ can be approximated, as shown in equation 2.52:

$$\left.\frac{\partial u}{\partial n}\right|_j \approx \frac{4u_{j+1} - u_{j+2} - 3u_j}{2\Delta} \tag{2.52}$$

2.2.2.4 Jacobian Calculation

Like EIT, the jacobian matrix for ECT (J_{ECT}) should be calculated to solve the inverse problem. Instead of perturbing each piece-wise constant permittivity value corresponding to individual triangular FE voxel in Ω, Frechet derivative of the measured capacitance with respect to a small perturbation in the permittivity is estimated for calculating J_{ECT} [125]. From the weak form of ECT forward problem (*i.e.*, equation 2.43), power conservation formula can be derived:

$$\int_{\Omega} \varepsilon \left|\nabla u\right|^2 dx^2 = \int_{\Gamma} u\varepsilon \frac{\partial u}{\partial n} dx \tag{2.53}$$

As the Neumann boundary term (*i.e.*, $\partial u/\partial n$) is zero between two electrodes, the right-hand side of the equation 2.53 can be expressed only for the electrode region, as shown in equation 2.54:

$$\int_{\Omega} \varepsilon \left|\nabla u\right|^2 dx^2 = \sum_{i=1}^{L} V_L \int_{e_l} \varepsilon \frac{\partial u}{\partial n} dx = \sum_{i=1}^{L} V_L Q_L \tag{2.54}$$

Here, Q_L is the total charge stored on the e_l electrode. Taking a derivative of equation 2.54, equation 2.55 can be obtained:

$$\int_{\Omega} \partial\varepsilon \left|\nabla u\right|^2 dx^2 + 2\int_{\Omega} \varepsilon \nabla u \cdot \nabla \partial u dx^2 \approx \sum_{i=1}^{L} V_L \partial Q_L \tag{2.55}$$

Applying divergence theorem on the second term of equation 2.55, equation 2.56 is obtained:

$$\int_{\Omega} \partial\varepsilon \left|\nabla u\right|^2 dx^2 + 2\int_{\Gamma} \partial u \varepsilon \frac{\partial u}{\partial n} dx = \sum_{i=1}^{L} V_L \partial Q_L \tag{2.56}$$

As u is constant on the boundary electrodes and $\partial u/\partial n$ = 0 between two electrodes, the second term in the left-hand side of the equation 2.56 can be set to 0:

$$\int_{\Omega} \partial\varepsilon \left|\nabla u\right|^2 dx^2 = \sum_{i=1}^{L} V_L \partial Q_L \tag{2.57}$$

Equation 2.57 can be expressed in the form of equation 2.58 to estimate the change in Q on electrode e_i due to a small perturbation in ε while the electrode e_i is excited with the voltage V_L and measurement is made on electrode e_j:

$$\frac{\partial Q_{i,j}}{\partial \varepsilon} = \frac{1}{V_L} \int_{\Omega} \nabla u_i \cdot \nabla u_j dx^2 \tag{2.58}$$

where ∇u_i and ∇u_j are the solution of the forward problem when e_i and e_j electrodes are excited with the AC voltage, respectively. $\partial Q_{i,j}/\partial\varepsilon$ is used to calculate each term of the J_{ECT}. Equation 2.58 is a robust and efficient method to calculate J_{ECT}. The right-hand side of the equation 2.58 can be calculated while estimating the boundary capacitance responses by solving the forward problem over the discretized domain. Figure 2.7 shows the sensitivity distribution of an 8-electrode ECT

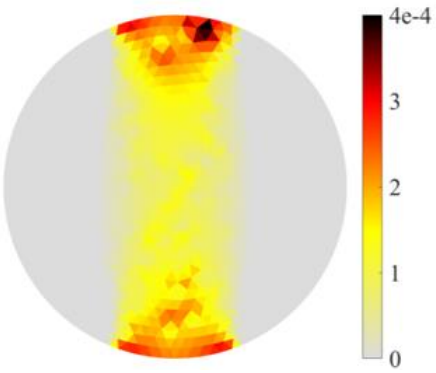

Figure 2.7 The sensitivity map for an empty sensing domain between electrodes 1 and 5 is shown.

system when electrodes 1 and 5 are excited. It can be observed that the sensitivity of the ECT system is smaller at the center compared to the boundary region.

2.3 Inverse Problem

As mentioned earlier, the inverse problem needs to be solved to reconstruct the electrical parameters (*i.e.*, σ or ε) within Ω from a limited number of boundary electrical response measurements. However, tomographic inverse problems are ill-posed in nature as a small change in σ or ε can cause a significant change in boundary electrical responses [144]. The experimentally measured difference in boundary responses (Δy) before and after a damage event can be expressed as a product of jacobian matrix (J) and the change in an electrical parameter ($\Delta\theta$):

$$\Delta y = J\Delta\theta \tag{2.59}$$

The reconstruction of $\Delta\theta$ is unstable because of the ill-posed nature of the inverse problem. The ill-posed nature of the tomographic inverse problems can be examined through the singular value decomposition of J. As shown in Figure 2.8, the singular values of J_{EIT} *and* J_{ECT} decay in the singular value spectrum, indicating the ill-posed nature of the corresponding inverse problems. In

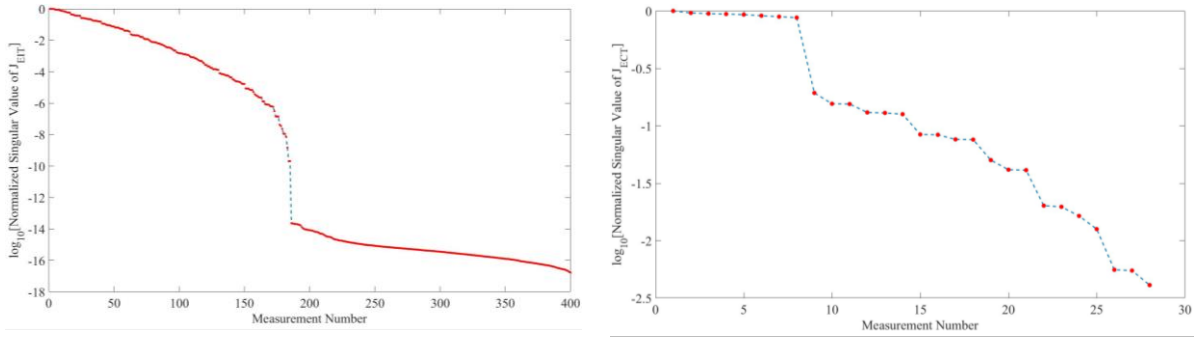

(a) (b)

Figure 2.8 Singular values (a) J_{EIT} and (b) J_{ECT} are shown. The singular values were normalized with the largest singular value and plotted in log scale as a function of measurement number.

addition, the large numerical values of the ratio of the largest and smallest singular values of J reveal the ill-posed nature of the inverse problems.

2.3.1 Least Square Approach

The least-square approach is generally implemented to obtain a generalized solution of the inverse tomography problems. Generally, the weighted least square approach is adopted to reconstruct the electrical parameters from the boundary responses:

$$\min_{\theta} \left\| \Delta y - J \Delta \theta \right\|^2 \tag{2.60}$$

2.3.1.1 Inversion of The Jacobian Matrix

If J is a square matrix, θ can be obtained by directly inverting J and multiplying it with Δy. However, J cannot be inverted as this is not a square matrix. J is a rectangular matrix because of the fact that the number of parameters in θ is much larger than the number of measurements obtained at the boundary of Ω. For this case, J needs to be pseudo-inversed, as shown in equation 2.61:

$$\Delta \theta = J^{+} \Delta y \tag{2.61}$$

where J^+ is the Moore-Penrose pseudo inversed form of J. For an under-determined problem, J^+ can be evaluated by equation 2.62 [125]:

$$J^+ = J^T (JJ^T)^{-1} \tag{2.62}$$

2.3.1.2 Difference Imaging

Being an ill-posed problem, the optimization problem defined in equation 2.60 fails to generate meaningful results. In order to overcome this difficulty, the ill-posed tomographic inverse problems need to be regularized with additional information about the solution. A penalty term is generally added with the cost function (equation 2.60), as shown in equation 2.63:

$$\Delta\theta_{\text{Tikhonov}} = \text{argmin} \left\| \Delta y - J\Delta\theta \right\|^2 + \alpha^2 \, \| R(\Delta\theta - \Delta\theta_0) \|^2 \tag{2.63}$$

where R, α, and $\Delta\theta_0$ are the regularization matrix, regularization parameter, and some prior assumption about the conductivity change, respectively. Here, α controls the optimization path by trading-off between the prior assumptions and the fitting data. Tikhonov regularization can be implemented to obtain a reliable solution to the inverse problem specified in equation 2.63 [145]. Tikhonov regularization aims to reduce instability in the inverse problem by damping out the small singular values from the system. The implementation of regularization produces an artificially smooth image. To formulate the inverse problem with Tikhonov regularization, the right-hand side of the equation 2.63 is expanded in its quadratic form as a function (f) of $\Delta\theta$.

$$\begin{aligned} f(\Delta\theta) = \Delta\theta^T J^T J \Delta\theta - 2\Delta\theta^T J^T \Delta y + \Delta y^T \Delta y + \alpha^2 \Delta\theta^T R^T R \Delta\theta \\ - 2\alpha^2 \Delta\theta^T R^T R \Delta\theta_0 + \alpha^2 \Delta\theta_0^T R^T R \Delta\theta_0 \end{aligned} \tag{2.64}$$

For the optimization of equation 2.64, its derivative is calculated in an arbitrary direction (x), as shown in equation 2.65.

$$x^T \nabla f(\Delta\theta) = 2x^T J^T J \Delta\theta - 2x^T J^T \Delta y + 2\alpha^2 x^T R^T R \Delta\theta - 2\alpha^2 x^T R^T R \Delta\theta_0 \tag{2.65}$$

Equation 2.65 is set to zero to evaluate $\Delta\theta_{Tikhonov}$ for any x:

$$\Delta\theta_{Tikhonov} = (J^T J + \alpha^2 R^T R)^{-1}(J^T \Delta y - \alpha^2 R^T R \Delta\theta_0) \tag{2.66}$$

In general, R is set to an identity matrix (I), and $\Delta\theta_0$ is set to 0 to obtain the most generalized form of Tikhonov regularization:

$$\Delta\theta_{Tikhonov} = (J^T J + \alpha^2 I)^{-1}(J^T \Delta y) \tag{2.67}$$

$R^T R$ can also be set to the diag($J^T J$) for Newton one-step reconstruction (NOSER) [146].

2.3.1.3 Absolute Imaging

While the method described in Section 2.3.1.2 is suitable for difference imaging, the regularized iterative method can be implemented for absolute image reconstruction. The cost function of the regularized optimization problem can be written in the form of equation 2.68:

$$\theta = \text{argmin}\left(\left\| F(\theta) - y_m \right\|^2 + \alpha^2 \left\| R(\theta - \theta_0) \right\|^2 \right) \tag{2.68}$$

where F is the forward problem operator, y_m is the measured set of boundary responses, θ_0 is the initial guess of the parameter to be estimated, and θ is the solution of the optimization problem specified in the right-hand side of equation 2.68 (*i.e.*, electrical property distribution corresponding

to measurement y_m). For $i+1^{th}$ iteration step, the parameter (θ_{i+1}) can be written as equation 2.69 on the basis of the linear approximation around the solution of i^{th} iteration step (θ_i):

$$\theta_{i+1} = \text{argmin}\left(\left\|F(\theta_{i+1}) - y_m\right\|^2 + \alpha^2 \left\|R(\theta_{i+1} - \theta_0)\right\|^2\right) \tag{2.69}$$

θ_{i+1} can be written by linearizing the solution of the optimization problem for θ_i:

$$\begin{aligned}\theta_{i+1} = \arg\min[\| F(\theta_i) + F'(\theta_i)\Delta\theta_i - y_m \|^2 + \\ \alpha^2 \| R(\theta_i + \Delta\theta_i - \theta_o) \|^2]\end{aligned} \tag{2.71}$$

where $F'(\theta_i)$ is the first derivative of $F(\theta_i)$ with respect to θ_i. The difference of the predicted electrical property distribution between the $i+1^{th}$ and i^{th} iterations (*i.e.*, $\Delta\theta_i$) can be estimated in discrete form as follows:

$$\begin{aligned}\Delta\theta_i = (J_i^T J_i + \alpha^2 R^T R)^{-1}\{J_i^T [y_m - F(\theta_i)]\} \\ + \alpha^2 R^T R(\theta_o - \theta_i)\end{aligned} \tag{2.72}$$

where the jacobian matrix (J_i) is the discrete representation of $F'(\theta_i)$ evaluated at the i^{th} step. In this study, the regularization parameter α was an estimated *a priori*. The estimated $\Delta\theta_i$ from equation 2.72 is used to update the electrical parameter distribution and thereby to predict a new electrical parameter distribution for $i+1^{th}$ iteration step.

$$\theta_{i+1} = \theta_i + \Delta\theta_i \tag{2.73}$$

The optimization scheme continues to execute until the error ratio (e) becomes smaller than the specified threshold value (λ), as shown in equation 2.74.

$$e = \frac{\| F(\theta_i) - y_m \|^2}{\| y_m \|} \leq \chi \tag{2.74}$$

2.4 Results and Discussions

2.4.1 EIT Image Reconstruction Validation

Two sets of experiments were performed for spatial damage detection validation. Conductive specimen of size 80 × 80 mm^2 was instrumented with six equally spaced boundary electrodes on each side of the specimen. The electrodes were equidistantly placed from each other for EIT interrogation. This conductive specimen was an MWCNT-latex thin film whose fabrication process will be discussed in detail in Chapter 4. A specialized data acquisition (DAQ) system was employed to obtain the dataset for mapping the distribution of electrical resistivity of the EIT specimen. The EIT DAQ included a Keithley 6221 current source, which supplied direct current (DC) on the order of 1 mA to a specific boundary electrode with another electrode set as ground. It should be noted that the DC magnitude was set to span the voltage measurement range of the DAQ, thereby maximizing the signal-to-noise ratio (SNR). On the other hand, an Agilent 34980A multifunction switch was employed for measuring boundary electrode voltages (using a built-in digital multimeter (DMM)) and for directing current input/output to appropriate electrode pairs. The EIT DAQ was controlled using a customized *MATLAB* program. In this study, DC was injected across electrodes on opposite edges of the square mortar specimen, while voltage was measured across adjacent boundary electrodes; a similar approach was used by Loyola *et al.* [147]. The experimentally obtained voltage measurement obtained by interrogating the undamaged specimen was compared with the EIT forward problem-evaluated voltage response, as shown in Figure 2.9. It can be seen that computational and experimental results match well; however, the

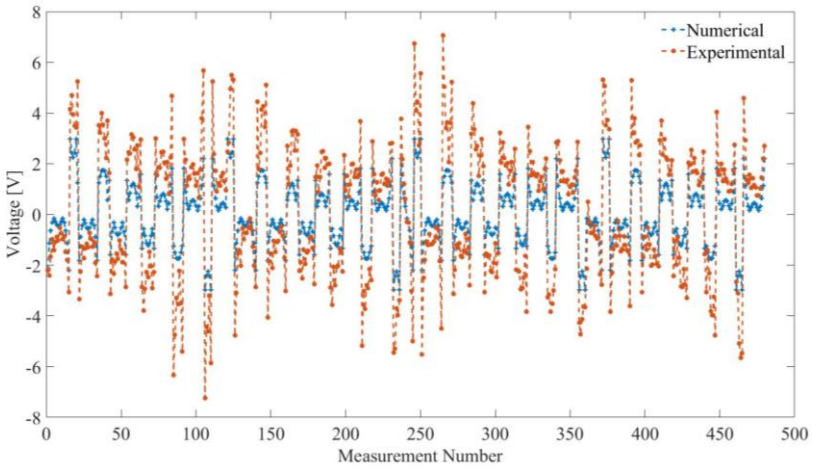

Figure 2.9 The computationally obtained voltage responses obtained from EIT forward problem is compared with the experimentally measured voltage responses.

difference exists mostly because of nonuniform conductivity distribution of the object, electrode position mismatches between the numerical model and EIT test setup, and variable contact impedance between the boundary electrodes and the EIT specimen.

The experiment started by interrogating the undamaged specimen with DC for baseline conductivity reconstruction. The measurement was used as the input of the GN iterative inverse algorithm to reconstruct the conductivity distribution of the undamaged specimen. Next, damage was introduced at the bottom-left corner of the specimen by mechanically scratching the thin film as shown in Figure 2.10a. The damaged specimen was also subjected to EIT interrogation. The second damage was introduced diagonally opposite to the previous damage near the top-right corner of the MWCNT-latex thin film specimen (Figure 2.10b). Similar to the previous case, the damaged specimen was subjected to EIT interrogation, and boundary voltage measurements were recorded.

Similar to the baseline conductivity reconstruction, the measured sets of boundary voltage from the damaged specimen were used as the input for the EIT inverse algorithm. The change in

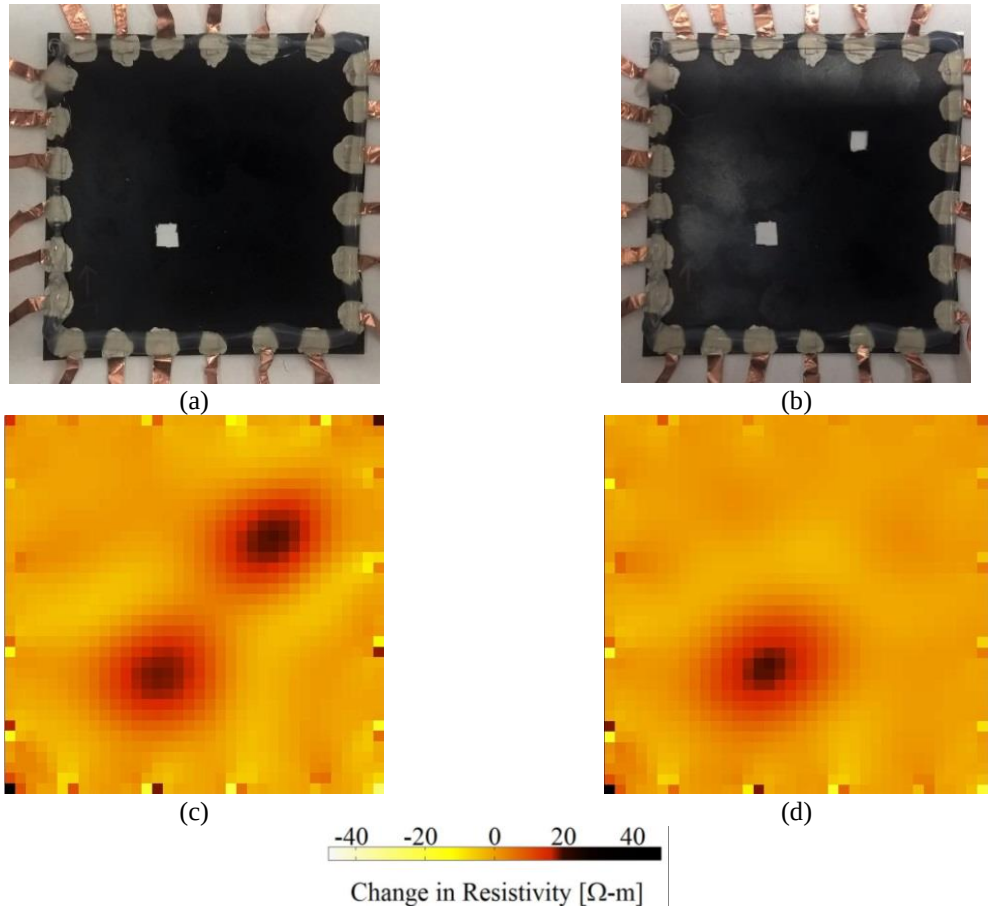

Figure 2.10 Damage was introduced in the conductive specimen at (a) bottom-left and (b) top-right corner. EIT estimated resistivity maps corresponding to these two damage cases are shown in (c) and (d), respectively.

resistivity distributions were estimated by subtracting the baseline resistivity from the damaged-states' resistivities. It can be observed from Figures 2.10c and 2.10d that a localized increment in the resistivity was observed at the region closed to the actual damage (Figures 2.10a and 2.10b). These results make sense as the thin film was mechanically scratched; the conductivity of these regions went to zero (*i.e.*, resistivity is very large), resulting in negligible propagation of DC through that region. Perturbation in electrical current propagation resulted in a change in boundary voltage responses. The proposed inverse algorithm was able to reconstruct this resistivity change from the measured set of boundary voltages validating the spatial damage detection capability of the proposed EIT algorithm.

In addition to showing the right locations of the introduced damage, the area of the resistivity change detected by EIT resembles the actual shape of the damage. However, the EIT-estimated damage sizes were slightly larger than the actual size of the damage. This could have been resulted due to the smoothing effect due to the regularization of the inverse problem. Nevertheless, these experimental results validate that the proposed EIT algorithm can detect spatially distributed damage in the structures.

2.4.2 ECT Image Reconstruction Validation

For the experimental validation of the proposed ECT forward and inverse algorithm, a 13 mm-diameter polyvinyl chloride (PVC) rod was placed at 13 different locations in the sensing area (*i.e.*, from P1 to P13) as shown in Figure 2.11a. In order to accurately maintain the positions of the rod, a customized holder, shown in Figure 2.11b, was fabricated using a Type A Series 1 Pro 3D printer. This holder was fitted below the ECT electrode array and served as a receptacle for the PVC rod, where the rod could be fitted in any of the 13 positions. Prior to putting the rod in the ECT electrode array, a set of boundary capacitances was obtained with the ECT electrode array empty and filled with air. Here, the excitation was a 10 V peak-to-peak, 1.25 MHz, AC signal. The collected measurement was compared with the ECT forward problem result, as shown in Figure 2.12, and a good agreement was found.

The inverse problem was then solved, and the corresponding reconstructed permittivity distribution was used as the baseline. Next, the rod was placed at the designated locations, and ECT measurements were obtained for permittivity reconstruction. The change in permittivity distributions was obtained by subtracting out the previous baseline, and the results are shown in

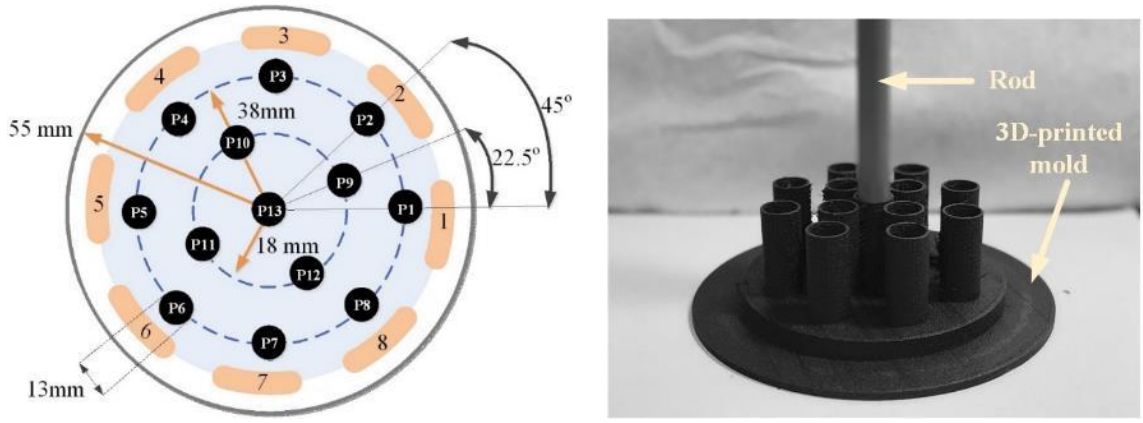

(a) (b)

Figure 2.11 (a) To characterize ECT permittivity imaging accuracy, a 13 mm-diameter PVC rod was fixed at 13 different locations in the ECT electrode array. Their positions were marked as P1, P2, P3, …, and P13. (b) A 3D-printed mold was employed to accurately maintain the locations of the rod, and the mold was fitted below the ECT electrode array.

Figure 2.13. It can be observed from Figure 2.13 that the ECT inverse algorithm was able to detect the location and size of the PVC rod for all of the 13 cases from P1 to P13.

2.4.2.1 Resolution Study

After successfully detecting the locations of the PVC rod in the ECT electrode array, different image parameters were computed to quantitatively assess the quality of reconstructed images. A series of different image parameters were proposed by Adler *et al*. [148] to study the image quality of EIT images. In this work, three of these evaluation criteria were adopted and implemented for ECT image quality analysis. First, the one-fourth amplitude set or $[\varepsilon_q]_i$, which contains all the image pixels ($[\varepsilon]_i$) greater than one-fourth of the maximum amplitude of all the image pixels, was determined. Mathematically, $[\varepsilon_q]_i$ can be expressed as:

$$[\varepsilon_q]_i = \begin{cases} 1 \text{ if } [\varepsilon]_i \geq \frac{1}{4}\max[\varepsilon] \\ 0 \text{ otherwise} \end{cases} \tag{2.75}$$

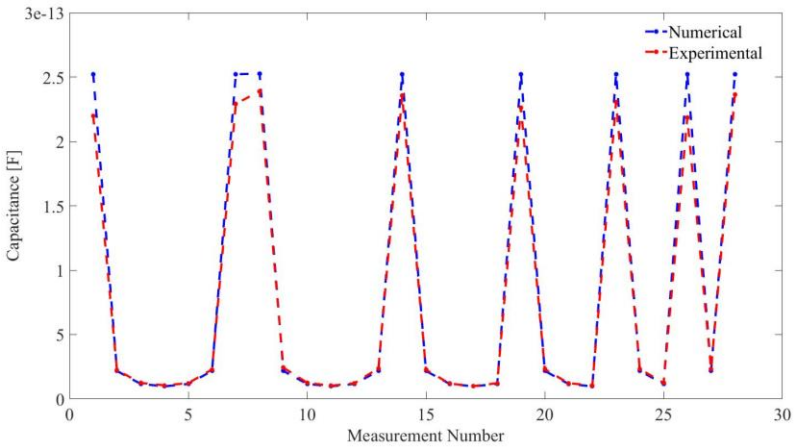

Figure 2.12 Calculated capacitance values between pairs of electrodes are compared with the experimentally measured capacitance response of a 8-electrode ECT system filled with air.

where [ε] is the reconstructed permittivity distribution. Position error (*PE*) was estimated by calculating the distance between the center of gravity (CG) of the target object (*i.e.*, the PVC rod) and the CG of $[\varepsilon_q]_i$. *PE* measures the extent to which reconstructed images accurately represent the position of the target object and is computed by:

$$PE = r_t - r_q \tag{2.76}$$

where r_t and r_q are the distances of the CG of the target object and $[\varepsilon_q]_i$, respectively, where both are with respect to the center of the ECT electrode array. Second, to estimate the resolution (*RES*) of the reconstructed images, the square root of the ratio of the area (A_q) corresponding to $[\varepsilon_q]_i$ and the total sensing area (A_0) was evaluated [148]:

$$RES = \sqrt{A_q / A_0} \tag{2.77}$$

Last, a shape deformation (*SD*) factor is defined as the fraction of the reconstructed one-fourth amplitude set that does not fit into a circle (*C*) of the equal area:

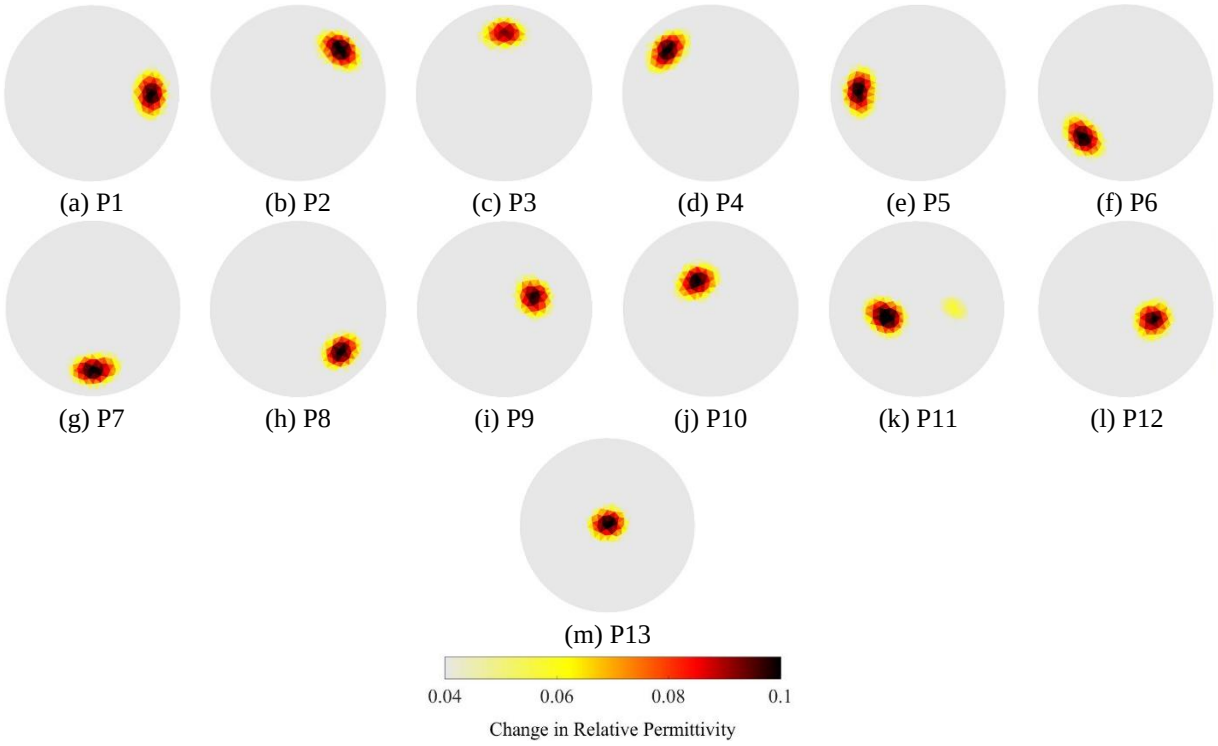

Figure 2.13 The ECT images were determined when the PVC rod was fixed at (a) P1, (b) P2, …, to (m) P13.

$$SD = \sum_{i \notin C} [\varepsilon_q]_i \Big/ \sum_i [\varepsilon_q]_i \tag{2.78}$$

2.4.2.2 Resolution Study Results

These three performance parameters (*i.e.*, *RES*, *PE*, and *SD*) were computed for all 13 rod-position cases from P1 to P13 (Figure 2.11a) to evaluate the performance of the ECT algorithm. Figure 2.14 shows each of the evaluation criterion results calculated for each rod position, while Table 2.1 summarizes the statistical properties of each criterion considering all positions. In general, smaller standard deviations indicate better accuracy of reconstructed images in terms of the rod's location, shape, and size. Even though the magnitudes of *PE* are very small over the

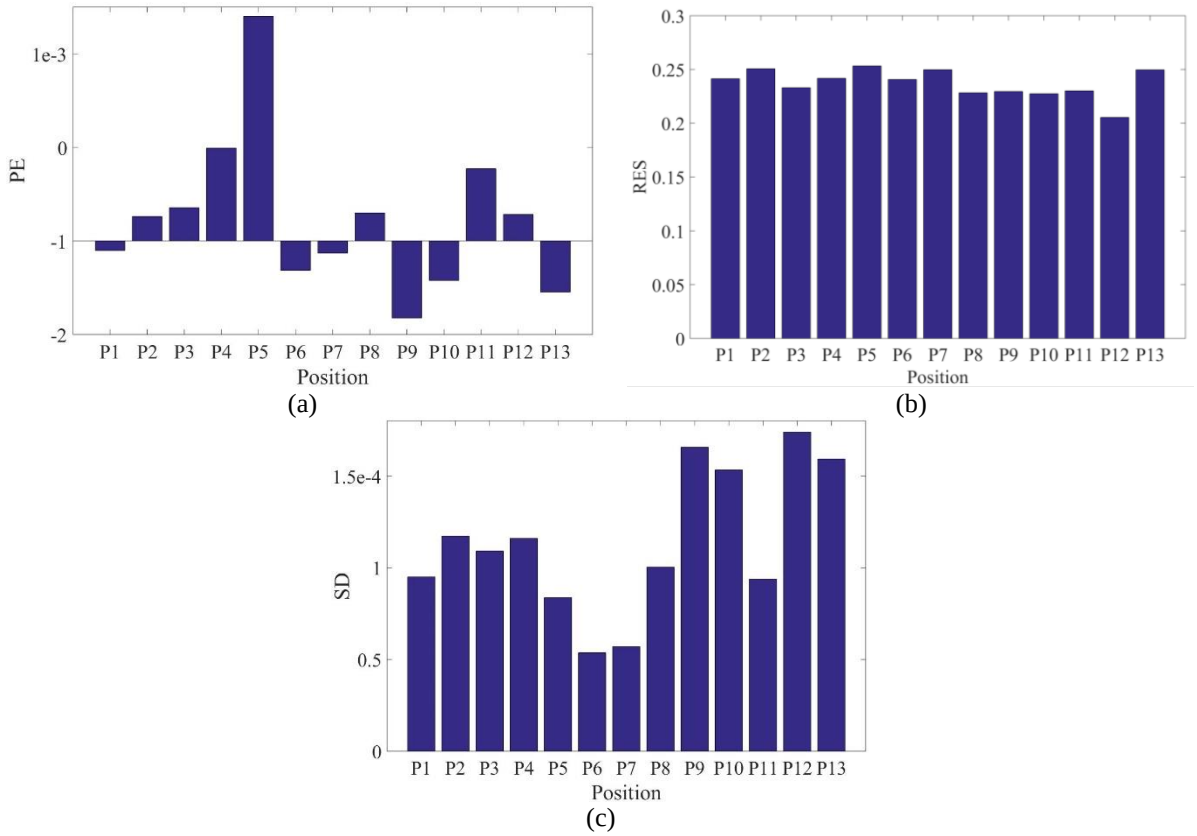

Figure 2.14 The results of (a) *PE*, (b) *RES*, and (c) *SD* of the reconstructed images are plotted with respect to each of the P1 to P13 test cases.

Table 2.1 ECT imaging accuracy evaluation results

Statistical results / **Parameters**	**Mean**	**Standard deviation**
***PE* [mm]**	4.65E-04	0.0017
RES	0.237	0.0133
SD	1.14E-04	3.94E-05

entire ECT electrode array (Figure 2.14a), their bipolar distribution suggests that reconstructed images are sometimes pushed towards or away from the center of the sensing domain. The slightly larger values of *RES* indicate that the ECT algorithm tends to overestimate the size of the target object (Figure 2.14b). The smoothing effect of the regularization scheme used in this study may

contribute to this overestimation. Despite this, the incredibly small values of *SD* (*i.e.*, on the order of 10^{-4}) and its small standard deviations indicate the low risk of incorrect interpretation of the reconstructed permittivity maps, thereby successfully validating its position-detection robustness. In summary, these results successfully validated the ECT system, where the locations, shapes, and sizes of permittivity changes were visualized fairly accurately.

2.5 Summary and Conclusions

In this chapter, EIT and ECT were introduced as two soft-field imaging techniques to reconstruct the spatial distribution of electrical properties within a predefined sensing domain. First, A physical model of EIT was derived and used to solve the EIT forward problem, which aims to estimate the boundary voltage responses while the electrical conductivity distribution is explicitly known. FE method was implemented to solve the EIT forward problem. CEM was used as the boundary condition in the physical model of the EIT to accurately predict the boundary voltage responses. The set of the linear equations obtained from the FE model of the EIT forward problem was solved to estimate the boundary voltage responses. The forward problem was also used to calculate the sensitivity matrix of the EIT, which contains the information on how the boundary voltage changes in response to a small perturbation in the conductivity distribution. An efficient way to calculate the EIT sensitivity matrix was proposed.

Similar to EIT, a physical model for ECT was also developed. Capacitance measurements were obtained in a noncontact fashion and used to reconstruct the electrical permittivity distribution of a predefined sensing region. Similar to EIT, the FE method was implemented to solve the ECT forward problem to estimate the mutual capacitance between boundary electrode pairs. Frechet derivative method was used to calculate the sensitivity matrix for ECT.

The formulation of the EIT and ECT inverse problems were also discussed in this chapter. EIT and ECT inverse problems are ill-posed in nature as a small perturbation in electrical property may result in a large change in boundary electrical responses. As a result, the inverse problem was regularized to obtain a meaningful solution. The Tikhonov regularization method was implemented to solve the EIT and ECT inverse problem. Single-step image reconstruction for difference imaging and iterative GN algorithm for absolute image reconstruction were developed and implemented to solve the EIT and ECT image reconstructions. Lastly, the proposed forward and inverse algorithm of EIT and ECT were experimentally validated. The accuracy of the ECT algorithm was also investigated based on various image metrics.

The EIT and ECT algorithm developed in this chapter will be used in conjunction with stimuli-responsive nanocomposite thin films for various spatial sensing applications. In particular, Chapters 3 and 4 will explore EIT for spatial damage detection in self-sensing concrete and distributed strain field mapping over large structural surfaces, respectively. ECT will be used in Chapters 5 and 6 as a noncontact imaging tool for OIP monitoring and subsurface damage detection in composites.

CHAPTER 3 SELF-SENSING CEMENTITIOUS COMPOSITES

3.1 Introduction

As mentioned in Chapter 1, previous research efforts have demonstrated that strain-sensitive nanocomposite, fabricated through the LbL process, can be applied on structural surfaces as a coating for spatial damage detection [105]. Hence this method was mainly limited to structural sensing at surface level. Additionally, the LbL method is not economical for the large-volume fabrication of the thin film. Instead of using the thin film as a structural coating, this chapter investigates a scalable, low-cost fabrication method to integrate the nanocomposite with structural materials. Such nanocomposites-enhanced structural materials can perform self-sensing along with load-bearing. Additionally, EIT can also be implemented for direct spatial damage detection in such self-sensing materials.

This chapter shows how self-sensing property can be encoded in cementitious composites. Among many structural materials, cementitious composites is selected as they are one of the most commonly used materials for civil infrastructure systems worldwide [149-151]. In general, its intrinsic properties, versatility, and cost-effectiveness make it ideally suited as a civil infrastructure construction material. Unfortunately, cementitious composites are susceptible to damage during service due to extreme loads, long-term degradation, fatigue, and environmental effects, among others [152, 153]. Over time, deterioration and damage can propagate to cause catastrophic structural collapse [154].

Thus, detecting the onset and monitoring the progression of damage is critical for facilitating necessary maintenance and for preventing catastrophic failure. In addition to traditional NDE methods [155-157], over the last few decades, a different approach for damage detection has

been proposed based on designing a new generation of multifunctional cementitious composites. In general, the addition of conductive additives to the cement matrix has enabled multifunctional cementitious composites to bear loads while possessing self-sensing properties [158]. As early as 1995, Chen and Chung [159] demonstrated that the electrical resistance of concrete mortars with carbon fibers dispersed in the mortar matrix changed in response to cyclic loading. While resistance change was reversible during cyclic loading, cracks or damage caused irreversible changes in the "smart" concrete's resistance. Later improvements involved using ozone-treated carbon fibers, which led to improvements in the sensing response's sensitivity and repeatability. The incorporation of steel and carbon fibers together in concrete beams was also studied; not only was this combination successful in altering the concrete's mechanical properties (*i.e.*, flexural strength and toughness), but its electrical resistance was also sensitive to crack width [160]. However, it should be mentioned that a limitation of using these fibers as conductive additives is to make sure that they are evenly distributed within the composite. Poor dispersion or agglomerations would diminish material properties. Besides, existing construction practices need to be modified for casting fiber-reinforced cementitious composites, which may be a deterrent for practical implementations.

More recently and with the advent of nanotechnology, the design of multifunctional or smart cementitious composites focused on leveraging the unique properties of conductive nanomaterials such as CNTs [161-164]. For example, Yu and Kwon [165] fabricated cement paste specimens and investigated two methods for dispersing CNTs, namely using acid treatment to form functionalized carboxylic groups on CNT surfaces and using noncovalent suspension in surfactants. In fact, different groups used various surfactants, including sodium dodecyl sulfate [165, 166], sodium dodecyl benzene sulfonate [166, 167], and PSS [168], to name a few. Han *et*

al. [161] showed that CNT-based cementitious pavements could be used for traffic monitoring. Besides CNTs, other nanomaterial additives were also investigated, such as carbon nanofibers [169], carbon black [162], and graphite [170]. While these studies demonstrated promise for achieving next-generation, self-sensing, cement composites, it remains challenging to scale up due to dispersion issues, specialized casting procedures, and cost. Wong [171] dispersed MWCNTs in different surfactants (*e.g.*, PSS and superplasticizers) in ultra-low concentration and used for self-sensing cementitious composite casting.

This work is a continuation of Wong's work [171]. However, instead of dispersing the MWCNT in the surfactants prior to casting, this work is focused on modifying the cement–aggregates interfaces of mortar and concrete specimens with MWCNT-based thin films [26]. In short, the airbrushing technique was employed for spraying the electrically conductive MWCNT-latex thin films onto dry sand and coarse aggregates. The film-coated sand and aggregates were then used for casting cementitious composite specimens. This technique was applied to both mortar and concrete. In the case of mortar, sand was spray-coated with MWCNT-latex thin film. Like the mortar specimens, sand and coarse aggregates were spray-coated with the MWCNT-latex thin film for concrete casting. By doing so, direct spatial sensing and damage identification could be accomplished through EIT since localized changes in electrical resistivity would suggest the presence of cracks, spalling, or other types of damage.

This chapter begins with the experimental details, namely the mix design, MWCNT thin film fabrication, thin film-coated sand and aggregate preparation, casting procedures, and testing protocols for mortar and concrete specimens. Then, the chapter continues with a discussion of the mechanical and electromechanical test results of mortar and concrete specimens. Spatial damage

detection using the “self-sensing” cementitious composite specimens coupled with the EIT algorithm was also validated. This chapter ends with a brief conclusion.

3.2 Experimental Details

An experimental program was devised for characterizing the mechanical and sensing properties of self-sensing cementitious composites. As mentioned in Section 3.1, the cement–aggregate interfaces of the cementitious composite were nano-engineered by directly depositing MWCNT-latex thin films onto aggregates prior to using them for cementitious composites casting. Although other studies demonstrated some success by dispersing nanomaterials in cement matrices [163], the objective of this study was to explore a new and more efficient method of incorporating CNTs and for enhancing electromechanical performance. The following sections explain the nanocomposite fabrication process, mortar, and concrete mix design, casting, and testing procedures.

3.2.1 Nanocomposite Fabrications

As stated earlier, the sand and aggregates were coated with an MWCNT-based thin film prior to using them for casting. In this study, the MWCNT thin film was sprayed and deposited onto dry sand and aggregates using an airbrush, as was described by Mortensen *et al.* [172]. Prior to spraying films, an MWCNT solution was prepared. First, MWCNTs were dispersed in 2 *wt*.% PSS solution with a small amount of N-methyl-2-pyrrolidinone (NMP). After achieving adequate suspension by bath and high-energy tip sonication [173], a latex solution was added to create the MWCNT-latex ink, which was used as is for spraying using a Paasche airbrush. As was discussed in Mortensen *et al.* [172], both the PSS and latex facilitated MWCNT suspension and the deposition of films characterized by a percolated morphology and high homogeneity, as can be

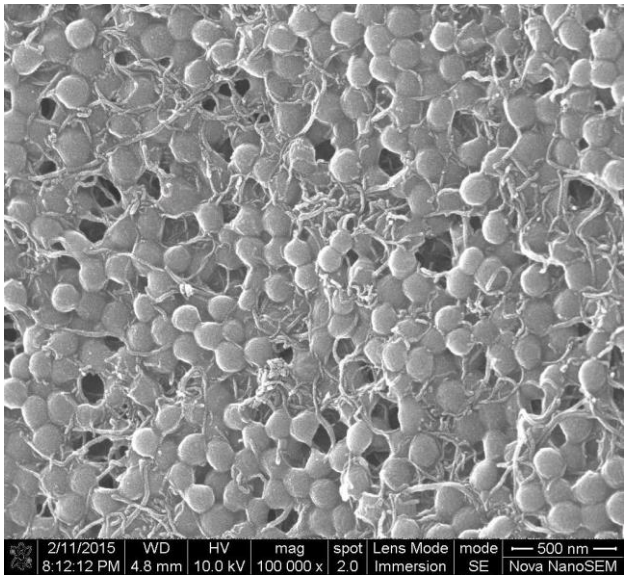

Figure 3.1 The scanning electron microscope image shows the morphology of the MWCNT-latex thin film, which consists of dispersed nanotubes and latex spheres.

seen from the SEM image in Figure 3.1.

3.2.2 Sand and Aggregate Coating

Spray fabrication of coarse aggregates and sand was performed manually by holding a Paasche airbrush 30 cm (12 in) above the aggregate surface and then spraying the MWCNT-latex ink by hand, as shown in Figure 3.2. Once a uniform film was deposited onto the surfaces of aggregates, the film-coated aggregates were manually mixed with a plastic spatula to expose uncoated aggregate surfaces. Airbrushing was then repeated. To obtain uniform coatings, sand required twice as much MWCNT-latex ink than the large aggregates; a total of six coatings were applied for sand and three for large aggregates. After spraying was finished, the treated aggregates were air-dried at room temperature for 30 min and then placed in a vacuum oven set to 80 °C for 30 min. The film-coated sand and aggregates were allowed to cool to room temperature prior to being used for concrete casting. Figure 3.3 shows an SEM image of an MWCNT-latex thin film,

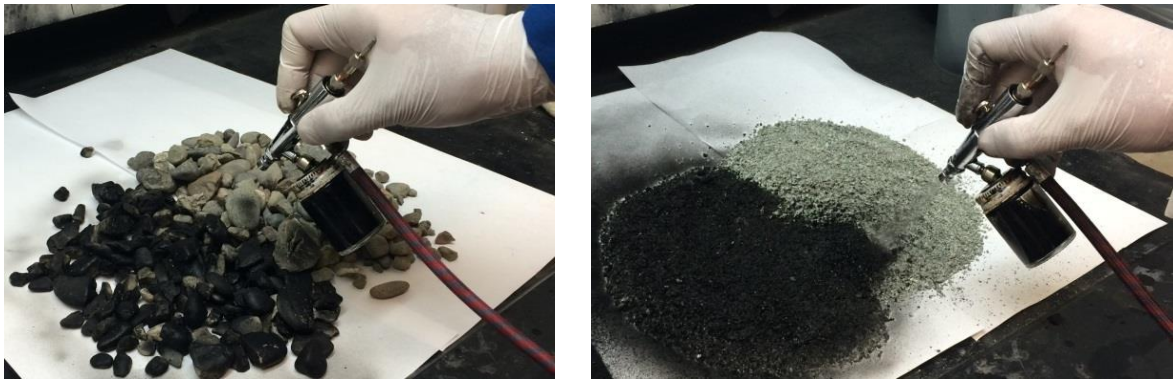

(a) (b)

Figure 3.2 MWCNT-latex inks are airbrushed to form thin films on (a) large or coarse aggregates and (b) sand.

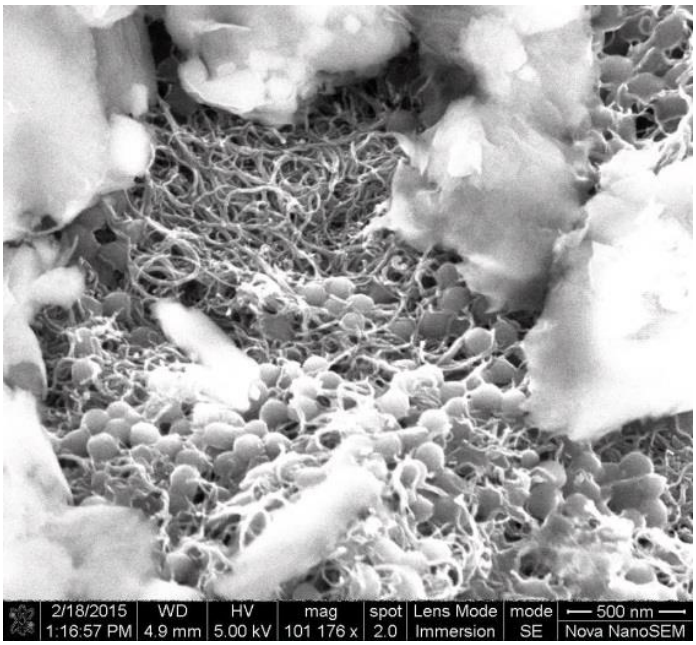

Figure 3.3 An SEM image of a thin film deposited on a sand particle shows that carbon nanotubes (thin, white lines) and latex spherical particles are uniformly deposited.

which in this case, was deposited onto a sand particle. It should be mentioned that, while uniform films can be deposited onto flat surfaces, it is likely that the films on sand and aggregates exhibited non-uniform thicknesses (*i.e.*, due to the orientation, angularity, and gradation of sand particles). However, it is hypothesized that this would not affect the electrical and electromechanical properties of the bulk cementitious composite.

3.2.3 Experimental Details for Self-Sensing Mortar

3.2.3.1 Mortar Mix Design and Casting

Mortar specimens were cast following the procedure as a combination of the Federal Aviation Administration (FAA) guidelines for runway concrete pavement [174] and ASTM C109 for mortar specimen strength testing. The cementitious material used was a mixture of Type I/II Portland cement and 25 *wt.*% (of total cementitious material) Type F ground granulated blast furnace slag (GGBFS). Specimens were cast using a 2.75:1 sand-to-cement ratio, as stated in ASTM C109 [34]. The sand used was crushed granite with a density of 2.71 g/cm^3 and a minimum particle size of 0.149 mm. Prior to its use and/or the deposition of the MWCNT-latex thin film, sand was dried in a vacuum oven operated at 80 °C for 24 h. A water-to-cement ratio (w/c) of 0.52 was used, along with 2.9 mL/kg of Advacast superplasticizer (SPL), for reducing water content and increasing mix workability.

Casting the mortar cubes and plate specimens began with mixing the various constituents using a Hobart N-50 mixer. First, the cementitious material, water, and Advacast SPL were mixed at a low speed of 60 rpm for 30 s. While the mixer was still operated at 60 rpm, sand (*i.e.*, either pristine or coated with the MWCNT-latex thin film) was gradually added. Upon doing so, the mixer was set to medium-speed (124 rpm) for 1 min, so as to obtain an even mixture. Then, the mixer was turned off, and any material on the walls of the bowl was scraped off. Finally, the mixture was set aside for 15 s before being poured into individual molds.

Two different types of molds were used for casting mortar specimens in this study. The first type was $5 \times 5 \times 5$ cm^3 ($2 \times 2 \times 2$ in^3) cubic molds. These molds were oiled with WD-40 as a releasing agent, and the seams were sealed with petrolatum. In addition to subjecting these cubic

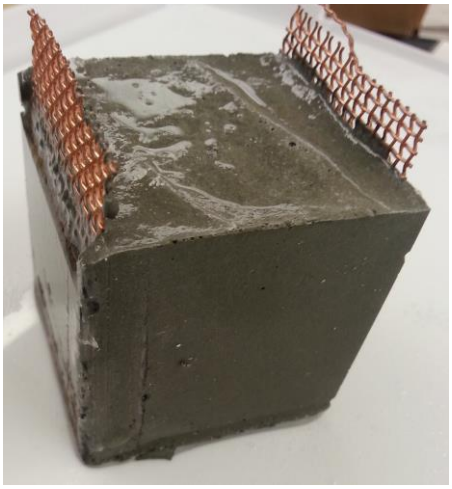

Figure 3.4 A saturated 5 × 5 × 5 cm^3 mortar specimen with embedded copper mesh electrodes is shown.

specimens to mechanical tests, the sensing characterization tests required that their electrical properties be measured during applied strains and stresses. For this reason, 4.5 × 6.5 cm^2 (1.75 × 2.25 in^2) copper mesh electrodes were cut and inserted at opposite ends in certain molds (*i.e.*, those designated for casting specimens for electromechanical characterization). Electrode placement was done so that the mesh covered the entire specimen's cross-section while having a small portion extended outwards for measurement purposes. Once the electrodes were in place, the mix was scooped into each mold, filling them halfway. Each mold was then tamped for 10 s before being filled completely and tamped again for another 10 s. After tamping, the molds were sealed with plastic wrap and stored at room temperature in a sealed container for 24 h. Finally, the specimens were demolded and placed in a limewater solution to cure for 28 days prior to testing. A saturated mortar specimen with embedded electrodes is shown in Figure 3.4. For this study, mortar cube specimens using pristine sand and film-coated sand were cast for testing purposes and for comparison.

On the other hand, two PVC plate molds that measured 25 × 12.5 × 1 cm^3, pre-oiled with WD-40, and the contact surfaces sealed with white petrolatum were used. Because these specimens

were designed for damage detection validation studies (as will be discussed later), electrodes were also embedded during casting. Here, 16 copper mesh electrodes (6×50.8 mm^2) spaced 4 mm apart to form a 4×4 pattern were attached to square Balsa wood forms. Three of these forms were placed into each mold so that three different plate specimens could be obtained. After placing the electrode formwork, the mortar mixture was meticulously poured into the mold to avoid bending or moving the electrodes. Tamping and gentle shaking was done to ensure that no voids were present in the plate. Then, the molds were covered with plastic wrap, sealed with packing tape, and stored at room temperature for 24 h before they were demolded and placed into a lime bath curing solution for 28 days. Once cured, each plate was removed and cut using a diamond saw to form individual specimens for testing. It should be noted that specimens were placed in a vacuum oven for 1 h at 80 °C and then allowed to cool down to room temperature before testing.

3.2.3.2 Load Testing

An MTS load frame equipped with a 407 controller was employed for testing mortar specimens and for characterizing their mechanical and electromechanical properties. The cubic mortar specimens (Section 0) were used for two types of tests. First, specimens without embedded electrodes were subjected to monotonic, uniaxial, compressive loading until material failure so that their mechanical properties could be characterized. The displacement-controlled test was conducted using a ramp rate of 1.905 mm/min. Eight pristine and seven thin film-enhanced mortar specimens were tested for this case.

The second set of tests was for characterizing the electromechanical response of mortar specimens. Thus, cubic specimens with embedded copper mesh electrodes were used. The specimens were initially preloaded to 5,000 N, before the load frame executed a 0.1 Hz

compressive cyclic load pattern to a peak strain of -0.45%; they were subjected to a minimum of five load cycles. The load frame's load and displacement data were recorded using a customized *LabVIEW* client (sampling rate: 55 Hz). In addition, its DC resistance was also recorded simultaneously using an Agilent 34401A DMM recording at a sampling rate of 2.8 Hz. It should be mentioned that, prior to each test, ~ 20 s of resistance data was recorded first. This data was used for quantifying the specimen's nominal resistance, as well as for identifying any possible drift in its electrical response.

It should be mentioned that all of the specimens tested in this study were dried at 50 °C for 6 h in a vacuum oven immediately prior to testing. It was common to conduct multiple tests on the same specimen. However, the time between each test was minimized so as to reduce experimental error induced by possible moisture changes that could occur in each specimen. In total, six pristine and six film-enhanced mortar specimens were subjected to electromechanical tests.

3.2.3.3 Spatial Damage Detection Validation

A testing protocol was established to validate the use of EIT for detecting the spatially distributed damage occurring in mortar specimens. For this test, only plate specimens (that have been enhanced with MWCNT-latex films airbrushed onto dry sand particles) with the 4×4 copper mesh electrodes were used. In this study, DC was injected across electrodes on opposite edges of the square mortar specimen, while voltage was measured across adjacent boundary electrodes; a similar approach was used by Loyola *et al.*[137].

Two sets of tests were conducted for validating spatial damage detection using the film-enhanced mortar specimens coupled with the EIT algorithm. Prior to each test, an initial baseline (or undamaged) EIT measurement was obtained. The first damage scenario entailed drilling four

holes using a 6.4 mm (0.25 in) masonry drill bit. Holes were drilled close to each corner of the square mortar plate. It should be noted that EIT measurements were obtained after drilling each hole. The second case employed a grinder for cutting a slit (to simulate a crack) on the backside of the plate. The average depth of cut was ~ 2.4 mm, although the depth was not uniform along its length.

3.2.4 Experimental Procedures for Self-Sensing Concrete

Similar experimental procedures were followed to validate that the self-sensing property can be encoded in the concrete by nanoengineering the cement-aggregate interfaces as done for mortar. This section describes the spray-coated sand and coarse aggregate preparation process, concrete mix-design, casting, compression and flexural test protocols, and the spatial damage detection test procedures.

3.2.4.1 Mix Design

The concrete mix design employed in this study followed the FAA runway rigid pavement guidelines [175]. Here, type I/II Portland cement and 25 *wt.%* (of total cementitious material) type F GGBFS were used. The fine aggregates were crushed granite with a density of 2.71 g/cm^3 and a minimum sieve size of 0.149 mm, and a 2:1 sand-to-cement ratio was employed. The large aggregates were 19 mm (0.75 in) river rock with a specific gravity of 2.7, and an aggregate-to-cement ratio of 3:1 was used. Selection of both fine and large aggregates conformed to the FAA guidelines on gradation46. All of the aggregates were cleaned and oven-dried at 80 °C for 24 h and then allowed to cool to room temperature for 1 h, before MWCNT-latex thin films were deposited on their surfaces, which will be explained in the next section. W/c ratios ranging from 0.42 to 0.44 were used along with an Advacast SPL. A range of w/c ratios was used due to different

casting environments and ambient temperatures, but the SPL concentration was maintained at 3.5 mL/kg for all the specimens.

3.2.4.2 Concrete Casting Procedure

Due to smaller volumes of material, concrete plate specimens were cast using a small-scale Hobart N-50 mixer. First, cementitious material and water were added to the mixing bowl. The mixer speed was set to 60 rpm and was run for 30 s to evenly hydrate the cementitious mixture. Second, after initial mixing, SPL was added, and the contents were mixed for another 2 min. During this time, sand (either pristine or coated with thin films), was added to the mixer in equal proportions every 30 s. Once all of the sand had been incorporated, the mixer was stopped, and the bowl was removed so that the large aggregates could be added. The large aggregates were poured into the bowl in small proportions, and a garden trowel was used to manually mix the contents for 30 s before more aggregates were added. This process was repeated until an even and workable mixture was obtained.

Plate specimens were cast using two custom PVC molds that measured 125 × 350 × 18 mm^3. Like the mortar specimen casting, the molds had their seams sealed with white petrolatum and their surfaces oiled with WD-40 as a releasing agent before the concrete mix was poured into the molds. The objective was to use each large plate to obtain three individual smaller plate specimens that each measured 80 × 80 × 18 mm^3. Since these concrete specimens would be subjected to spatial damage detection tests using EIT, custom Balsa wood formworks for placement of boundary electrodes were also fabricated and used during casting. The formwork held 24 equally spaced copper mesh electrodes arranged in a 6 × 6 square pattern, and the formwork was placed on top of the PVC concrete molds so that the electrodes could be embedded

and cast with the specimens. Upon pouring the mix into the molds, a 3.2 mm (0.125 in) steel rod [176] was employed for tamping the concrete for 1 min, and further compaction was performed using a shake table operated at 5 Hz for 1 min. Finally, the top of the molds was covered with clear plastic wrap to avoid surface cracking due to uneven curing and drying. They were stored at room temperature for 24 h before being demolded and placed in a curing solution for 14 days.

Cylinder and beam specimens were also cast for compressive and flexural strength tests, respectively, using the same mix design. For these specimens, a MultiQuip large capacity cement mixer was employed for casting. The casting procedure was similar, in which the dry ingredients (cement and aggregates) were mixed for 30 s before water and SPL were added. The mixture was then mixed for 5 min. For the cylinder specimens, 10-mm-diameter (4 in) and 20-mm-tall (8 in) cylinder molds were used. These cylinders were filled with two lifts of concrete, where each lift was tamped 25 times using a 14 mm (0.55 in) steel rod. Cylinders were capped and placed in a water bath for three days before being demolding, followed by a curing bath for 28 days. On the other hand, beam specimens were cast using a custom $15 \times 15 \times 46$ mm^3 ($6 \times 6 \times 18$ in^3) PVC molds. The interior of the molds was coated with WD-40 as a releasing agent and its seams sealed with white petrolatum. Casting was done by adding the mix in three lifts, and tamping was performed after each pour [48]. After filling the mold, additional compaction was achieved using a concrete vibrator. Beam specimens were then covered in clear plastic wrap and stored at room temperature for 48 h before being demolded and placed in a curing solution for 28 days. In total, four unique sets of cylinder and beam sample sets were cast. The four types were the sample sets that used film-treated sand, film-treated large aggregates, both film-treated sand and large aggregates, and control (*i.e.*, no coating).

3.2.4.3 Compression and Flexural Tests

The compressive strength of concrete was determined by conducting cylinder load tests following ASTM C39 [177]. Before testing, specimens were demolded, capped with sulfur mortar, [178] and placed in a water bath for 24 h. Specimens were then removed from the bath and mounted in an MTS load frame. Testing was done using a displacement-controlled rate of 0.51 mm/min (0.02 in/min), and this yielded an equivalent load rate that was within the range allowed as set forth in the ASTM guidelines [177]. On the other hand, beam specimens were subjected to four-point bending tests for determining their flexural strength, otherwise known as the modulus of rupture. Following ASTM guidelines, the beam specimens were mounted in an MTS load frame. Testing was performed using force-control and operated using a load rate of 8 kN/min. All of the cylinder and beam specimens were tested until failure, and during which, displacement and load data were recorded through the MTS DAQ system interfaced with *LabVIEW*. Fracture patterns for each specimen were recorded and were compared to the fracture pattern figures provided in the ASTM guidelines for cylinder and beam tests [177].

3.2.4.4 Spatial Damage Detection Tests

Validation of spatial damage detection was performed using concrete plate specimens. Before testing, each plate was removed from its curing solution, rinsed with water, and then dried in a vacuum oven set to 75 °C for 24 h. Damage detection tests were performed on the plate specimens after they cooled down to room temperature, since their electrical resistance can be lower at elevated temperatures. The DAQ system described in Chapter 1 was used for EIT interrogation and data acquisition. Across injection pattern was used for the EIT interrogation of the self-sensing concrete specimens.

Before damage was introduced to a specimen, a baseline EIT measurement of the undamaged specimen was obtained, using the aforementioned DAQ system and measurement strategy. Next, the specimens were subjected to localized damage by drilling 6.35 mm (0.25 in) holes, using a masonry drill bit, and at various locations in the plate. Drilling was done slowly to minimize excessive heating of the bit, since no coolant or lubricant was used. A total of three holes were drilled in each specimen. After drilling each hole, the DAQ system was employed for obtaining the corresponding EIT boundary voltage measurements.

3.3 Results and Discussions

3.3.1 Self-Sensing Mortar

As mentioned in Section 0, mortar specimens were cast and subjected to both mechanical and sensing characterization tests. This section discusses the results obtained and compares the results from pristine mortar versus specimens casted using MWCNT-latex thin film-coated sand.

3.3.1.1 Mechanical Properties

Tables 3.1 and 3.2 summarize the Young's modulus (E) of the pristine and MWCNT-latex thin film-enhanced mortar specimens' mechanical properties. The first '#M' denotes mechanical tests, and the second character denotes the type of specimen, namely 'P' for pristine and 'M' for MWCNT. The data presented in Table 3.1 was obtained from monotonic, uniaxial, compressive tests performed using $5 \times 5 \times 5$ cm^3 cubic mortar specimens, as was discussed in Section 3.2.3.3. It should be mentioned that these tests loaded the mortar specimens until failure. However, Young's modulus was derived from the slope of the linear least-squares best-fit line applied to the initial linear portion of the stress-strain raw data. The average Young's modulus of the pristine and

MWCNT-latex thin film-enhanced mortar specimens was 14.0 ± 1.2 and 6.03 ± 0.64 GPa, respectively (Table 3.1). The peak compressive strength (f_c') was taken as the peak value of the stress-strain raw data (Table 3.2).

From the results presented in Tables 3.1 and 3.2, it was clear that the MWCNT-latex films affected the stiffness and strength of pristine mortar. It is known that the strength and stiffness of cementitious composites are derived from the cement-particle interactions. It was possible that MWCNT-latex films coated on sand prevented those same types of chemical bonds to form, hence decreasing Young's modulus and strength of the bulk mortar specimen. Another reason may because of particle smoothing due to the MWCNT-latex coating, which reduced the ability of particles to interlock and resist loads.

3.3.1.2 Nominal Electrical Properties

In addition to the specimens' mechanical properties, their nominal or unstrained electrical properties were also quantified. As was discussed in Section 3.2.3.3, DC resistances of six pristine and six MWCNT-latex thin film-enhanced mortar cubic specimens were measured prior to electromechanical testing. For each specimen, ~ 20 s of resistance data (sampling rate: 2.8 Hz) was collected. The average DC resistance for each specimen was computed and presented in Table 3.3. In Table 3.3, '#E' denotes nominal electrical characterization tests, and 'P' and 'M' refer to the two different types of sample sets tested in this work.

Table 3.1 Comparison of mortar specimens' Young's modulus

Pristine mortar	*E* [ksi]	*E* [GPa]	MWNT mortar	*E* [ksi]	*E* [GPa]
#M-P1	2,060	14.2	#M-M1	800	5.52
#M-P2	1,980	13.7	#M-M2	905	6.24
#M-P3	2,210	15.2	#M-M3	820	5.65
#M-P4	2,280	15.7	#M-M4	750	5.17
#M-P5	1,890	13.0	#M-M5	950	6.55
#M-P6	1,730	11.9	#M-M6	1020	7.03
#M-P7	1,990	13.7	#M-M7	876	6.04
#M-P8	2,100	14.5			
Average	**2,030**	**14.0**	**Average**	**874**	**6.03**
Standard deviation	**175**	**1.2**	**Standard deviation**	**92.7**	**0.64**

Table 3.2 Comparison of mortar specimens' compressive strength

Pristine mortar	f_c' [psi]	MWNT mortar	f_c' [psi]
#M-P1	5,290	#M-M1	3,220
#M-P2	4,820	#M-M2	3,270
# M-P3	5,160	#M-M3	3,740
# M-P4	4,830	#M-M4	2,900
# M-P5	4,630	#M-M5	3,300
# M-P6	4,110	#M-M6	3,560
# M-P7	4,550	#M-M7	3,190
# M-P8	4,720		
Average	**4,760**	**Average**	**3,310**
Standard deviation	**370**	**Standard deviation**	**270**

One can see from the results shown in Table 3.3 that the average resistivity values of mortar specimens without and with MWCNT-latex thin films were drastically different. Outliers were present (*i.e.*, indicated as underlined values in Table 3.3), and they could be a result of improper drying or electrode corrosion during curing. Without considering these potential outliers in the nominal resistivity data, it was found that the average resistivity was 23.8 ± 2.7 and 2.14 ± 0.48

Table 3.3 Comparison of mortar specimen nominal electrical properties

Pristine mortar	Average resistivity [kΩ-m]	MWNT mortar	Average resistivity [kΩ-m]
#E-P1	22.9	#E-M1	38.5
#E-P2	21.9	#E-M2	2.8
#E-P3	27.8	#E-M3	2.38
#E-P4	22.5	#E-M4	2.12
#E-P5	2.73	#E-M5	1.82
#E-P6	2.77	#E-M6	1.56
Average	**23.8**	**Average**	**2.14**
Standard deviation	**2.7**	**Standard deviation**	**0.48**

kΩ-m for the pristine and film-enhanced mortar, respectively. The resistivity difference between the two sets was more than one order of magnitude, which is expected given the high electrical conductivity of carbon nanotubes and of the MWCNT-latex thin films [172]. It should be mentioned that a few of the specimens tested exhibited significant nominal resistance drifts, and those results were not included in this study.

3.3.1.3 Sensing Response Characterization

The electromechanical properties of cubic mortar specimens were characterized by conducting compressive cyclic tests, as was discussed in Section 3.2.3.2. During these tests, the specimen's DC resistance was recorded, along with its force-deformation response. It should be noted that the applied peak compressive strain was approximately -0.45%. This peak strain was selected to ensure that the mortar specimens remained linear-elastic and undamaged.

Figures 3.5a and 3.6a plot two representative results of the electromechanical tests; the plots show the mortar specimen's resistivity time histories overlaid with that of the applied strain patterns. Both sets of these results were for mortar specimens that incorporated MWCNT-latex

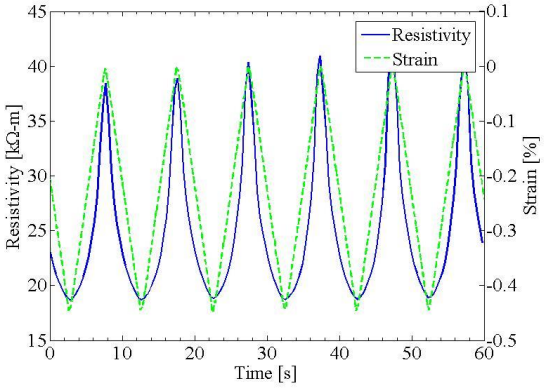

(a)

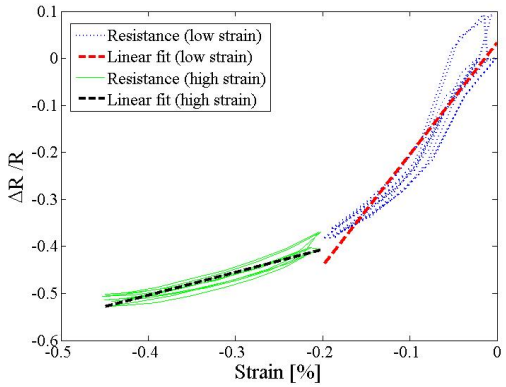

(b)

Figure 3.5 (a) The resistivity time history response of mortar specimen #S-M1 (*i.e.*, with MWNT-latex thin film) is overlaid with the applied strain time history. The results clearly show that the specimen's electromechanical properties are sensitive to applied strains. (b) Upon plotting the normalized change in resistance with respect to applied strains, it was found that the electromechanical response was bilinear.

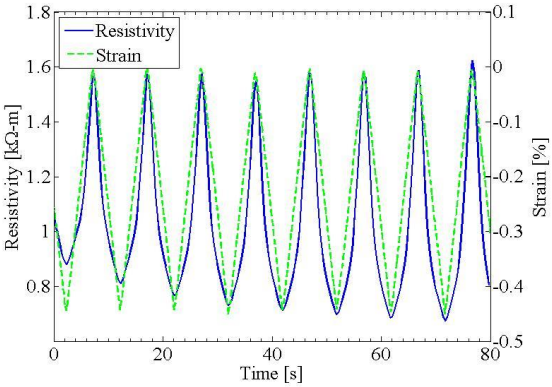

(a)

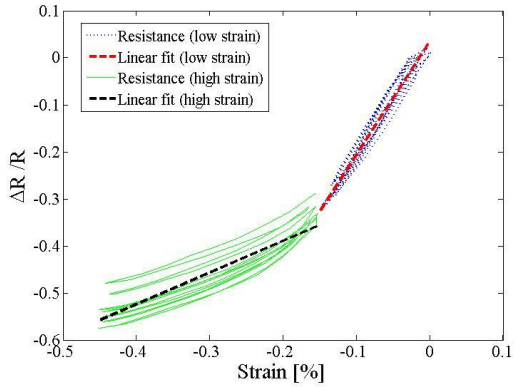

(b)

Figure 3.6 (a) The resistivity time history response of mortar specimen #S-M6 (*i.e.*, with MWCNT-latex thin film) is overlaid with the applied strain time history. The results clearly show that the specimen's electromechanical properties are sensitive to applied strains. (b) Upon plotting the normalized change in resistance with respect to applied strains, it was found that the electromechanical response was bilinear.

thin films. As expected, the test results showed that the mortar specimens' electrical properties were sensitive to applied strains. In addition, resistivity decreased in tandem with decreasing strains (*i.e.*, with greater magnitudes of applied compressive strains). It should be mentioned that the pristine mortar specimens also exhibited similar resistivity changes with respect to applied compressive loading. It can also be seen from Figures 3.5a and 3.6a that resistivity change was synchronized with that of the applied strains, and the specimen's sensitivity to strain was stable and repeatable.

While no significant nominal resistivity drift was observed during loading, resistivity drift due to potentially polarization was present during the initial 20 s of resistance measurements. For most cases, the nominal resistivity drift plateaued quickly, and tests were conducted after such drifts disappeared. In fact, an earlier studied showed that the nominal resistivity drift of cement paste specimens with ultra-low concentrations of MWCNTs would eventually plateau after repeated cyclic loading [168]. It was suspected that resistivity drift occurred because of electric charging or polarization. While the cement paste specimens tested by Wong *et al.* [168] were different than those presented in this study, polarization could still occur. It is worth noting that other researchers also observed similar charging effects, and its effect could be counteracted by applying AC excitations, using techniques such as applying a linear fit to the data [166], or by pre-charging the cementitious composite [179], just to name a few. Nevertheless, one can see from Figure 3.6a that the specimen's nominal resistivity was just beginning to plateau during the first few loading cycles.

For both of the aforementioned specimens, the same sets of data were converted such that normalized change in resistivity was plotted with respect to applied strains, as can be seen in Figure 3.5b and Figure 3.6b. Both Figure 3.5b and Figure 3.6b show that the electromechanical response of the mortar specimens (*i.e.*, for ones enhanced with the MWCNT-latex thin film interface) exhibited a polynomial relationship with respect to applied strains but was approximated as bi-linear for the purposes of quantifying strain sensitivities. This observation was true and applicable for all of the specimens tested in this study. In addition, a linear least-squares regression line was fitted to each of the two linear portions for each dataset so as to determine the strain sensitivity (S) or gage factor, which can be calculated by the following:

$$S = \frac{\Delta r / r_0}{\Delta e} \tag{3.1}$$

where ρ_0 is the nominal or unstrained resistivity, and $\Delta\rho$ is the change in specimen resistivity corresponding to the change in applied strains ($\Delta\varepsilon$).

Equation 3.1 was employed for estimating the low-strain and high-strain strain sensitivities for all the electromechanical test results. Since each mortar specimen was subjected to multiple loading cycles, low-strain *S* and high-strain *S* were calculated for each cycle, and the average strain sensitivities were computed. The results are summarized in Table 3.4. Here, the specimens are denoted as '#S' for sensing characterization; the notations for 'M' and 'P' follow the same definitions in Section 3.2.3.2.

It should be mentioned that the pristine mortar specimens did not exhibit bi-linear strain sensitivity. As a result, each pristine mortar specimen was characterized by an average strain sensitivity value, as opposed to being separated to that of low-strain and high-strain; those results are tabulated in Table 3.5. For comparison purposes, Table 3.4 also includes the strain sensitivities computed using the entire dataset ($S_{complete}$); to be specific, a linear least-squares regression line was fitted to the entire data for each cycle of loading; while this was not accurate, this calculation was performed so that a direct comparison can be made between the film-enhanced and pristine mortar specimens.

One can observe from the results shown in Table 3.4 that the average low-strain gage factor ($S_{low\text{-}strain}$) was very impressive at 229 ± 60. This sensitivity was valid for applied strains between 0% and ~ 0.2%. It is hypothesized that such high strain sensitivities were obtained, because the embedded thin film-coated sand in unstrained mortar specimens was near or at the electrical

Table 3.4 Strain sensitivities of mortar specimens enhanced with MWCNT-latex thin films

Low-strain gage factor							
Specimen	#S-M1	#S-M2	#S-M3	#S-M4	#S-M5	#S-M6	**Average**
$S_{low\text{-}strain}$	273	136	178	292	253	242	**229±60**
High-strain gage factor							
$S_{high\text{-}strain}$	56.5	87.2	59.6	62.9	61.0	63.9	**65±11**
Entire dataset gage factor							
$S_{complete}$	114	128	111	144	131	119	**125±12**

Table 3.5 Strain sensitivities of pristine mortar specimens

Specimen	#S-P1	#S-P2	#S-P3	#S-P4	#S-P5	#S-P6	**Average**
$S_{complete}$	77.7	85.0	75.6	58.8	40.3	30.2	**61±22**

percolation threshold. Any minor compressive load would cause a dramatic change in percolation properties, which would result in a large gage factor [40]. Applications of greater loads should cause strain sensitivity to decrease thereafter (*i.e.*, after exceeding the percolation threshold).

In fact, after the low-strain regime, the average $S_{high\text{-}strain}$ was 65 ± 11. From representative plots shown in Figures 3.5 and 3.6, it is clear that bi-linear sensitivity was a good approximation and that within each low- or high-strain regime, linearity was strong. It is hypothesized that this bi-linear response was observed because, during initial loading, slight changes in orientation of MWCNT-latex thin film-coated sand particles could occur and make contact with another particle, thereby changing the bulk specimen's electrical properties in a dramatic fashion. Localized high stresses acting on the film surface could also explain why such drastic changes in electrical properties were observed, especially since these MWCNT-latex thin films are piezoresistive [35]. After this point, it is hypothesized that strain sensitivity is dominated by the cementitious matrix,

although the electrical conductivity of the bulk mortar is still enhanced with the presence of the MWCNT-latex thin film.

In contrast, the pristine mortar specimens did not exhibit bi-linear strain sensitivity, and its average strain sensitivity was much lower, approximately 61 ± 22. As compared to the MWCNT-latex thin film-enhanced mortar, the pristine mortar possessed gage factors similar to that of $S_{high\text{-}strain}$ for the MWCNT-based specimens. The comparable strain sensitivity makes sense, since it was hypothesized that the cementitious matrix was contributing to most of the electromechanical response observed. However, it should be mentioned that the standard deviation for the pristine mortar was 22, which is twice that of the MWCNT-based specimens (*i.e.*, 11). In fact, the SNR and sensing resolution of the pristine mortar specimens was fairly low. Thus, despite comparable high-strain gage factors, the advantages offered by modifying the cement-sand particle interface with MWCNT-latex thin films were improved SNR, sensing resolution, and repeatability of measurements.

3.3.1.4 Spatial Damage Detection

Once the electromechanical properties of mortar specimens were characterized, the final phase of this study was to validate spatial damage detection. Plate specimens with 16 embedded copper tape or mesh electrodes were cast, following steps outlined in Section 3.2.3.3. It should be mentioned that only MWCNT-based mortar plates were investigated because preliminary tests showed that electrical current could not be effectively propagated through pristine mortar specimens. Because of this, spatial resistivity mapping of pristine mortar using the EIT algorithm was not possible.

According to Section 3.2.3.3, an additional set of tests using these plates with 16 boundary

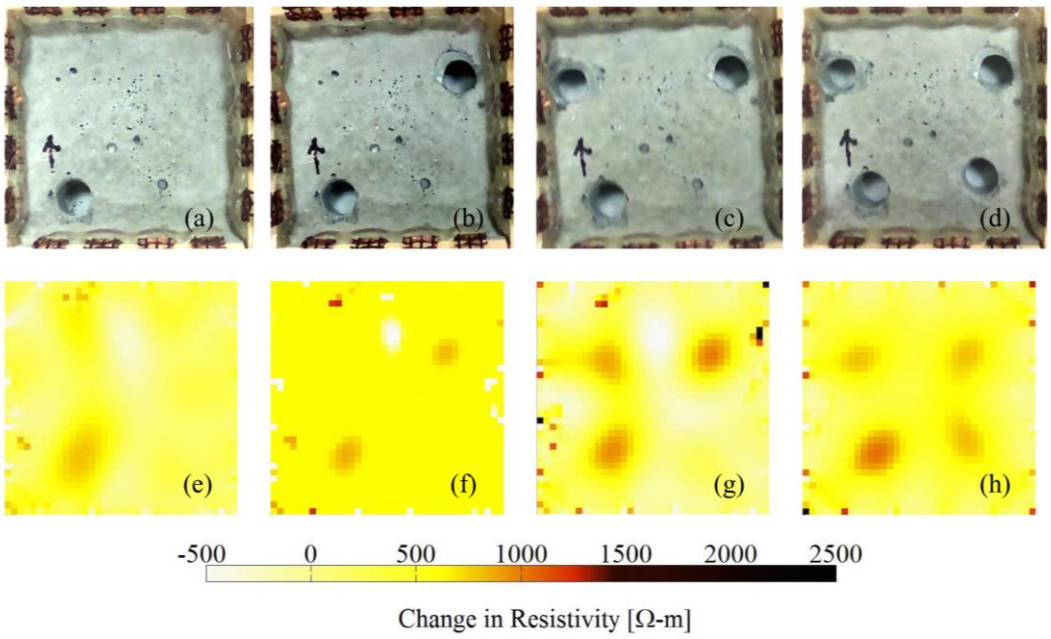

Figure 3.7 A masonry drill bit was used to drill holes in the smart mortar specimen and in a sequential fashion, that is, at the (a) bottom-left, (b) top-right, (c) top-left, and then (d) bottom right. The EIT spatial resistivity maps (*i.e.*, the change of resistivity relative to the undamaged baseline) after drilling the (e) bottom-left, (f) top-right, (g) top-left, and then (h) bottom right holes are shown.

electrodes, were also conducted. Instead of single damage, this test sought to validate the performance of the MWCNT-based mortar and EIT algorithm for monitoring and detecting the severity and location of multiple damage. To be specific, one can see from Figure 3.7 that a 6.4-mm-diameter hole was drilled through the plate and near the bottom-left corner. The corresponding EIT result shown in Figure 3.7e clearly identifies significant localized changes in resistivity at the same vicinity. The same conclusion can be reached by examining the other three drilled-hole locations (Figures 3.7b to 3.7d) and the respective EIT change in resistivity maps (Figures 3.7f to 3.7h). While some of the identified damage locations may not be exact (*e.g.*, Figure 3.7g) the technique suggests great promise for detecting damage severity and for identifying its general location. These experimental results validated that mortar casted with nanocomposite-coated sand provided sufficient electrical conductivity while using fewer additives for EIT to work.

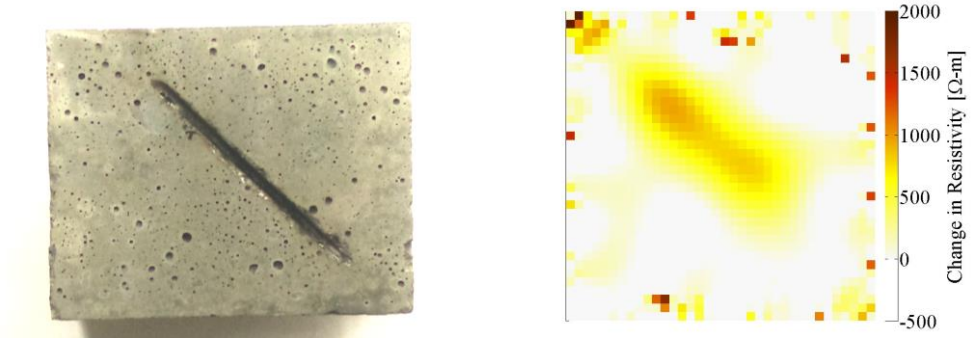

Figure 3.8 (a) An artificial crack was introduced along the diagonal of a smart mortar plate. (b) The reconstructed EIT resistivty map clearly identifies the location and severity of the damage.

Besides drilling holes, a crack-like damage was introduced by cutting a ~ 2.4 mm-deep slit on the plate's surface. Figure 3.8a shows a picture of the crack-like damage on the backside of a smart mortar plate, and Figure 3.8b shows the corresponding EIT result. As with the previous case, the EIT result shows the change in resistivity of the smart mortar with respect to the initial undamaged specimen. It can be seen from Figure 3.8b that the slit or crack can be identified as a significant and localized increase in resistivity, which was expected. In addition, the remainder of the specimen did not exhibit any changes in resistivity, since they were not damaged in the process.

3.3.2 Self-Sensing Concrete

3.3.2.1 Mechanical Properties

The compressive and flexural strength results are summarized in Tables 3.6 and 3.7. Here, values for compressive and flexural strengths are presented with the corresponding sample sets' w/c ratios and amount of SPL used during casting. Fracture patterns for all of the cylinders tested were type 1-3, following the diagrams given in ASTM C3949, which means that the sulfur caps were level and provided uniform loading throughout the tests. From the results shown in Table

3.6, it can be seen that the lowest average compressive strength was for the aggregate-coated mix at 6,500 psi.

Despite this, the compressive strength is well above the FAA guideline required strength of 4,400 psi [46]. The sand-coated and both sand- and aggregate-coated sample sets exhibited average compressive strengths of 6,860 and 7,580 psi, respectively. On the other hand, the pristine specimens (*i.e.*, untreated or no thin film coating) had an average strength of 7,030 psi. From these results, it can be inferred that the mechanical properties of concrete can be maintained or even exceeded when cement-aggregate interfaces are modified with MWCNT-latex thin films.

Overall, Table 3.6 suggests that sand-coated specimens could achieve the same, if not greater, compressive strengths as pristine concrete. However, coating the large aggregates degraded their inherent mechanical properties. While this can be perceived as a disadvantage of the approach of modifying the cement-aggregate interface with MWCNT-latex thin films, the objective was to meet or exceed design guidelines (*i.e.*, 4,400 psi limit) [175] as opposed to deriving a technique that would not influence the material properties of concrete. Nevertheless, it was postulated that coating the aggregates diminished strength since the MWCNT-latex coating modified the chemistry and bonds that would have formed between the cement matrix and large aggregates. Coating the large aggregates could potentially create a smoother surface that would reduce the effectiveness of bonding. Future studies will explore partial coatings on large aggregates as a compromise for enhancing electrical properties while mitigating the adverse impacts on compressive strength. In contrast, coating sand did not seem to produce adverse effects. This could be due to sands' smaller particle size and intrinsic jagged nature.

Table 3.6 Average compressive strengths of concrete cylinders.

Mix Design	w/c ratio	SPL [mL/kg]	Average compressive strength [psi]
Pristine (or untreated)	0.44	3.5	7,030
Aggregate-coated	0.44	3.5	6,500
Sand-coated	0.44	3.5	6,860
Sand- and aggregate-coated	0.44	3.5	7,580

Table 3.7 Flexural strengths of concrete beam specimens.

Mix Design	w/c ratio	SPL [mL/kg]	Modulus of Rupture [psi]
Pristine	0.44	3.5	953
Aggregate-coated	0.42	3.5	950
Sand-coated	0.42	3.5	903
Sand- and aggregate-coated	0.43	3.5	821

The beam tests and flexural strength results also provide a direct comparison on the differences in the mechanical properties of different sample sets, since they were cast using approximately the same w/c ratio and SPL content. All beam specimens fractured within the middle-third of the span, and based on ASTM C78 [178], the modulus of rupture was calculated using equation 3.2:

$$R = \frac{PL}{bd^2} \tag{3.2}$$

where R is the modulus of rupture in [psi], P is the maximum applied load before failure in [lbf], L is the span length in [in], and b and d are the average width and depth of the specimen, respectively, at the failure plane and in [in]. Here, it can be shown that the average flexural strength of aggregate-coated beams was close to that of the pristine sample set. The sand-coated beam had a slight lower rupture modulus, but this value only differed by 6% as compared to the pristine

specimen. Finally, the sample set with both types of aggregates coated with the films had a 14% flexural strength reduction. Despite this, these values are well above the minimum FAA requirements for rigid pavement design, which states that the modulus of rupture should give a minimum of 600 to 700 psi [174].

3.3.2.2 Spatial Damage Detection Validation

In order to validate spatial damage detection using EIT, three different types of concrete plates were cast, each with dimensions of $80 \times 80 \times 20$ mm^3. As mentioned earlier, six 6-mm-wide copper mesh electrodes, separated 4 mm apart, were embedded along each side of the square plates. The damage was induced by drilling three holes at different locations in the plate.

First, damage detection tests were performed on pristine concrete plates (*i.e.*, concrete without any embedded MWCNT-latex thin films), and the test specimen and corresponding EIT results are shown in Figure 3.9. As with all tests, the EIT DAQ system was employed for measuring the boundary voltages before and after the introduction of damage. It can be seen from the reconstructed resistivity distributions of the concrete plates (Figures 3.9e to 3.9h) that no apparent changes in resistivity distributions were observed due to damage. The application of EIT on its own on concrete did not enable damage detection. A reason for this could be the fact that the resistivity of pristine concrete is too high. Hence, applied electrical current could not sufficiently propagate through the entire material (*i.e.*, electrical current only flowed through the path of least resistance), and the measured boundary voltage responses were not sensitive to damage features created by drilling holes. The same testing procedure was also repeated for concrete casted using large aggregates coated with MWCNT-latex thin films, and a set of representative results are shown in Figure 3.10. Similarly, spatial damage detection was unsuccessful for the same reasons

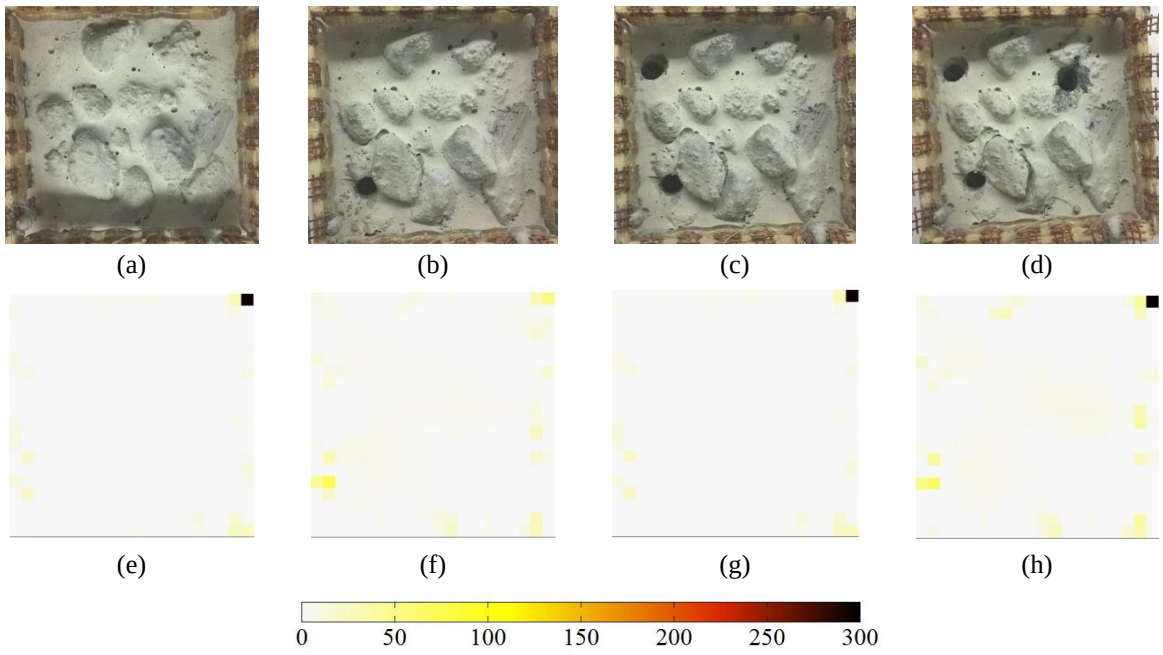

Figure 3.9. Damage detection tests were performed on (a) pristine concrete plates. Holes were drilled near the (b) bottom-left, (c) top-left, and then (d) top-right corners of the plate. (e) The spatial resistivity distribution of the undamaged plate is shown. The change in resistivity distribution was also calculated with respect to the undamaged baseline after the introduction of drilled-hole damage near the (f) bottom-left, (g) top-left, and (h) top-right corners.

mentioned previously. It was hypothesized that coating the large aggregates alone did not create sufficient amounts of conductive interfaces for electrical current to propagate effectively throughout the entire plate. As a result, a percolation (or near-percolation) system was not formed, and applied electrical current did not generate boundary voltage responses that were sensitive to damage.

In contrast, sand-coated and both sand- and aggregate-coated concrete plates, when coupled with the EIT algorithm, yielded drastically different results, as shown in Figures 3.9 and 3.10, respectively. For these two sample sets, electrical current applied across two opposite electrodes was able to propagate throughout the entire plate, and the EIT spatial resistivity maps clearly show

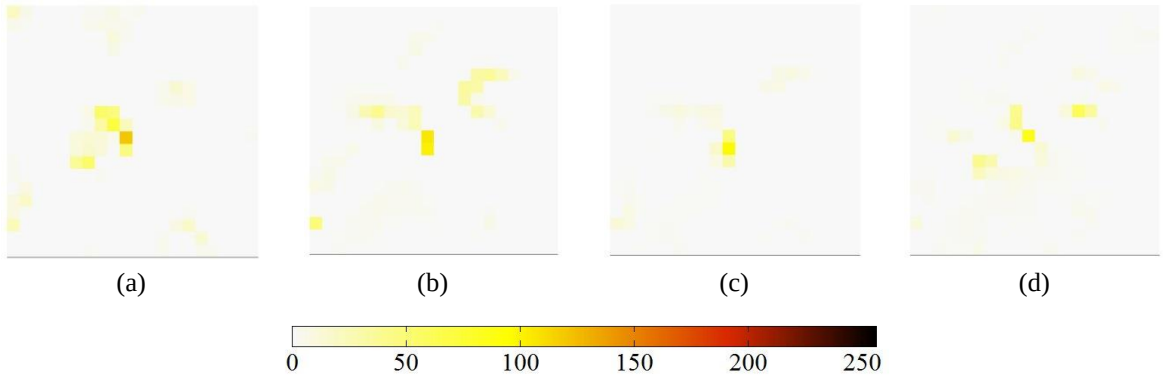

Figure 3.10. Damage detection tests were performed on aggregate-coated concrete plates. The spatial resistivity map for the (a) undamaged and the change in spatial resistivity distribution corresponding to a hole drilled near the (b) bottom-left, (c) top-left, and (d) top-right did not successfully detect damage.

localized increases in resistivity that coincided with the locations of drilled holes. When comparing the results shown in Figures 3.11 and 3.12, it can be seen that the SNR is higher (*i.e.*, the magnitude of the change in resistivity is larger) for concrete casted using both sand and aggregates coated with the MWCNT-latex thin films. This result was observed because these specimens were characterized by higher electrical conductivity due to the presence of more conductive cement-aggregate interfaces. In short, spatial damage detection is only possible when current can propagate through the entire body, and its path is perturbed significantly by damage (or localized resistivity or conductivity changes) so that boundary voltage changes can be observed. Otherwise, EIT cannot detect changes in resistivity from inverse analysis, as can be seen from the results shown in Figures 3.9 and 3.10.

3.3.2.3 Cost Analysis

A simple cost analysis was performed to compare the proposed technique of modifying cement-aggregate interfaces using MWCNT-latex thin films versus the current state-of-art of directly dispersing carbon nanotubes in the cement matrix. Table 3.8 shows a summary of the increase in estimated costs (in U.S. dollars) of MWCNTs required assuming A simple cost analysis

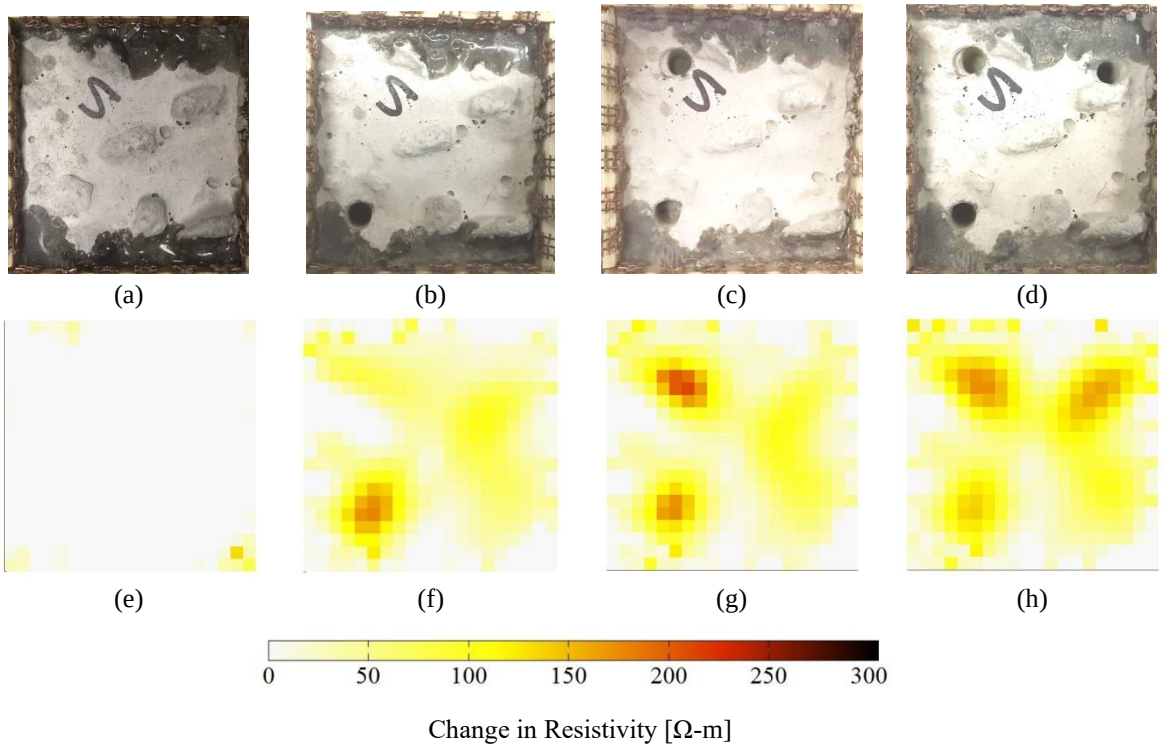

Figure 3.11 Damage detection tests were performed on (a) concrete plates cast using sand coated with MWNT-latex thin films. Holes were drilled near the (b) bottom-left, (c) top-left, and then (d) top-right corners of the plate. (e) The spatial resistivity distribution of the undamaged specimen is shown. The change in resistivity distribution was also calculated with respect to the undamaged baseline after the introduction of drilled-hole damage near the (f) bottom-left, (g) top-left, and (h) top-right corners.

was performed to compare the proposed technique of modifying cement-aggregate interfaces using MWCNT-latex thin films versus the current state-of-art of directly dispersing carbon nanotubes in the cement matrix. Table 3.8 shows a summary of the increase in estimated costs (in U.S. dollars) of MWCNTs required assuming that 256 kg of cementitious content is needed for 1 m^3 of concrete (based on FAA guidelines) [174]. All weight percentage concentrations of carbon nanotubes are with respect to the amount of cement or cementitious material used in the mix design. The larger weight percentages are comparable to the quantities used by Yu and Kwon [180]. The last two rows correspond to concrete specimens presented in this work, and MWCNT concentrations were calculated based on the total weight of nanotubes used during ink preparation and spray fabrication

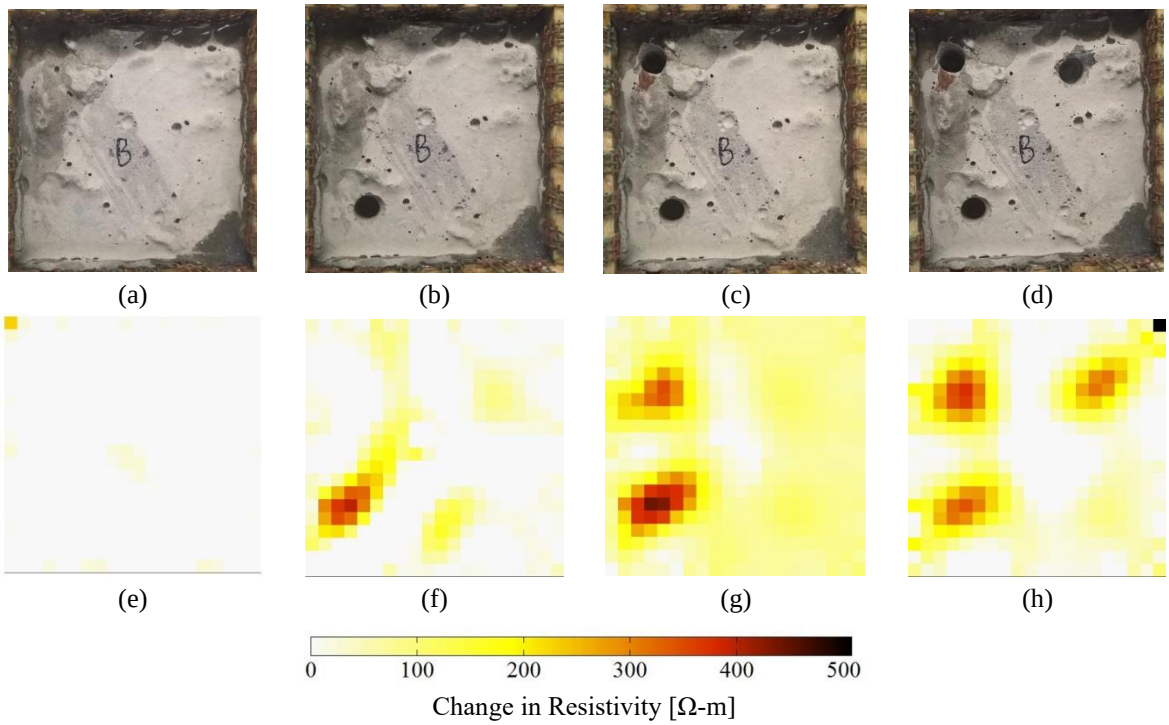

Figure 3.12. Damage detection tests were performed on (a) concrete plates cast using sand and large aggregates coated with MWCNT-latex thin films. Holes were drilled near the (b) bottom-left, (c) top-left, and then (d) top-right corners of the plate. (e) The spatial resistivity distribution of the undamaged specimen is shown. The change in resistivity distribution was also calculated with respect to the undamaged baseline after the introduction of drilled-hole damage near the (f) bottom-left, (g) top-left, and (h) top-right corners.

(*i.e.*, material lost during spray coating was accounted for in these calculations and represents opportunities for further lowering the cost of this technique).

Given that the average price of concrete is ~ $122 per cubic meter [181], significant increases in costs can be observed if MWCNTs are directly dispersed in the cement matrix. For instance, concrete containing 0.5 *wt.*% of MWCNTs would incur [181] times additional costs as compared to pristine concrete. In comparison, sand-coated specimens in this study would incur dramatically less increases in cost (Table 3.8). The lower cost of modifying cement-aggregate interfaces makes this an attractive technique for real-world, practical implementations of this material. It should be noted that the specimens casted in this study have not been optimized for

Table 3.8 Cost matrix comparing additional costs of incorporating carbon nanotubes in concrete.

Unit price	MWNT content	Additional cost
MWNT: $5,000 / kg	0.5 *wt.*%	$6,400
	0.1 *wt.*%	$1,280
	0.05 *wt.*%	$640
	0.034 *wt.*% (sand-coated)	$435
	0.025 *wt.*% (aggregate-coated)	$320

Note: All prices are shown in U.S. dollars.

sensing and mechanical performance, and further reductions in cost are possible and will be reserved for future studies.

3.4 Summary and Conclusions

In this study, a novel technique of incorporating CNTs in cementitious composites was proposed, which is by modifying the cement-sand particle interface using highly conductive, percolated MWCNT-based thin films. In particular, an airbrushing technique was employed for depositing MWCNT-latex thin films onto the sand and aggregates before being used for casting cementitious composite specimens. Then, untreated and film-coated sand were used for casting 5 $\times$ 5 $\times$ 5 cm^3 cubic and 7 $\times$ 7 $\times$ 1 cm^3 plate specimens. The mechanical, nominal electrical and electromechanical properties of both pristine and MWCNT-based mortar specimens were characterized and compared.

First, monotonic, uniaxial compressive load tests revealed the stress-strain characteristics of these mortar specimens. It was found that Young's moduli of pristine and MWCNT-based mortar were 14 and 6 GPa, respectively. The differences were statistically significant in that the MWCNT-latex coating on the sand appeared to have modified the mortar's intrinsic mechanical

properties. Similar degradations were also observed for compressive strength results.

Second, the electrical and sensing characterization tests showed that the incorporation of MWCNT-latex thin films decreased their resistivity by more than an order of magnitude. In addition, while both types of mortar specimens exhibited electrical properties that were sensitive to strain, those with the films showed bi-linear response to applied strains. At low strains, the sensitivity was extremely high, with an average of ~ 229. At applied strains greater than 0.2%, both types of specimens had comparable sensitivities of ~ 61 to ~ 65. However, mortar with embedded thin films exhibited greater SNR, sensing resolution, repeatability, and less nominal resistance drift.

Lastly, the EIT algorithm described in Chapter 2, was implemented for back-calculating the spatial resistivity map (or distribution) of MWCNT-based mortar specimens for damage detection applications. Plate specimens instrumented with 16 boundary electrodes (in a 4 × 4 pattern) were subjected to artificial damage due to drilled holes and slit cut at the four corners and the back-side of the specimens. The results from all the tests showed very promising results, in which the EIT algorithm correctly estimated the spatial resistivity distribution of the mortar plates. In addition, the spatial resistivity maps also showed localized increases in resistivity corresponding to the locations and sizes of damage. These tests successfully validated EIT for spatial damage detection in nanocomposite-enhanced self-sensing mortar specimens.

A similar procedure was used for encoding self-sensing property in concrete. Fine and coarse aggregates were pre-coated with a highly conductive MWCNT-latex thin film that was deposited using airbrushing or spray coating. In doing so, CNTs remained dispersed within the films, which could then be uniformly dispersed throughout concrete along with the aggregates. A

direct result is dramatic reductions in the amount of nanotubes used during casting and associated costs while still providing enough conductive material for establishing a conductive network within the bulk material for damage detection purposes. In addition, the proposed technique does not modify existing mix designs nor construction practices.

Four unique concrete sample sets were cast; they were the control (pristine or untreated concrete) and concrete cast using MWCNT-latex thin films coated onto sand, large aggregates, and both sand and large aggregates. Compression and bending tests were conducted on cylinder and beam specimens, respectively, for assessing their mechanical properties. First, all of the specimens exceeded the minimum strength requirements as set forth by FAA rigid concrete pavement design guidelines. Second, the sand-coated and aggregate-coated sample sets exhibited comparable flexural strengths as compared to the control, whereas the sand-coated and sand- and large aggregate-coated sample sets were characterized by similar, if not higher, compressive strengths versus the control. Then, using concrete plate specimens coupled with an EIT algorithm, spatial damage detection tests were conducted. The results showed that the sand-coated and both sand- and aggregate-coated concrete sample sets enabled damage detection, due to the fact that electrical current was able to propagate throughout the entire bulk material. EIT was able to map the spatial resistivity distributions of plate specimens, and damage (in the form of drilled holes) were successfully detected as highly localized resistivity changes that coincided with the locations of those holes. In contrast, EIT was unable to detect damage in untreated concrete and large aggregate-coated specimens. In general, spatial damage detection is only possible if applied electrical current could propagate throughout the entire material so as to generate boundary voltage responses that are sensitive to damage.

Overall, this chapter successfully demonstrates that instead of using the nanocomposite thin film as a surface coating, it can also be integrated with structural materials by scalable, low-cost technique for encoding self-sensing property in them. The conductive network created by the integration of nanocomposite with structural materials facilitates thorough propagation of electrical current; hence EIT can be applied for distributed damage detection in such materials. However, strain induced in a different direction can not be measured by this technique. Chapter 3 shows how the nanocomposite design and EIT algorithm can be modified to achieve strain measurement in different directions over a large structural surface.

This chapter, in part, is a reprint of the materials as it appeared in Multifunctional Cement Composites Enhanced with Carbon Nanotube Thin Film Interfaces, J. G. Gonzalez, S. Gupta, and K. J. Loh, 2016; Self-Sensing Concrete Enabled by Nano-Engineered Cement Aggregate Interfaces, S. Gupta, J. Gonzalez, and K. J. Loh, 2016; and Damage Detection using Smart Concrete Engineered with Nanocomposite Cement-Aggregate Interfaces, S. Gupta, J. Gonzalez, and K. J. Loh, 2015.

CHAPTER 4 GRAPHENE SENSING MESH FOR DENSELY DISTRIBUTED STRAIN FIELD MONITORING

4.1 Introduction

As mentioned earlier, EIT, when coupled with piezoresistive nanocomposite thin films, could be used for distributed strain sensing and damage mapping [105, 137, 182]. However, only distributed strain magnitudes could be determined but not their directionalities. In order to address this limitation, a net- or mesh-like, graphene-based, nanocomposite sensing mesh that featured high aspect ratio "struts" was designed so that the entire sensing mesh behaved like an interconnected network of strain gages. The sensing mesh was coupled with a modified EIT algorithm to achieve distributed strain field monitoring over large structural surfaces.

Strain is an important parameter that is often directly measured for SHM. However, as mentioned in Chapter 1, current-state-of-the-art strain sensors have many limitations [183, 184]. As a result, these limitations have spurred the development of other types of strain sensors derived from different sensing mechanisms. For example, Glisic *et al.* [185] studied large-area electronics and crystalline silicon complementary metal-oxide-semiconductor integrated-circuit-based strain sensors for large-scale structural sensing applications. Kharroub *et al*. [186] developed soft elastomeric capacitor-based thin film sensors for detecting and localizing fatigue-induced cracks in steel structures. More recently, another approach is to design and tune materials to enable them with desired sensing functionalities. However, to fully take advantage of the fact that these materials and nanocomposites are sensitive to some stimulus at every location in the material, it was shown that spatial sensing could be achieved using an EIT measurement technique and algorithm. Piezoresistive sensing skins coupled with the EIT algorithm opened up vast

opportunities for distributed strain sensing. However, two main drawbacks persist. First, a separate analytical inverse piezoresistive numerical model is required to extract strain directionality from the reconstructed EIT conductivity maps [187]. Second, comparatively low strain sensitivities of the CNT thin films make it challenging for detecting small changes in strain.

To address these limitations, this study introduces a new "sensing mesh" concept. First, a graphene-based thin film of high strain sensitivity was designed and fabricated. The nanocomposite films were deposited onto laser-cut patterned polyethylene terephthalate (PET) substrates by means of spray coating to form the sensing meshes. Each strut of the sensing mesh was designed to have a high aspect ratio, thereby forming an interconnected equivalent network of uniaxial linear distributed strain sensors. Second, an EIT algorithm was updated and implemented for reconstructing the spatial conductivity distribution of the sensing mesh.

This chapter begins with the mathematical detail of the modified EIT algorithm, followed by a discussion of the sensing mesh fabrication procedure and experiments. Upon confirming the enhanced strain sensing response of the graphene-based films, the sensing mesh was experimentally validated to measure distributed strain fields. As further validation, the sensing mesh was also employed to measure spatial strain distribution of different structural surfaces subjected to different levels of tensile loading. Finally, the sensing mesh was demonstrated for its ability to monitor different damage states in a seven-story RC structure subjected to shaking table tests.

4.2 Modified EIT Formulation

As mentioned earlier, the EIT forward problem is solved to estimate the boundary voltage distribution of a conductive body with an explicitly known σ. Mathematically, the EIT forward problem can be described by two-dimensional (2D) Laplace's equation as shown in equation 2.16.

In general, a FE method is used to solve equation 2.16 with boundary conditions known as the CEM discussed in Chapter 2 [188]. In many cases, Ω is modeled as a simple 2D plate and discretized using linear triangular [111, 137, 188] or bilinear quadrilateral elements [189]. In this study, the sensing meshes are not continuous thin films but rather patterned grid-like piezoresistive networks. Because of the high aspect ratio of each "strut" in the sensing mesh, induced strains in each strut are confined along their longitudinal axes, experiencing either uniaxial tensile or compressive strains. This is analogous to the axial elements that make up a truss structure. Therefore, this same idea is adopted to capture the uniaxial changes in the conductivity of each strut in the sensing mesh. However, this also requires a different FEM implementation for EIT spatial conductivity mapping. Here, the high aspect ratio of each strut and the entire sensing mesh was modeled as a 2D truss structure discretized using 1D linear bar elements. By doing so, the computational cost to solve the forward problem, as well and the sensitivity matrix (J), was significantly reduced. A reduction in the size of the sensitivity matrix eases its inversion during the execution of the inverse problem. In addition, a point electrode model[22] was implemented; the specified boundary conditions are shown in equation 4.1 below:

$$\sigma \frac{\partial u}{\partial n} = f \text{ on } \Gamma$$
$$f = \sum_{i=1}^{M} I\delta_{x_i} \tag{4.1}$$

where I is the magnitude of current injected into Ω during EIT interrogation, Γ is the boundary of Ω, M is the number of boundary electrodes, n is the outward unit normal at the boundary, and δ_{x_i} is the Dirac-Delta function on Γ supported at x_i. An essential boundary condition (*i.e.*, $u = 0$) should also be imposed on the electrode that is grounded during electrical excitation. A weak form of equation 2.16 was derived by multiplying it with a sufficiently smooth test function (φ) and integrating over Ω as shown in equation 4.2:

$$\int_{\Omega} \sigma \nabla u \cdot \nabla \varphi d\Omega = \int_{\Gamma} f \varphi d\Gamma \tag{4.2}$$

Then, a set of linear equations obtained from equation 4.2, is solved to obtain *u* at each node of the discretized Ω.

The EIT inverse problem aims to reconstruct the conductivity distribution using an experimentally measured set of boundary voltage responses. A single-step linear inverse solver with Tikhonov regularization was used to estimate the conductivity change ($\Delta\sigma$) from the observed change in boundary voltage distribution (ΔV) between two states. More details of the EIT theory and implementation can be found in Chapter 2.

4.3 Experimental Details

4.3.1 Nanocomposite Thin Film Preparation

In order to achieve distributed strain field monitoring, the first step was to design and fabricate a nanocomposite thin film whose electrical conductivity (or resistivity) was sensitive to applied strains and deformation. Among the variety of nanomaterials that are available today, a significant body of current research focuses on GNS, which exhibits outstanding intrinsic properties, with piezoresistivity being just one of them. For example, Chen *et al*. [190] demonstrated that Young's modulus of single-layer graphene sheet could be as high as 1 TPa with a gage factor of 11.4. Several studies already showed that GNS could be integrated into polymer matrices to form high-performance strain sensors [191-193].

The GNS that was used in this work was synthesized using water-assisted liquid-phase exfoliation. The synthesis procedure was explained in detail in Manna *et al.* [194, 195] but is also

summarized here for completeness. The process began by mixing microcrystalline graphite powder with an aqueous solution of NMP, followed by 6 h of bath sonication at a fixed nominal power (100 W) and frequency (37 kHz). Thereafter, the sonicated graphene-NMP solution was centrifuged at 3,000 rpm for 30 min. The upper 75% of the centrifuged colloidal solution (*i.e.*, the supernatant) was collected and then dried to obtain agglomerated GNS. The GNS-based thin film strain sensor was then fabricated by dispersing them in a PVA polyelectrolyte solution. The GNS-PVA ink fabrication process is discussed in the next two sub-sections.

4.3.1.1 PVA Solution Preparation

GNS, which is hydrophobic, requires a hydrophilic group to facilitate dispersion. Steric stabilization of GNS in PVA (Sigma-Aldrich), which is hydrophilic in nature, not only disperses GNS in the solution but also allows them to adsorb onto various substrates and form thin films. The PVA used in this work is amorphous and has a molecular weight of 146,000 – 186,000 g/mol and a hydrolysis degree of ~ 99%+. Preparation of the 5 *wt*.%. PVA solution began by boiling 95 mL of deionized (DI) water using a hot plate while continuously stirring the solution using a magnetic stirrer operated at 300 rpm. Then, 5 g of PVA powder was slowly added to the boiling DI water. The mixture was stirred until a visibly clear and fully dissolved PVA solution was obtained. The final step was to cool the PVA solution to room temperature.

4.3.1.2 GNS-PVA Ink Preparation

The aforementioned 5 *wt*.% PVA solution was directly used to prepare the GNS-PVA ink. While various methods could be used to disperse GNS in aqueous media, ultrasonication was employed due to its simplicity and effectiveness. In short, ultrasonication of fluidic solutions, such as GNS in PVA, by creating cavitation [196]. Cavitation forms relatively low-pressure zones and

creates bubbles. Bubbles formed at the surface of solid particles (*i.e.*, on the GNS) rapidly expand, causing the solid particles to break apart and separate from each other. The size of the bubble produced during cavitation is governed by the frequency of the ultrasound, where higher frequencies produce smaller bubbles [196].

In this study, a 1 *wt*.% GNS-PVA mixture was prepared by subjecting it to high-energy probe sonication (150 W, 22 kHz, and running a 5-s-on/5-s-off sonication cycle) for 1 h. The dispersed GNS-PVA ink was then used as is and directly spray-coated onto PET substrates using a Paasche airbrush operated at a constant air pressure of ~ 10 psi to avoid droplet scattering in the air and splashing on the substrate. Spray fabrication was performed manually by holding the airbrush ~ 15 cm above the substrates. After depositing a uniform layer of thin film on the PET substrate, they were kept inside the fume hood and allowed to dry completely. Thereafter, airbrushing was repeated. This spraying and drying cycle was repeated three times to obtain a consistent and uniform thin film on the PET grid. The entire GNS-PVA thin film fabrication process is illustrated in Figure 4.1.

Spray fabrication was adopted in this study because one could produce high-quality and large-scale GNS-PVA thin films quickly. Although a manual procedure was employed in this work, spraying can be fully automated through the use of robotic spray systems. Furthermore, spraying is beneficial as one can directly deposit films onto various (and masked) structural surfaces, thereby eliminating problems associated with gluing sensing meshes and issues regarding nonuniform strain transfer from the structural surface to the sensing element.

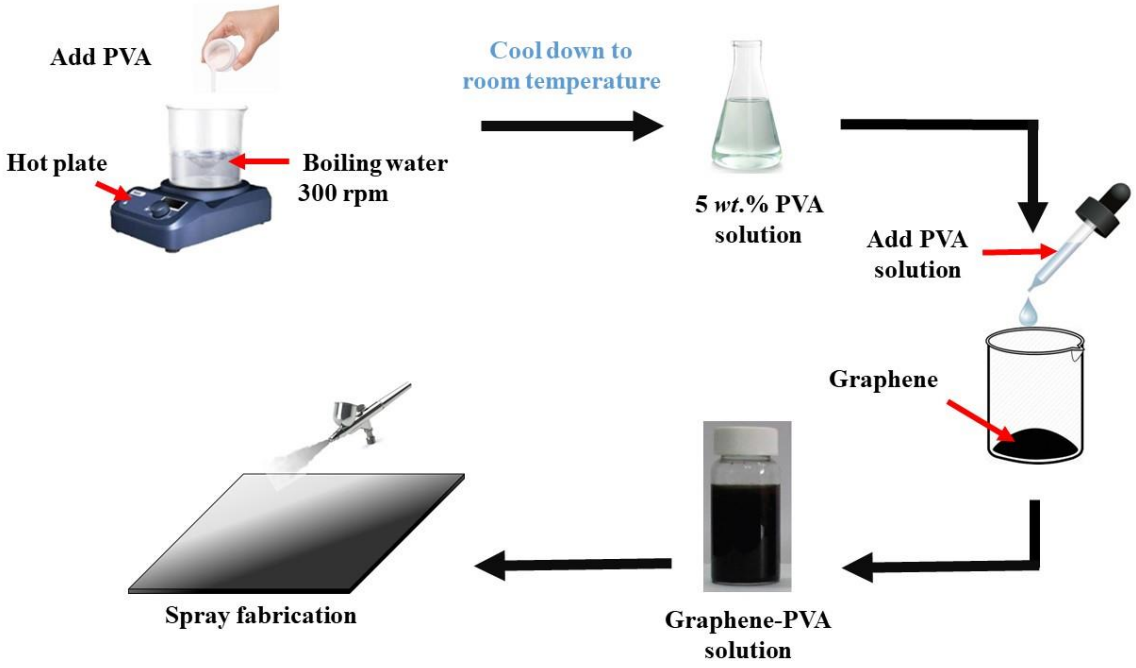

Figure 4.1 The GNS-PVA ink preparation and spray fabrication process are illustrated.

4.3.2 Strain Sensing Characterization

The strain sensing performance of the GNS-PVA thin films that were deposited onto PET substrates was characterized by subjecting them to uniaxial tensile cyclic strains, while their electrical responses were simultaneously measured. First, the air-dried thin film specimens were cut to form thin rectangular strips (60 mm × 10 mm) and instrumented with two electrodes at its opposite ends, as is shown in Figure 4.2. Conductive threads (Adafruit) were used as electrodes and attached to the films using conductive colloidal silver paint (Ted Pella). A total of four specimens were prepared and tested.

The GNS-PVA thin film strips were mounted in a Test Resources 150R load frame with a 1.1 lbf (4.9 N) load cell as shown in Figure 4.2. Upon ensuring that the thin film was taut, the load frame was programmed to execute a three-cycle tensile cyclic strain pattern to a maximum of 5,000 με at a constant strain rate of 15,000 με/min. A Keysight 34465A DMM was used throughout

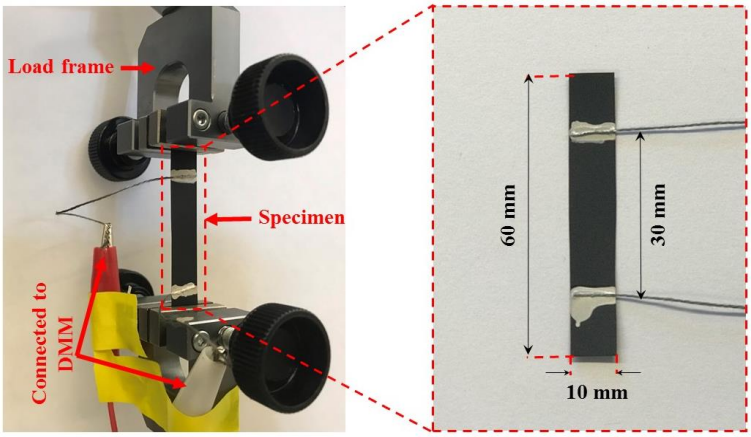

Figure 4.2 GNS-PVA thin films were deposited onto PET rectangular strip substrates. These rectangular specimens were instrumented with two electrodes for electrical measurements and then mounted in a load frame for strain sensing characterization tests.

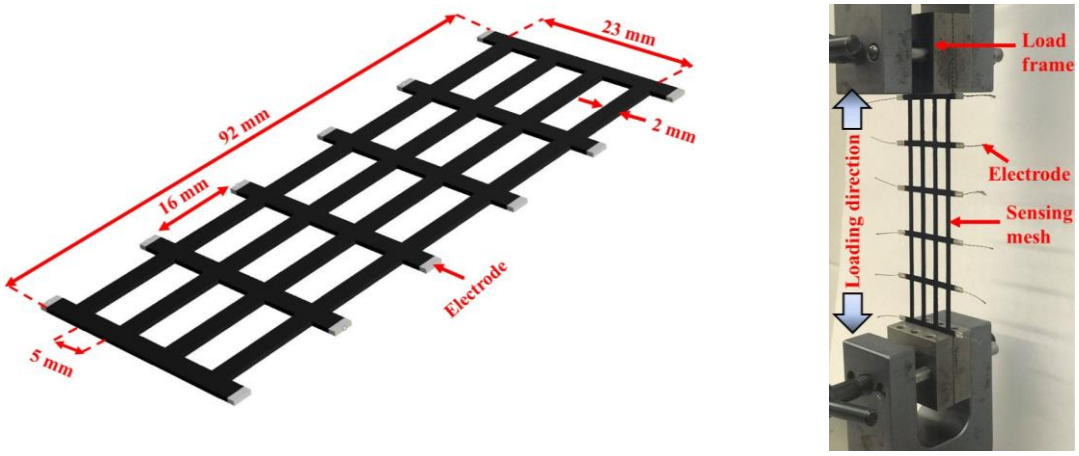

(a) (b)

Figure 4.3 (a) PET sheets were cut into grid-like patterns using a laser cutter, followed by spray-coating them with GNS-PVA ink to form the sensing mesh specimens. (b) The sensing mesh was mounted in a load frame and subjected to uniaxial tensile loading. EIT measurements were acquired at different strain states, while the load frame was paused.

testing to measure thin film resistance. *BenchVue* data logging software was used to record all the measurements at a sampling rate of 2 Hz.

4.3.3 Sensing Mesh Validation

As was mentioned earlier, GNS-PVA thin films were deposited onto PET grids to form sensing mesh specimens. The patterns were first sketched in AutoCAD and then exported to

LaserDRW. A 40 W CO_2 laser cutter (Orion Motor Tech) was used for patterning the PET grids. Three sets of sensing mesh tests were conducted.

First, the sensing mesh was instrumented with 12 boundary electrodes (Figure 4.3a) for EIT interrogation and loaded in the Test Resources 150R load frame for spatial strain sensing characterization, as is shown in Figure 4.3b. It should be observed from Figure 4.3 that the sensing mesh consisted of only horizontal and vertical struts. The load frame was programmed to stretch the sensing mesh from 0 to 5,000 με at a constant rate of 15,000 με/min. An initial baseline measurement was recorded prior to applying any load. At every 1,000 με increments, the load frame was manually paused, and EIT measurements were collected. EIT DAQ system described in Chapter 2 was used for EIT interrogation and voltage measurements. Current injection and boundary voltage measurements followed the adjacent electrode model, as was done in previous studies [197]. Boundary voltage measurements were then used as inputs to the EIT inverse problem for reconstructing the conductivity distribution of the sensing mesh loaded to different strain states. The change in conductivity distributions of different strain states with respect to the baseline was then computed.

Second, a sensing mesh with diagonal struts was fabricated (Figure 4.4), which followed the same fabrication process as discussed earlier. A total of 12 boundary electrodes were used. Instead of directly stretching the sensing mesh, it was affixed, using quick-curing superglue, at the center of a 125 × 25 mm^2 PET strip (Figure 4.4). After the glue fully dried, the entire specimen was mounted in the Test Resource 150R load frame. A baseline EIT measurement was recorded when the specimen was unstrained (0 με). In contrast to the previous experiment, the test specimen was subjected to uniaxial tensile strain from 0 to 8,000 με in 2,000 με increments to allow for EIT testing. Here, loading rate was kept the same as previous tests (*i.e.*, 15,000 με/min).

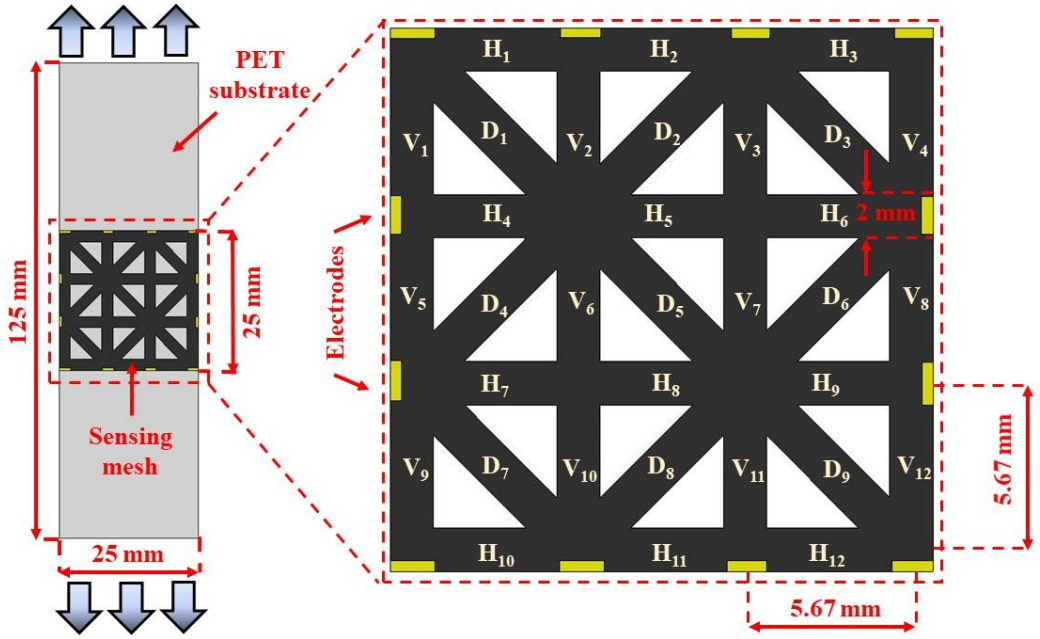

Figure 4.4 A sensing mesh with diagonal struts was fabricated and affixed onto a PET strip. The dimensions of the PET strip and the sensing mesh are highlighted. The specimen was subjected uniaxial loading. H, V, and D indicate the horizontal, vertical, and diagonal struts, respectively.

Third, and following validation of the spatial strain sensing capabilities of the sensing mesh, a larger, 7 × 5 grid-like sensing mesh (Figure 4.5a) was fabricated and affixed onto a PVC plate (610-mm-long, 76.2-mm-wide, and 9.25-mm-thick) using quick-curing epoxy. A total of 16 EIT electrodes were attached to the boundaries of the sensing mesh. Because epoxy would infiltrate and affect the electrical and electromechanical properties of polymer-based nanocomposites, a Krylon acrylic coating was sprayed onto the sensing mesh to serve as a protective layer before it was attached to the PVC plate. For reference, a metal-foil strain gage (Tokyo Sokki Kenkyuio Co. Ltd. and gage factor = 2.13 ± 1%) was also mounted onto the PVC plate for measuring the induced strains in the longitudinal direction, as is illustrated in Figure 4.5b.

After the epoxy was fully cured for ~ 6 h, the PVC plate, instrumented with the sensing mesh and strain gage, was mounted in an MTS-793 load frame. Like the previous experiments, a baseline EIT dataset was recorded prior to applying any load to the PVC plate. The load frame was

programmed to apply monotonic uniaxial tensile loading to 10,000 με at a fixed strain rate of 1,000 με/min. The experimental setup is shown in Figure 4.5c. The load frame was manually paused every 2,000 με, and the EIT DAQ interrogated the sensing mesh as described in the previous section. In all these three sets of experiments, applied strains were calculated using the recorded grip displacements of the load frame in the vertical direction.

4.3.4 Damage Detection Validation

To further demonstrate its applicability for SHM, the sensing mesh was employed to detect damage and propagating cracks in an RC building subjected to shaking-table-induced earthquake excitations (Figure 4.6a). The plan and isometric views of the seven-story, two-bay, test structure are schematically shown in Figures 4.6b and 4.6c, respectively. It can be seen from Figure 4.6c that the height of the first floor (3.73 m) was greater than that of the other floors (1.5 m), which created a soft-story effect. In addition, the frame was designed such that the stiffnesses of columns C1, C2, and C3 were higher (due to their larger cross-sectional area) as compared to columns C4, C5, and C6 (Figure 4.6b). The effect of this design means that the majority of damage would be concentrated in the first-floor.

Thus, a 5 × 5 sensing mesh was affixed near the base of column C4 (Figure 4.6c) following the same mounting procedure discussed in Section 4.3.3. For continuous and real-time data acquisition, a National Instruments (NI) PXIe-4302 system was customized with a PXIe-4139 source measuring unit (SMU), PXIe-4303 DAQ, and PXIe-2535 field-effect transistor (FET)

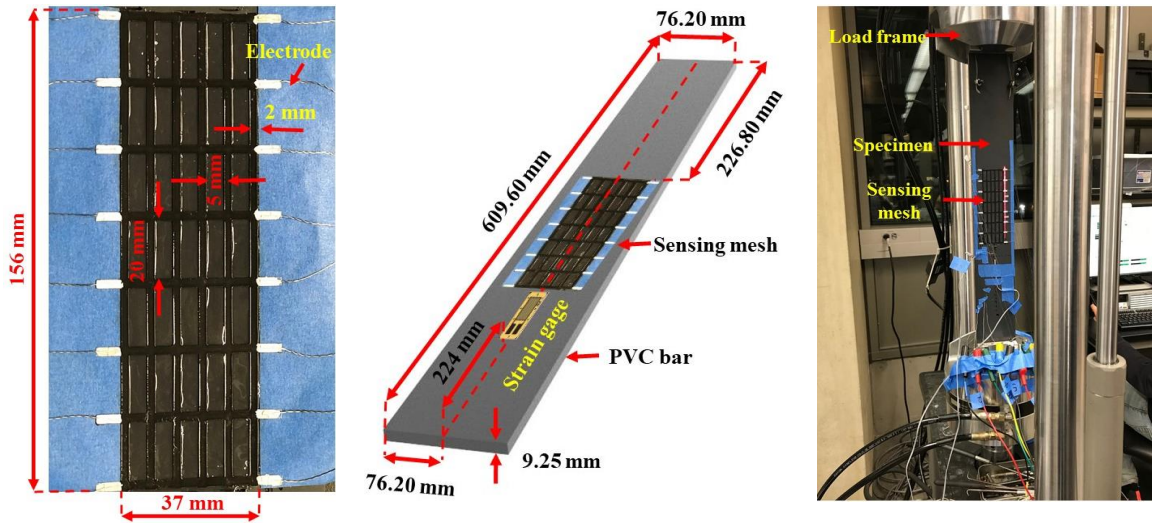

(a) (b) (c)

Figure 4.5 (a) A 7 × 5 sensing mesh was prepared and (b) epoxy-mounted onto a rectangular PVC plate. The PVC plate was also instrumented with a strain gage for measuring longitudinal strains in the PVC. (c) The entire test specimen was mounted in a load frame and subjected to uniaxial tensile testing. The sensing mesh was interrogated at different strain states for EIT image reconstruction, while the strain gage simultaneously recorded the magnitude of induced strains in the plate.

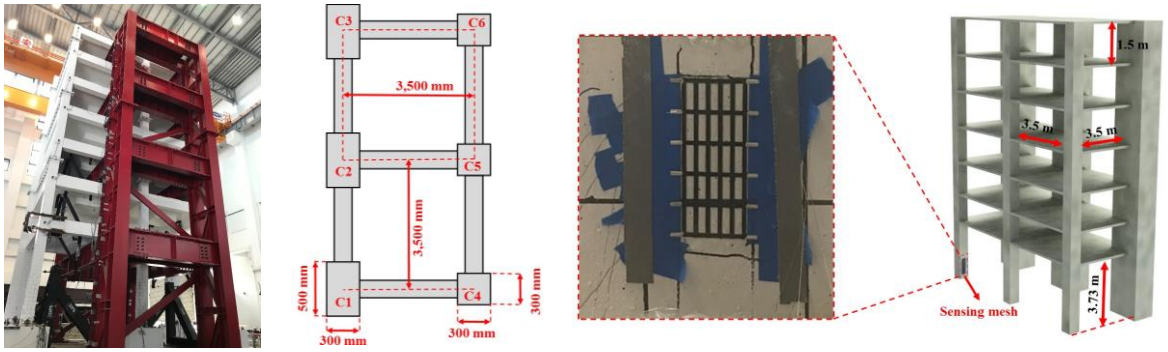

(a) (b) (c)

Figure 4.6 (a) A seven-story RC building was subjected to shaking table tests. (b) The plan view of the building and the dimensions of the structural components are shown. (c) The schematic of the entire test building is shown, where a 5 × 5 sensing mesh was affixed near the base of the left-most weak column (*i.e.*, C4).

switch. The SMU was used to supply the excitation current for EIT interrogation. As described in the previous section, two adjacent electrodes were selected at a time, one for current injection and the other as ground, all controlled by a customized *LabVIEW* program. DC voltage measurements were continuously recorded at all analog input (AI) channels of the PXIe-4303 DAQ. The effective sampling rate of the DAQ was such that EIT sensing mesh results could be acquired at 25 frames/s (or images/s).

The shaking table tests were conducted using a large-scale, high-performance shake table at the National Center for Research on Earthquake Engineering (NCREE) in Tainan, Taiwan. The entire structure was subjected to a sequence of dynamic loadings ranging from white-noise tests to different scaled earthquake ground motions of increasing intensity. The RC structure was tested until the weaker columns (*i.e.*, C5, C6, and C7) underwent catastrophic failure (*i.e.*, loss of load-carrying capacity).

4.4 Results and Discussion

4.4.1 Strain Sensing Characterization

The strain sensing properties of the GNS-PVA thin films was characterized by conducting tensile cyclic tests, as was discussed in Section 4.3.2. The thin films' resistance was measured throughout testing, as was the applied strains. A peak tensile strain of 5,000 με was applied to the specimens so that the films remained undamaged and linear-elastic.

Figure 4.7a shows a representative GNS-PVA thin film's resistance response overlaid with the applied strain pattern. This result confirmed that the resistance of the thin film changed in tandem with applied strains. In addition, its electromechanical response was stable and repeatable. Furthermore, the same set of data was used to plot the normalized change in resistance versus strain, as shown in Figure 4.7b. Although Figure 4.7b shows that the electromechanical performance of the GNS-PVA thin film was slightly nonlinear, a linear least-squares regression line was fitted to estimate their gage factor (G) or strain sensitivity (*i.e.*, the slope of the fitted line).

$$G = \frac{\Delta R / R_0}{\Delta \varepsilon} \tag{4.5}$$

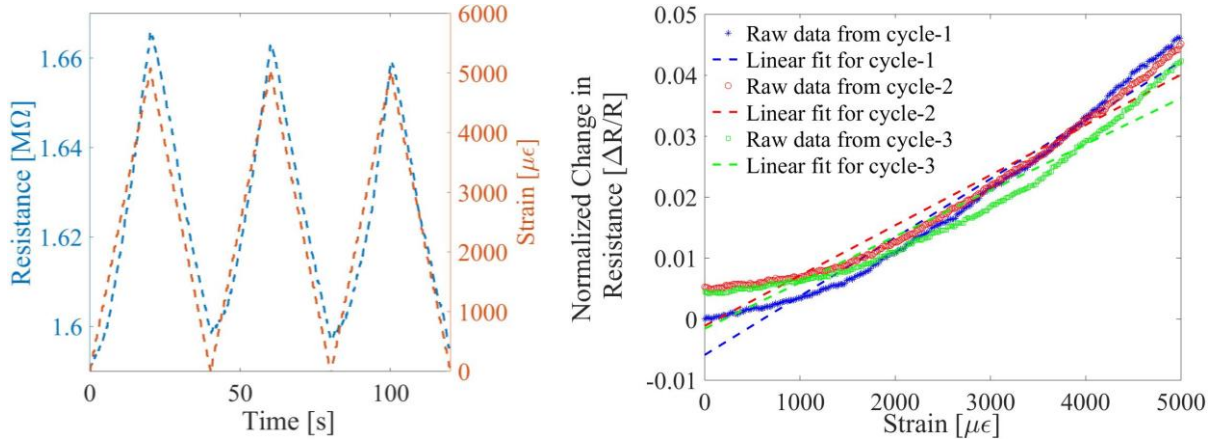

(a) (b)

Figure 4.7 (a) The electrical resistance time history of a strained GNS-PVA thin film specimen is overlaid with the applied strain pattern. (b) Its normalized change in resistance over different loading cycles were computed and plotted as a function of applied strains.

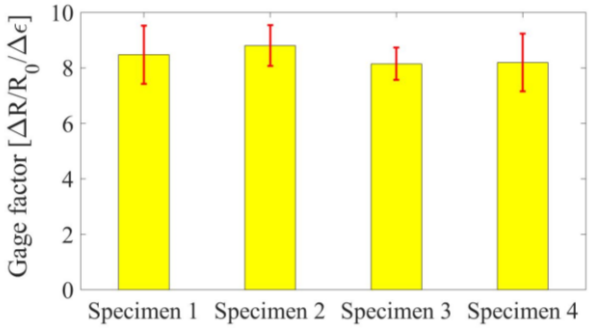

Figure 4.8 The average gage factors for four different thin film specimens tested are shown. The error bars indicate the standard deviations of the calculated gage factors over different loading cycles.

where R_0 is the initial or unstrained resistance of the thin film, and ΔR is the change in resistance with respect to R_0 when strain ($\Delta\varepsilon$) is applied.

Figure 4.8 plots the average G of each of the four specimens tested. The error bars in Figure 4.8 indicate the standard deviations of G over different loading cycles. One can observe from the results that all of the four specimens exhibited comparable strain sensing properties, and the overall average gage factor was 8.20. Lee *et al*. [102] explained that high G of nanocomposite-based thin film strain sensors could be achieved if the concentration of nanomaterials were near or at the percolation threshold. As a result, minute tensile strains disrupt the electrically conductive

pathways formed by the nanomaterials, thereby increasing strain sensitivity. As compared to the spray-fabricated MWCNT-based thin films with a G of ~ 0.77 ± 0.02, which was reported by Mortensen *et al*. [172], the GNS-PVA thin films' were characterized by ~ 10 times higher G.

4.4.2 Sensing Mesh Verification

To demonstrate distributed strain field monitoring, GNS-PVA thin films were deposited onto PET grids to form sensing mesh specimens (Figure 4.3a). EIT was used to determine the change in electrical conductivity of the sensing mesh corresponding to different strain states, and the results are shown in Figure 4.9. It can be seen from Figure 4.9 that the conductivity of the vertical thin film grid elements in the sensing mesh decreased (or resistivity increased) with greater applied tensile strains. These results were expected based on findings from Section 4.4.1. Furthermore, Figure 4.9 also shows that the horizontal struts experienced an increase in conductivity, which is because of the induced compression due to stress concentrations at the junctions of the horizontal and vertical struts.

To investigate the accuracy of the experimental EIT spatial strain sensing results, a linear-elastic FE model of the sensing mesh was created in ABAQUS. PET was defined as having a Young's modulus and Poisson's ratio of 2 GPa and 0.44, respectively. The GNS-PVA film was not explicitly modeled, since its thickness and stiffness were negligible relative to PET. The entire model was discretized into 935 bi-linear quadrilateral elements as shown in Figure 4.10. With the PET sensing mesh being only ~ 0.2-mm-thick and negligible compared to its other two dimensions (92 mm × 23 mm), plane stress was assumed. A pinned boundary condition was assigned for the bottom edge of the FE model, and tensile strain was applied at the top edge. The FE-estimated strain distributions (*i.e.*, ε_{11} and ε_{22}) corresponding to different applied global strain states are

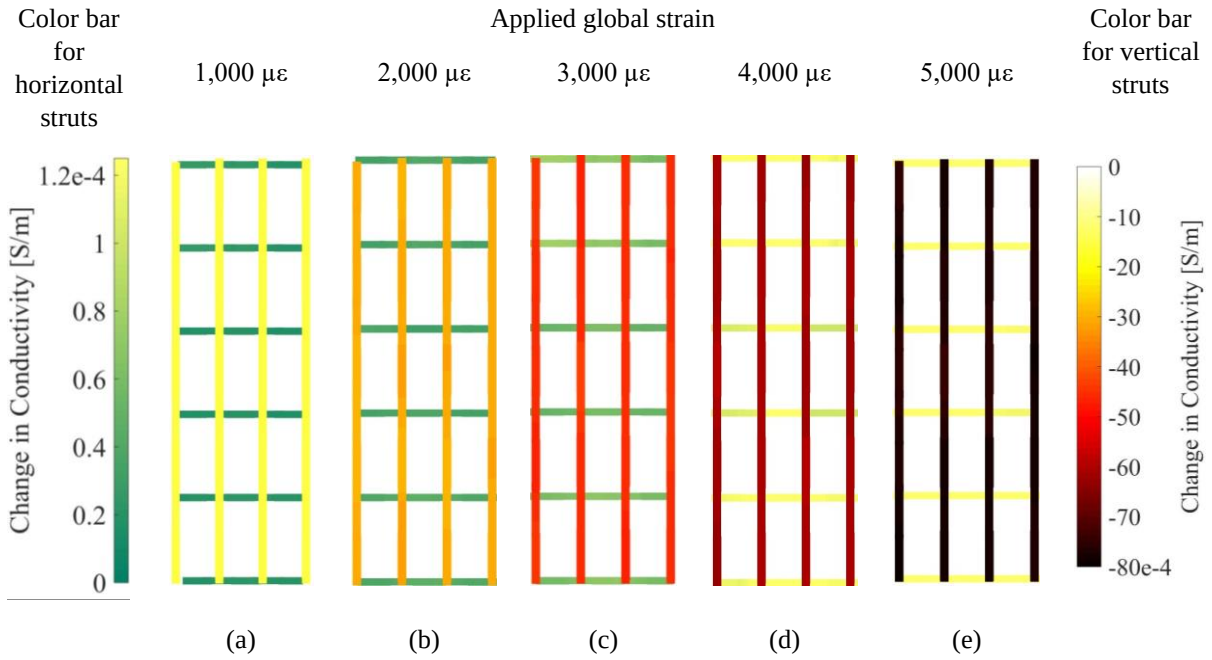

Figure 4.9 The sensing mesh was subjected to tensile strains, and the corresponding changes in electrical conductivity with respect to the undeformed state are shown in (a) to (e). Two separate color bars are used for visualizing conductivity changes for the horizontal (left) and vertical (right) struts, especially due to their different magnitudes of strains.

shown in Figure 4.10. Similar to the experimental results (Figure 4.9), ε_{22} (or strain in the vertical direction) increased with increasingly applied loads, while ε_{11} (or strain in the horizontal direction) was negative due to compression caused by Poisson's effect.

To compare the experimental EIT and FE simulation results, vertical (*i.e.*, $V_1 \ldots V_{12}$) and horizontal elements (*i.e.*, $H_1 \ldots H_{12}$) in the sensing mesh were identified according to Figure 4.11. First, the EIT results were converted from conductivity distributions to strain maps. Here, the strains induced at the different elements in the struts were estimated by averaging the conductivity changes in all the finite elements of that particular strut and then normalizing with respect to the sensing mesh's initial conductivity (*i.e.*, unstrained conductivity) and *G*. In doing so, the EIT experimental results were directly comparable to the FE simulation strain maps. Second, the EIT-based strains corresponding to different struts when subjected to different global applied strains

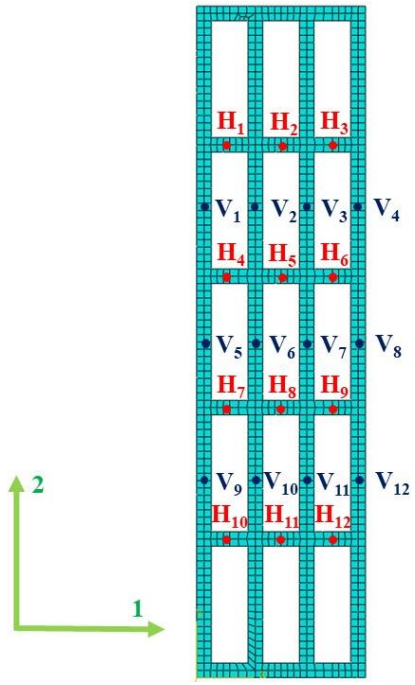

Figure 4.10 Discretized FE model of the sensing mesh is shown. $H_1 \ldots H_{12}$ and $V_1 \ldots V_{12}$ indicate midpoints of the corresponding horizontal and vertical struts, respectively.

were compared against the FE model outputs (Figure 4.12). Figure 4.12 shows good agreement between the experimental and simulation results, where only an average of ~ 3% mismatch exists.

Three possible reasons could have contributed to these errors. First, misalignment and minor slippage of the sensing mesh from the load frame's grips during testing could have reduced the actual magnitude of applied strains. Second, the sensing meshes may have some slight inhomogeneities and nonuniform thickness due to fabrication error. Third, although it was assumed that the strains in the vertical members are uniform and equal to the applied global strains, there may be stress concentrations close to the grips. The nonuniform strain distribution can be explained by Saint Venant's principle. In addition, the EIT results could have been affected by regularization incorporated as part of the inverse problem. Nevertheless, the 3% error was deemed acceptable.

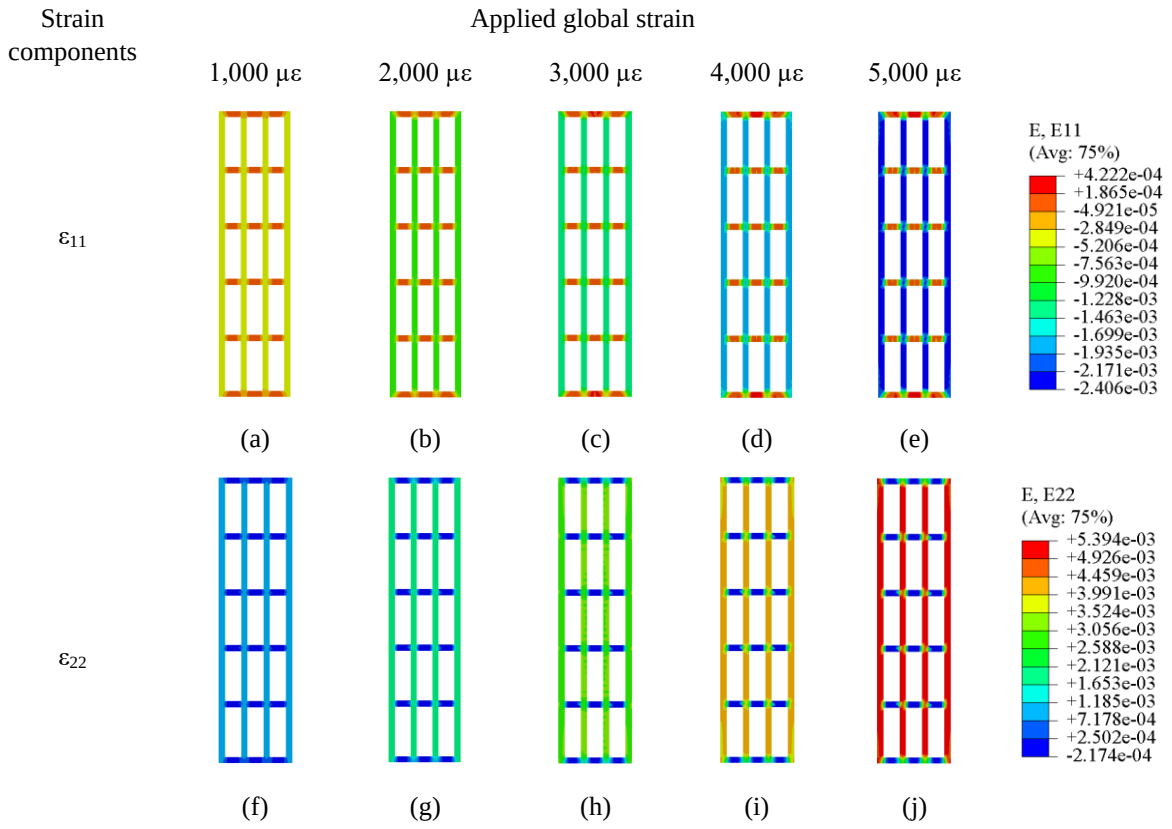

Figure 4.11 (a) to (e) and (f) to (j) show the distributions of ε_{11} and ε_{22}, respectively, over the entire sensing mesh when subjected to different tensile strains ranging from 0 to 5,000 με.

Besides testing and loading the sensing mesh directly, a sensing mesh with diagonal struts was affixed onto a PET strip as shown in Figure 4.4. Figure 4.13 shows the reconstructed EIT conductivity maps of the sensing mesh corresponding to different applied global strain states. It can be observed that the conductivity of the vertical (*i.e.*, V_1, V_2,…,V_{12}) and diagonal struts (*i.e.*, D_1, D_2,…, D_9) decreased, while an opposite trend was observed for the horizontal members (i.e., H_1, H_2, H_3,.., H_{12}). These results were expected, since the vertical and diagonal struts were subjected to tension, while the horizontal members experienced compression due to Poisson's effect. As a result, the magnitudes of induced strains in the horizontal members were ~ 42% of the tensile strains experienced by the vertical struts (Figure 4.14).

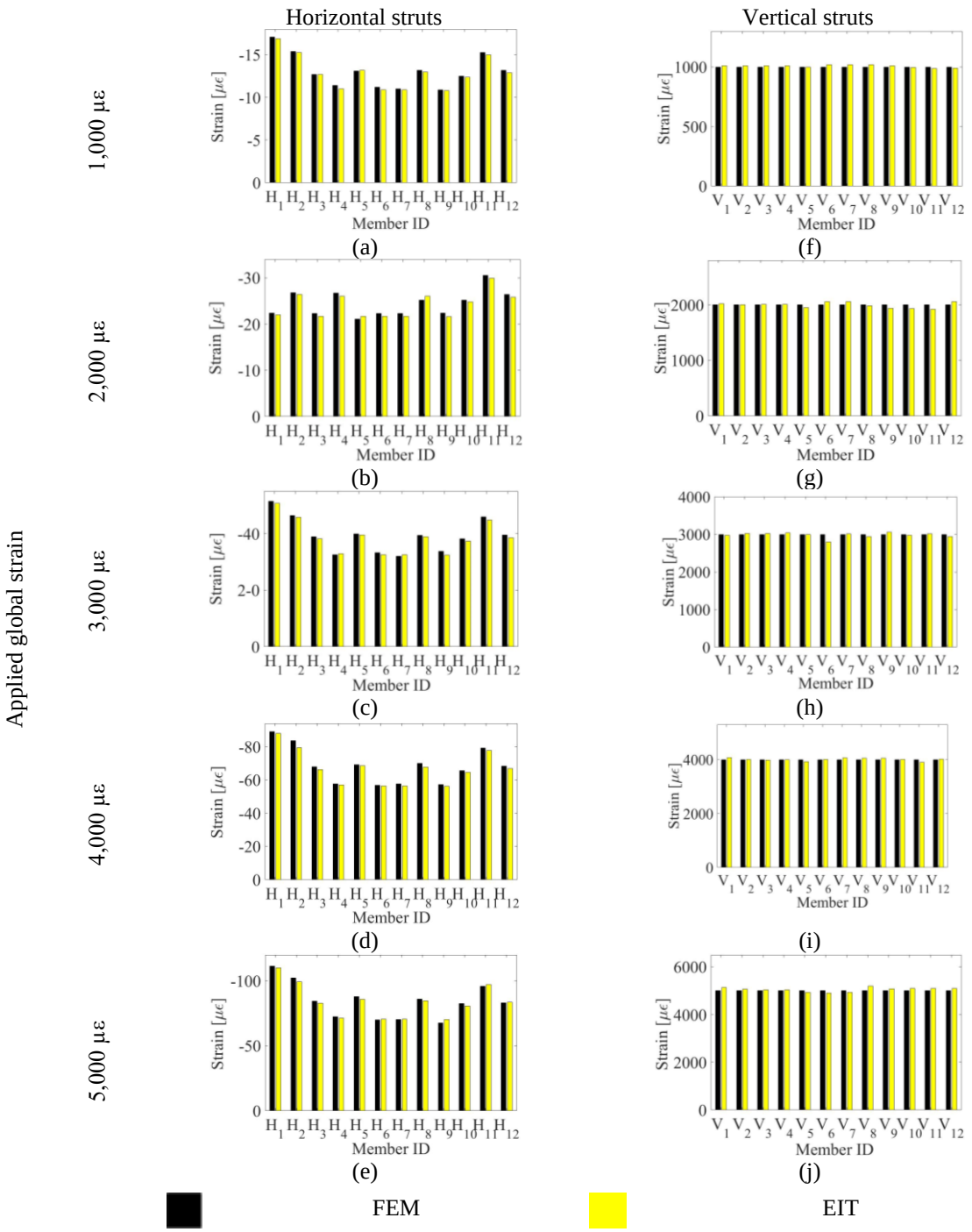

Figure 4.12 (a) to (e) The horizontal and (f) to (j) vertical struts' FE- and EIT-based strain results are compared according to the different applied strain states.

Again, a similar plane stress FE model of the specimen was created in ABAQUS and discretized using 8,852 bi-linear quadrilateral elements. The same boundary condition was implemented (*i.e.*, pinned boundary condition) at one end of the PET strip. However, $\Delta\varepsilon$ was

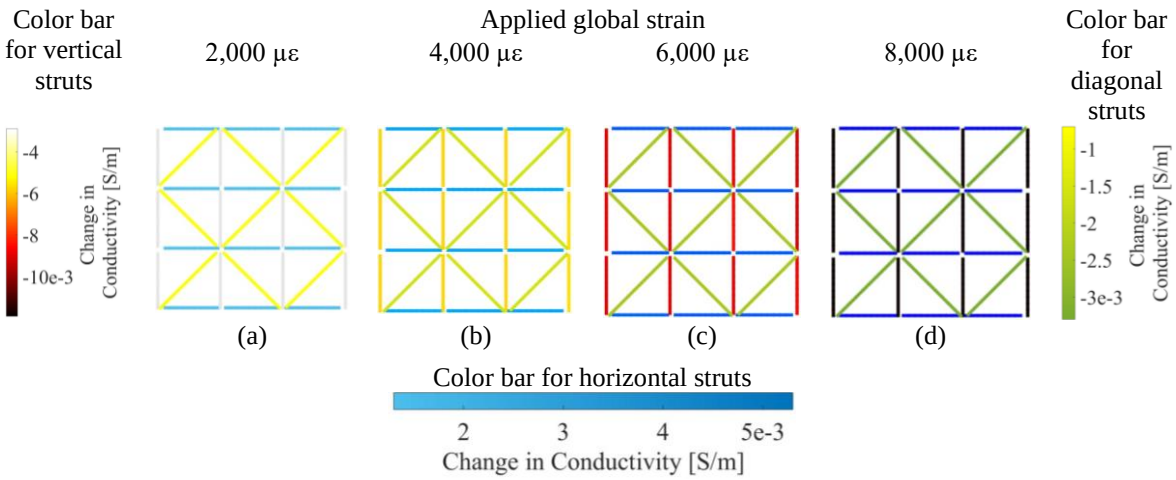

Figure 4.13 The estimated average conductivity changes of each strut with respect to their undeformed states are shown when the specimen was stretched to (a) 2,000 με, (b) 4,000 με, (c) 6,000 με, and (d) 8,000 με.

evaluated by estimating the change in their axial length (Δl) from the FE results and then dividing it by its original length (l_0), as is shown in equation 4.6:

$$\Delta\varepsilon = \frac{\Delta l}{l_0} \tag{4.6}$$

The EIT-estimated conductivity changes of all the finite elements in each strut were averaged and used to calculate the average induced strain in that strut using equation 4.6. The EIT-estimated strain of each strut was compared with the corresponding FE results and is shown in Figure 4.14. Although good agreement between experimental and numerical results was found, a ~ 5% difference was observed. While Figure 4.9 only demonstrated sensing strains in the horizontal and vertical directions, the results shown in Figure 4.13 confirm the ability of the sensing mesh to measure strains along different directions.

4.4.3 Scaling Up the Sensing Mesh

A larger sensing mesh was also affixed onto PVC plates and loaded, as was described in Section 4.3.3. Figure 4.15 plots a set of EIT sensing mesh conductivity maps when the PVC plate

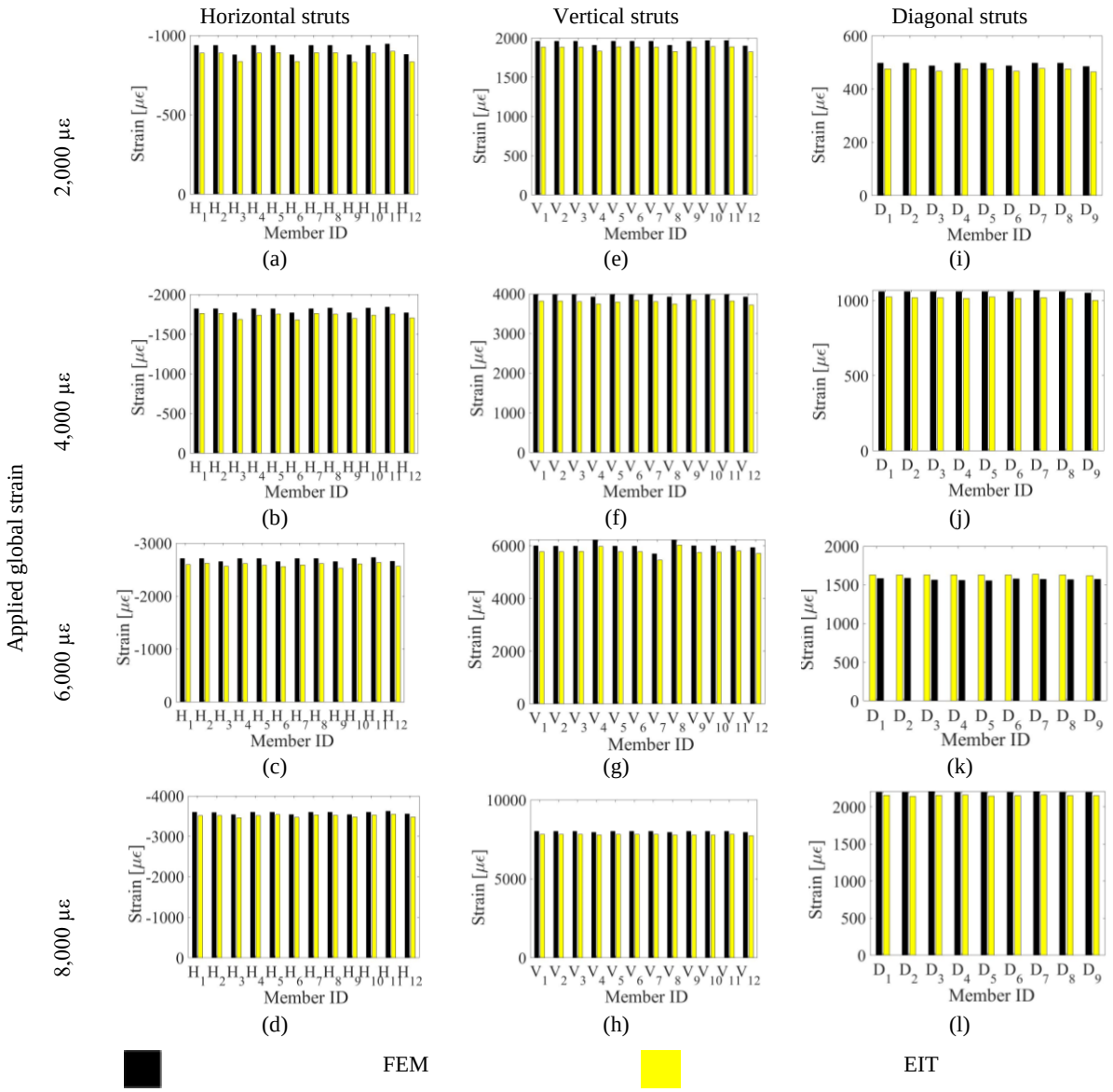

Figure 4.14 (a) to (d), (e) to (h), and (i) to (l) show the EIT- and FE-estimated strains in horizontal, vertical, and diagonal struts respectively when the specimen was subjected to different tensile strains.

was strained to 10,000 με. As expected, Figure 4.15 clearly shows that the conductivity decreased in the vertical struts, while conductivity increased in all the horizontal struts. The magnitude of conductivity changes also increased as greater global tensile loading was applied to the PVC plate.

To further quantify the accuracy of these EIT sensing mesh results, they were compared to strain gage measurements of longitudinal strains in the PVC plate. Assuming strain was uniformly

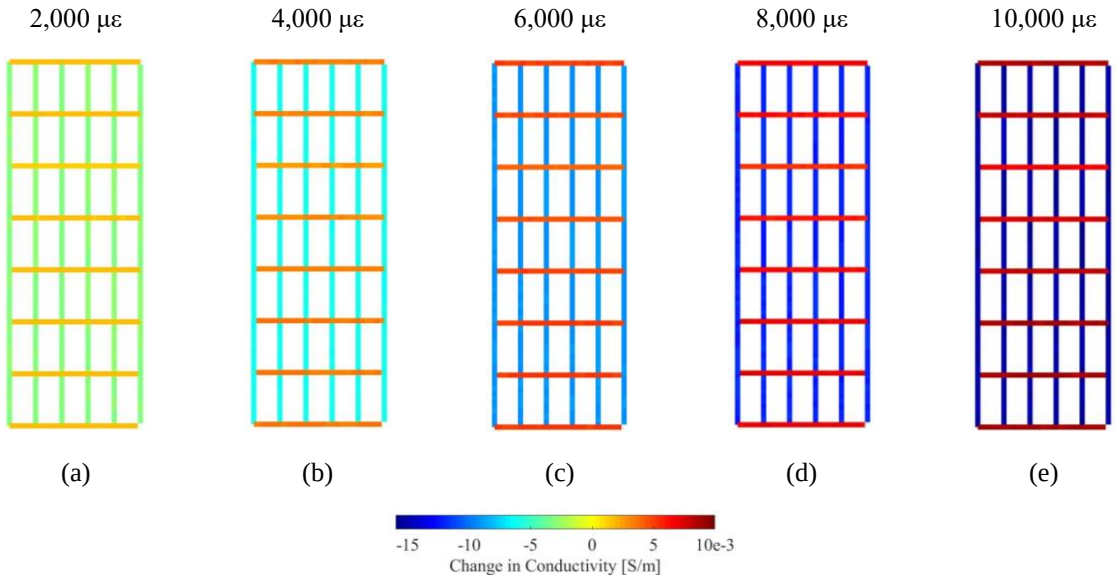

Figure 4.15 Tensile tests were performed on a PVC plate instrumented with a sensing mesh. EIT conductivity maps were obtained for the different strain states applied, namely, at (a) 2,000 με, (b) 4,000 με, (c) 6,000 με, (d) 8,000 με, and (e) 10,000 με. The changes in conductivity distributions with respect to the unstrained baseline are shown.

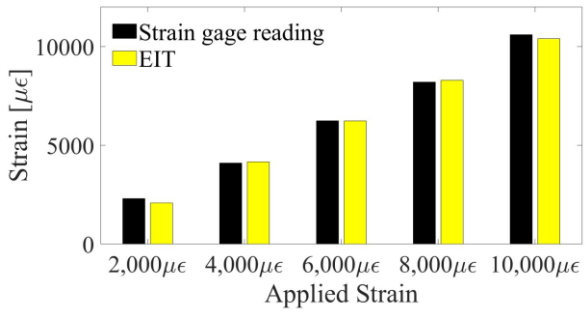

Figure 4.16 The EIT-based strain measurements are compared with strain gage readings of the PVC plate subjected to uniaxial tensile loading. Good agreement was observed

applied to the PVC plate, the resulting strains in all the vertical struts of the sensing mesh should be almost identical. Thus, the EIT strain measurements of the six vertical struts were directly compared with the strain gage readings in Figure 4.16, where the results were found to be comparable with an average of ~ 4% error.

Some possible reasons for the errors observed could be due to imperfect strain transfer from the structural surfaces to the sensing meshes. In addition, the vertically applied tensile strains

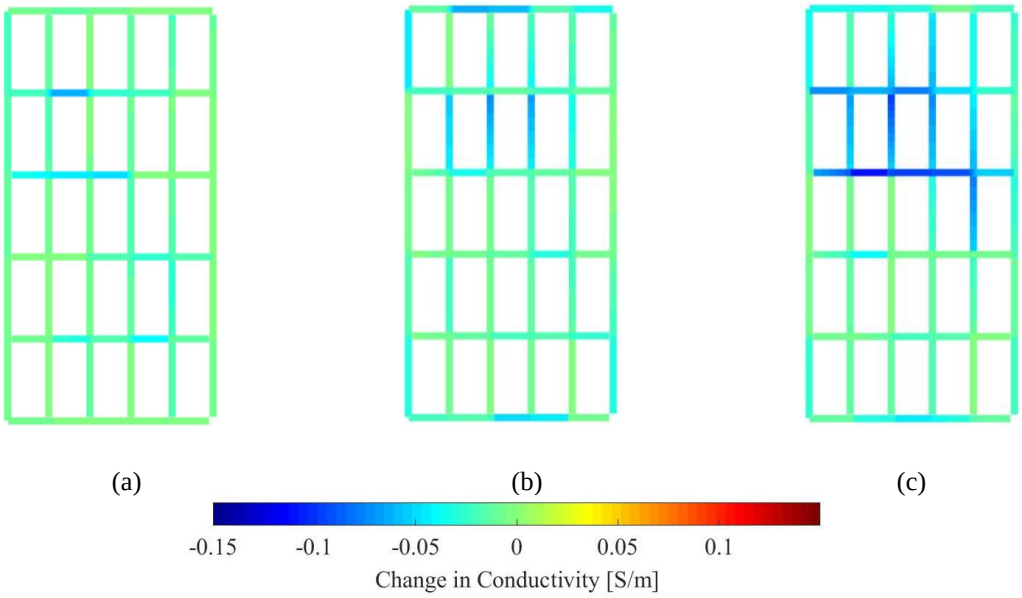

Figure 4.17 The changes in conductivity distributions of the sensing mesh with respect to the baseline (*i.e.*, before the building was subjected to shaking table earthquake excitations that generated a crack underneath the skin) were determined. EIT results (a) before, (b) during, and (c) after the earthquake ground motion excitation test are shown.

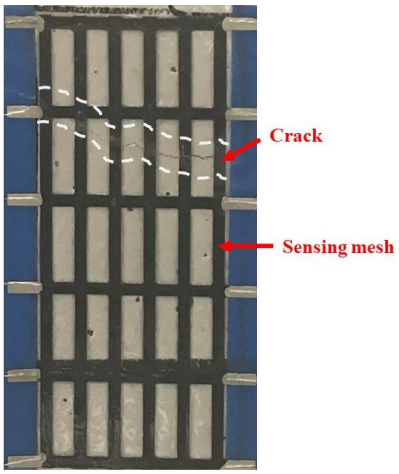

Figure 4.18 A transverse crack developed underneath the sensing mesh (near its second row) after the test structure was subjected to strong ground shaking.

might not be uniformly distributed over the entire substrate, which again can be explained by Saint Venant's principle. Nevertheless, the results shown in Figures 4.12 and 4.14 clearly show that the

sensing mesh, when coupled with EIT, could effectively measure both the magnitude and directions of induced strains.

So far, the tests performed and the results obtained corresponded to situations when the structure was loaded and strained, and damage (*e.g.*, crack) was not present. If damage, such as a crack, occurs near the vicinity of the sensing mesh (but not directly underneath it), the local strain distribution underneath the sensing mesh will change due to the presence of the crack. In this scenario, the sensing meshes could capture the corresponding strain distribution of the structure but not necessarily identify the properties of the nearby crack. The next section examines the scenario when a crack in the structure propagates directly beneath the sensing mesh.

4.4.4 Damage Detection Validation

This study also investigated whether the sensing meshes could detect spatially distributed structural damage (*e.g.*, cracking) in a column of a seven-story RC building subjected to shaking table tests (Section 4.3.4). EIT measurements were recorded continuously by the customized NI DAQ, while the building was subjected to near-fault earthquake excitations that caused severe damage in the structure. Figure 4.17 plots three representative EIT sensing mesh results corresponding to before, during, and after shaking. First, it should be clarified that multiple shaking events were conducted during this test. However, the test results presented here only focused on one shaking event, specifically, when damage was induced at the location of the sensing mesh. Thus, previous shaking table events induced inelastic behavior in the structure and resulted in residual strains (and minor damage) in the column. The results shown in Figure 4.17a shows that the sensing mesh strain map was nonuniform because of this.

Second, Figure 4.17b captured the sensing mesh strain distribution of the column when the structure (and column) was subjected to strong ground motions. It can be observed that localized changes in conductivity were observed in the second row of the sensing mesh. Finally, after shaking, Figure 4.17c shows that the same vertical and horizontal struts exhibited a significant change in conductivity corresponding to the location of the crack that developed (Figure 4.18). Thus, it was possible that Figure 4.17b captured damage onset immediately prior to the crack opening to give the final results shown in Figure 4.17c.

Although crack propagation was successfully captured by the sensing mesh, conductivity changes in the other parts of the sensing mesh were observed in the reconstructed images. It was possible that, during shaking, the electrical cables connecting the sensing mesh were subjected to rigorous vibrations, thereby inducing more noise in the EIT boundary voltage measurements. Furthermore, unexpected changes in conductivity could have resulted from localized deformations of the column during shaking. Despite these, this preliminary large-scale test demonstrated the feasibility of using sensing meshes for crack damage detection and localization. Future research will focus on using sensing meshes for capturing dynamic structural response.

4.5 Summary and Conclusions

In this study, nanocomposite sensing meshes were designed for distributed strain field monitoring. Previous studies showed that piezoresistive thin films, when coupled with EIT, could monitor distributed strains and damage. However, the low strain sensitivity of the thin film and the inability of EIT to resolve the directionality of strain components were two barriers for field deployment. To overcome these challenges, highly strain-sensitive GNS-PVA thin films were designed and fabricated by spray coating. The characterization study revealed that the gage factor

of the thin film strain sensor was more than 10 times higher than previous carbon nanotube-based films. Then, sensing meshes were fabricated by spray coating GNS-PVA thin films onto grid-like PET cutouts. An updated EIT algorithm was also implemented to more efficiently capture changes in sensing mesh conductivities.

The test results showed that EIT was able to identify if any of the struts aligned at different directions in the sensing mesh was subjected to tension or compression (*i.e.*, in their respective orientations). These experimental EIT results were compared with FE analysis for verification, and good agreement was observed. A larger-scale sensing mesh was also employed for monitoring strain distributions in a PVC plate subjected to uniaxial tensile loading. The EIT-derived strain measurements that were compared with strain gage readings showed good agreement. Last, for validation, the sensing mesh was utilized for damage detection in a column of a seven-story RC building subjected to earthquake excitations. The reconstructed spatial conductivity maps showed localized decreases in conductivity corresponding to locations where a crack propagated. Overall, the results successfully validated sensing meshes for strain field monitoring and spatial damage detection.

Although the GNS-PVA thin film had high strain sensitivity and could be scaled up through the use of spray fabrication, the high electrical resistance of the polymer matrix (*i.e.*, PVA) can pose a challenge for large-scale applications. Since EIT requires propagating electrical current through the entire sensing mesh, the electrical resistance of the film should be managed accordingly. Future work will consider alternative polymer matrices or additional additives for tuning the overall resistivity (or conductivity) of the films. In addition, the thin film's sensitivity can also be further improved to enhance sensing resolution.

Despite the successful demonstration of EIT-based spatial strain and damage mapping, EIT is a contact-based method. A series of electrodes need to be installed at the boundary of the object for EIT interrogation and voltage measurements, which can potentially limit its applications. For example, the installation of electrodes at some inaccessible locations of the structures could be challenging. Besides such limitations of the proposed method during structural applications, EIT may not be suitable for OIP monitoring. The installation of electrodes on the residual limb of the amputees can cause discomfort. On the other hand, contact impedance between the electrodes and the interrogated specimen causes a local voltage drop, hence resulting in inaccurate voltage measurements. Although local voltage drop due to contact impedance is taken into account through CEM, experimental measurement of the contact impedance could be challenging. Additionally, electrodes can easily get detached from the nanocomposite thin film's surface. The broken electrodes cause an incomplete set of voltage measurements that could result in erroneous conductivity maps. In the next chapters, ECT will be explored as a potential solution for these abovementioned limitations.

This chapter is a reprint of the materials as appeared in Graphene Sensing Meshes for Densely Distributed Strain Field Monitoring, S. Gupta, G. Vella, I-N Yu, C-H Loh, W-H Chiang, and K. J. Loh, 2019.

CHAPTER 5 OSSEOINTEGRATED PROSTHESES MONITORING

5.1 Introduction

The main focus of this chapter is to develop and implement a noncontact, noninvasive, radiation-free, imaging tool that can be used by physicians (or even patients) to accurately detect prostheses-related issues (*e.g.*, subcutaneous infection occurring at the tissue-prosthesis interface, excessive strains in OIPs, and prosthesis loosening, as well as loosening-induced bone fractures). ECT described Chapter 2 is used in conjunction with embedded, passive, nanocomposite thin film sensors that exhibit changes in its dielectric property due to external stimuli (*e.g.*, pH and strain). It is envisioned that the results from the proposed method can reduce the amount of unnecessary, complicated, expensive, and painful medical tests while facilitating the diagnosis and use of appropriate infection treatment strategies.

As mentioned in Chapter 1, OIP is gaining popularity among the amputees as a viable alternative to conventional socket prosthesis. Studies have shown that patients with OIP can lead to a better quality of life [3]. Despite the benefits, amputees with OIP can suffer from various issues at the tissue-prosthesis interface, as discussed in Chapter 1 (Section 1.1.2). If such issues are undetected at an early stage, they can lead to total prosthesis failure. Hence to ensure the safety of the amputees, OIP monitoring is necessary. Various techniques for OIP monitoring, and their limitations are described in the following sections.

5.1.1 Infection Monitoring

Daily skin inspections can help detect anomalies that suggest infection. Superficial infections can be treated with appropriate oral antibiotics to resolve issues within a few weeks

[198]. Unfortunately, infection can initiate subcutaneously and remain undetected for longer periods to cause severe complications. In these circumstances, a more detailed clinical assessment of the infected region is needed. C-reactive protein is a high sensitivity, high specificity, preoperative blood test for detecting infection [48]. However, false positives often occur with patients previously treated with antimicrobial agents or subjected to less virulent bacterial attack (*e.g*., *P. acnes*). Histopathological examination of periprosthetic tissues [49] and intraoperative microbiological testing [50] are two other methods used when microbiological tests are not performed preoperatively, but specimens need to be collected at the time of surgery with antimicrobial therapy suspended at least two weeks prior to the patient's surgery. Uncertainties associated with diagnosis of infection can be addressed by synovial-fluid test, but its sensitivity diminishes drastically if patients have had earlier microbial treatment [51].

Aside from the aforementioned methods, imaging can also be used for detecting infection. Plain radiography, computed tomography (CT), and magnetic resonance imaging (MRI) are three commonly adopted techniques. However, plain radiography suffers from low sensitivity with limited specificity [199]. Diagnosis of infection by CT or MRI is often hindered by artifacts produced by the prosthesis itself [26]. PET, or 18F-fluorodeoxyglucose positron-emission tomography, is an emerging imaging modality with higher sensitivity (~ 82%) and specificity (~ 87%) [200]. Scintigraphy with antigranulocyte monoclonal antibodies coupled with hybrid imaging is gaining popularity, but its merit is still under investigation [26].

Another potential sensing modality that one might be able to use for detecting infection is by monitoring changes in the biochemical environment in the human body. It has been found that infection caused by different microorganisms at the human-prosthesis interface influences the pH of infected cells. Sebaceous glands in the human body support the growth of *P. acnes*, which can

hydrolyze the triglycerides present in sebum to release fatty acids and decrease the pH of infected cells to as low as ~ 5 [201]. On the other hand, infection associated with *S. aureus* is mainly due to their adhesion on the implanted prosthesis surface, which forms a biofilm and prohibits the penetration of antibiotics, resulting in chronic inflammation.

5.1.2 Strain Sensing

Currently, the mechanical loading applied during static LBE is generally monitored using a bathroom scale, which provides immediate visual feedback, but its application is limited as it can only measure the vertical component of applied load [31]. Assessment of the applied force on the implant during LBE can also be performed with the aid of the advanced inverse dynamic method used in a motion analysis system laboratory [202]. A force plate instrumented with external force measuring transducers is generally employed to directly measure the forces experienced by the implant during rehabilitation [203]. One of the main drawbacks of this method is that only the first few steps of walking can be accurately measured. This method can also result in an altered gait, thereby limiting the accuracy of the calculated load. On the other hand, it is difficult to simulate other daily activities in these laboratory environments [204].

To overcome these aforementioned limitations, attempts have been made to directly mount a load sensor onto the prosthesis. Frossard *et al*. [205] presented a kinetic portable system that relies on a commercial transducer to measure the actual load applied to the distal end of the implant. They successfully recorded the triaxial forces and moments applied to the implant. However, these transducers are point-sensors that require multiple transducers for estimating the load distribution over the entire prosthesis. Each transducer would also require lead wires connected to a separate sensing channel, and this requirement can make it difficult for practical

implementations because of the number of tethered connections needed. Thus, a wireless modem was investigated for directly measuring and transferring data to a centralized data repository [206]. Such a wireless measuring system adds fidelity to record reliable and accurate measurements of load during daily activities. The iPecsTM load cell is a wireless unit that was used to measure three-dimensional (3D) forces and moments in OIPs [207]. However, *in vivo* measurement of strains in OIPs remains extremely challenging, because most of the transducers need to be mounted on the external surface of the implant, where it is almost impossible to mount strain gages onto the prosthesis while it is embedded in the patient's body. Besides, as a rigid connection between the implant and transducers is one of the primary requirements for accurately measuring force or implant strains, this may cause patient discomfort.

5.1.3 Monitoring Prostheses Loosening and Bone Fracture

Besides regular clinical visits, different nuclear scanning techniques (*e.g.*, CT, positron emission tomography (PET), bone scintigraphy, single-photon emission computed tomography, and MRI) remain the most common, reliable, and accurate diagnostic tools for detecting prosthesis loosening [208, 209]. An advantage of MRI, CT, and PET is their ability to produce 3D images. Bone scintigraphy can also be used for the characterization of bone metabolism. However, many of these imaging techniques require radiation, which is harmful at high doses. In addition, the radiation used sometimes induces bone loss at the bone-OIP interface [210]. Artifacts due to the presence of metallic prosthesis are also a well-known problem in cross-sectional imaging (*e.g.*, in the case of MRI). Besides these aforementioned nuclear scanning tests, the ultrasonic imaging technique is regarded as one of the most widely used and low-cost non-nuclear scanning techniques for peri-prosthetic assessment. However, its accuracy depends on its operator. In some cases, it also fails to detect the exact location of abnormalities [208].

In this chapter, ECT has been explored in conjunction with nanocomposite thin film sensors as a noncontact imaging system to monitor OIPs. This chapter begins with a discussion of the experiments to realize noncontact OIP monitoring. Noncontact pH and strain sensing results are presented, followed by prosthesis loosening bone fracture monitoring. Various techniques to enhance the resolution and the accuracy of ECT images are proposed and discussed in detail.

5.2 Experimental Details

5.2.1 ECT Imaging for Biological Specimen

The first experiment was performed to validate ECT's ability to image real biological specimens. A lamb shank (Figure 5.1a) was used to ECT testing to verify that ECT could resolve features of tissue versus bone and to demonstrate its merit for future implementations in human beings. Furthermore, a 6.35-mm-diameter steel rod, as an OIP surrogate, was press-fitted into the bone of the lamb shank, as shown in Figure 5.1b. The lamb shank was then placed in the ECT electrode array for ECT scanning. The collected ECT measurements were used as the input of the inverse problem for electrical permittivity reconstruction.

5.2.2 Noncontact Infection Monitoring

As mentioned in Section 5.1.1, infection can alter the pH of tissue, a thin film pH sensor based on MWCNT and PANI was fabricated, where the film can exhibit permittivity changes due to different pH and then be imaged by ECT without making contact with the residual stump or prosthesis. First, the fabrication procedure of the MWCNT-PANI thin film pH sensor is discussed. Second, a parallel-plate capacitor-based test setup was devised for characterizing the sensitivity of its dielectric properties when the film was exposed to different pH buffer solutions. Finally, after

(a) (b)

Figure 5.1 (a) A lamb shank was used for ECT testing. (b) The lamb shank with an embedded prosthesis phantom was scanned by the ECT electrode array.

depositing the films onto a representative surrogate of an OIP, the specimen was exposed to different pH buffer solutions and subjected to ECT testing.

5.2.2.1 Nanocomposite pH Sensor Fabrication

In recent years, medical imaging is significantly influenced by advancements in the nanotechnology domain. Nanomaterials' unique structure, size, shape, and resemblance to various molecules have made them suitable for biomedical applications. Examples are CNTs, silicon dioxide, boron nitride, titanium dioxide, and organic nanotubes. In particular, CNTs have received significant attention, where Li *et al*. [211] showed that the growth of osteoblastic cells could be accelerated by CNTs, which could produce extracellular matrix during the formation of bone tissue. Hirata *et al*. [212] surface-coated MWCNTs onto 3D collagen scaffold for bone tissue engineering of primary osteoblasts of rats and observed more bone formation around the coated collagen sponge than uncoated ones. On the other hand, a wide variety of polymers, such as PANI, are used with CNTs to encode desirable properties in nanocomposites for biomedical engineering [213]. It was shown that PANI could be used to produce a wide range of nanostructures when coupled with CNTs, and their use in biomedical applications has been recently investigated.

Humpolicek *et al*. [214] studied the effects of PANI in the human body, and the conclusion was that it does not have any sensitization or skin irritation effects but could exhibit cytotoxicity. However, it was also reported that cytotoxicity could be significantly reduced by a deprotonation and re-protonation procedure, which proves that cytotoxicity was not caused by PANI itself but by the reaction by-products. PANI could also be used as a sensor, where its electrical properties were demonstrated to exhibit pH sensitivity in aqueous environments [215]. In addition, previous work by Vandenberg and Loh [216] showed that the LbL technique was suitable for fabricating CNT-PANI thin film pH sensors, and different dopants could be used to tune its pH sensitivity. In this work, an airbrushing technique [172] was adopted, since it is more time- and labor-efficient and can be easily scaled up for large-scale applications. Preparation of the ink solution for spraying involved two main steps. In the first step, 10 mg/mL solutions of polyaniline emeraldine base dissolved in N-N dimethyl formaldehyde (DMF) were prepared by stirring the mixture using a magnetic stirrer for 24 h. The resulting PANI-DMF solution was then vacuum-filtered using 0.45 μm membrane filters to eliminate undissolved particles. This was followed by a 10-fold dilution by adding appropriate amounts of deionized water, and its pH was adjusted to between 2.5 to 2.6 using 10 *vol*.% hydrochloric acid in deionized water.

For the second step, the final MWCNT-based ink described in Chapter 3 (Section 3.2.1) was prepared. It is also described here briefly for completeness. In short, MWCNTs were mixed with 2 *wt*.% PSS solution and dispersed by ultrasonication. Thereafter, the MWCNT-PSS solution was mixed with the diluted and pH-adjusted PANI-based solution in equal proportions. The binder, which was a Kynar Aquatec latex solution, was then added to the solution to obtain the sprayable ink. Spray-coating was performed manually using a Paasche airbrush as illustrated in Figure 5.2a. Previous works showed that these MWCNT-based inks could be deposited onto a variety of

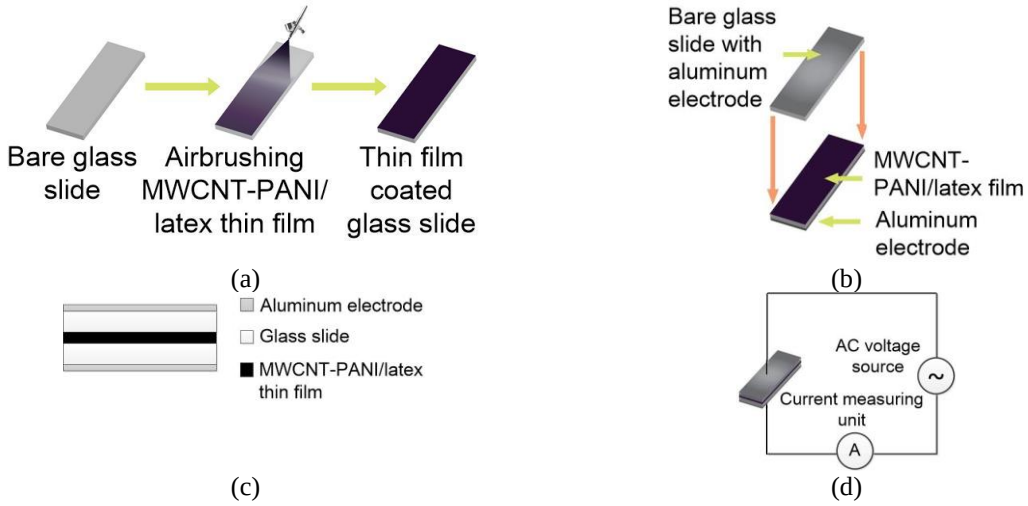

Figure 5.2 (a) MWCNT-PANI/latex thin film was deposited onto glass slides by airbrushing. (b) The thin film was sandwiched between two glass slides with aluminum electrodes to (c) form a parallel-plate capacitor. (d) Testing involved measuring the current flow through the circuit.

substrates such as glass, plastics, metals, textiles, and fiber-reinforced polymer composites, among others [105, 137, 189].

5.2.2.2 pH Sensing Characterization

A simple parallel-plate capacitor arrangement was employed for characterizing how the dielectric properties of the MWCNT-PANI/latex thin films varied when exposed to different pH buffer solutions. First, Figure 5.2a shows that thin film pH sensors were airbrushed onto one side of microscope glass slides. A conductive aluminum tape was affixed onto the other side of the film-coated slide. Another glass slide, with aluminum tape affixed onto one side of it, was also prepared. The two slides were then sandwiched together with the MWCNT-PANI/latex thin film in between the glass and the aluminum tape electrodes on the outside faces, as shown in Figure 5.2b. This setup created a parallel-plate capacitor, which is depicted in Figure 5.2c and Figure 5.2d. It is known that the capacitance of a parallel-plate capacitor depends on its geometry and dielectric property between its two electrodes. It was hypothesized that pH would alter the

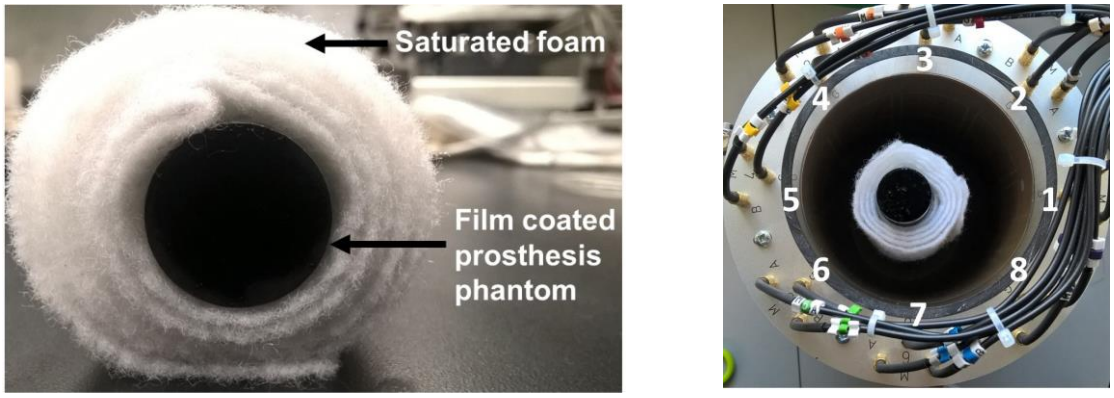

(a) (b)

Figure 5.3 (a) An aluminum rod was used as a surrogate for a prosthesis, and it was coated with a pH-sensitive MWCNT-PANI/latex thin film and then wrapped with saturated foam to simulate human tissue. (b) The OIP surrogate was placed at the center of the sensing region for ECT interrogation.

electrical permittivity of the MWCNT-PANI/latex film. Since the geometry (*i.e.*, length and width of electrodes) was constant, any variations in measured capacitance would be due to dielectric property changes of the thin film alone. Here, the test began by disassembling the parallel-plate capacitor to expose the thin film, and a pH 1 buffer solution was pipetted onto its surface for 30 s and then dried using compressed air. Then, the parallel-plate capacitor was reassembled and subjected to capacitance testing, where the parallel plate-capacitor was excited using a 16 kHz, 10 V peak-to-peak, square- wave generated by an Agilent 33250A function generator. Instead of directly measuring capacitance, current in the circuit was measured using a Keysight 34460A DMM and recorded using Keysight *BenchVue* data logging software, since it is directly proportional to the capacitance. Figure 5.2d illustrates the circuit and measurement setup. Capacitance was calculated by averaging 10,000 current measurements.

5.2.2.3 Noncontact pH Sensing Validation

After designing and characterizing pH-sensitive nanocomposite thin film, ECT tests were conducted to simulate infection occurring at the tissue-prosthesis interface and to see if it was

possible to detect changes in electrical permittivity due to pH (or infection). First, the ECT hardware was employed to obtain a set of boundary capacitance measurements when nothing was present in the sensing domain. This set of measurements served as the raw data used for computing the baseline permittivity distribution (of air). Second, a representative surrogate (or phantom) of an OIP was needed. In this case, a 25-mm-diameter aluminum rod was selected, followed by spray-coating a layer of insulating primer and then the MWCNT-PANI/latex thin film. Primer was deposited to electrically isolate the MWCNT-PANI/latex film from the rod. In reality, another biocompatible polymer coating could also be applied and will be investigated in future studies. Nevertheless, the phantom was then wrapped with foam, which was saturated with water, as shown in Figure 5.3a. The purpose of including the saturated foam was to simulate an environment similar to that of human tissue. The entire test setup is shown in Figure 5.3b.

To expose the phantom to pH buffer solutions, the film-coated rod was carefully removed without disturbing the saturated foam and then immersed in different pH buffer solutions. This was followed by drying the film-coated rod using compressed air and inserting it back into the cylindrical saturated foam layer so that the entire system was in the same location in the sensing domain as before. At this point, the sensing domain was interrogated, and boundary capacitance measurements were recorded. This procedure was repeated using the same film-coated prosthesis phantom, where, in total, the system was exposed to pH 1 to 13 buffers, in increments of 2. Lastly, changes in spatial permittivity were obtained by comparing each result with respect to the reconstructed permittivity distribution of the baseline (or just air).

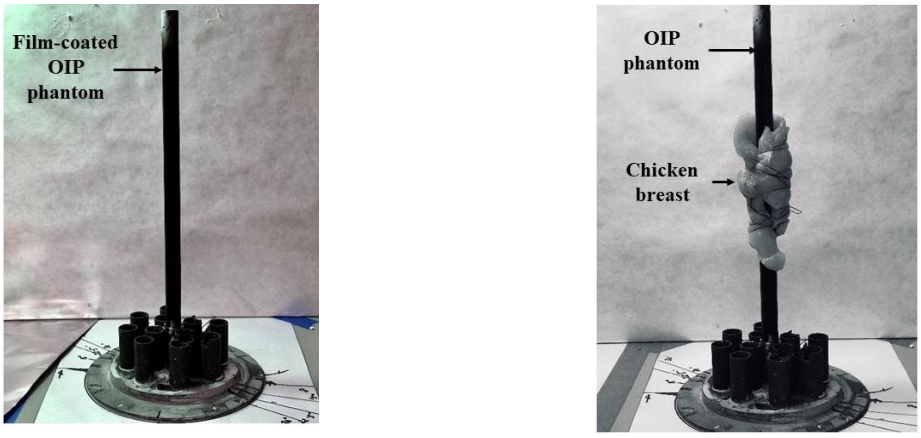

(a) (b)

Figure 5.4 A 12.5-mm-diameter aluminum rod was coated with an MWCNT-PANI thin film and served as the OIP phantom. (b) A piece of chicken meat was wrapped around the phantom to simulate the human tissue, which formed the OIP surrogate.

5.2.2.4 Noncontact pH Sensing in Biological Specimen

Similar to Section 5.2.2.3, the pH-sensitive nanocomposite thin film was also spray-coated on a 12.5-mm-diameter aluminum rod was used as an OIP phantom as shown in Figure 5.4a. To simulate a similar environment as human tissue, a piece of chicken meat was wrapped around the OIP phantom. The OIP surrogate (*i.e.*, the thin film-coated OIP phantom wrapped with the chicken meat) is shown in Figure 5.4b. Before interrogating the OIP surrogate with the ECT system, a baseline measurement was taken when the ECT electrode array was empty (*i.e.*, filled with only air). Then, during each ECT test, the surrogate was taken out from the electrode array, and the chicken meat was unwrapped. Different pH buffer solutions (pH 1, 3, 5, 7, 9, 11, and 13) were successively applied onto the surface of the film-coated OIP phantom to simulate infection at the tissue-prosthesis interface. Upon the application of each pH buffer solution, the rod was dried using compressed air (~ 10 psi), and the chicken meat was re-wrapped around the OIP surrogate. The entire sample was placed back at the same location inside the ECT electrode array. The relative changes in permittivity distributions for all the pH cases were computed with respect to the recorded baseline.

5.2.3 Noncontact Strain Monitoring in OIP

The second part of the study is focused to develop a noncontact, noninvasive strain sensing technique that can be potentially used for monitoring *in situ* strains in OIP. First, a new type of MWCNT-based nanocomposite thin films, whose electrical permittivity is sensitive to strain, were designed and fabricated. The nanocomposite used in this study was an MWCNT and PSS-based thin film that can be deposited onto the surface of OIP by spray coating [172], and they served as a passive sensor whose strain-induced permittivity changes could be quantified (in a noncontact manner) by ECT. Furthermore, this study also investigated the effects of patterning on strain sensitivity. When subjected to strain and deformation, these stacks of patterned films change their dimensions, thus leading to intensified local changes in electrical permittivity distribution. As the change in dielectric property gets magnified as a result of the incorporation of this strain-sensitive thin film, ECT can be employed to detect the permittivity change during deformation in a noncontact fashion.

5.2.3.1 Strain-Sensitive Nanocomposite Fabrication

The formulation of the MWCNT-latex thin film used in this study was based on studies reported in Section 3.2.1. Similar studies were performed by Loyola *et al.* [137] and Mortensen *et al.* [172]. For all types of specimens tested in this study, a thin layer of paint primer was first deposited onto the surface of the substrate to serve as an electrically insulating layer and to ensure that the film adheres to the substrate. While paint primer is obviously not biocompatible, future studies will investigate other biocompatible thin film precursor alternatives that could be implemented on OIP. Nevertheless, once the primer fully dried, the MWCNT–latex film was spray-coated. Two different types of films were fabricated, which are herein referred to as Thin

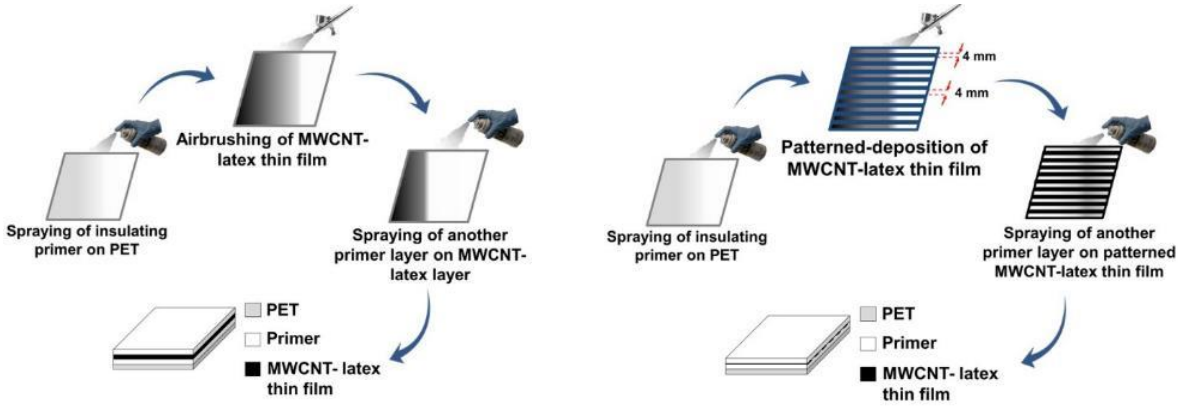

Figure 5.5 The fabrication procedure for (a) Thin film-A and (b) -B are illustrated.

film-A and Thin film-B. Both films were MWCNT–latex films but were deposited differently to create specific patterns. First, Thin film-A was created by spray-coating a uniform MWCNT–latex film. After the film completely dried, another layer of insulating primer was deposited on top of it. Second, Thin film-B was a patterned thin film. The hypothesis was that patterning could enhance the electrical permittivity's sensitivity to applied strains. Using the primer-coated substrate, 4-mm-wide strips of masking tape were applied to form a multi-striped pattern, with each mask separated by a 4-mm-gap from its adjacent ones. Then, a layer of MWCNT–latex thin film was deposited, followed by removal of the masks to leave behind patterned strips of nanocomposites. The final step entailed spraying another layer of primer over the entire patterned film. Effectively, the alternating strips of conductive MWCNT-latex films and insulating layers served as a compound parallel-plate capacitor, which changed its perceived capacitance and permittivity due to strain, thus enhancing its strain sensing performance. The fabrication procedures of Thin films-A and -B are schematically shown in Figure 5.5a and 5.5b, respectively. It should be mentioned that spray-coating can be performed manually or using a robotic spray fabrication system.

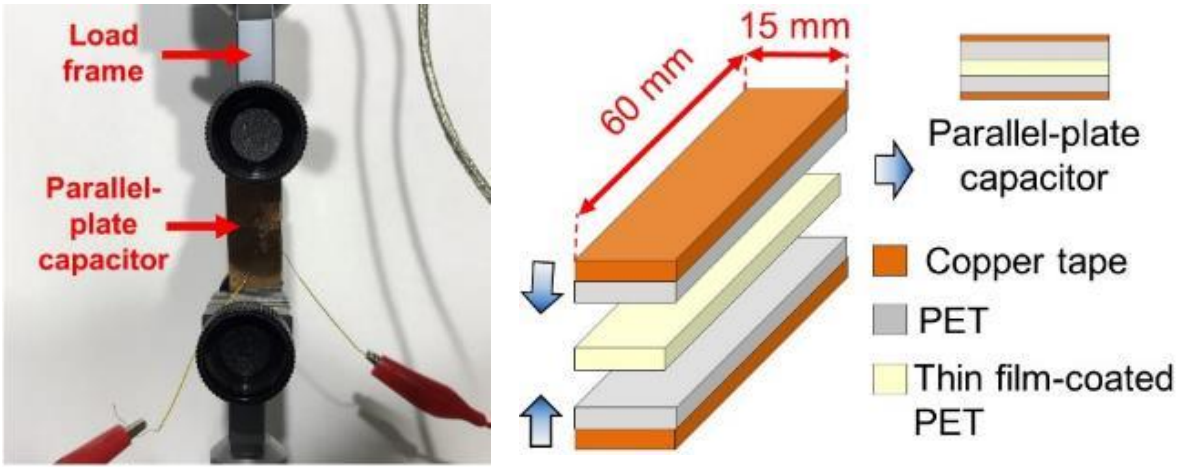

(a) (b)

Figure 5.6 (a) A nanocomposite-coated PET strip was mounted in the load frame for characterizing its strain sensitivity. (b) Copper tape electrodes were used to interrogate the capacitance response of the film-coated PET.

5.2.3.2 Strain-Sensing Characterization

To characterize how the nanocomposites' permittivity responded to applied strains, Thin films-A and -B were deposited onto primer-coated PET sheets, and a parallel-plate capacitor test setup was employed. First, the film-coated PET was cut into a rectangular strip and mounted in a Test Resources 150R load frame. Second, using two separate (and pristine) PET strips of identical size, conductive copper tape was affixed onto one side of each of those PET strips. These copper tape–PET strips were then mounted adjacent to the film-coated PET specimen and clamped in the load frame (Figure 5.6a). Such an arrangement formed a parallel-plate capacitor with the film-coated PET (and additional layers of PET) as the dielectric medium between the two copper tape electrodes. This setup also ensured that the electrodes are not strained when the film-coated PET was loaded. The test setup and its assembly processes are illustrated in Figure 5.6b.

Using this test setup, the load frame was commanded to apply uniaxial tension to the specimen at a constant strain rate (588 με/min) from 0 to 4902 με, pausing every 980 με for capacitance measurements using a Keysight E4980A LCR meter. This was followed by unloading

the specimen to 0 με and pausing accordingly for capacitance measurements. It should be mentioned that the LCR meter applied a 1 V, peak-to-peak, 1.25 MHz sinusoidal excitation signal; capacitance was also measured in parallel-circuit mode (C_p), because the impedance of all the specimens was greater than 10 kΩ. Five specimens of each type were prepared and tested to study the dielectric behavior of Thin films-A and -B when subjected to tensile loading and unloading.

5.2.3.3 Noncontact Strain Monitoring

After quantifying the accuracy of the ECT inverse algorithm, a set of experiments was performed to verify if deformation in the prosthesis phantom could be monitored in a noncontact fashion via ECT. A 20-mm-diameter plastic rod (Figure 5.7a) was used as the prosthesis phantom and subjected to uniaxial and bending loads, while its change in electrical permittivity due to strain/deformation was monitored with ECT. Although a plastic rod was used, it could be replaced with a metallic specimen. A previous study by Gupta and Loh [36] demonstrated that ECT could also detect strain-induced permittivity changes of a nanocomposite-coated metallic prosthesis phantom.

In this study, a customized load frame (designed and built by Elintrix), shown in Figure 5.7b, was configured to apply different types of loads (*i.e.*, uniaxial compression and bending) to an OIP surrogate. First, the surrogate was fitted in the load frame via a four-jaw-chuck so that one end was completely fixed. Second, the ECT electrode array was slipped over the 400-mm-long rod such that the rod was located at the center of the ECT electrode array cross-section, as shown in Figure 5.7c. Next, two sets of experiments were performed. The first set of tests subjected the phantom to uniaxial one-cycle compressive loading and then unloading as described below.

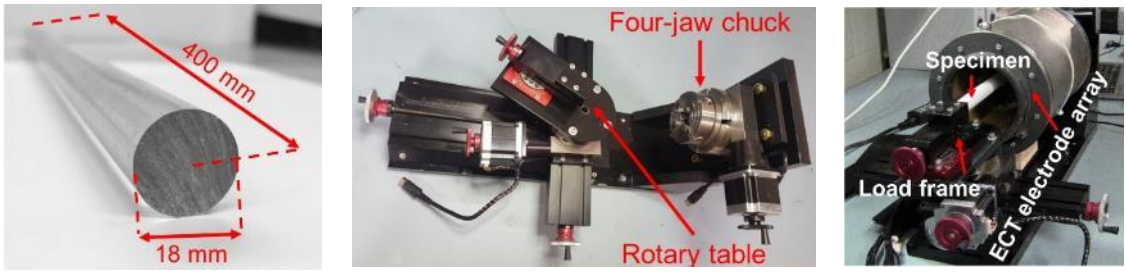

(a) (b) (c)

Figure 5.7 (a) In this study, 18 mm-diameter, 400 mm-long plastic rods were used as the test structure and were subjected to different types of loading. (b) A customized prototype load frame was designed and built by Elintrix. (c) The specimen was fitted into the load frame with the ECT electrode array for testing.

First, strain-sensitive Thin films-A and -B were deposited onto the surfaces of the test specimens and were subjected to uniaxial one-cycle compressive loading and then unloading, as shown in Figure 5.8. Second, the test specimen was subjected to transverse displacements (V) to cause bending, as shown in Figure 5.9. A major benefit of the Elintrix load frame was the fact that one of its four-jaw adjustable grips was fitted onto a rotary table, thereby allowing the load frame to apply mixed-mode loading to the specimen (*i.e.*, bending, compression, or a combination). It should be mentioned that, before the application of any load to the specimen, a baseline set of capacitances was obtained, and the corresponding permittivity distribution (*i.e.*, baseline) was reconstructed.

5.2.4 Bone Fracture and Prostheses Loosening Monitoring

This study presents the investigation of the potential of ECT as a noncontact, portable, non-radiation-based imaging technique to detect the onset of and diagnose prosthesis loosening, as well as loosening-induced bone fractures. Since bone and metallic prostheses are characterized by drastically different electrical permittivity, it is hypothesized that ECT can map changes in electrical permittivity and detect dislocation and loosening of the OIP. In addition, loosening-induced bone fracture can also be identified and localized using ECT. In addition to just testing

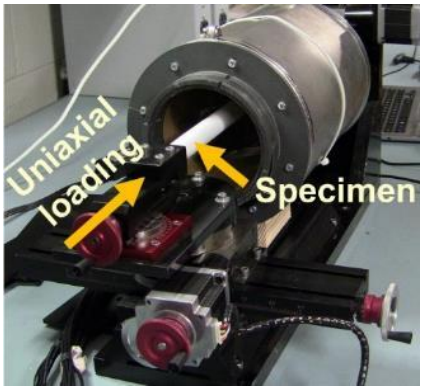

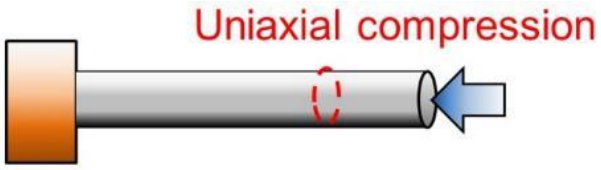

(a) (b)

Figure 5.8 (a) The picture of the load frame and (b) the schematic shows that uniaxial compressive load was applied to the test specimen, and ECT measurements were recorded at different strain states.

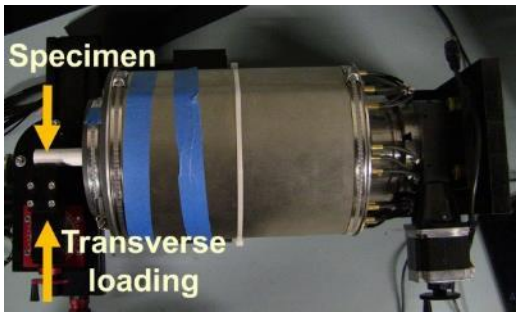

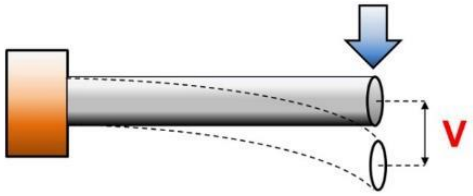

(a) (b)

Figure 5.9 The picture of the load frame and (b) the schematic shows that transverse loads were applied to the specimen to induce bending.

the ability of ECT to map prosthesis loosening/ bone fracture-induced permittivity changes, the quality of the reconstructed images is also assessed. This section begins with a brief description of the different image matrices used to study the quality of the ECT images, followed by the test protocols and corresponding laboratory validation results.

5.2.4.1 Prosthesis Loosening Monitoring

The first set of experiments was performed to validate that ECT can detect OIP loosening. Instead of performing an *in vivo* test, an OIP surrogate was prepared and used for this preliminary

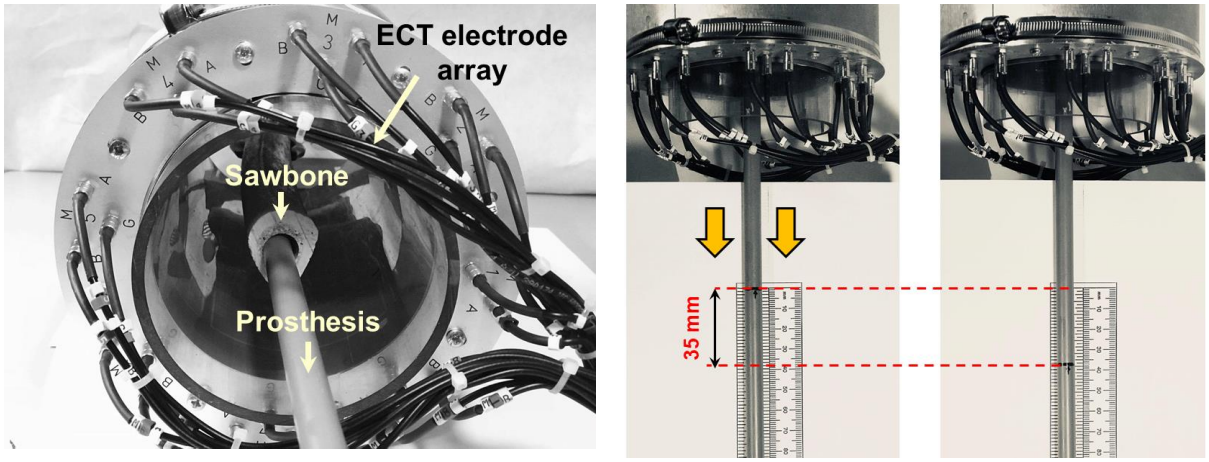

Figure 5.10 (a) Prosthesis loosening monitoring tests were conducted using a bone-prosthesis phantom by placing it near the center of the ECT electrode array for interrogation. (b) The prosthesis phantom was gradually pulled out from Sawbone femur (from 0 to 35 mm), while ECT measurements were recorded every 5 mm.

study, where a 12.8-mm-diameter PVC rod was slipped into the medullary cavity of a femur Sawbone. A previous study already demonstrated that ECT can accurately reconstruct the permittivity distribution of actual tissue-and-bone specimens, as well as Sawbone with metallic OIP. A PVC OIP surrogate was chosen as a more challenging environment for spatial permittivity reconstruction since the electrical permittivity of PVC is considerably less than that of metal and more comparable to bone.

For this test, the entire surrogate was placed in the central region of the ECT electrode array as shown in Figure 5.10a. The prosthesis was gradually pulled out from the medullary cavity starting from 0 mm to 35 mm and at 5 mm increments to simulate the effect of prosthesis loosening (Figure 5.10b). At the end of each 5 mm movement, the system was interrogated by the ECT system, and the corresponding electrical permittivity distributions were reconstructed from the measured set of boundary capacitance responses.

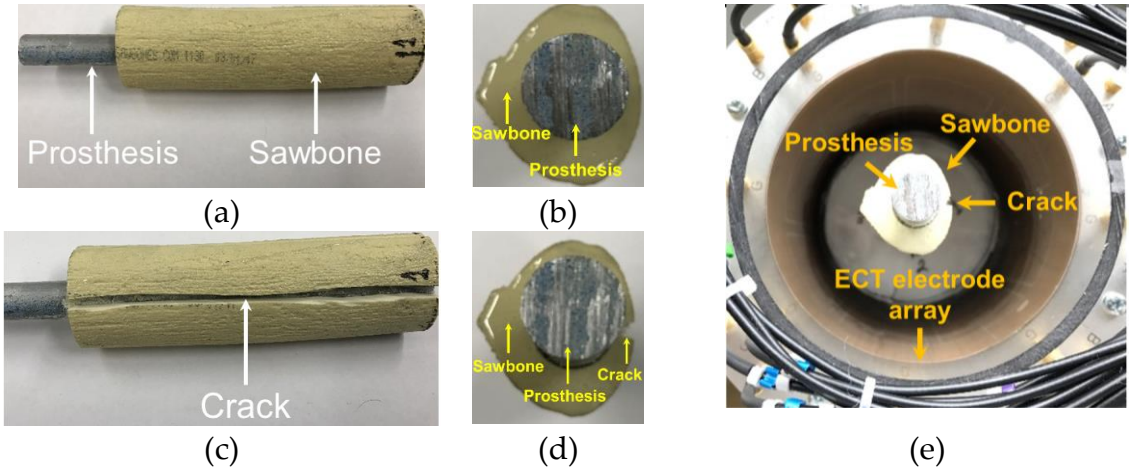

Figure 5.11 An aluminum rod was inserted in a Sawbone femur to create the OIP surrogate, and (a) its longitudinal and (b) cross-sectional views are shown. (c) A longitudinal cut is made along the Sawbone, and (d) its cross-section is also shown. (e) The OIP surrogate was placed in the center of the ECT electrode array for ECT interrogation and data acquisition.

5.2.4.2 Fracture Detection at Bone-Prosthesis Interface

As mentioned earlier, prosthesis loosening, if undetected at an early stage, can cause stress concentrations in bone and, ultimately, cracks (or fracture) can propagate at the bone-prosthesis interface, thereby leading to OIP failure and extreme pain for the amputee. Thus, the second experiment aims to investigate whether ECT can be applied as a noninvasive imaging tool to detect the location and severity of cracks at the bone-prosthesis interface. Similar to the previous test surrogate, a Sawbone femur was selected. Instead of a plastic rod, an aluminum rod that is 12.8 mm in diameter was inserted into the medullary cavity to create the OIP surrogate. To ensure a secure fit, quick-setting epoxy was employed to bond the metal rod with the femur replica. A side- and top-view of the surrogate can be seen in Figure 5.11a and Figure 5.11b, respectively. A slit (*i.e.*, ~ 3-mm- deep and ~ 3-mm-wide) was then cut along the side and in the direction of the longitudinal axis of the femur using a Dremel tool, as shown in Figure 5.11c and Figure 5.11d, for emulating fracture. Thereafter, the surrogate was placed at the middle of the ECT electrode array for ECT interrogation and data acquisition as shown in Figure 5.11e.

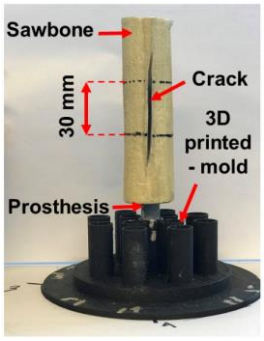

(a)

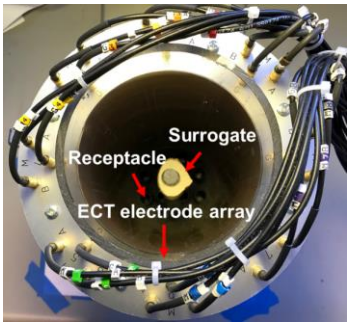

(b)

Figure 5.12 The OIP surrogate was inserted in a 3D-printed mold to maintain its position in the ECT electrode array during imaging. (b) The 3D-printed mold was placed at the bottom of the ECT electrode array, and the entire test setup is shown.

After validating that ECT can detect fracture location at the bone-prosthesis interface, additional tests were performed to see if ECT can also be used to quantify fracture size (*i.e.*, its length and depth). Like the previous fracture detection test, similar experimental procedures were followed. Here, a 12.8-mm-diameter PVC rod was employed for the rest of this study. A slit (*i.e.*, ~ 14-mm- deep and ~ 3-mm-wide) was cut using a Dremel tool along the longitudinal axis of the OIP surrogate as shown in Figure 5.12a. The length of the fracture was gradually increased from 5 to 30 mm at 5 mm increments. After each increment in fracture, ECT measurements were recorded for permittivity reconstruction. In order to accurately maintain the position of the OIP surrogate in the ECT electrode array (*i.e.*, during removal of the OIP surrogate for cutting), a ProMatte fixture was printed using a Type A Series 1 Pro 3D printer. This receptacle was placed at the bottom of the ECT electrode array, and the OIP surrogate was inserted into the middle slot in the ECT electrode array as shown in Figure 5.12b.

Finally, the depth of the fracture was quantified using a similar experimental setup as before. Here, a 35-mm-long slit was cut along the longitudinal axis of the OIP surrogate. The depth of the fracture was gradually increased from an undamaged state to 14.25 mm in ~ 2.85 mm

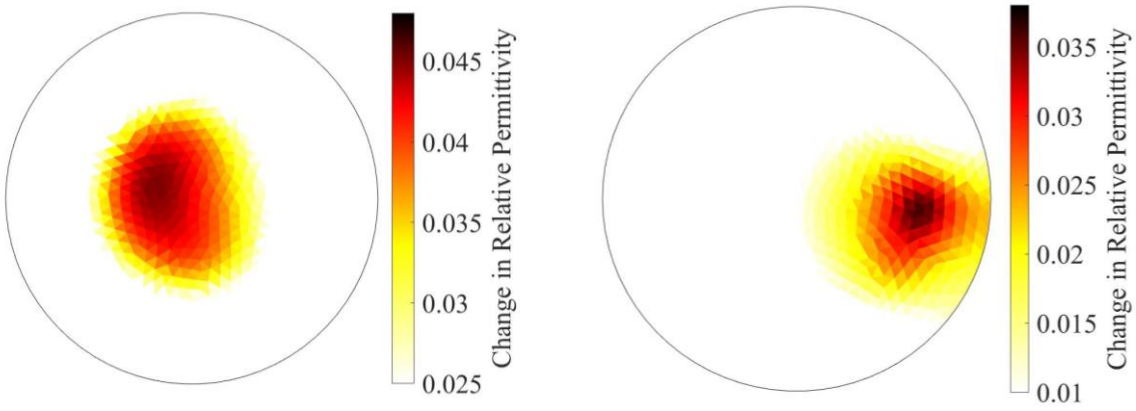

(a) (b)

Figure 5.13 (a) the relative change in permittivity map successfully identified the bone and tissue regions that corresponded to the lamb shank specimen. (b) The change in electrical permittivity distribution with respect to the empty baseline of air (*i.e.*, empty ECT electrode array) is presented.

increments. ECT measurements were obtained after each additional ~ 2.85 mm increment of depth in cut.

5.3 Results and Discussions

5.3.1 Dielectric Property Imaging of Biological Specimens

A simple experiment was conducted using a lamb shank as the specimen to demonstrate that ECT has the potential for imaging tissues and bones (and in the future, human beings) (Section 5.2.1). The lamb shank, as shown in Figure 5.1a, was placed in the ECT sensing domain and interrogated, followed by reconstructing its change in relative permittivity distribution with respect to an empty sensing domain as the baseline. It can be seen from Figure 5.13a that the shape of the lamb shank was successfully captured by ECT. In addition, greater changes in permittivity were observed near the vicinity of the bone, while the remainder of the permittivity changes were due to the presence of tissues. Although Figure 5.13a is only a preliminary validation of this technique for use in biological systems, the result shown in Figure 5.13a is promising.

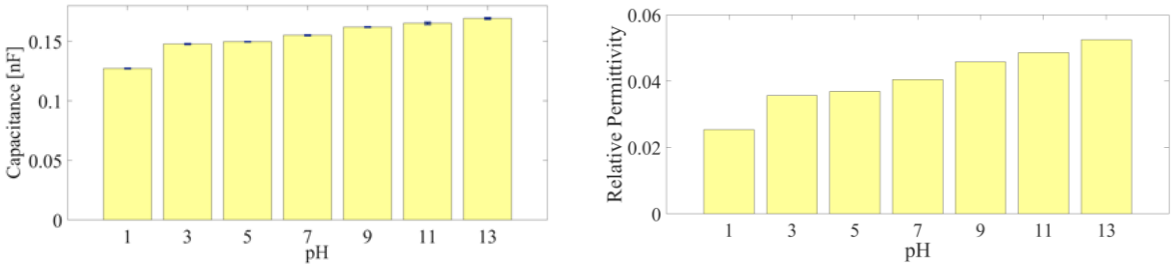

(a) (b)

Figure 5.14 The permittivity of the MWCNT-PANI/latex film changed as the film was exposed to different pH buffer solutions, which changed the (a) measured capacitance of the test setup. Standard deviations of measured capacitance are also shown (for 10,000 measurements). (b) The relative permittivity of the film, corresponding to different pH, was computed.

The second experiment was conducted on the same lamb shank with a surrogate prosthesis (*i.e.*, a steel rod of 6.25-mm-diameter) press-fitted in the bone of the lamb shank. It can be observed from Figure 5.13b that the location and the shape of the lamb shank was successfully captured by ECT. A higher change in electrical permittivity was observed near the vicinity of the region where the prosthesis rod was located. A gradual decrease in permittivity is also seen radiating outward from the OIP region as a result of the presence of materials with lower dielectric properties (*i.e.*, bone and soft tissue). These preliminary results demonstrate that ECT has the potential for imaging the OIP system implanted in the biological system.

5.3.2 Infection Monitoring

5.3.2.1 Thin Film pH Sensing

As was described in Section 5.2.2.2, MWCNT-PANI/latex thin films exposed to different pH buffer solutions were sandwiched between two aluminum electrodes and glass slides to create a parallel-plate capacitor test setup. Figure 5.14a plots a representative set of capacitance results with respect to different pH, where the error bars correspond to the standard deviation of each dataset. It can be observed that capacitance increases in tandem with increasing pH. Since the

geometry of the parallel-plate capacitor was fixed, it can be concluded that the electrical permittivity of MWCNT-PANI/latex thin films increased with increasing pH. In addition, using known dimensions of the test setup and by estimating the permittivity of glass as 4.7, the film's relative permittivity when exposed to different pH could be calculated and plotted, as presented in Figure 5.14b. In order to estimate the electrical permittivity of the thin film, it was assumed that each layer of the dielectric materials (*i.e.*, glass and MWCNT-PANI/latex thin film) act as separate dielectric materials that were connected in series. It should be mentioned that the thickness of similar spray-coated MWCNT-based films were determined by scanning electron microscopy and was ~ 10 μm [48], which was also assumed here.

5.3.2.2 ECT-Enabled Noncontact pH Sensing

After validating the potential of ECT for imaging bone and tissue, this study continued with investigating whether ECT could noninvasively identify pH changes as an indication of infection occurring at tissue-prosthesis interfaces. A prosthesis phantom pre-coated with an MWCNT-PANI/latex thin film was used for the next set of tests. The rod was wrapped in foam saturated in deionized water (*i.e.*, to simulate the simultaneous presence and properties of human tissue), as shown in Figure 5.3a. ECT was performed on the film-coated rod prior to it being exposed to pH buffers, and the resulting relative permittivity distribution is presented in Figure 5.15a.

From Figure 5.15a, one can identify three distinct regions of different electrical permittivity. First, the center portion of the highest relative permittivity (of ~ 120) corresponded to the prosthesis phantom. Second, a large ring with a relative permittivity of ~ 80 can be seen, whose value is close to that of deionized water, and its size is comparable to the experimental

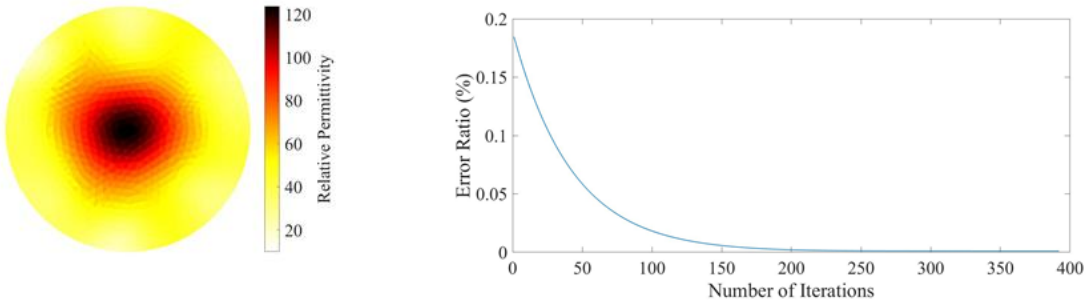

(a) (b)

Figure 5.15 (a) The ECT relative permittivity distribution reconstruction of a film-coated phantom rod wrapped in saturated foam is shown. (b) The plot shows the number of iterations required for the algorithm to converge to different error thresholds.

setup. Last, the outermost region is air. While metals are characterized by infinite electrical permittivity, ECT and FE method are unable to reconstruct this but instead converges to a large number. In addition, regularization inherently smooths sharp edges (*e.g.*, the interface between foam and air) to show a gradient of change in relative permittivity. Figure 5.15b shows that the ECT algorithm could converge at ~ 125 iterations when the error threshold reaches 0.01% (*i.e.*, the threshold set in this case), and negligible changes in error threshold is observed after ~ 200 iterations. In general, Figure 5.15 successfully validated that ECT was able to reconstruct the absolute relative permittivity of materials in its sensing domain (*i.e.*, to within a reasonable degree of accuracy given estimation and experimental errors).

The next test involved exposing the film-coated rod to pH buffer solutions. As discussed in Section 5.2.2.3, the filmcoated rod was immersed in a pH 1 buffer solution, dried using compressed air, and placed back in the saturated foam. The entire tissue-prosthesis surrogate was centered in the sensing domain as shown in Figure 5.3b. Boundary capacitance measurements (*i.e.*, mutual capacitance between the boundary electrode pairs) were obtained, and the raw data was used as inputs for solving the ECT inverse problem and for obtaining its respective relative permittivity distribution. As discussed in Section 5.2.2.3, this procedure was repeated using the

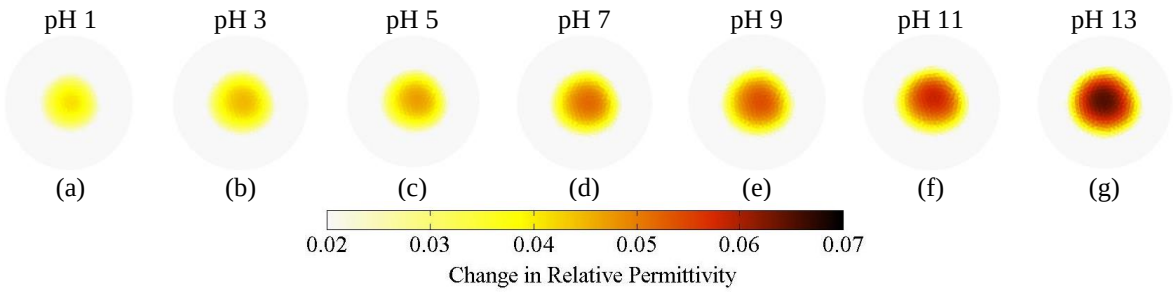

Figure 5.16 The film-coated rod (*i.e.*, prosthesis phantom) was exposed to pH (a) 1, (b) 3, (c) 5, (d) 7, (e) 9, (f) 11 and (f) 13 buffer solutions, and the corresponding reconstructed change in permittivity distributions with respect to the baseline (*i.e.*, the empty sensing domain case) are shown.

same phantom rod for pH 3, 5, 7, 9, 11, and 13 buffers. The permittivity map for an empty sensing domain was employed as the baseline, and the relative change in permittivity distributions for all the pH cases were computed with respect to this baseline.

The ECT permittivity maps for one set of tests are shown in Figure 5.16. First, it can be observed from Figure 5.16 that ECT successfully identified the location of the prosthesis phantom, and it compares well with its actual location shown in Figure 5.3; the film-coated phantom was located in the center of the sensing domain. Similarly, since the remainder of the sensing domain was air throughout the entire test, the reconstructed permittivity maps do not show any permittivity changes there, but a comparatively small change in permittivity can be observed around the prosthesis phantom. It is anticipated that this change was caused due to the presence of saturated foam.

Second, one can also observe changes in localized electrical permittivity due to the application of different pH. This result was only possible with the introduction of the MWCNT-PANI/latex thin film on the prosthesis phantom since it was already demonstrated in Section Figure 5.14. As expected, the ECT permittivity maps shown in Figure 5.16 also confirmed that permittivity increased with increasing pH. Overall, these results suggest that ECT, when used in

conjunction with pH-sensitive thin films, can potentially serve as a noninvasive tool for monitoring pH (as a precursor for infection occurring near tissue-prosthesis interfaces). Future tests will consider the embedment of a prosthesis surrogate in tissue and bone samples while conducting simulated infection tests.

5.3.2.3 Noncontact pH Sensing in Biological Specimen

As stated earlier, ECT was employed for monitoring the change in the dielectric property as an indicator of infection at the tissue-OIP interface. The thin film-coated prosthesis phantom was exposed to different pH buffer solutions and subjected to ECT interrogations. The measured sets of boundary capacitance responses were used as inputs to solve the ECT inverse problem. The estimated changes in permittivity distributions with respect to the baseline (*i.e.*, when the ECT electrode array was full with only air) corresponding to different pH states are shown in Figure 5.17. First, it can be observed that ECT was able to identify the location of the OIP surrogate in the ECT electrode array. Like the previous results shown in Figure 5.16, a distinct increase in electrical permittivity in the central region of the sensing domain where the surrogate was located physically was observed. Second, it can be seen that the electrical permittivity of the region corresponding to the OIP surrogate increased as the film-coated OIP surrogate was subjected to acidic to alkaline pH buffer solutions. Overall, the results in Figure 5.17 demonstrated that ECT, when coupled with the MWCNT-PANI thin film, could be used as a noncontact subcutaneous infection monitoring tool in a simulated biological environment. Although ECT was able to successfully capture the location and gradual changes in electrical permittivity as the film-coated surrogate was subjected to different pH buffer solutions, it was observed that the size of the infected region was overestimated, where the ECT results showed an increase in electrical permittivity over a larger area than the actual size of the surrogate. This undesirable effect was

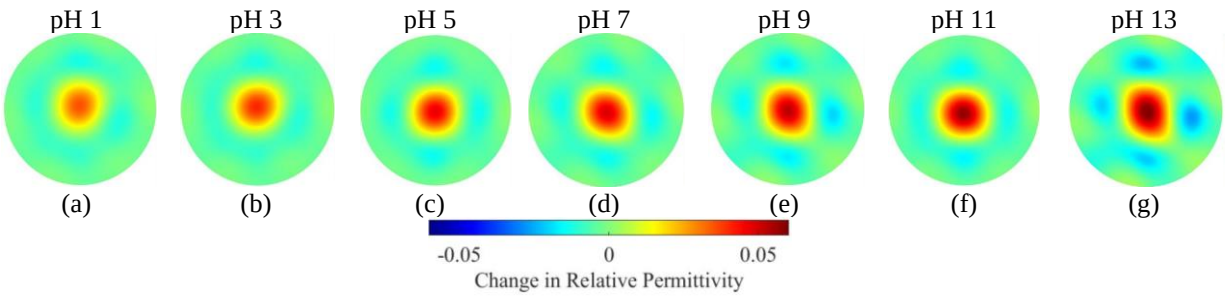

Figure 5.17 The OIP phantom was exposed to pH (a) 1, (b) 3, (c) 5, (d) 7, (e) 9, (f) 11 and (g) 13 buffer solutions, and the corresponding reconstructed permittivity distributions with respect to the baseline are shown.

likely due to the artifacts produced by the ECT inverse algorithm because of the sparse boundary measurements and regularization scheme employed. Furthermore, the reconstructed images also suffered from poor resolution, where the exact shape and size of the infected region was not clearly identified.

5.3.2.4 ECT Image Resolution Enhancement

Previous studies demonstrated that ECT could be used as a noncontact, radiation-free imaging tool for monitoring the OIP-related issues. In addition, ECT could be coupled with an implantable, passive, and pH-sensitive thin film sensor (deposited onto the OIP prior to implant surgery) to reveal pH changes at tissue-OIP interface indicative of infection. The location and severity of infection can also be identified from the reconstructed spatial permittivity maps. However, the reconstructed ECT images suffer from limited resolution, which limits the accuracy of the proposed technique.

In this section, a rotational electrical capacitance tomography (RECT) system is proposed, in which the circular ECT electrode array is rotated with respect to its central axis [217]. It is hypothesized that RECT is capable of producing higher quality images since a larger number of electric field excitations and corresponding independent capacitance measurements could be

obtained. Furthermore, this study also investigated the use of a limited region tomography (LRT) algorithm to further enhance the imaging resolution [218]. Laboratory experiments were performed to test this hypothesis and to demonstrate proof-of-concept. The experimental details and the results are discussed in the following sections.

A. RECT

As mentioned earlier, the limited number of measurements makes the ECT inverse problem challenging to solve with high accuracy and resolution. A better-quality image can be obtained by employing more electrodes for ECT measurements at the boundary. However, this is not always feasible as the number of electrodes is often restricted by the area of Ω. The ECT hardware system also needs sophisticated instrumentation to accommodate more electrodes for interrogation and measurements. This study used a rotational measurement scheme to increase the number of independent measurements that more independent boundary capacitance measurements as a result of physically rotating the electrode array resulted in a higher SNR for ECT permittivity reconstruction. Similar rotational systems have been implemented for EIT and magnetic induction tomography [217].

In conventional ECT systems, the electrodes are equidistantly arranged at the boundary of Ω. For an eight-electrode ECT system, the angle between two adjacent electrodes is 45˚. In this study, 22.5˚ and 15˚ were selected as the angles of the single rotation steps of the ECT electrode array. For the 22.5˚ angle-of-rotation case, the ECT electrode array was rotated by 22.5˚ with respect to its longitudinal axis upon collecting the first 28 independent boundary capacitance measurements. After a rotation was performed, the next 28 measurements were recorded. Since the data acquisition process needed to be repeated twice (*i.e.*, 45/22.5 = 2), a single rotation

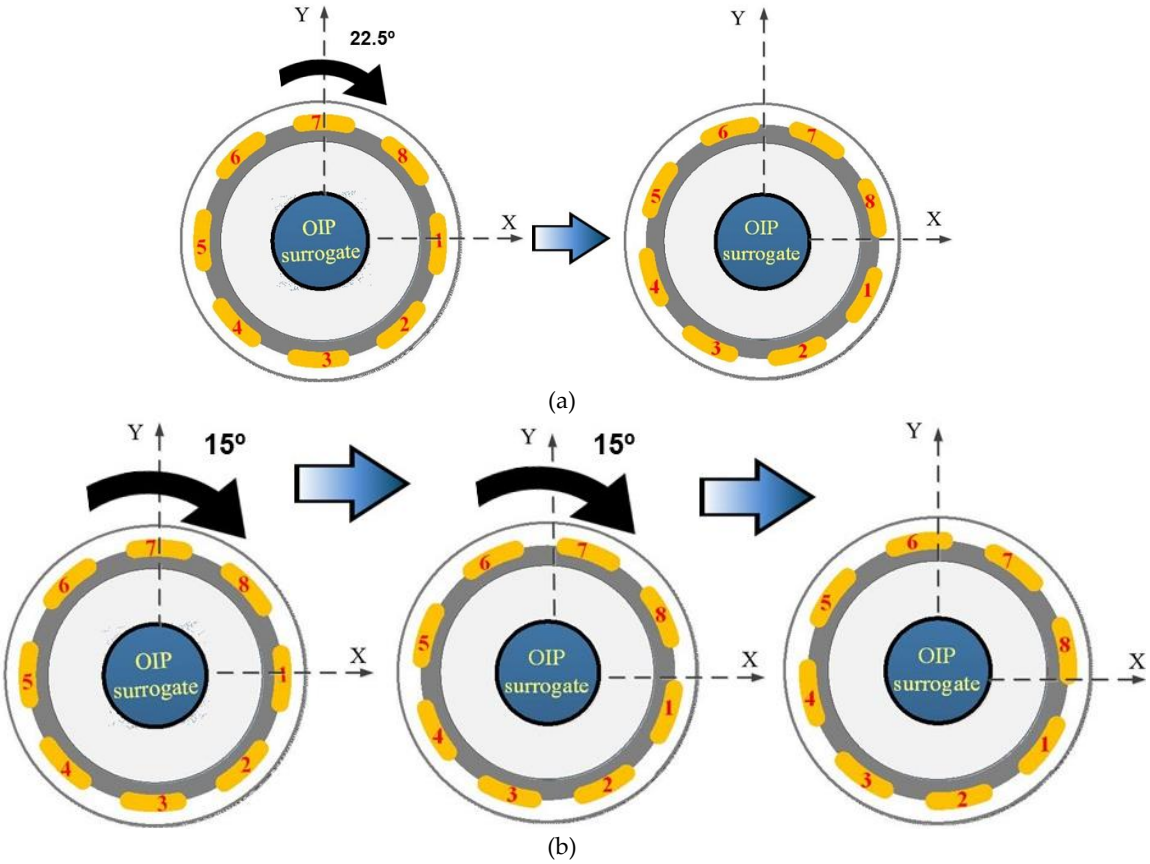

Figure 5.18 The schematics illustrate the rotational schemes for RECT with a stepping angle of (a) 22.5º and (b)15º.

produced 56 (*i.e.*, 28 × 2 = 56) independent boundary capacitance measurements. Similarly, in the case of the 15˚ angle-of-rotation case (where the electrode array was rotated twice), three sets of measurements were collected (*i.e.*, 45/15 = 3). Here, 28 × 3 = 84 independent measurements were recorded for ECT image reconstruction. The rotation processes are illustrated in Figure 5.18.

Laboratory experiments were performed to realize the potential of the RECT system as an enhanced ECT imaging tool. The OIP surrogate was subjected to RECT interrogations after exposing the phantom to different pH buffer solutions. The reconstructed images corresponding to different pH states with different rotation numbers are shown in Figure 5.19. Like the results shown in Figure 5.17, first, it can be observed that the RECT measurement strategy was able to identify

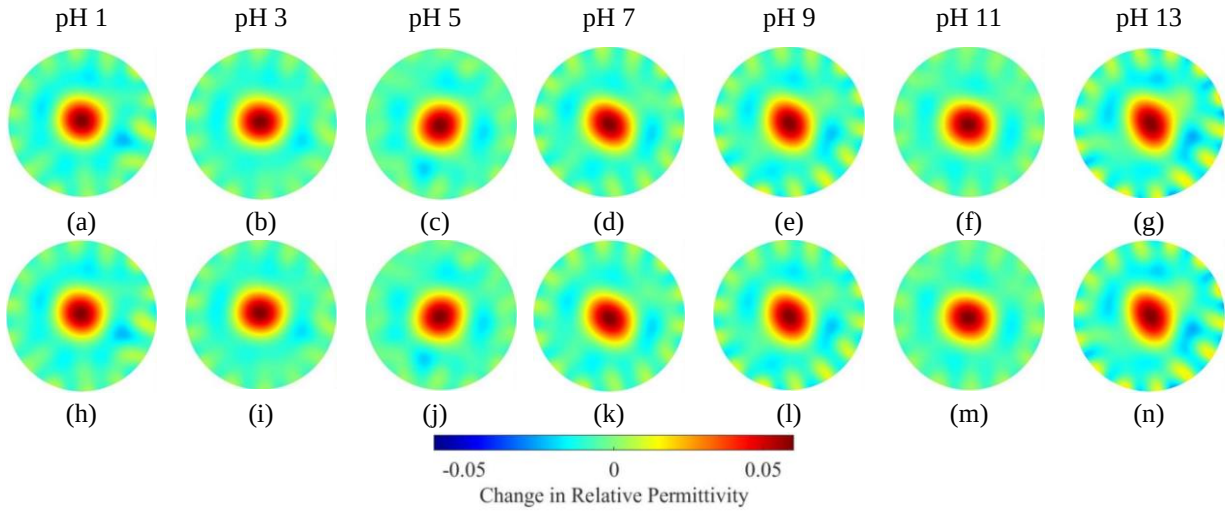

Figure 5.19 Here, pH-induced electrical permittivity changes in the OIP surrogate were mapped by RECT and ECT. (a) to (g) and (h) to (n) show the reconstructed electrical permittivity distributions from two (*i.e.,* one rotation at 22.5º) and three (*i.e.*, two rotations at 15º each) sets of measurements at each corresponding pH state.

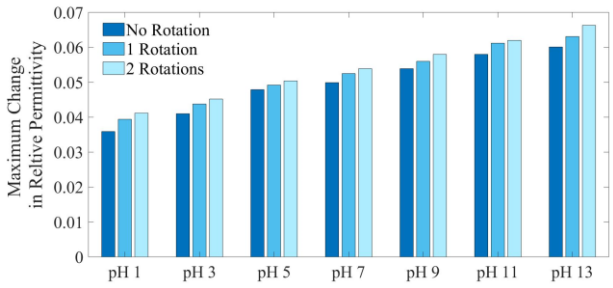

Figure 5.20. The maximum change in relative permittivity results for cases of zero rotation (conventional ECT), one rotation, and two rotations are shown.

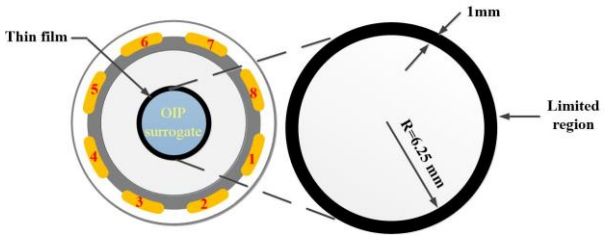

Figure 5.21. A 1-mm-thick circular region was considered as the limited region for RECT-LRT-based image reconstruction. The electrical permittivity of this limited region was reconstructed.

the location of the OIP surrogate. Second, the electrical permittivity of the region corresponding to the surrogate increased when the film-coated prosthesis was exposed to solutions of increasing pH. The results of Figure 5.19 are summarized in Figure 5.20, which plots the maximum change in permittivity of each ECT result shown in Figure 5.18 and 5.19. It can be seen from Figure 5.20 that RECT was able to identify that the maximum change of electrical permittivity increased as the thin film-coated prosthesis was exposed to increasing pH buffer solutions. Besides, it can be

observed that greater changes in electrical permittivity were observed as compared to conventional ECT as more rotations were performed. Even with the RECT measurement scheme, it was still unable to identify the exact location of the region where pH changes were occurring (*i.e.*, the MWCNT-PANI film). Ringing effects (*i.e.*, a negative change in electrical permittivity around the sharp positive change in permittivity) were also prominent in the reconstructed images, which are believed due to experimental error when rotating the ECT electrode array with a manual rotational scheme.

B. LRT-RECT system for enhanced ECT imaging performance

In order to overcome the aforementioned limitations, an LRT algorithm was developed and implemented and combined with the RECT measurement scheme [218]. As it is assumed that ECT captures the change in electrical permittivity of the nanocomposite thin film due to the application of different pH buffer solutions, the location of permittivity change can be assumed to be known *a priori*. In this study, a 1-mm-thick circular ring around the 12.5-mm- diameter OIP phantom is considered as the limited region (Figure 5.21). Only the electrical permittivity of this limited region was reconstructed, while it the permittivity of the remaining portion of the sensing region was assumed to be constant. The main objective of LRT is to reduce the ill-posed nature of the ECT inverse problem by significantly reducing the number of unknowns (*i.e.*, the electrical permittivity values of each finite element in Ω). As RECT gave more independent measurements to solve the ECT problem, coupling RECT with LRT was hypothesized to produce an enhanced ECT image. Using the same sets of measurements as those presented in Figure 5.19, the RECT-LRT system was employed to reconstruct the ECT images of the tissue-prosthesis interface, and the results are shown in Figure 5.22. It can be observed from Figure 5.22 that the ECT results are of visually higher resolution as compared to Figure 5.19. Two consecutive pH states can be better

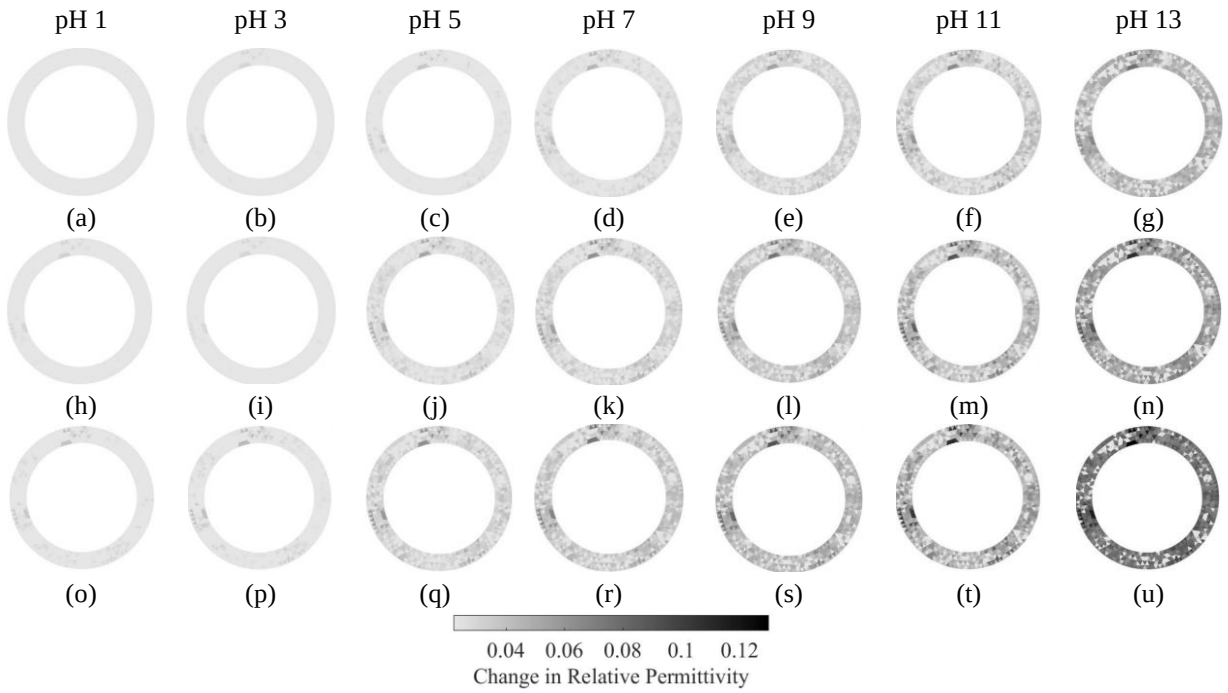

Figure 5.22 The RECT measurement scheme was combined with an LRT algorithm, and the permittivity of the region adjacent to the prosthesis (phantom rod) was reconstructed. The reconstructed electrical permittivity distributions of the limited region at different pH-states are shown. Conventional ECT results, as well as RECT with two and three sets of measurements, are shown in (a) to (g), (h) to (n), and (o) to (u), respectively.

distinguished from the reconstructed permittivity maps obtained by RECT-LRT. Overall, the conclusion is that RECT-LRT coupled with pH-sensitive nanocomposite thin films can be used together to generate high-resolution ECT images for detecting infection at the tissue-prosthesis interface. The potential advantages of RECT-LRT over conventional ECT can be realized from the singular value decomposition of J_{ECT}. Figure 5.23 shows that the singular values of J decay with respect to the number of measurements. In case of an ill-posed inverse problem like ECT, the amount of information that can be extracted from the measured set of boundary responses strictly depends on the number of singular values that are above the noise level [217]. The singular values of J_{ECT} were calculated and shown in Figure 5.23. As it can be seen that with 1% measurement noise, 25 singular values from the conventional ECT system contributed to image reconstruction.

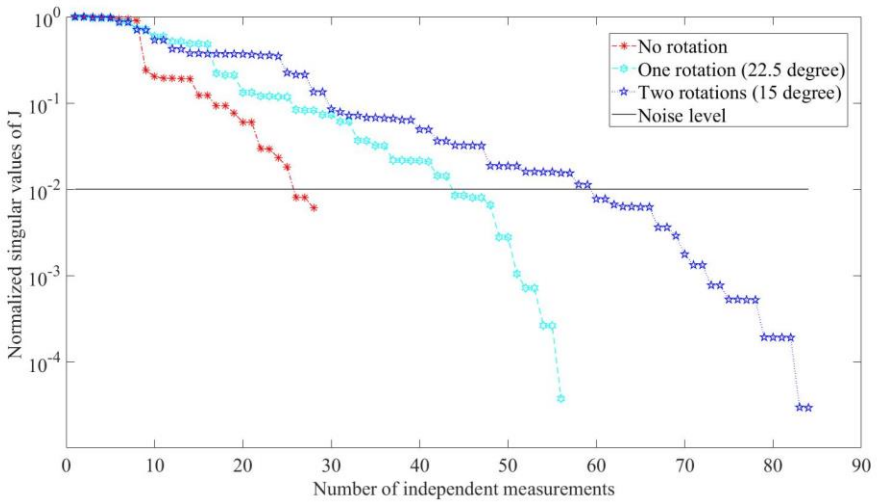

Figure 5.23 A comparison of singular values of the sensitivity matrices corresponding to different rotation cases are shown.

If the noise level remained the same in the case of 22.5˚ of rotation, 42 singular values were effective for image reconstruction. This number went up as high as 59 for the 15˚ case. However, resolution cannot be increased after a certain level by adding more rotations, since the number of singular values above the noise level will become saturated. Nevertheless, the first few rotations (*e.g.*, 22.5˚ and 15˚) contribute to a reasonable improvement in image quality as shown in Figure 5.22.

5.3.3 Strain Sensing

5.3.3.1 Strain Sensing Characterization

Figures 5.24a and 5.24b show the average capacitances of the Thin film-A and Thin film-B parallel-plate capacitors, respectively, during loading and unloading. Although the results shown here were obtained from only one loading cycle, it can be observed that the capacitance corresponding to the same strain-state during loading and unloading is nearly identical, which

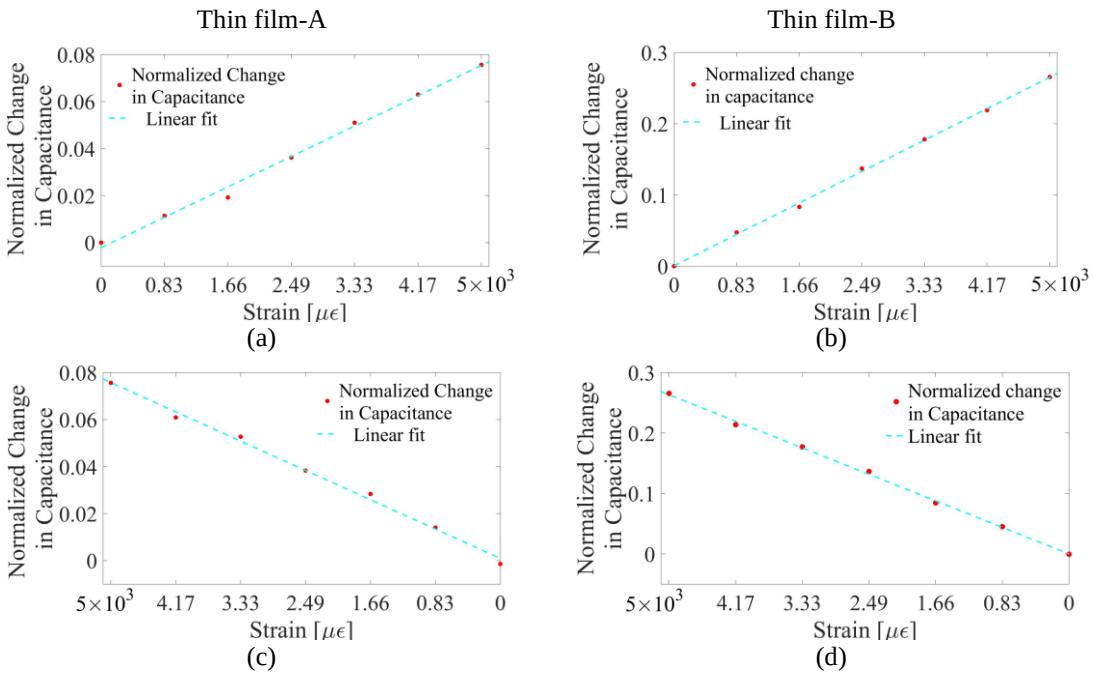

Figure 5.24 (a) Thin films-A and (b) -B were stretched, and the change in capacitance with respect to their undeformed states are shown, respectively. The change in capacitance during the unloading cycle for (c) Thin films-A and (d) -B are shown, respectively. Strain sensitivity of the Thin films-A and -B was found to be ~ 1.58 × 10^{-5} and ~ 5.37 × 10^{-5}, which was based on the slope of the linear best-fit line.

demonstrated their repeatability and suitability for strain sensing. However, it is important to study the long-term electromechanical behavior of the nanocomposite thin film to establish this thin film as a reliable

To better compare the capacitance results of different specimens, normalized capacitance (C_N) was computed as follows:

$$C_N = \frac{\Delta C_i}{C_0} \tag{5.1}$$

where C_0 is the film's capacitance prior to applying any strains, and ΔC_i is the change in capacitance of the specimen (at any given strain state, i) with respect to C_0. Representative results for Thin films-A and -B during loading and unloading are plotted in Figure 5.25. From the results shown in Figure 5.25, it is evident that both types of films exhibited strain-sensitive-dielectric

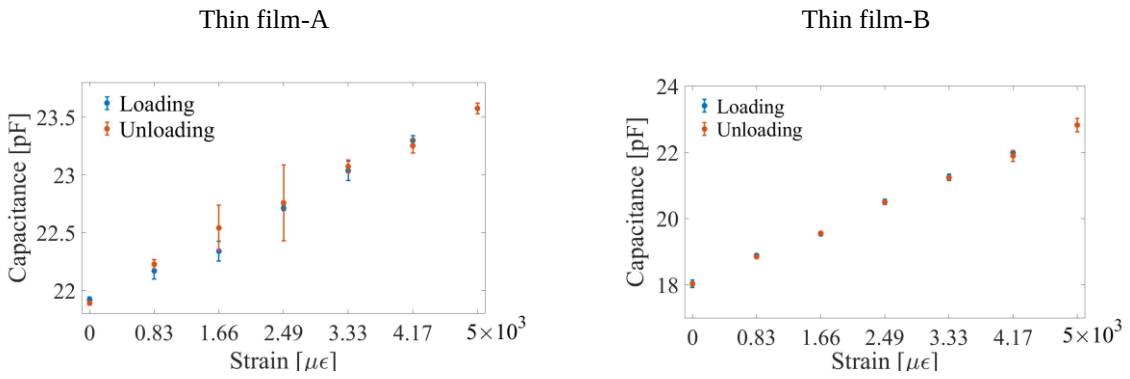

(a) (b)

Figure 5.25 The capacitance of the film-contained parallel-plate capacitor during loading and unloading are shown for (a) Thin films-A and (b) -B. Standard deviations of measured capacitances are also shown (based on five specimens tested).

behavior, where their capacitance increased in tandem with increasingly applied tensile strains and decreased when load was gradually removed.

It was also observed that the strain sensitivity of Thin film-B was ~ 4 times higher than that of Thin film-A, and this was true for both loading and unloading. Here, the strain sensitivity of these experimental results can be assumed to be equal to the slope of the linear least-squares best-fit line. Thus, it can be concluded that patterning the conductive MWCNT–latex thin film could enhance strain sensitivity. The patterns can be optimized for maximizing strain sensitivity, but this will be done in the future.

5.3.3.2 Noncontact Strain Monitoring

A. Uniaxial strain monitoring

ECT measurements were obtained at the same strain levels, and the corresponding changes in their electrical permittivity distributions with respect to their undeformed states are shown in Figure 5.26. It can be observed from these results that both of the thin film-coated specimens

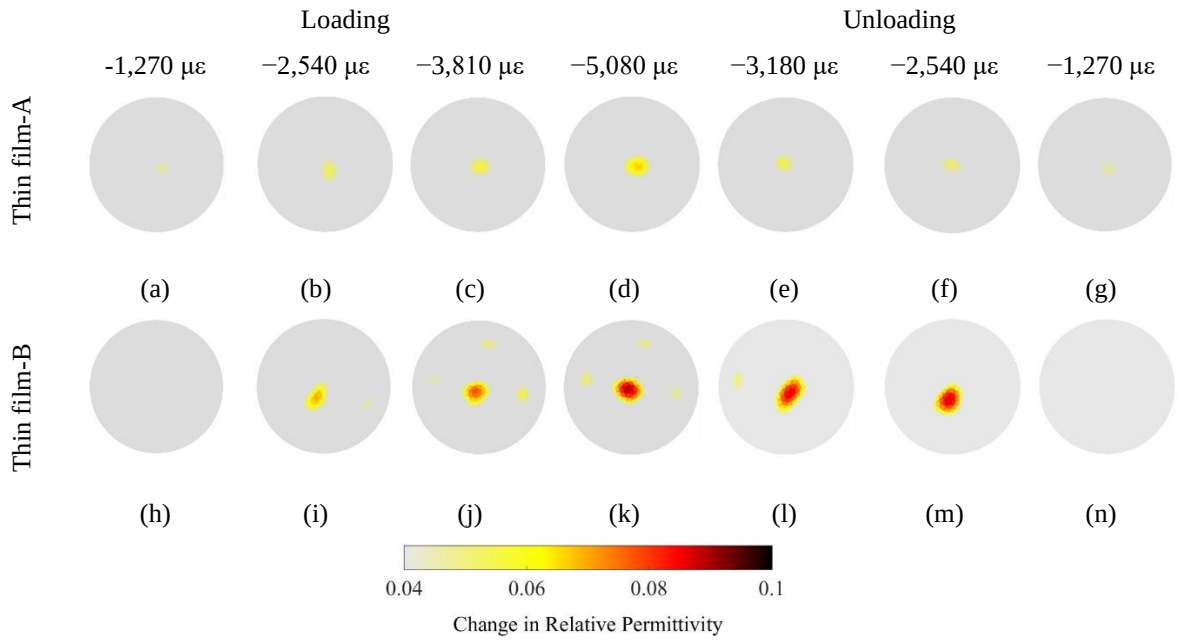

Figure 5.26 (a–d) show the changes in electrical permittivity of the Thin film-A-coated test specimen subjected to uniaxial compressive strain, while (e–g) describe the change in electrical permittivity during unloading. The Thin film-B-coated specimen was also subjected to the same loading conditions, and its changes in permittivity are shown during loading (*i.e.*, (h–k)) and unloading (*i.e.*, (l–n)).

exhibited electrical permittivity changes as they were subjected to uniaxial compression. Permittivity changes occurred where the rod was physically located in the sensing domain (*i.e.*, in the center). Some permittivity changes were also observed near the boundary regions, but this was likely due to measurement and environmental noise that corrupted capacitance measurements and influenced ECT reconstruction results. Second, the magnitudes of permittivity changes as a result of applied strains as determined by ECT (Figure 5.26) were comparable to the aforementioned parallel-plate capacitor tests (Figure 5.25). Because the strain sensitivity of Thin film-A was lower than that of Thin film-B, it can be seen in Figure 5.26 that the SNR is higher (*i.e.*, the magnitude of the change in electrical permittivity is larger) for the patterned specimen (Thin film-B).

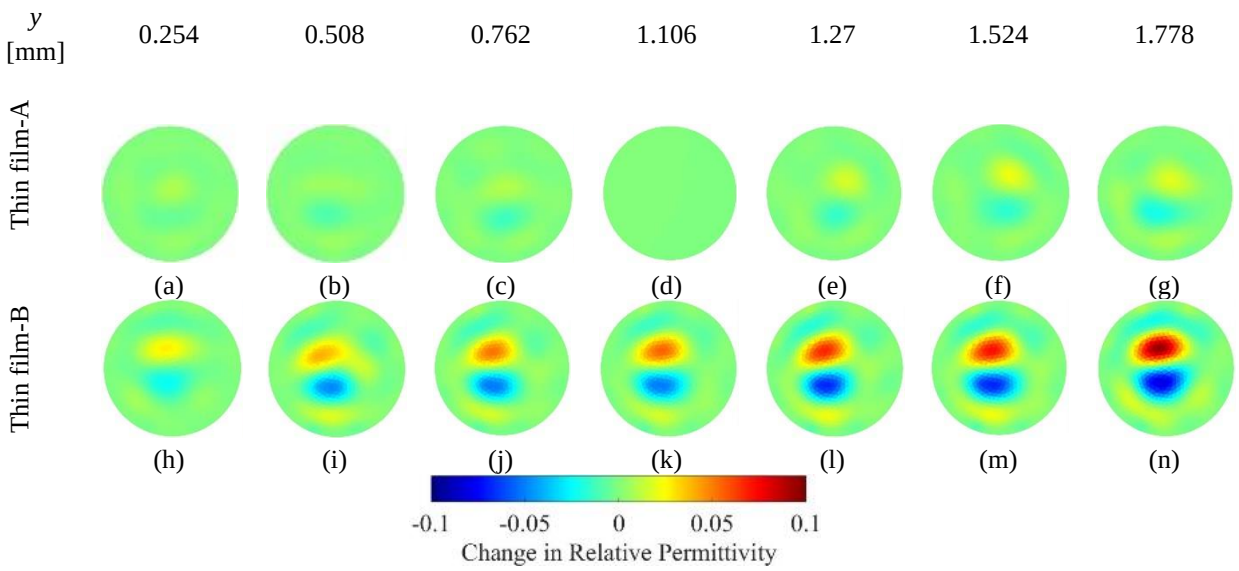

Figure 5.27 Thin films-A and -B coated onto osseointegrated prostheses phantoms were subjected to transverse loading. The corresponding changes in electrical permittivity with respect to the undeformed states are shown. (a–g) describes the permittivity changes for the specimen coated with Thin film-A, while (h–n) illustrate the electrical permittivity changes of the Thin film-B-coated specimen.

B. Cantilever bending monitoring

It is known that bending of a cantilever beam induces tension in one side with respect to the neutral axis and compression in the other. In this study, the custom Elintrix load frame was adjusted to apply transverse displacements (y) or loads to the free-end of the film-coated OIP phantoms, as was discussed earlier. Loading was paused at different displacement intervals to allow the ECT system to interrogate the sensing region and the specimen. Figure 5.27 shows a representative set of results. Although no significant changes in electrical permittivity were observed near the central region when a Thin film-A-coated specimen was subjected to bending (first row of Figure 5.27), a bipolar change in electrical permittivity was observed in the Thin film-B-coated specimen (bottom row of Figure 5.27). The reason that only the Thin film-B-coated specimens produced a response was because of its higher strain sensitivity and larger SNR. The bipolar response was also expected (*i.e.*, given that the rod was simultaneously experiencing tension and compression), and these results validated the fact that the film could sense both tensile

and compressive strains when coupled with ECT. However, the size of the specimen was exaggerated by ECT, which could be because of the particular regularization scheme employed.

It should be mentioned that the ECT electrodes have a finite length (~ 35 mm). This means ECT would output an average of any strain changes occurring over the interrogated region of the cantilevered OIP phantom. This effect can be mitigated by redesigning the electrode array to feature shorter electrodes. Another possibility is to move the electrode array along the length of the specimen to determine average strain-induced permittivity changes over a given segment. Such an approach can lead to the generation of 3D ECT-reconstructed permittivity distributions, which is the subject of future investigations. Overall, these results successfully demonstrated noncontact strain monitoring.

The data from Figure 5.27 were also further processed to reveal the change in electrical permittivity at different depths of the OIP surrogate's cross-section. To do this, a 25-mm-long, 2-mm-wide rectangular section (*R*) of the OIP specimen was considered (Figure 5.28a), and its center coincides with the center of the OIP rod in the previous test. From the FE modeling, it was found that *R* bounded 18 triangular elements spanning two columns (Figure 5.28b). The permittivity values of these elements in *R* were extracted, corresponding to the different stain states tested. Here, only data for the Thin film-B-coated specimen was processed because of its greater sensitivity to strain.

Figure 5.29 plots how the electrical permittivity of the Thin film-B-coated specimen varied as a function of depth. First, the results show that strain varied almost linearly, from tension (positive strain) in the upper portion to compression (negative strain) in the lower section of the OIP phantom. Second, the permittivity change is close to 0 near the neutral axis (*i.e.*, the center of

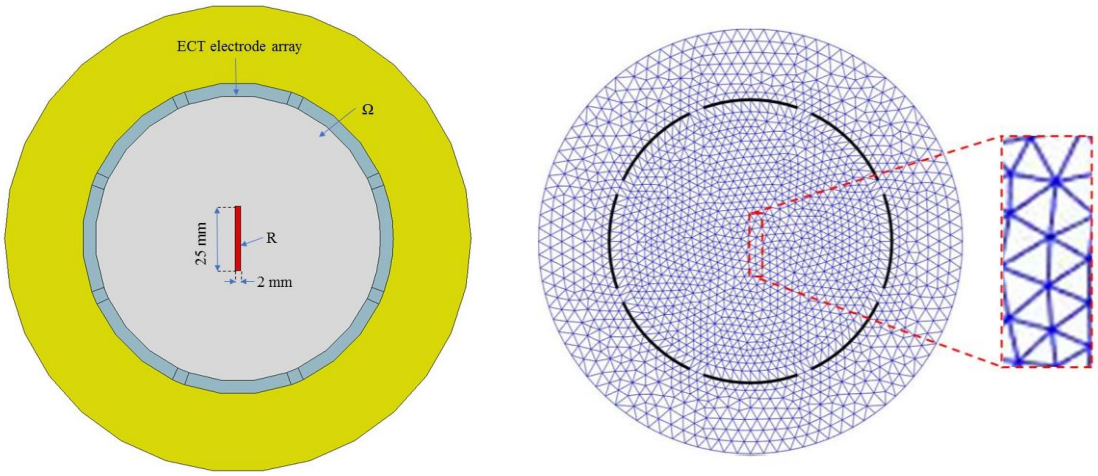

(a) (b)

Figure 5.28 (a) A 25-mm-long, 2-mm-wide rectangular region was considered at the center of the sensing region and coincided with a portion of the OIP phantom. (b) The rectangular strip consisted of 18 triangular elements.

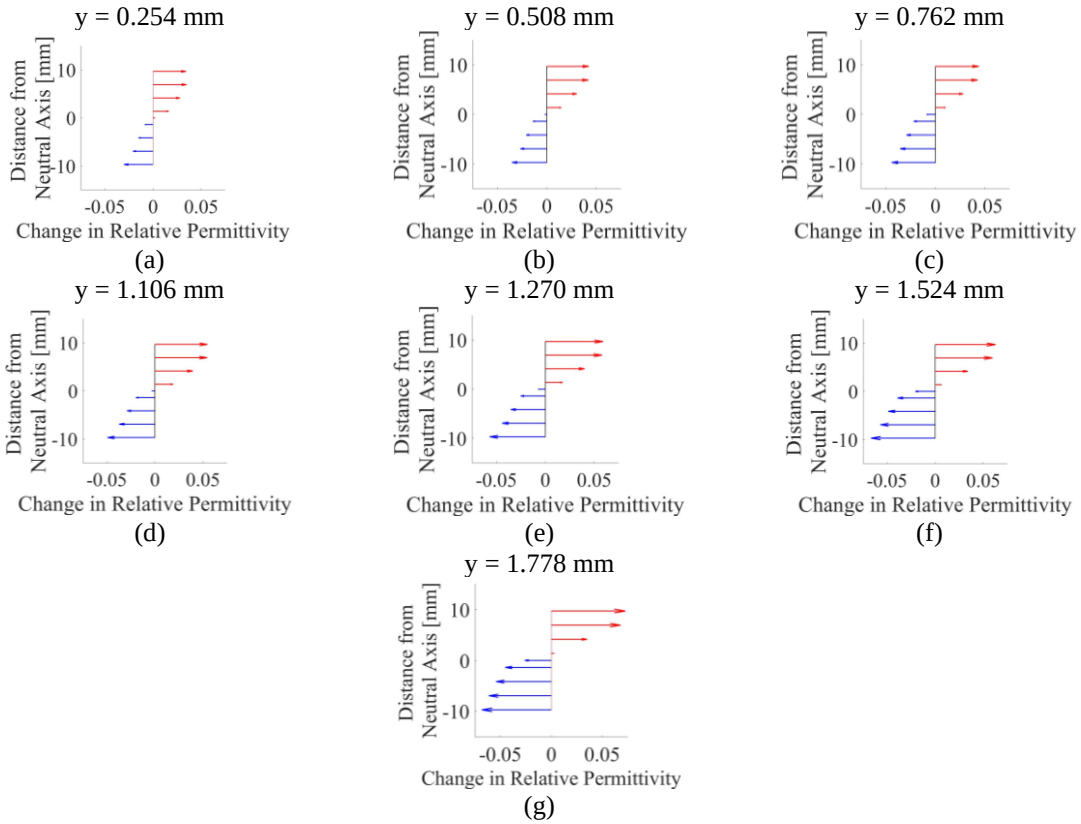

(a) (b) (c) (d) (e) (f) (g)

Figure 5.29 The change in electrical permittivity in *R* at different distances from the neutral axis position (*i.e.*, the center of the OIP surrogate) corresponding to different *y* are plotted in (a–g).

the rod), which is expected, while gradually increasing and moving towards the extreme values near the top or bottom. Third, the maximum absolute change in electrical permittivity increased as *y* was gradually increased from 0.254 to 1.778 mm, which is shown by the length of the top and bottom arrows in Figure 5.29. The linear change in electrical permittivity over the cross-section of the specimen shown in Figure 5.29 resembles the same strain distribution pattern as one would expect for a cantilevered beam subjected to bending. Overall, these results also show that the bending strain distribution over the cross-section of a nanocomposite-coated prosthesis surrogate could be captured with the aid of ECT.

5.3.4 Bone Fracture and Prosthesis Loosening Monitoring

This section presents the investigation of the potential of ECT as a noncontact, portable, non-radiation-based imaging technique to detect the onset of and diagnose prosthesis loosening, as well as loosening-induced bone fractures. Since bone and metallic prostheses are characterized by drastically different electrical permittivity, it is hypothesized that ECT can map changes in electrical permittivity and detect dislocation and loosening of the OIP. Additionally, loosening-induced bone fracture can also be identified and localized using ECT. In addition to just testing the ability of ECT to map prosthesis loosening/ bone fracture-induced permittivity changes, the quality of the reconstructed images is also assessed. This section begins with a brief description of the different image matrices used to study the quality of the ECT images, followed by the test protocols and corresponding laboratory validation results.

5.3.4.1 ECT Image Evaluation Criteria

Two image parameters were evaluated and studied to characterize quality of the reconstructed images. Similar image parameters were also used for checking the quality of ECT-

reconstructed permittivity maps in Chapter 2. However, in this chapter, they were formulated to study how accurately the reconstructed images can capture the location, shape, and size of the bone fracture.

The image parameters were evaluated on the basis of $[\varepsilon_q]_i$, (*i.e.*, one-fourth amplitude set) Mathematically, one-fourth amplitude set can be defined by equation 2.75. *PE* is evaluated by calculating the distance between the CG of the defects (*e.g.*, crack, prosthesis loosening) and $[\varepsilon_q]_i$.

$$PE = | r_t - r_q | \tag{5.2}$$

where r_t and r_q are the position vectors of the CG of the defects and $[\varepsilon_q]_i$, respectively. *PE* measures how accurately reconstructed images can identify the location of the defects. A small value of *PE* signifies a better accuracy of the reconstructed image. Area ratio (*AR*) is defined as the fraction of the area of all the pixels of $[\varepsilon_q]_i$ located in the damaged region to the actual damage size (*D*).

$$AR = \sum_{i \in D} {[\varepsilon_q]_i} \Big/ D \tag{5.3}$$

AR represents the accuracy of the reconstructed images in terms of the shape and size identification. *AR* closer to 1 represents a better-quality image.

5.3.4.2 Prosthesis Loosening Results

As stated earlier, ECT was employed for monitoring OIP loosening. Figure 5.30 shows the change in relative permittivity distributions acquired at different stages of displacement of the prosthesis phantom as it was gradually pulled out from 5 mm to 35 mm. It should be mentioned that the results in Figure 5.30 plot the change in electrical permittivity distribution with respect to the initial stage (*i.e.*, 0 mm) or pristine specimen's permittivity distribution. A baseline was used

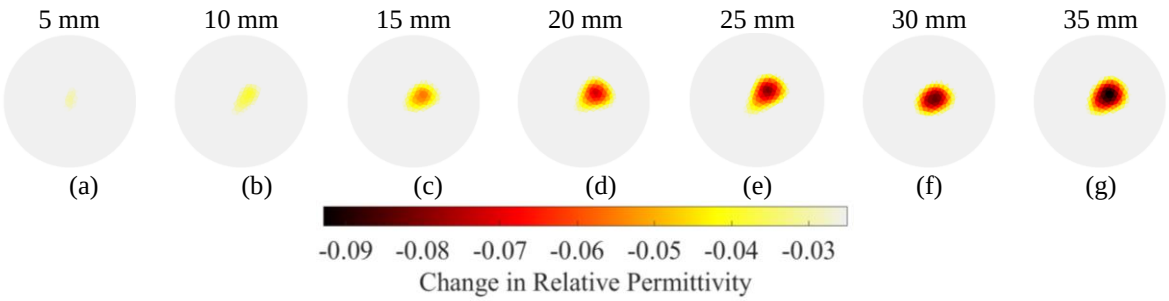

Figure 5.30 Relative permittivity distributions due to prosthesis loosening at different loosening states were reconstructed and compared to the baseline (*i.e.*, undamaged state). ECT results corresponding to OIP pull-out of (a) 5, (b) 10, (c) 15, (d) 20, (e) 25, (f) 30, and (g) 35 mm are shown.

in this case to highlight changes in relative permittivity due to prosthesis loosening. First, it is clear that ECT can successfully identify the location of permittivity changes due to loosening of the prosthesis. Second, a decrease in electrical permittivity was observed with increasing pull-out, because the pulled-out section or void was filled with air, which has a lower permittivity than the PVC rod. The magnitude of permittivity change was smaller at initial stages of prosthesis pull-out, because a portion of the prosthesis rod was still within the interrogating electric field. As the prosthesis phantom was loosened further, a higher decrement in electrical permittivity was observed as expected.

After successfully detecting the location and extent of the prosthesis loosening, *PE* and *AE* were evaluated for qualitative assessment of the reconstructed images (Figure 5.31). The maximum change in electrical permittivity was found among all the reconstructed images and used for the setting one-fourth amplitude set. In order to calculate *PE* and *AR*, it is assumed that the center of the OIP surrogate coincided with the center of the ECT electrode array. Although *PE* was smaller than ~ 2 mm, it was found that it was increased after first 5 mm pull-out. On the other hand, it was found that *AR* was ~ 1 during first 5 mm pull-out and its value was gradually decreased

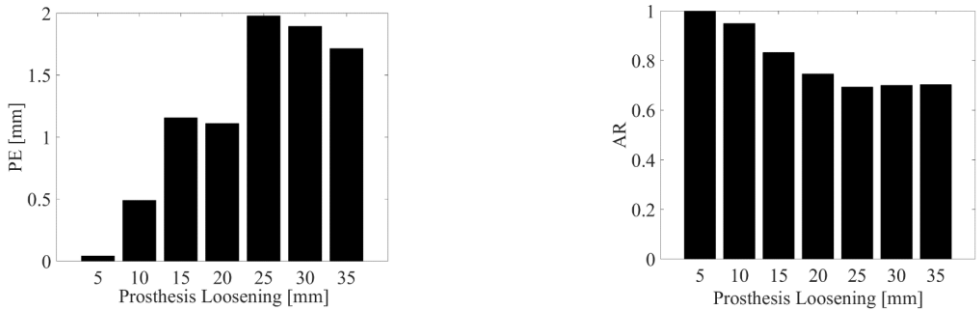

(a) (b)

Figure 5.31 ECT image resolution criteria (a) *PE* and (b) *AR* were evaluated for the reconstructed images corresponding to different extent of OIP pull-out are shown.

from ~ 1 to ~ 0.6. These may be due to the reason that the OIP surrogate was displaced from the center of the ECT electrode array during the first pull-out.

5.3.4.3 Bone Fracture Detection Validation

In the second part of this study, a fracture was introduced by cutting a slit in the Sawbone at the bone-prosthesis interface, and the surrogate was subjected to ECT testing. It should be mentioned that this test involved obtaining two different baseline permittivity maps of the sensing region. The first was the permittivity distribution of an empty ECT sensing region (*i.e.*, with only air). The second was obtained by interrogating the pristine or undamaged surrogate when placed at the center of the ECT electrode array. Figure 5.30a shows the electrical permittivity distribution of the pristine OIP surrogate, and the change in permittivity was calculated with respect to the baseline of an empty sensing region. Figure 5.30b shows the permittivity distribution of the fractured OIP surrogate (*i.e.*, with respect to the undamaged case shown in Figure 5.32a). It can be observed from Figure 5.32b that a sharp decrease in electrical permittivity can be observed near the vicinity of the area where the crack was located. This result makes sense since fracture (*i.e.*, bone loss) corresponds to the creation of a void (or air) at the location of fracture. Since air has a lower electrical permittivity than Sawbone, the permittivity maps show a decrease in permittivity.

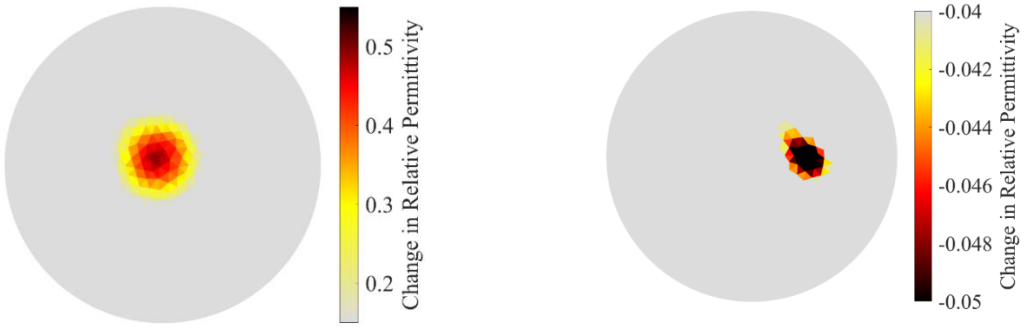

(a) (b)

Figure 5.32 (a) The permittivity distribution corresponding to the pristine OIP surrogate was reconstructed, and the change in relative permittivity with respect to an empty electrode array is shown. (b) The change in permittivity distribution due to the introduction of a fracture in the Sawbone femur (taken with respect to the pristine case) is shown.

5.3.4.4 Bone Fracture Monitoring Results

The next set of experiments was focused on detecting the longitudinal growth of a fracture along the length of the Sawbone and OIP surrogate. Similar to the previous test, changes in permittivity due to increases in fracture length was compared to that of the undamaged state, and the results are shown in Figure 5.33. It can be noticed that the ECT results showed a decrease in electrical permittivity corresponding to the location of the fracture. The absolute magnitude of permittivity change increased in tandem with increasing fracture length (*i.e.*, from 0 to 30 mm). Figure 5.34 summarizes the results of and plots the maximum change in permittivity of each ECT result in Figure 5.31 with respect to crack size. It can be seen from Figure 5.32 that the maximum change of electrical permittivity continued to decrease as the length of the fracture increased. After successfully detecting the location and extent of the bone fracture along the length of the OIP surrogate, *PE* and *AE* were evaluated for ECT image evaluation and the results are shown in Figure 5.35. It should be mentioned that OIP surrogate was taken out every time from the ECT electrode array to increase the crack length. A variation in *PE* was observed (Figure 5.35a) which could be due to the position mismatch resulted during this process. Initially, the crack was just ~ 5 mm and

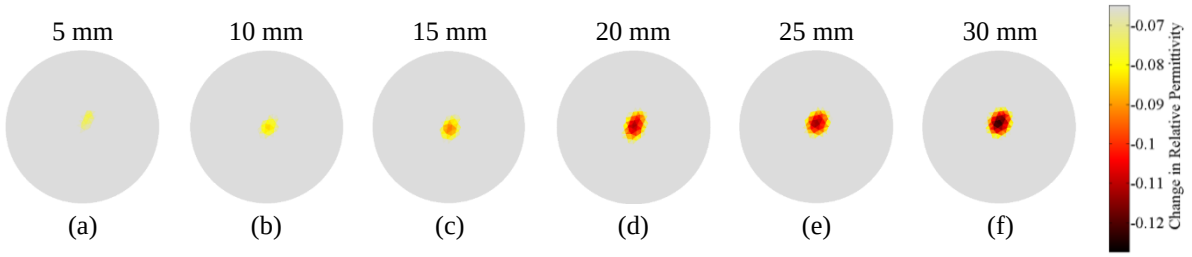

Figure 5.33 The change in relative permittivity distributions due to the gradual increase in fracture length along the length of the Sawbone femur, starting from (a) 5, (b) 10, (c) 15, (d) 20, (e) 25, to (f) 30 mm, are shown.

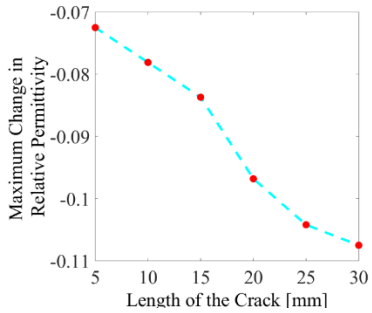

Figure 5.34 The maximum change in relative permittivity from the ECT results and due to the introduction of a longitudinal fracture of different lengths (from 5 to 30 mm) are plotted.

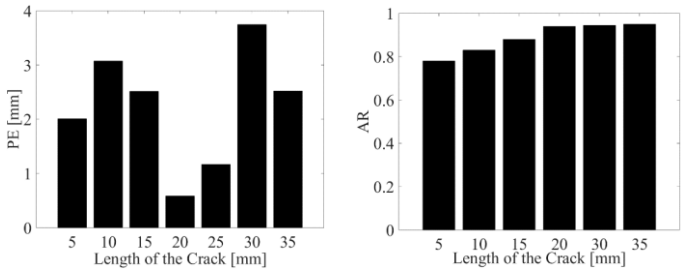

(a) (b)

Figure 5.35 *PE* and (b) *AE* were evaluated from the reconstructed images corresponding to differnet crack lengths are plotted.

.

it was located far away from the center of the plane of ECT scanning electrodes. As a result, *AR* was comparatively small (~ 0.8). As the crack length was increased, *AR* reached a value closer to 1 (~ 0.97).

As mentioned earlier, the last set of ECT experiments were performed to monitor fracture depth occurring at the bone-prosthesis interface. In this case, fracture depth was gradually increased, by sawing the bone using a Dremel tool, from its initial pristine state to ~ 14.25 mm in depth. The electrical permittivity distributions of different fracture states (*i.e.*, changes in electrical permittivity with respect to the pristine OIP surrogate) are shown in Figure 5.36. Although ECT

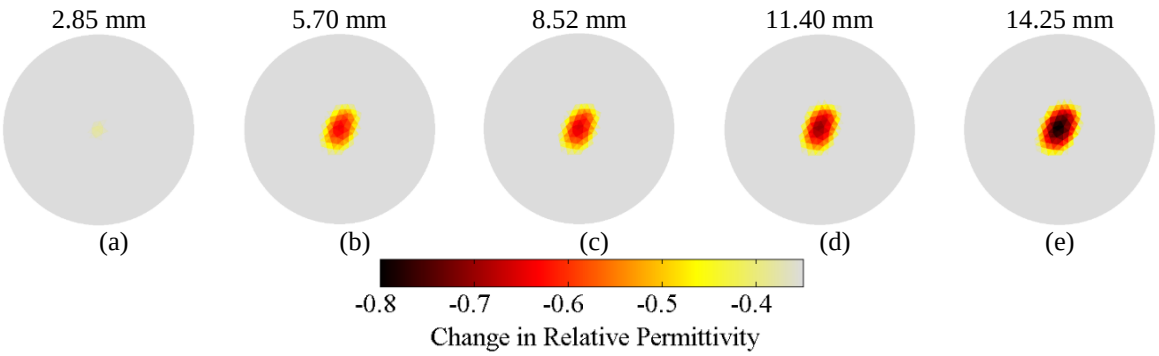

Figure 5.36 ~ 35-mm-long fracture was introduced along the longitudinal direction of the OIP surrogate, and its depth was gradually increased from its pristine state to ~ 14.25 mm at ~ 2.85-mm increments. The corresponding change in electrical permittivity with respect to the pristine state are shown for (a) 2.85, (b) 5.70, (c) 8.52, (d) 11.40, and (e) 14.25 mm, respectively.

was able to successfully capture the location and gradual changes in electrical permittivity due to the increase in fracture depth, it was observed that fracture size was overestimated, especially since the ECT results show a decrease in electrical permittivity over a larger area than the actual size of the fracture. This undesirable effect was likely due to the inherent smoothing effect of the regularization technique employed while solving the inverse problem. Furthermore, the reconstructed images also suffer from poor resolution, where the exact shape and size of the fracture were not clearly identified.

5.3.4.5 ECT Image Reconstruction Enhancement

In order to overcome the aforementioned shortcomings concerning ECT image accuracy and resolution, an LRT image reconstruction algorithm was developed and implemented [53]. Only the region corresponding to the area of the Sawbone was reconstructed to monitor fracture propagation near the bone-prosthesis interface. Figure 5.37a describes the dimensions of the "limited region" considered (*i.e.*, the area surrounding the OIP surrogate). The main objective of LRT is to enhance the imaging performance of the inverse algorithm by limiting the reconstruction region to a particular zone where changes in electrical permittivity are expected to occur. In doing

so, the number of unknown image pixels can be significantly reduced with LRT imaging, thereby reducing the ill-posed-ness of the inverse problem as compared to conventional ECT image reconstruction algorithms.

For the ECT sensing region considered in this study (Figure 5.37a), the original FE mesh constituted 4,020 linear triangular elements (Figure 5.37b), among which 393 were used for LRT reconstruction (Figure 5.37c). Using the same sets of data as those presented in Figure 5.36, the LRT algorithm was employed for reconstructing higher resolution ECT images, which are shown in Figure 5.38 First, it can be observed from Figure 5.36 that the ECT results are of higher resolution and accuracy as compared to Figure 5.36. Second, gradual shape changes in the reconstructed electrical permittivity maps were observed near the location of the fracture, and these corresponded to the depth of the fracture increasing. Finally, the shape of the change in electrical permittivity also resembled the actual cross-sectional shape of the fracture. In this case, *PE* and *AE* were calculated and compared to these of the full region tomographic (FRT) images (*i.e.*, Figure 5.36) and shown in Figure 5.39. It can be observed from Figure 5.39a that by using LRT, *PE* was significantly reduced to ~ 0.45 mm from ~ 5 mm. Figure 5.39b shows that *AE* is almost equal to 1 in case of LRT images for all the crack sizes. Overall, the conclusion is that LRT can be used to generate high-resolution ECT images for detecting the shape and size of fractures occurring near the bone-prosthesis interface.

5.4 Summary and Conclusions

In this chapter, a noncontact, noninvasive, capacitance-based tomographic imaging technique was proposed for monitoring OIP-related issues. First, ECT was implemented to image the cross-section of a lamb shank, to demonstrate its potential for imaging tissue and bone.

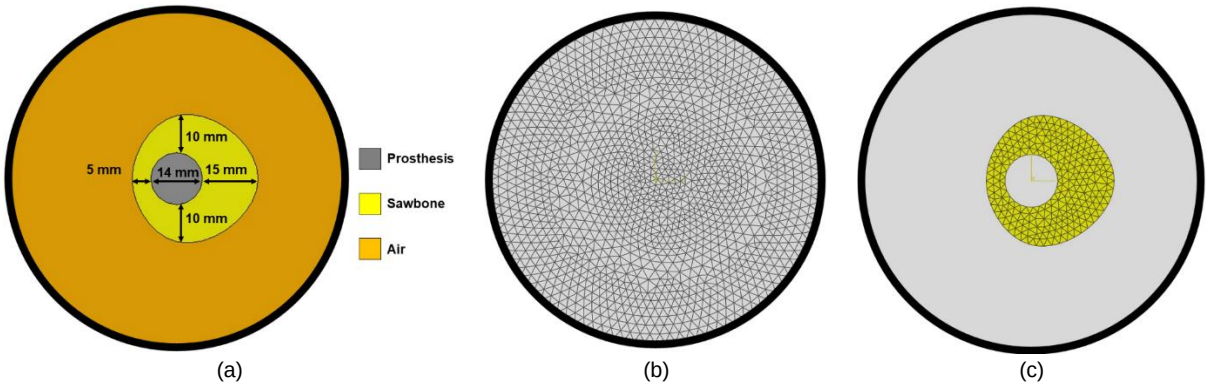

Figure 5.37 (a) The OIP surrogate was placed in the middle of the ECT electrode array, and the dimensions of the OIP surrogate are shown. (b) The entire ECT electrode array was modeled by FEM and discretized using linear triangular element. (c) The elements corresponding to the OIP surrogate was considered for image reconstruction by LRT.

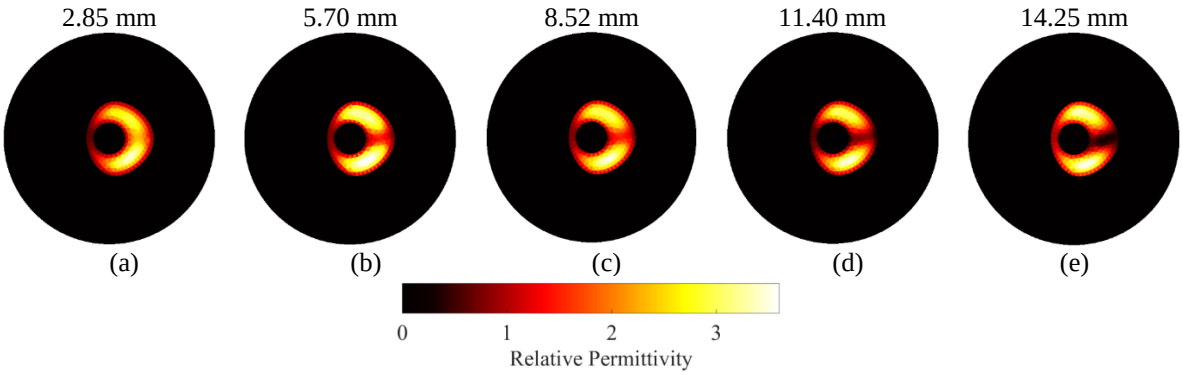

Figure 5.38 Electrical permittivity distributions corresponding to different crack depths (*i.e.*, (a) 2.85, (b) 5.70, (c) 8.52, (d) 11.40, and (e) 14.25 mm) obtained by solving the LRT algorithm are shown.

As infection due to various microorganisms change the localized pH of human tissue, second, an MWCNT-PANI/latex thin film whose electrical permittivity was sensitive to pH was designed and fabricated. A parallel-plate capacitor test arrangement was devised, and the film's capacitance was measured as it was exposed to different pH. It was found that its electrical permittivity increased as the film was exposed from pH 1 to 13 buffer solutions. Since the objective was to detect and monitor subcutaneous infection, direct probing was avoided, and ECT was employed. The system

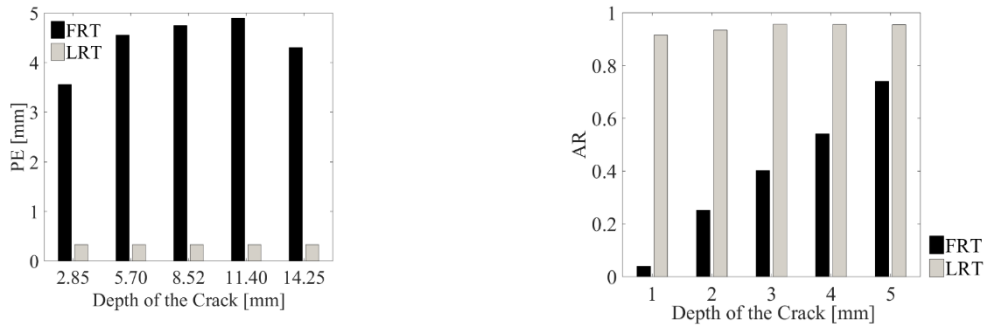

(a) (b)

Figure 5.39 (a) *PE* and (b) *AE* were compared for LRT and FRT images.

was validated for identifying, in a noncontact fashion, the location of aluminum rods placed inside the sensing domain defined by a circular ring of noncontact electrodes. Thereafter, different replicas of an OIP was created, and a pH-sensitive MWCNT-PANI/latex thin film was spray-coated onto the rod. To simulate infection occurring at the tissue-prosthesis interface, the prosthesis phantom was exposed to different pH buffer solutions. ECT was then used to interrogate the system and to reconstruct the spatial permittivity maps. The experimental results showed that ECT successfully identified the location of the prosthesis phantom, as well as changes in permittivity due to exposure of its pre-coated film to different pH.

Third, to enhance the resolution of the reconstructed images, a RECT measurement technique and algorithm was developed and implemented. Furthermore, RECT was combined with an LRT algorithm to further enhance the resolution of the reconstructed permittivity images. It was found that the resolution of the reconstructed ECT images can be significantly enhanced using RECT-LRT, where the results identified different pH states at the tissue-prosthesis interface.

Fourth, ECT was also investigated for monitoring the strain and deformation states of OIP. To achieve this goal, passive nanocomposite thin films, whose electrical permittivity changes in response to applied tensile and compressive strains, were designed as a coating for OIP implants.

The nanocomposite thin films' electromechanical responses were characterized. It was found that patterning the film to form alternating strips of films and insulating coatings enhanced strain sensitivity. These films were then deposited onto OIP phantoms and subjected to both uniaxial and bending tests, while ECT was used to measure their strain-induced permittivity changes in a noncontact manner. Not only did the films enable noncontact strain monitoring, but it was also found that the patterned film exhibited ~ 4 times higher strain sensitivity. The patterned film could not only detect uniaxial strains, but bending tests also revealed that it could simultaneously monitor and localize tensile and compressive strains that developed on opposite faces of the test specimens. The results showed that permittivity varied linearly through the thickness of the specimen in a similar manner as one would expect for a cantilevered beam under bending. These results successfully validated noncontact strain sensing and open up new avenues for ECT to be used in conjunction with passive nanocomposite thin films for monitoring the strain-states of OIP.

Fifth, ECT was also implemented as an imaging technique for monitoring OIP loosening and bone fracture occurring near the bone-prosthesis interface. Several laboratory-based tests were performed using OIP surrogates made using plastic or metallic rods and Sawbone femurs. First, prosthesis loosening tests were performed by gradually pulling out the OIP surrogate from the Sawbone while ECT interrogated the system. The change in dielectric property due to prosthesis loosening was successfully captured by ECT. Second, ECT was also applied for detecting and monitoring bone fracture propagation near the bone-prosthesis interface. The results showed that ECT was able to detect the change in electrical permittivity due to increases in both the length and depth of fractures. Two image evaluation metrics were defined and used to evaluate the quality of the reconstructed images obtained from ECT. To enhance the resolution of the reconstructed images, an LRT algorithm was developed and implemented. These two metrics were also used to

compare the accuracy of the reconstructed images obtained by FRT and LRT for crack depth monitoring. It was found that the resolution of the reconstructed ECT images can be dramatically enhanced, where the results correctly identified the shape and depth of longitudinal fractures in the Sawbone. In the near future, actual bone specimens and *in vivo* tests will be performed to better characterize the ability of ECT to detect prosthesis loosening and bone fracture in more realistic conditions.

Although this chapter mainly demonstrates the application of ECT for OIP monitoring, this study can be extended for noncontact strain mapping and subsurface corrosion sensing for structures. Additionally, being a noncontact, subsurface imaging tool, ECT can also be applied for subsurface damage monitoring in structures. However, the circular geometry of the ECT electrode array could potentially limit its application as an SHM/ NDE tool for large scale structures. Chapter 6 shows how the geometry of the ECT electrode array can be modified to make it suitable for subsurface scanning of the large-scale structures.

This chapter is a partial reprint of the materials as it appeared in Noncontact Electrical Permittivity Mapping and pH-Sensitive Thin Films for Osseointegrated Prosthesis and Infection Monitoring, S. Gupta and K. J. Loh, 2017; Monitoring Osseointegrated Prosthesis Loosening and Fracture using Electrical Capacitance Tomography, S. Gupta and K. J. Loh, 2018; Noncontact Strain Monitoring of Osseointegrated Prostheses, S. Gupta, H-J. Lee, K. J. Loh, M. D. Todd, J. Reed, and A. D. Barnett, 2018; and Enhancing the Imaging Performance of Electrical Capacitance Tomography for Monitoring Osseointegrated Prostheses, S. Gupta, T. Zhang, and K. J. Loh, 2019.

CHAPTER 6 PLANAR ARRAY CAPACITIVE IMAGING FOR SUBSURFACE DAMAGE DETECTION IN COMPOSITE STRUCTURES

6.1 Introduction

In this chapter, the geometry of the ECT electrode array is modified from circular to a planar arrangement so that it can be used by the technicians as a hand-held instrument to rapidly assess the subsurface condition of the large-scale aerospace structures. As mentioned in Chapter 1, CFRP composites have become increasingly more popular for aerospace structures, mainly due to their high specific strength as compared to metals [11]. In particular, CFRP composites are fabricated from stacked fiber fabrics (with fibers oriented in a certain direction in each layer) and then infused with epoxy, which can be performed by wet layup or by vacuum bagging process. Although CFRP composites derive their unique mechanical properties from their unique structure, their structural anisotropy and dissimilar phases of its constituents (*i.e.*, fibers and epoxy matrix) can lead to the formation of unique damage modes (*e.g.*, delamination) due to low-velocity impact as described in Chapter 1. The growth of undetected, subsurface delamination under external loads can ultimately cause catastrophic structural failure [219]. Therefore, regular inspection and routine maintenance of CFRP composite structures are needed in order to ensure structural integrity and safety.

Besides visual inspections and traditional sensors [220], various nondestructive condition monitoring techniques have been developed and implemented for CFRP structures' condition assessments. Ultrasonic inspection is considered as the gold standard of inspection methods. In short, an ultrasonic transducer propagates concentrated, high-energy acoustic waves through the thickness of a component, where the wave can interact with hidden damage features and generate

a change in measured response [221]. Here, C-scanning can be employed to obtain a spatial map of surface and subsurface damage features in the composite specimens [222]. However, the structural component needs to be completely disassembled and fully immersed in water for C-scanning, which is often not practical, too costly, or impossible to perform in the field. Laser-generated ultrasound can be employed to overcome the need for immersing structures in a water bath for C-scanning [223]. However, the amplitudes of laser-generated excitations are generally small, and low SNR can be an issue. On the other hand, the eddy current method identifies damage by measuring the electrical impedance of the composite structure [224]. Radiographic imaging and transient thermography are two other emerging methods that have been implemented for CFRP composite structures' condition assessment. In order to enhance image resolution, radiography often requires a liquid penetration (*e.g.*, zinc iodide solution) in the composite, which requires a break in the structural surface to allow thorough penetration of the liquid [225]. The liquid penetrant should be selected in such a way that it does not adversely affect the properties of the CFRP composite. Thermography, on the other hand, uses an infrared camera to visualize the temperature distribution of a structural component, where localized changes in temperature can be due to damage. Although quite effective, thermography requires that the structure be uniformly heated, which is difficult to attain in the field, its sensitivity may change as a function of surface conditions. Despite the advantages of these NDE techniques as compared to visual inspection, they can still be time-, labor-, and cost-intensive to realize in the field.

Therefore, the objective of this work is to devise a noncontact, portable, and NDE tool that can be used by technicians for *in situ* subsurface damage characterization in large composite structures. The proposed method works based on the principle of ECT, where the 3D distribution of electrical permittivity of a sensing region can be estimated by interrogating it with electric field

excitations [226]. Unlike conventional ECT that uses electrodes placed in a circular array to interrogate the region enclosed by these electrodes, this study employs adjacent electrodes arranged in a single plane. The planar electrode array can be placed directly above and be used to interrogate a composite panel or specimen. It is hypothesized damage in composite would cause localized changes in electrical permittivity, which can be noninvasively captured using the proposed planar ECT system.

This chapter employed a numerical as well as experimental approaches to demonstrate the feasibility of the planar ECT system for damage detection. For the numerical study, FE models of composite structures (with and without damage) and the ECT electrode array were created. Damage was introduced by intentionally perturbing the electrical permittivity at specific locations within the composite structures. After computationally validating the subsurface damage detection in composite specimens, experimental studies were employed to demonstrate the feasibility of the proposed system for characterizing subsurface damage in composites.

6.2 Planar ECT Background

As mentioned in Chapter 2, ECT is a soft-field imaging technique that can reconstruct the distribution of dielectric properties of a region of space using a limited number of boundary capacitance measurements. In conventional industrial ECT systems, electrodes are arranged in a circular array. An AC electrical excitation is applied at one electrode, while the remaining electrodes are grounded. This allows the AC electric field to propagate through the sensing domain or area enclosed by the electrodes, as shown in Figure 2.4. The mutual capacitances between the excitation and each grounded electrode are recorded for all possible combinations of electrode

pairs. This set of raw data is then used as inputs to solve the ECT inverse problem and to reconstruct the electrical permittivity of the sensing domain.

Despite the advancements of the traditional ECT system [128, 129, 143-145], it should be clarified that the specimen or structure of interest needs to be placed in the sensing domain to be imaged. However, this requirement becomes challenging if ECT was to be used for nondestructive inspection of aerospace structures, where the majority of its structural components are large and cannot fit between a circular array of electrodes. In fact, a handheld, planar, electrode array can facilitate the inspection of large aerospace systems. The vision is that technicians can scan different areas of a structure and directly visualize, in real-time, structural features and damage within the structural component.

Therefore, and in this study, a planar ECT system is proposed as a 3D subsurface imaging tool for detecting damage in composite structures. In fact, there have been growing interests over the past few years in a planar capacitive imaging system for applications such as security scanning [227]. For this system, the electrodes are arranged to form a rectangular planar array. The electrode array shown in Figure 6.1 can then be used to interrogate structural components or, in general, the region of space above the array. Similarly, the region below this plane of electrodes is not of interest. Thus, to account for this and to reduce the effects of external EM wave interference with the excitation filed, a grounded metallic shield can be attached to the opposite face of the electrode array shown in Figure 6.1.

Similar to conventional ECT as well as other tomographic imaging methods, the planar ECT spatial permittivity imaging algorithm also consists of the forward and inverse problems. First, the forward problem determines the mutual capacitance between the excitation and

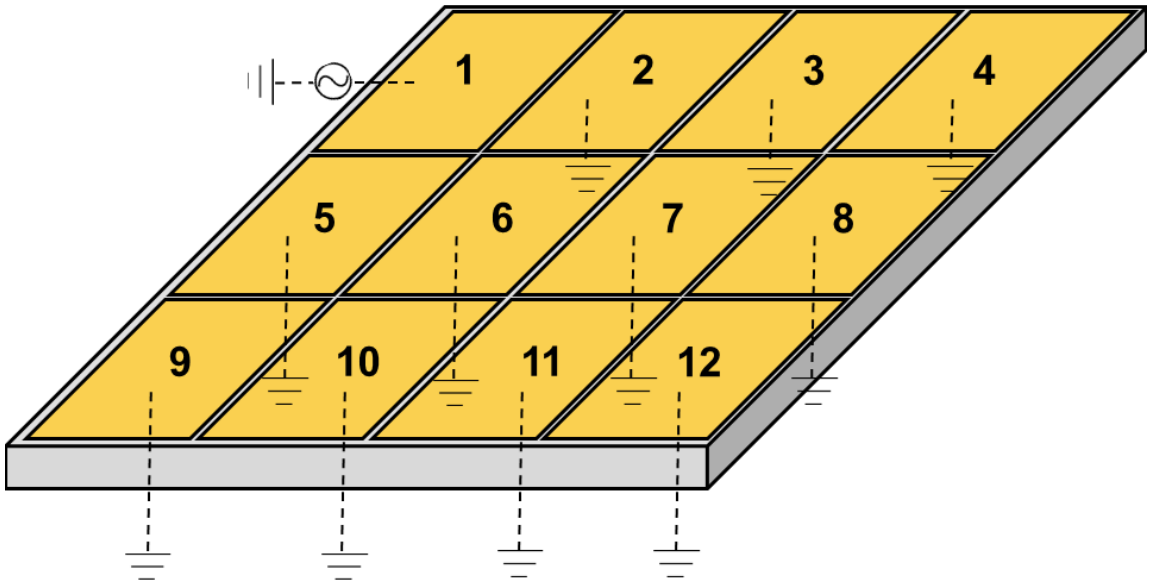

Figure 6.1 For planar ECT systems, electrodes are arranged on a rectangular planar surface and each of them are excited with an AC signal and the other electrodes remain grounded for ECT interrogation.

measurement electrodes, given that the 3D electrical permittivity of the region of space near the electrode array is known *a priori*. Second, the inverse problem aims to reconstruct the 3D distribution of electrical permittivity using the measured set of boundary capacitance responses. The theoretical formulation of the planar ECT is described in the next sections.

6.2.1 Mathematical Modeling

As mentioned earlier, the ECT forward problem calculates the mutual capacitance between excitation and measurement electrode pairs. Here, an electrode in the planar ECT is excited with an AC signal, while all other remaining electrodes are grounded, which is illustrated in Figure 6.1. By doing so, an electric field is propagated through the 3D medium surrounding the electrodes (Ω). Electric field (u) propagation through Ω can be approximated as an electrostatic problem. If steady-state approximation can be implemented, the diffusion of electric charge through Ω can be mathematically explained by the 3D Laplace's equation:

$$\nabla \cdot (\varepsilon \nabla u) = 0 \tag{6.1}$$

where ε is the electrical permittivity distribution inside Ω. Proper boundary conditions should be implemented to achieve the most accurate solution of this second-order partial differential equation:

$$u = V \tag{6.2}$$

where V is the magnitude of applied voltage at the excitation electrode. For all other electrodes, V is set to zero. Finite element modeling is often adopted to solve equation 6.1 using boundary conditions stated in equation 6.2. The corresponding weak form of equation 6.1 can be derived by multiplying it with a sufficiently smooth test function (v) and thereafter integrating it over the entire domain Ω:

$$\int_{\Omega} \varepsilon \nabla u \cdot \nabla v dx^3 = 0 \tag{6.3}$$

In this study, Ω was discretized using four node-linear tetrahedral elements. Upon implementation of the boundary conditions (equation 6.2), produces a set of linear equations, which is expressed in matrix form as follows:

$$KU = I \tag{6.4}$$

where K is the stiffness matrix of the system, u, contains the values of electric potentials at the nodes, and I is the force vector, which is obtained from the specified boundary conditions. Once U is evaluated, one can utilize equation to estimate the mutual capacitance ($C_{i,j}$) between the i^{th} excitation and j^{th} measurement electrodes:

$$C_{i,j} = \frac{1}{V}\int_{e_j} \varepsilon \frac{\partial u_i}{\partial n} dx^2 \qquad i=1:l\ ;\ j=i+1:l \tag{6.5}$$

where e_j is the area corresponding to the j^{th} electrode, u_i is the solution of the forward problem when the i^{th} electrode is used for excitation, n is the unit inward normal to the electrode plane, and l is the total number of boundary electrodes. FD technique described in Section 2.2.2.3 was adopted to numerically evaluate the integration in equation 6.1 over the area of the sensing electrodes. Although the equations 6.1 to 6.3 are similar to the traditional ECT, the main difference between the forward problem of traditional ECT and planar ECT is that Laplace's equation needs to be solved for 3D space instead of 2D to capture the 3D electrical field distribution.

Although the implementation of the planar ECT forward problem is different than the traditional ECT forward problem, the same inverse algorithm described in Sections 2.3.1.2 and 2.3.1.3, can be implemented for planar ECT image reconstruction. In this study, the iterative GN algorithm and single-step NOSER algorithm were used for Planar ECT image reconstruction.

6.3 Numerical Simulations and Results

One of the primary objectives of this study is to use numerical simulations to assess the sensing and damage detection performance of a planar ECT system. In general, the simulation began with the initial assumption that the entire sensing region was filled with air (ε = 1). The planar electrode array, which was 250 × 250 × 2 mm^3, consisted of 4 × 3 = 12 rectangular electrodes that were 73.33-mm-long and 53.75-mm-wide. The electrode array is illustrated in Figure 6.2a, which also shows the numbering scheme employed for the electrodes. In order to allow an electric field to propagate through the sensing region in the FE model, one electrode was set to a higher potential of 1 V, while the remaining electrodes were grounded. The resulting

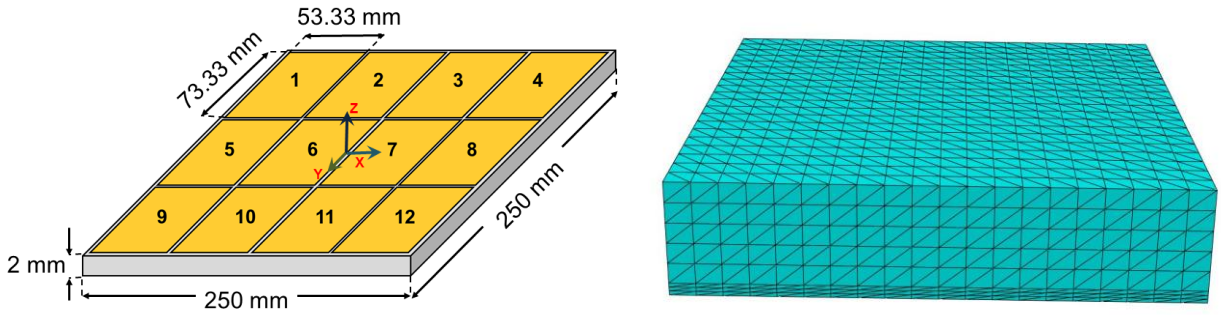

(a) (b)

Figure 6.2 (a) 12 electrodes were arranged on a 2-mm-thick plate in a 4 × 3 rectangular array. The dimension of entire electrode array and the Cartesian coordinate system considered for FE modeling are shown. (b) The entire sensing domain is discretized using linear tetrahedral elements.

mutual capacitance between the excitation and other sensing electrode pairs were calculated using the aforementioned ECT forward problem. The FE model of the sensing region and electrode array is shown in Figure 6.2b. In general, for N number of electrodes, $N \cdot (N\text{-}1)$ capacitance measurements are possible. However, only independent measurements were used for permittivity reconstructions, which is equal to 66 for this 12 electrode system. Thus, given any 3D permittivity distribution, the ECT forward problem is solved to determine the 66 electrode capacitance responses for all the different excitation-measurement patterns. Figure 6.3a shows the set of capacitance results when each of the electrode was excited with a 1 V signal and that the entire sensing domain was filled with air ($\varepsilon = 1$). Furthermore, Figure 6.3b shows that the GN iterative algorithm could take on the order of 80 to 100 iterations to converge to the error threshold of 0.001% for this specific case. The rate of change in error ratio exponentially decays with the number of iterations, and it can be observed from Figure 6.3b that negligible changes in error threshold occurred after ~ 80 iterations.

6.3.1 Structural Feature Detection and Localization

The first planar ECT numerical case study sought to validate its ability to identify and localize structural features (*e.g.*, cylinders) in the sensing region but without making contact with

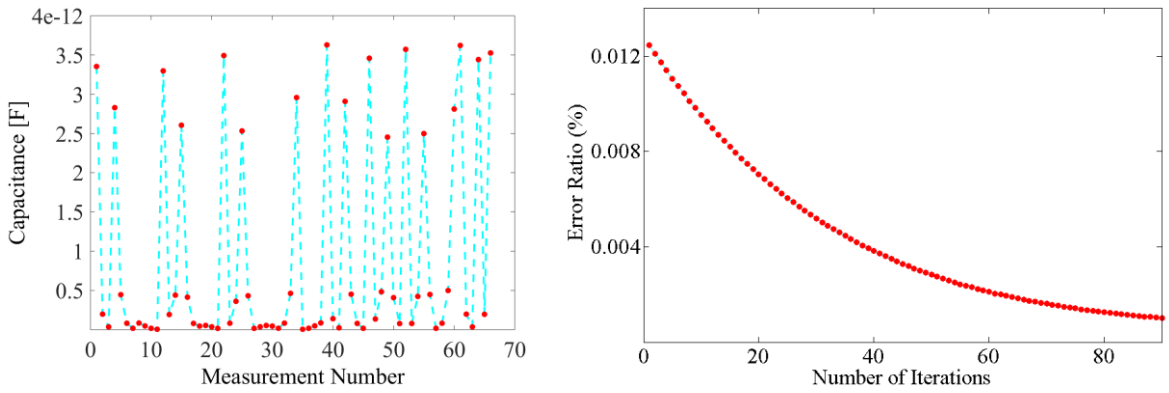

(a) (b)

Figure 6.3 (a) Estimated independent mutual capacitances between excitations and sensing electrode pairs are shown when 1V electrical signal is used for excitation and the entire sensing domain is filled with air. (b) The plot shows the trend of convergence of the inverse problem and the number of iterations required to achieve the specified threshold limit.

the electrodes. Cylinders of 50 mm in diameter and 45-mm-tall were defined in the FE model and placed in the sensing region, as shown in Figure 6.4. The electrical permittivity of the cylinders (*i.e.*, C1, C2, C3, and C4) were set to a slightly higher value ($\varepsilon = 2$), while the sensing region was assumed to be filled with air ($\varepsilon = 1$). Doing so simulated the inclusion of foreign objects or structural features of different electrical characteristics than air in the sensing region.

For each case shown in Figure 6.4, the ECT forward problem was solved to estimate the mutual capacitance responses when electric fields were propagated between the various electrodes. It should be mentioned that these capacitance values were assumed to be what one would obtain if a planar ECT experiment was performed. However, to further add realism to this simulation study, the computed capacitance results were purposefully corrupted with Gaussian white noise (*i.e.*, 1% of the median of all computed capacitances responses). This was done to simulate the noise present during actual experimental measurements. The corrupted capacitance responses were then used as inputs to the ECT inverse problem to estimate the electrical permittivity distributions of the entire sensing region. Once the inverse problem was executed and that *e* (equation 2.74) was at or below the 0.001% criterion, the ECT algorithm then outputs the reconstructed 3D permittivity

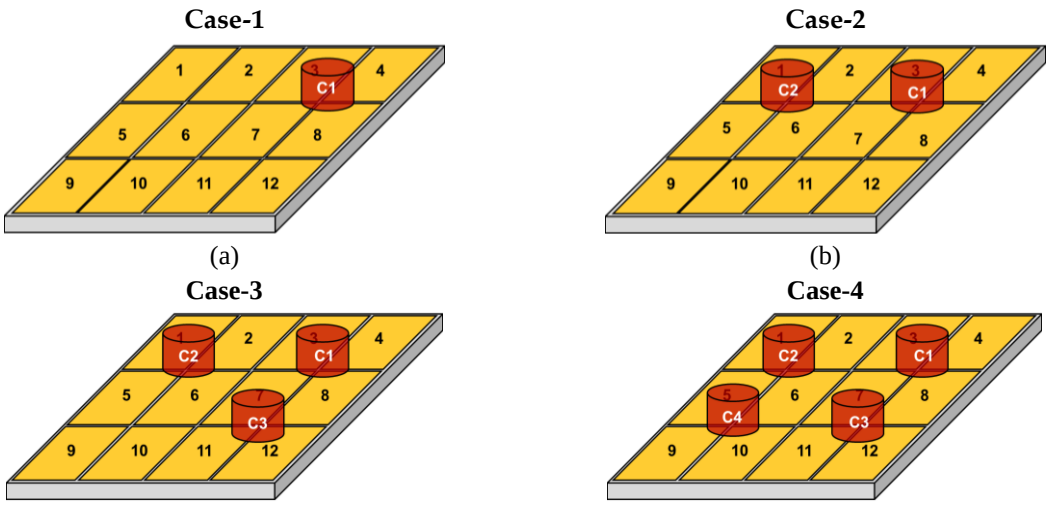

Figure 6.4 (a) One, (b) two, (c) three, and (d) four cylindrical objects with $\varepsilon = 2$ were modeled as the foreign objects in the sensing region.

distribution of the sensing domain. In order to best visualize these 3D ECT results, sections of the sensing domain were cut at different depths and locations to generate 2D permittivity images at different locations. These 2D visualization planes or sections are illustrated in Figure 6.5, and their equations are given in Table 6.1. The sections were chosen such that they pass through the centers of the cylinders.

Figure 6.6 shows the various 2D sections of the 3D ECT results corresponding to the four different cases (Figure 6.4). In general, it can be seen from Figure 6.6 that the shapes, sizes, and locations of the cylindrical objects were successfully identified. First, in Figure 6.6a, the X1 plane result shows that nothing was observed in Case-1 and Case-2 since X1 does not pass through C1 and C2. C3 and C4 were clearly observed in Case-3 and Case-4, respectively. Second, the same conclusion can be drawn for X2 and Figure 6.6b, where it successfully identified C1 and C2 for Case-1 and Case-2, respectively. Even as more cylinders were introduced to the model, the X2 ECT results remained fairly consistent and stable between Case-2 to Case-4. For all these cases, the height of the cylinder was captured fairly accurately. Finally, Figure 6.6c shows the Z section;

Table 6.1 Details of structural feature detection and localization numerical study

Cylindrical Objects				Visualization Sections	
Name	***x* coordinate**	***y* coordinate**	***z* coordinate**	**Plane**	**Equation**
C1	59.345	-78.33	28	**X1**	$y = 59.345$
C2	-59.345	-78.33	28	**X2**	$y = -59.345$
C3	59.345	78.33	28	**Z**	$z = 28$
C4	-59.345	78.33	28		

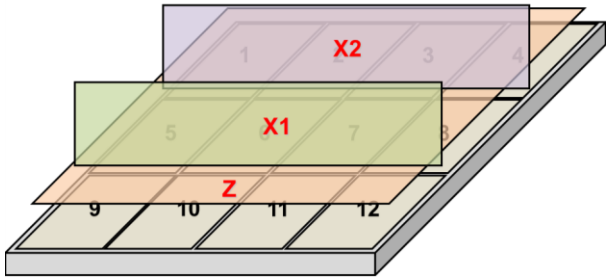

Figure 6.5 X1, X2, and Z planes were considered for the visualization of spatial distributions of reconstructed permittivity.

the locations and cross-sections of the cylinders were clearly captured. Besides successfully identifying the locations of the cylinders, one can observe that the amplitude of the reconstructed permittivity values (of the cylinders) closely matched their theoretical electrical permittivity of 2. Overall, these results demonstrated the validity of the planar ECT forward and inverse problems.

6.3.2 Delamination in Composite Panels

With the planar ECT system validated in the previous section, the objective of this second numerical simulation study was to investigate a more realistic system. Here, a $250 \times 250 \times 50$ mm^3 composite panel was modeled (with an electrical permittivity of 5) and positioned on top of the ECT planar electrode system, as shown in Figure 6.7. Note that a 1 mm air gap was included between the composite panel and ECT electrode array. Furthermore, the damage was also

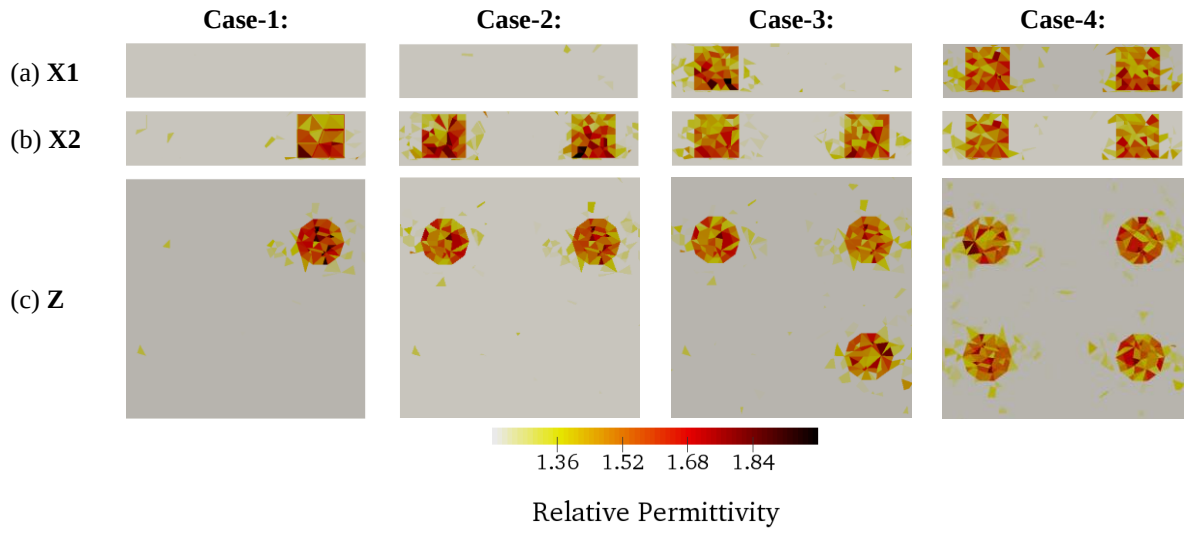

Figure 6.6 The planar ECT inverse problem was solved using data obtained for four different cases. 2D ECT images were obtained from the 3D ECT results by visualizing planar sections corresponding to the (a) X1, (b) X2, and (c) Z planes.

introduced to this composite panel by modeling a 50 × 50 × 3 mm^3 delamination in the center (Figure 6.7). The electrical permittivity of the delamination layer was assigned to be 1, where the delaminated portion was filled with air. For convenience, the center of the delaminated layer coincided with the center of the planar ECT electrode array. Then, similar to the previous numerical simulation study discussed in Section 6.3.1, the ECT forward problem was first executed to estimate the capacitance response at all electrodes and corresponding to different electric field propagation patterns. The estimated mutual capacitances were subsequently corrupted with Gaussian white noise and used as inputs to solve the 3D ECT inverse problem.

In order to visualize the 3D reconstructed permittivity map of the region above the electrode array, different 2D visualization planes were defined as shown in Figure 6.8. The equations of the planes are given in Table 6.2, where the origin of the coordinate axis is at the center of the composite panel and delaminated layer. Thus, the Z1, Z2, and Z3 planes considered different vertical distances away from the ECT planar electrode. Specifically, the Z2 plane passes

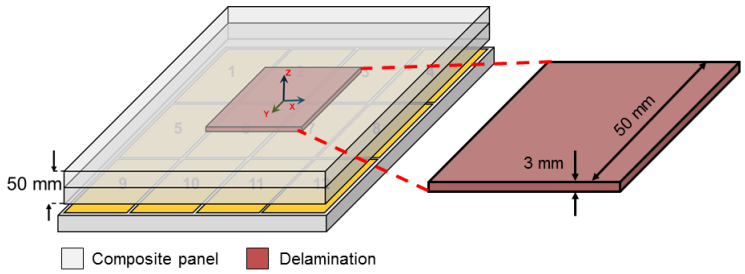

Figure 6.7 Delaminated composite panel was modeled by embedding a square-shaped 3 mm-thick layer into the composite laminate with different dielectric property.

through the center of the delaminated layer, while the Z1 and Z3 planes did not intersect the delamination. It can also be seen from Figure 6.8 that the X and Y planes cross the origin and intersect the delamination.

Figure 6.9 shows the different 2D planar cuts of the reconstructed 3D electrical permittivity distribution of the delaminated composite panel. First, Figures 6.9a, 6.9b, and 6.9c show the electrical permittivity distributions corresponding to the Z1, Z2, and Z3 planes, respectively. As expected, Figure 6.9a and 6.9c show a uniform electrical permittivity of ~ 5, since these planes do not intersect the delaminated layer and only consists of the pristine composite panel at these heights. On the other hand, Figure 6.9b clearly shows a square region in the center that corresponds to the delaminated region where the electrical permittivity is ~ 1. The shape and size of this square region are comparable to the actual delamination. Similarly, for the rest of the ECT permittivity map for the Z2 plane, the electrical permittivity is ~ 5 due to the composite panel. Second, when considering the cross-sectional visualization planes (*i.e.*, the X and Y planes), the thickness of the delamination was clearly captured, as shown in Figure 6.9d and 6.9e. However, the resolution of these reconstructed electrical permittivity images were a bit poor, which was hypothesized to be caused by the combined effect of the limited number of electrodes, noise, and the limited penetration depth of the electric field, to name a few. Future work will investigate a more optimal electrode array design that is tailored to detecting certain resolutions of electrical permittivity and

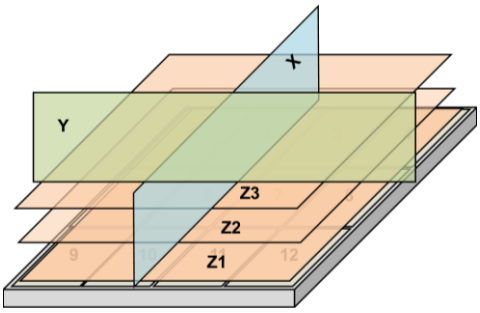

Figure 6.8 Different sections were considered at different locations of the sensing region for the visualization of the delamination in the composite panel.

Table 6.2 Visualization sections for delaminated panel

Visualization Plane	Equation
Z1	$z = 5$
Z2	$z = 25$
Z3	$z = 45$
X	$x = 0$
Y	$y = 0$

spatial features. Nevertheless, the results shown in Figure 6.9 successfully validated the proposed ECT measurement technique and algorithm, in a computational sense, for noncontact NDE of composite structural components.

6.4 Experimental Details

6.4.1 Experimental Setup

After successfully validating the planar ECT algorithm through computational studies, this section aims to experimentally validate the proposed planar ECT system. A planar electrode array was assembled in the laboratory. A 73 × 57 × 3 mm^3 polylactic acid (PLA) rectangular plate was 3D-printed using an Ultimaker 3+. A total of 12 copper tape electrodes, each with a dimension of 15 × 15 mm^2, was affixed onto the PLA plate. The opposite surface of the plate was wrapped with copper tape and grounded to minimize the influence of external EM interference. Electrical connections were achieved by soldering RG-174 cables to the electrodes and external shield. The schematic of the electrode array is shown in Figure 6.10.

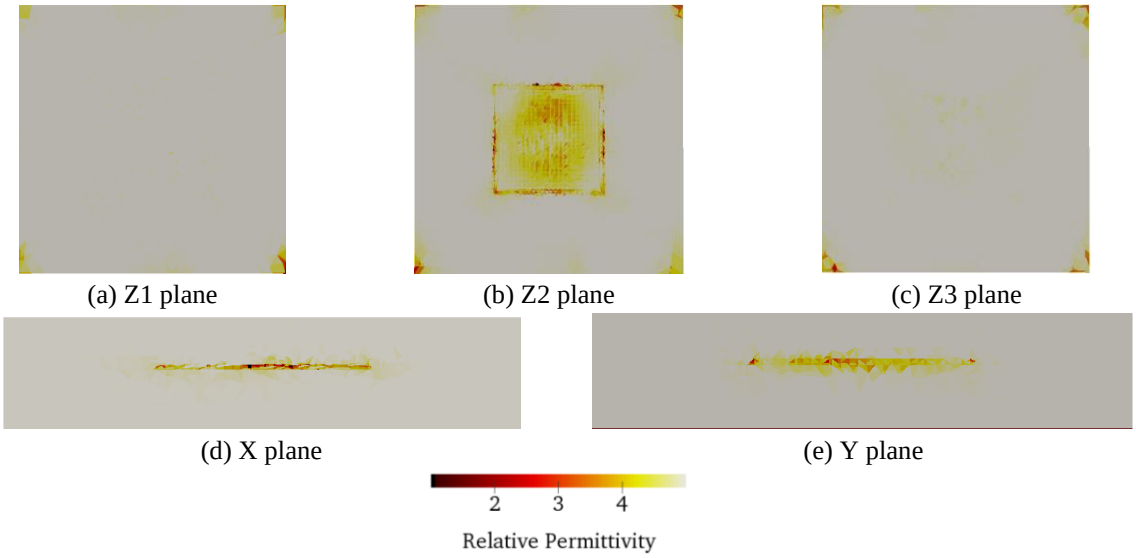

Figure 6.9 (a), (b), and (c) illustrate electrical permittivity distribution at Z1, Z2, and Z3 plane. (d) and (e) show the reconstructed permittivity distribution at X and Y plane respectively.

6.4.2 Planar ECT Validation

In order to validate volumetric permittivity mapping using the proposed planar ECT system, a series of experiments were performed by placing a 15 × 15 × 3 mm^3 3D-printed PLA block at the center of the sensing region. First, the PLA specimen was placed at the center of the sensing region as shown in Figure 6.11. A set of boundary capacitance measurements was recorded and used as inputs to the ECT inverse problem. To minimize the computational effort of the 3D inverse problem, only the 3-mm-thick rectangular region above the electrode plane was considered for volumetric permittivity reconstruction. It should be mentioned that, prior to placing any object in the sensing region, a baseline set of capacitance measurements was recorded, and the change in electrical permittivity due to the introduction of the foreign object with respect to the recorded baseline was reconstructed.

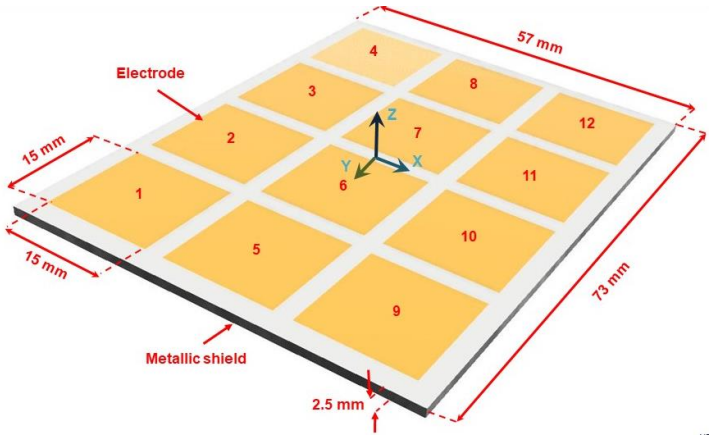

Figure 6.10 A planar ECT system with 12 electrodes arranged in a 4 × 3 rectangular array and deposited on a 2.5-mm-thick PLA plate is shown. The dimensions of the entire electrode array, the size of the electrodes, and the cartesian coordinate system considered for image visualization are indicated.

6.4.3 Subsurface Damage Detection Validation

The objective of the second set of tests was to validate subsurface damage detection using 3D-printed rectangular PLA specimens (30 × 30 × 5 mm^3) with purposefully introduced internal defects. Here, three PLA specimens with internal voids of different thicknesses (t) (*i.e.*, 2, 3, and 4 mm) were fabricated. The footprint of the delamination-like defects (15 × 15 mm^2) was kept the same for all three specimens. The specimens were then placed at the center of the planar ECT electrode array. Then, ECT measurements were recorded corresponding to each damage case, and the changes in electrical permittivity distribution with respect to an undamaged specimen were determined.

6.4.4 Barely Visible Impact Damage Detection

To validate this technology for NDI of composite structures, a 30 × 30 × 5 mm^3 CFRP specimen shown in Figure 6.12 was subjected to hammer impact and interrogated by the planar ECT system. First, a baseline measurement was recorded by placing the undamaged specimen at the center of the planar ECT electrode array. Thereafter, the specimen was subjected to low-

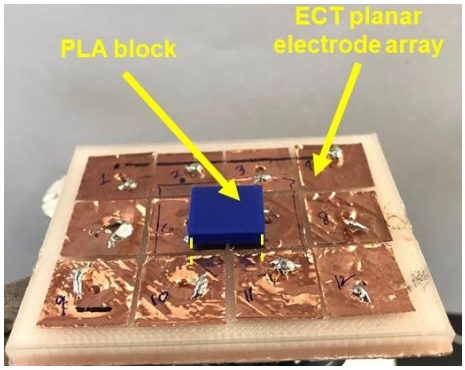

Figure 6.11 A 15 × 15 × 3 mm^3 PLA specimen was placed at the center of the sensing region and subjected to ECT interrogation.

velocity hammer impact, and the damaged specimen was placed at the same location in the sensing domain for ECT interrogation. The change in volumetric electrical permittivity distribution between the undamaged and damaged states was reconstructed.

6.5 Experimental Results

6.5.1 Foreign Object Detection

As mentioned earlier, a series of experiments was carried out to validate the proposed planar ECT system. First, a block was placed at the center of the sensing region (Figure 6.11), and the change in electrical permittivity distribution with respect to a recorded baseline (*i.e.*, nothing placed in the sensing region) was reconstructed. In order to best visualize these 3D ECT results, sections of the sensing domain were cut at different orientations (*i.e.*, X-, Y-, and Z-planes according to the coordinate system shown in Figure 6.11) through the center of the sensing domain to generate 2D permittivity images. The 2D sections of the 3D permittivity maps are shown in Figure 6.12a to 6.12c. It can be observed that a sharp change in electrical permittivity was observed at the center of the sensing region where the PLA specimen was placed. Although the exact shape of the square object was not precisely reconstructed, overall, the shape, size, and location of the

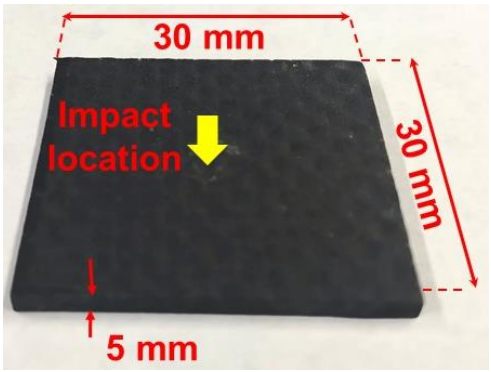

Figure 6.12 A 30 × 30 × 5 mm^3 CFRP specimen was subjected to hammer impact at the center.

specimen were successfully characterized as shown in the X-, Y-, and Z- section plots in Figures 6.12b to 6.12c, and 6.12a, respectively.

6.5.2 Delamination Monitoring

After planar ECT system validation, additional tests were conducted to validate its ability to quantify subsurface delamination in 3D-printed PLA specimens and to see if it was possible to detect changes in electrical permittivity due to these internal defects. Here, 15 × 15 mm^2 square voids of different thicknesses (*i.e.*, 2, 3, and 4 mm) were introduced at the central region of the test specimens during printing. Upon conducting the ECT tests. Three different 2D sections (*i.e.*, X-, Y-, and Z-planes) were considered to better visualize the ECT results.

The ECT results, which are the changes in electrical permittivity distributions with respect to an undamaged specimen, are shown in Figure 6.13. It should be noted that the size of the region of permittivity change and their absolute magnitudes increased in tandem with increasing damage thickness. These results make sense, since the volume of air was increased as the thickness of the delamination-like damage also increased; air also has lower electrical permittivity than PLA, hence the negative change in permittivity at the damage location. From Figure 6.13, it can be seen that the estimated damage sizes were slightly larger than the actual case, and these were most likely

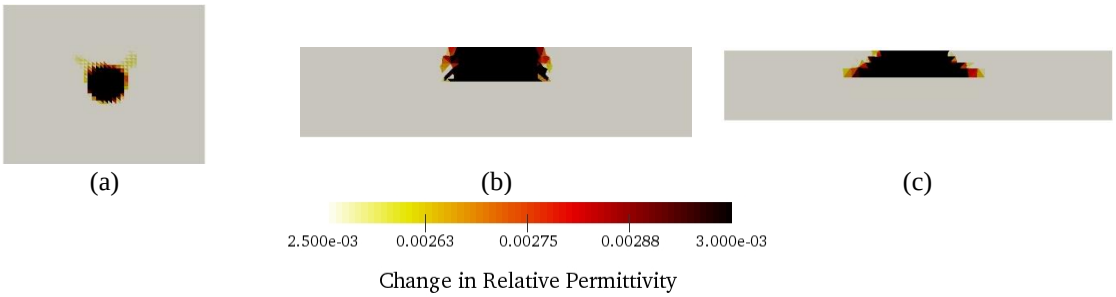

Figure 6.13 (a) Z-, (b), X- and (c) Y-planes taken with respect to the center of the ECT array are plotted to show successful detection of the foreign object in the sensing domain.

due to the resolution of the planar ECT system, which is governed by the number and size of electrodes, strength, and frequency of the AC signals used for ECT interrogations, and the regularization scheme adopted. Overall, Figure 6.14 confirmed the locations and sizes of subsurface delamination-like damage could be detected.

6.5.3 CFRP Impact Damage Characterization

The objective of this final experiment was to validate damage detection in CFRPs using a more realistic test setup. Here, a CFRP specimen was fabricated and subjected to a hammer impact. The planar ECT system was employed to interrogate the damaged specimen, and the change in electrical permittivity distribution (with respect to the pristine specimen) due to damage along the Z-plane is shown in Figure 6.15a. Although damage was not visible on the actual specimen, the reconstructed ECT map clearly indicates a decrease in electrical permittivity in the middle of the CFRP specimen, where it was subjected to impact. The corresponding C-scan image of the damaged CFRP specimen confirmed the presence of subsurface damage at the center and is shown in Figure 6.15b. It can be seen that the damage location identified by C-scan closely matches the region of electrical permittivity changes determined by the planar ECT system. It is hypothesized that impact caused the separation of the carbon fibers from the epoxy matrix, which then created

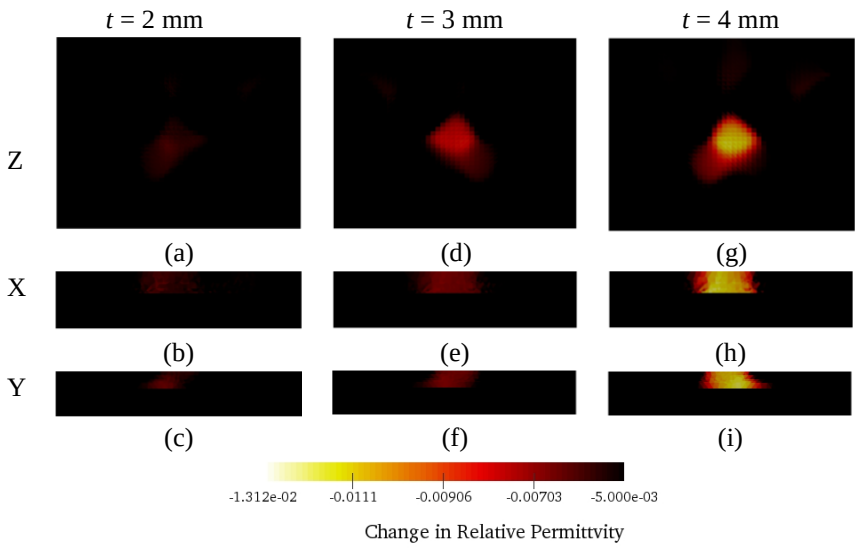

Figure 6.14 The change in permittivity distribution of the (a) to (c) Z-, (d) to (f) X-, and (g) to (i) Y-sections for delamination thicknesses of t = 2, 3, and 4 mm, respectively, are plotted to visualize subsurface damage.

a void or delamination in the specimen. The highly localized void or delamination caused a decrease in electrical permittivity.

Despite this successful validation test, it should be noted that the resolution of the reconstructed ECT image was poor. This could be due to the combined effect of using only a limited number of electrodes, as well as noise and the limited penetration depth of the interrogating electric field, to name a few. Nevertheless, the result shown in Figure 6.15a successfully validated the proposed planar ECT measurement technique and algorithm for noncontact NDI of CFRP-based structural components.

6.6 Summary and Conclusions

In this work, a noncontact, nondestructive, damage detection, and localization method based on ECT was proposed. The goal was to develop a system that could allow technicians to rapidly scan and assess the surface and subsurface conditions of CFRP composite structures. Instead of using conventional ECT systems that rely on a circular array of electrodes, this study

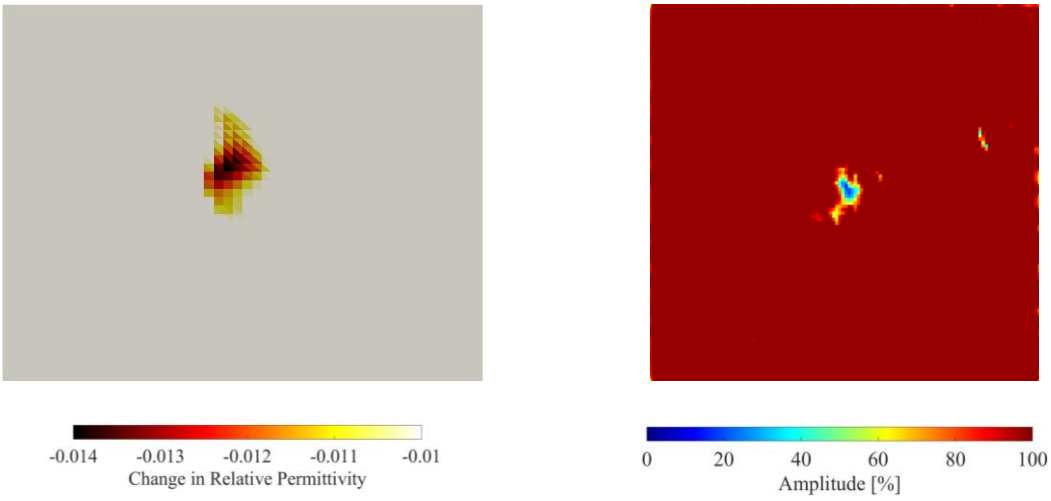

(a) (b)

Figure 6.15 (a) The damaged CFRP specimen was subjected to ECT testing, and the change in electrical permittivity distribution of the Z-section, with respect to the undamaged state, is shown. (b) The amplitude of reflected ultrasonic waves obtained from the C-scan of the CFRP specimen is shown for comparison.

investigated the use of a planar electrode array. This configuration allowed one to scan and probe the subsurface condition of any structural component, as opposed to conventional ECT, that requires the electrode array to surround the component of interest.

As a step towards this goal, first, this study undertook a numerical simulation approach to investigate the performance and feasibility of a planar ECT system. First, the planar ECT forward and inverse algorithms were implemented based on a finite element model framework. Second, two different numerical simulation studies were performed. The first study was focused on validating the planar ECT system, specifically for its ability to identify and localize four cylinders in the sensing region. The second numerical simulation study was based on a composite panel with delamination damage. For both cases, the forward problem was initially executed to estimate the mutual capacitance responses at the electrodes. The capacitance responses were then corrupted with Gaussian white noise and then used as inputs to solve the ECT inverse problem. The results showed that the shapes, sizes, and locations of the cylinders and delamination damage were accurately determined via ECT. In a broader sense, the results showed that the proposed technique

could be used as an NDE tool that has the ability to detect the shape, size, location, and severity of subsurface damage. In the near future, a prototype planar ECT system will be fabricated in the lab to validate its experimental and damage detection capabilities.

Second, for experimental validation, a planar ECT electrode array was assembled in the laboratory. The system was successfully shown to detect the locations, shapes, and sizes of foreign objects placed in the sensing region. Then, the system was employed to detect artificially induced subsurface delamination-like damage in 3D-printed PLA specimens. The results showed that the planar ECT system was able to detect the locations and extents of subsurface damage, where a localized decrease in electrical permittivity at the locations of these defects were observed. Last, for further validation, a rectangular CFRP specimen was subjected to impact and inspected using the planar ECT system. The results again showed that planar ECT was capable of mapping the change in electrical permittivity distribution caused by impact-induced subsurface damage. The ECT result was compared with its C-scan image, and good agreement was found. Future studies will focus on improving and optimizing the design of the planar electrode ECT system for high-resolution imaging.

This chapter is partially reprinted from Planar Array Capacitive Imaging for Subsurface Composite Damage Detection, S. Gupta, H (Eric) Kim, H-J. Lee, H. Kim, and K. J. Loh, 2019; and A planar Array Capacitive Imaging System for Detecting Damage in Composite Structures, S. Gupta and K. J. Loh, 2018.

CHAPTER 7 CONCLUSIONS

The main objective of this dissertation was to demonstrate the ability of nanocomposite thin film sensors coupled with tomographic mapping algorithm and measurement strategies to detect damage in structural and human health systems. Stimuli-sensitive polymeric thin films of MWCNT and GNS were fabricated through scalable and low-cost spray fabrication technique. The thin films were combined with structural materials or integrated with structural components to serve as distributed passive sensors. As every location on the thin films is sensitive external stimuli, tomographic mapping algorithm and measurement strategies (EIT and ECT) were implemented to achieve spatial sensing from a limited number of boundary electrical response measurements.

7.1 Summary of Results

The second chapter entails the detailed mathematical formulations of two different soft-field tomographic imaging techniques (*i.e.*, EIT and ECT). First, FE-based computer programmings were developed and implemented to solve the EIT and ECT forward problems. Second, the formulation for EIT and ECT sensitivity matrix have been described in detail. Third, a regularized iterative GN algorithm and linearized single-step algorithm were developed for conductivity and permittivity reconstructions through EIT and ECT, respectively. Experiments were performed to validate the spatial conductivity and permittivity reconstruction capability of the proposed EIT and ECT algorithm. The quality of the reconstructed images was also quantitatively assessed by evaluating different image metrics. EIT and ECT algorithms developed in this chapter were used in conjunction with nanocomposite thin film sensors for structural and human health monitoring.

In Chapter 3, an MWCNT-based nanocomposite thin film was used to nanoengineer the cement-aggregate interface of the cementitious composite to develop a self-sensing cementitious composite. The aggregates and sands were coated with MWCNT thin films and used for cementitious composite casting. The first set of experiments was performed on the mortar. It was found that, at a low strain regime, the MWCNT-enhanced mortar specimens exhibit very high strain sensitivity (~ 229). Over 0.2% strain, the sensitivity was comparable with the pristine specimen (~ 65). However, incorporation of MWCNT thin film helped the mortar specimens to exhibit higher SNR, sensing resolution, repeatability, higher conductivity, and less nominal resistance drift. Furthermore, EIT algorithm and measurement strategies described in Chapter 2, was implemented for spatial damage detection in these self-sensing mortar specimens. The same technique was applied to encode self-sensing properties in concrete. Like the mortar specimens, coarse aggregates and sand were coated with the MWCNT thin film and used for concrete casting. After ensuring the mechanical properties of the thin film-enhanced concrete specimens are higher than the FAA rigid pavement design guideline, spatial damage detection tests were performed on four different sets of concrete plate specimens. The results showed that the sand-coated and both sand- and aggregate-coated concrete sample sets enabled damage detection, due to the fact that electrical current was able to propagate throughout the entire bulk material.

Although EIT was able to detect spatially distributed damage in nanocomposite-enhanced structural materials, the technique is unable to estimate induced strain in different directions over a large structural surface. Thus, the approach employed in Chapter 4 was to pattern continuous films to form a grid- or mesh-like pattern. The sensing mesh pattern was designed such that each strut of the mesh or grid was of high aspect ratio, thereby enabling distributed sensing in each strut but limited to the direction of its length. However, to still use EIT for reconstructing the

conductivity distribution of the sensing mesh, a modified EIT algorithm was first implemented. A new GNS-based thin film strain sensor with a gage factor of ~ 8.25 was fabricated and characterized. The GNS-PVA film was then used to produce sensing mesh specimens of different patterns and sizes. Sensing mesh specimens were attached to various test structures and loaded to different strain states using the load frame, and EIT was utilized to interrogate the loaded specimens. The results showed the sensing mesh's ability to measure the magnitudes of strains at different directions strictly based on the locations and orientations of each strut in the mesh.

Besides structural applications, the nanocomposite thin film sensors and the tomographic methods were also used for human health monitoring. It was found that infection caused by the microorganism causes a variation in pH of the infected cells. pH-sensitive MWCNT-PANI/ latex thin film was coupled with noncontact ECT for infection monitoring at the tissue-OIP interface. The MWCNT-PANI/ latex thin film was deposited on the OIP surrogate by spray fabrication. Different pH buffer solutions were applied on the thin film-coated OIP surrogate to simulate different stages of infection. As the dielectric property of the thin film changes due to variation of pH, ECT was employed to capture the pH-induced dielectric permittivity changes at the tissue-prosthesis interface. Nanocomposite-enabled ECT was able to capture the electrical permittivity changes of the thin film caused by the infection. Besides pH sensing, a strain-sensitive thin film was coupled with ECT to monitor the strain and deformation in the OIP in a noncontact fashion. It was also demonstrated that the resolution of the ECT images could also be enhanced by modifying the deposition patterns of the thin films. Furthermore, ECT was also applied for prosthesis loosening and bone fracture at the bone-prosthesis interface. LRT and RECT approaches were demonstrated to enhance the resolution of the reconstructed images. The accuracy of the reconstructed images was also investigated by evaluating different image metrics.

Finally, the geometry of the ECT electrode array was modified to scan a large structural surface for subsurface damage detection in composite structures. This configuration allows the technicians to scan and probe the subsurface condition of the structural component, as opposed to conventional ECT, that requires the electrode array to surround the component of interest. Extensive numerical and experimental studies were performed to validate the subsurface imaging capability of the planar ECT system. It was shown that barely visible damage in CFRP structures could be identified by the proposed planar ECT system.

7.2 Contributions

As mentioned in Chapter 1, although nanocomposite-based thin film sensors have demonstrated their tremendous potentials to achieve distributed structural monitoring, more research works need to be performed to make them suitable for real-world applications. The main contribution of this research is to develop a new class of nanocomposite thin film sensors by scalable, low-cost fabrication methods and combining them with advanced tomographic mapping algorithms to achieve a more reliable materials-based spatial sensing platform for real-world structural and human health monitoring. Some key contributions of this dissertation are highlighted here.

- Instead of directly attaching the thin film sensor on the structural surface as a coating, this dissertation demonstrates that such thin films can be integrated with the structural materials to encode self-sensing property in material itself. Cement-aggregate interface was nanoengineered with an MWCNT-latex thin film by spray coating the aggregates and sand prior to casting. This process does not cause any change in the physical properties of the concrete and its casting procedure. Rather, it has been demonstrated that the consumption

of nanomaterials is significantly reduced compared to the other direct dispersion methods reported in the literature. As the entire structure becomes sensitive to damage, subsurface damage detection can also be achieved by using such self-sensing materials in conjunction with EIT.

- Distributed strain field monitoring over the large structural surface was achieved by coupling a modified EIT algorithm with a highly strain-sensitive GNS-based sensing mesh. The *in situ* application of the sensing mesh for distributed damage detection in large-scale structure is also demonstrated.

- In this dissertation, MWCNT-based nanomaterials were fabricated whose electrical permittivity is sensitive to external stimuli (*e.g.*, pH and strain). These thin films were fabricated by spray fabrication, and their sensing properties were characterized. Although some previous research efforts have utilized the capacitance measurements for various sensing applications, contact-based two- and four-point measurements were employed to achieve sensing. ECT algorithm and measurement strategies were developed and implemented in conjunction with these stimuli-responsive nanocomposites to achieve noncontact, spatial pH, and strain sensing. Besides, two separate techniques were proposed to enhance the resolution of the reconstructed images.

- Furthermore, the design of the ECT electrode array was modified to use it for structural inspection. The ECT algorithm was updated for 3D electrical permittivity reconstruction, and the experimental setup was assembled in the laboratory for the experimental validation of the proposed imaging system. It has been demonstrated that the proposed imaging system can detect barely visible subsurface defects in the composite structures. The

research findings showed that the geometry of the ECT electrode array can be modified in a desired way to achieve ECT scanning for subsurface damage identification in a complicated-shaped object. Additionally, as the electrical field can diffuse through a single layer of delamination and interact with the medium behind the first layer of delamination, multi-layer delamination can be detected from single-sided planar ECT inspection.

7.3 Future Research

7.3.1 Short Term Future Research

In the near future, research will be conducted to explore the long term behavior of thin film sensors. The long-term mechanical and electrical responses of the thin film sensors need to be studied prior to use them for structural monitoring over a longer period of time. The thin film sensors will be exposed to various ambient conditions (*e.g.*, temperature, sunlight, humidity, among others), and their electrical response will be studied to find the influences of such factors on the electrical property of the thin films.

It is shown that tomographic imaging suffers from poor resolution, which may limit their future applications where high-resolution imaging is required. Future research will also be focused on developing an efficient method for high-resolution tomographic image reconstruction. For example, to accurately estimate the location and shape of the damage in the structures, a narrow-band level set algorithm will be developed and implemented.

Data-driven algorithms will also be explored to achieve high-resolution tomographic imaging. For instance, the neural network-based deep learning algorithm can be developed and implemented for high-resolution imaging. Computationally obtained low-resolution tomographic

images will be used as the input of such a neural network model. The corresponding most accurate image sets will be cycled to train the neural network algorithm so that high-resolution images can be obtained from the low-resolution one. Such a data-driven imaging system would facilitate high-resolution image reconstruction while a series of uncertainties are present in the measurements (*e.g.*, measurement noises, electrode position mismatches, among others).

7.1.1 Long Term Future Research

The field of structural and human health monitoring requires advanced sensing technologies to assess the condition of the structural components to guide the engineers and physicians to take the next course of action. Despite the enormous improvement in sensing technologies, SHM still seeks advanced techniques to solve the engineering bottlenecks of the current-state-of-the-art. Spatial damage detection in large complex structures is extremely difficult as it requires a large number of point-sensors to be instrumented over the entire area of interests. Additionally, different types of sensors are needed to identify the damage caused by various external stimuli. For example, corrosion sensors are not capable of measuring strain/ deformation in the structure. A multi-modal sensing approach can be useful to overcome such limitations.

The nanocomposite thin film-enabled tomographic imaging techniques described in this thesis has the potential to overcome such limited bandwidth issue of the sensors. However, tomographic imaging techniques described in this thesis (*i.e.*, EIT and ECT) can estimate the conductivity and permittivity distribution separately. Three EM parameters (*i.e.*, conductivity, permittivity, and magnetic permeability) can be reconstructed together by interrogating the materials with an EM wave. EM responses can be measured in a noncontact fashion at the boundary of the object. Subsequent inverse problems can be solved to reconstruct the conductivity,

permittivity, and magnetic permeability distribution from the recorded set of boundary measurements. The forward model will be derived by solving full Maxwell's equation correlating the EM parameters with boundary excitation and measurements. The forward problem will be combined with an inverse algorithm to achieve distributed EM parameter mapping from experimentally measured boundary responses.

The second part of the proposed multi-modal sensing technique will attempt to develop stimuli-responsive nanocomposites whose EM parameters will be selectively sensitive to external stimuli (*e.g.*, magnetic permeability will be sensitive to strain while electrical permittivity will be sensitive corrosion/ pH). These thin films will be embedded in the structure at a critical region or will be integrated with the structural materials, thereby accentuating electrical property variations as detected by the multi-modal tomographic imaging technique. Such a multi-modal sensing system can be implemented to reveal the complex correlations between different modes of damage in various structural systems (*e.g.*, corrosion and corrosion-induced stress and fracture monitoring). Finally, electrical maps obtained from the multi-modal sensing system will be combined with a reliability model to estimate the residual life of our structural assets.

References

1. *Structure.* Available: https://en.wikipedia.org/wiki/Structure.

2. *Mianus River Bridge.* https://en.wikipedia.org/wiki/Mianus_River_Bridge.

3. *Hoan Bridge*. https://en.wikipedia.org/wiki/Hoan_Bridge.

4. *I-35W Mississippi River Bridge.* https://en.wikipedia.org/wiki/I-35W_Mississippi_River_bridge.

5. *Ponte Morandi*. https://en.wikipedia.org/wiki/Ponte_Morandi.

6. Ardagh MW, Richardson SK, Robinson V, Than M, Gee P, Henderson S, Khodaverdi L, McKie J, Robertson G, Schroeder PP, and Deely JM. The Initial Health-System Response to The Earthquake in Christchurch, New Zealand, in February, 2011. The Lancet. 2012; 379(9831): 2109-2115.

7. Gautam D, and Chaulagain H. Structural Performance and Associated Lessons To Be Learned From World Earthquakes in Nepal After 25 April 2015 (MW 7.8) Gorkha Earthquake. Engineering Failure Analysis. 2016; 68 222-243.

8. Saatcioglu M, Palermo D, Ghobarah A, Mitchell D, Simpson R, Adebar P, Tremblay R, Ventura C, and Hong H. Performance of Reinforced Concrete Buildings During The 27 February 2010 Maule (Chile) Earthquake. Canadian Journal of Civil Engineering. 2013; 40(8): 693-710.

9. *Shifting Into An Era of Repair: US Infrastructure Spending Trends.* https://www.brookings.edu/research/shifting-into-an-era-of-repair-us-infrastructure-spending-trends/.

10. Njord JR, and Meyer MD. Critical Issues in Transportation. Transportation Research Board of the National Academics. 2006; 1-13.

11. Hussain M, Nakahira A, and Niihara K. Mechanical Property Improvement of Carbon Fiber Reinforced Epoxy Composites by Al2O3 Filler Dispersion. Materials Letters. 1996; 26(3): 185-191.

12. Natali A, Manzi S, and Bignozzi MC. Novel Fiber-Reinforced Composite Materials Based on Sustainable Geopolymer Matrix. Procedia Engineering. 2011; 1124-1131.

13. Stark W, and Bohmeyer W. Non-destructive Evaluation (NDE) of Composites: Using Ultrasound to Monitor the Curing of Composites. 2013; 136-181.

14. Aoki Y, Suemasu H, and Ishikawa T. Damage Propagation in CFRP Laminates Subjected to Low Velocity Impact and Static Indentation. Advanced Composite Materials. 2007; 16(1): 45-61.

15. Ishai O, and Shragai A. Effect of Impact Loading on Damage and Residual Compressive Strength of CFRP Laminated Beams. Composite Structures. 1990; 14(4): 319-337.

16. Czepiel E. (2003, March). Practices and Perspectives in Outsourcing Aircraft Maintenance (DOT/FAA/AR-02/122).

17. Ziegler-Graham K, MacKenzie EJ, Ephraim PL, Travison TG, and Brookmeyer R. Estimating The Prevalence of Limb Loss in The United States: 2005 to 2050. Archives of Physical Medicine and Rehabilitation. 2008; 89(3): 422-429.

18. Owings MF, and Kozak LJ. Ambulatory and Inpatient Procedures in The United States, 1996. Vital and Health Statistics, Series 13, Data from The National Health Survey. 1998; 139 1-119.

19. Stinner DJ, Burns TC, Kirk KL, Scoville CR, Ficke JR, and Hsu JR. Prevalence of Late Amputations During The Current Conflicts in Afghanistan and Iraq. Military Medicine. 2010; 175(12): 1027-1029.

20. H. Fischer. (2010). US Military Casualty Statistics: Operation New Dawn, Operation Iraqi Freedom, and Operation Enduring Freedom. Congressional Research Service. Washington, DC.

21. Healthcare Cost Utilization Project. HCUP: A Federal-State-Industry Partnership in Health Data Sponsored by The Agency for Healthcare Research and Quality. (2012).

22. Adell R, Eriksson B, Lekholm U, Brånemark PI, and Jemt T. Long-Term Follow-up Study of Osseointegrated Implants in The Treatment of Totally Edentulous Jaws. The International Journal of Oral and Maxillofac Implants. 1990; 5(4): 347-359.

23. Branemark R, Berlin O, Hagberg K, Bergh P, Gunterberg B, and Rydevik B. A Novel Osseointegrated Percutaneous Prosthetic System For The Treatment of Patients With Transfemoral Amputation: A Prospective Study of 51 Patients. The Bone and Joint Journal. 2014; 96(4): 106-113.

24. Meent HVd, Hopman MT, and Frölke JP. Walking Ability and Quality of Life in Subjects with Transfemoral Amputation: A Comparison of Osseointegration with Socket Prostheses. Archives of Physical Medicine and Rehabilitation. 2013; 94(11): 2174-2178.

25. Tillander J, Hagberg K, Hagberg L, and Brånemark R. Osseointegrated Titanium Implants for Limb Prostheses Attachments: Infectious Complications. Clinical Orthopaedics and Related Research. 2010; 468(10): 2781-2788.

26. Zimmerli W. Prosthetic-Joint-Associated Infections. Best Practice and Research Clinical Rheumatology. 2009; 20(6): 1045-1063.

27. Tande AJ, and Patel R. Prosthetic Joint Infection. Clinical Microbiology Reviews. 2014; 27(2): 302-345.

28. Hagberg K, and Brånemark R. Consequences of Non-Vascular Trans-Femoral Amputation: A Survey of Quality of Life, Prosthetic Use and Problems. Prosthetics and Orthotics International. 2001; 25(3): 186-194.

29. Hagberg K, Brånemark R, Gunterberg B, and Rydevik B. Osseointegrated Trans-Femoral Amputation Prostheses: Prospective Results of General and Condition-Specific Quality of Life in 18 Patients at 2-Year Follow-up. Prosthetics and Orthotics International 2008; 32(1): 29-41.

30. Lee WC, Frossard LA, Hagberg K, Haggstrom E, Brånemark R, Evans JH, and Pearcy MJ. Kinetics of Transfemoral Amputees with Osseointegrated Fixation Performing Common Activities of Daily Living. Clinical Biomechanics. 2007; 22(6): 665-673.

31. Vertriest S, Coorevitsand P, and Frossard L. Static Load Bearing Exercises During Rehabilitation of Individuals With Transfemoral Amputation Fitted With Osseointegrated Implant: Kinetic Analysis, Conf Proc XIV World Congress of the International Society for Prosthetics and Orthotics (ISPO). 2013; 1-4.

32. Frost HM. A Determinant of Bone Architecture. The Minimum Effective Strain. Clinical Orthopaedics and Related Research 1983; 175 286-292.

33. Helgason B, Pálsson H, Rúnarsson TP, Frossard L, and Viceconti M. Risk of Failure During Gait For Direct Skeletal Attachment of A Femoral Prosthesis: A Finite Element Study. Medical Engineering and Physics. 2009; 31(5): 595-600.

34. Piscitelli P, Iolascon G, Innocenti M, Civinini R, Rubinacci A, Muratore M, D'Arienzo M, Leali PT, Carossino AM, and Brandi ML. Painful Prosthesis: Approaching The Patient With Persistent Pain Following Total Hip and Knee Arthroplasty. Clinical Cases in Mineral and Bone Metabolism. 2013; 10(2): 97-110.

35. Staszewski WJ, Mahzan S, and Traynor R. Health Monitoring of Aerospace Composite Structures–Active and Passive Approach. Composite Science and Technology. 2009; 69(11-12): 1678-1685.

36. Hallermann GMN. Quality Assessment of Unmanned Aerial Vehicle (UAV) Based Visual Inspection of Structures. Advances in Structural Engineering. 2014; 17(3): 290-302.

37. Eschmann C, Kuo CM, Kuo CH, and Boller C. Unmanned Aircraft Systems for Remote Building Inspection and Monitoring, Conf Proc 6th European Workshop on Structural HealthMonitoring. 2012.

38. Moreu F, Ayorinde E, Mason J, Farrar C, and Mascarenas D. Remote Railroad Bridge Structural Tap Testing Using Aerial Robots. International Journal of Intelligent Robotics and Applications. 2018; 2(1): 67-80.

39. Farrar CR, and Worden K. An Introduction to Structural Health Monitoring. Philosophical Transactions of the Royal Society A: Mathematical, Physical and Engineering Sciences. 2007; 365(1851): 303-315.

40. Cho S, Yun CB, Lynch JP, Zimmerman AT, Jr BFS, and Nagayama T. Smart Wireless Sensor Technology For Structural Health Monitoring of Civil Structures. Steel Structures. 2008; 8(4): 267-275.

41. Garcia-Palencia AJ, Santini-Bell E, Sipple JD, and Sanayei M. Structural Model Updating of An In-Service Bridge Using Dynamic Data. Structural Control and Health Monitoring. 2015; 22(10): 1265-1281.

42. Moaveni B, Stavridis A, Lombaert G, Conte JP, and Shing PB. Finite-Element Model Updating for Assessment of Progressive Damage in A 3-Story Infilled RC Frame. Journal of Structural Engineering. 2013; 139(10): 1665-1674.

43. Weng JH, Loh CH, and Yang JN. Experimental Study of Damage Detection by Data-Driven Subspace Identification and Finite-Element Model Updating. Journal of Structural Engineering. 2009; 135(12): 1533-1544.

44. Zimmerman AT, and Lynch JP. Data Driven Model Updating Using Wireless Sensor Networks, Conf Proc 3rd Annual ANCRiSST Workshop 2006; 29-30.

45. Tawil N, Sacher E, Mandeville R, and Meunier M. Surface Plasmon Resonance Detection of E. Coli and Methicillin-Resistant S. aureus Using Bacteriophages. Biosensors and Bioelectronics. 2012; 37(1): 24-29.

46. Vickers NJ. Animal Communication: When I'm Calling You, Will You Answer Too? Current Biology. 2017; 27(14): R713-R715.

47. Ahmed A, Rushworth JV, Hirst NA, and Millner PA. Biosensors for Whole-Cell Bacterial Detection. Clinical Microbiology Reviews. 2014; 27(3): 631-646.

48. Müller M, Morawietz L, Hasart O, Strube P, Perka C, and Tohtz S. Diagnosis of Periprosthetic Infection Following Total Hip Arthroplasty–Evaluation of The Diagnostic Values of Pre-and Intraoperative Parameters and The Associated Strategy to Preoperatively Select Patients with A High Probability of Joint Infection. Journal of Orthopaedic Surgery and Research. 2008; 3(31): 1-8.

49. Wong YC, Lee QJ, Wai YL, and Ng WF. Intraoperative Frozen Section For Detecting Active Infection In Failed Hip and Knee Arthroplasties. The Journal of Arthroplasty. 2005; 20(8): 1015-1020.

50. Atkins BL, Athanasou N, Deeks JJ, Crook DW, Simpson H, Peto TE, McLardy-Smith P, Berendt AR, and Group OCS. Prospective Evaluation of Criteria for Microbiological Diagnosis of Prosthetic-Joint Infection at Revision Arthroplasty. Journal of Clinical Microbiology. 1998; 36(10): 2932-2939.

51. Hughes JG, Vetter EA, Patel R, Schleck CD, Harmsen S, Turgeant LT, and Cockerill FR. Culture with BACTEC Peds Plus/F Bottle Compared with Conventional Methods for Detection of Bacteria in Synovial Fluid. Journal of Clinical Microbiology. 2001; 39(12): 4468-4471.

52. Hafner BJ, and Sanders JE. Considerations for Development of Sensing and Monitoring Tools to Facilitate Treatment and Care of Persons with Lower Limb Loss. Journal of Rehabilitation Research and Development. 2014; 51(1): 1.

53. Dickinson AS, Steer JW, and Worsley PR. Finite Element Analysis of The Amputated Lower Limb: A Systematic Review and Recommendations. Medical Engineering and Physics. 2017; 1(43): 1-8.

54. Hafner BJ, Willingham LL, Buell NC, Allyn KJ, and Smith DG. Evaluation of Function, Performance, and Preference as Transfemoral Amputees Transition from Mechanical to Microprocessor Control of The Prosthetic Knee. Archives of Physical Medicine and Rehabilitation. 2007; 88(2): 207-217.

55. Frossard L, Beck J, Dillon M, and Evans J. Development and Preliminary Testing of A Device for The Direct Measurement of Forces and Moments in The Prosthetic Limb of Transfemoral Amputees During Activities of Daily Living. Journal of Prosthetics and Orthotics. 2003; 15(4): 135-1442.

56. Lynch JP, and Loh KJ. A Summary Review of Wireless Sensors and Sensor Networks For Structural Health Monitoring. Shock and Vibration Digest. 2006; 38(2): 91-130.

57. Yan H, Xu LD, Bi Z, Pang Z, Zhang J, and Chen Y. An Emerging Technology–Wearable Wireless Sensor Networks with Applications in Human Health Condition Monitoring. Journal of Management Analytics. 2015; 3(2): 121-137.

58. Hackmann G, Guo W, Yan G, Sun Z, Lu C, and Dyke S. Cyber-Physical Codesign of Distributed Structural Health Monitoring with Wireless Sensor Networks. IEEE Transactions on Parallel and Distributed Systems. 2013; 2563-2572

59. Kim S, Pakzad S, Culler D, Demmel J, Fenves G, Glaser S, and Turon M. Health Monitoring of Cvil Infrastructures using Wireless Sensor Networks, Conf Proc 6th International Conference on Information Processing in Sensor Networks. 2007; 254-263.

60. Lynch JP, Wang Y, Loh KJ, Yi JH, and Yun CB. Performance Monitoring of The Geumdang Bridge using A Dense Network of High-Resolution Wireless Sensors. Smart Materials and Structures. 2006; 15(6): 1561.

61. Sundaram BA, Ravisankar K, Senthil R, and Parivallal S. Wireless Sensors For Structural Health Monitoring and Damage Detection Techniques. Current Science. 2013; 104(11): 1496-1505.

62. Perkins M, Correal N, and O'Dea B. Emergent Wireless Sensor Network Limitations: A Plea for Advancement In Core Technologies. IEEE Sensors. 2002; 2 1501-1509.

63. Anton SR, and Sodano HA. A review of Power Harvesting Using Piezoelectric Materials (2003–2006). Smart Materials and Structures. 2007; 16(3): R1.

64. Zhang J, Tian GY, Marindra AM, Sunny AI, and Zhao AB. A Review of Passive RFID Tag Antenna-Based Sensors and Systems for Structural Health Monitoring Applications. Sensors. 2017; 17(2): 265.

65. K. Finkenzeller. RFID Handbook: Fundamentals and Applications in Contactless Smart Cards and Identification. John Wiley & Sons: West Sussex, England (2003).

66. Yi X, Cho C, Cooper J, Wang Y, Tentzeris MM, and Leon RT. Passive Wireless Antenna Sensor for Strain and Crack Sensing—Electromagnetic Modeling, Simulation, and Testing. Smart Materials and Structures. 2013; 22(8): 085009.

67. Cho C, Yi X, Li D, Wang Y, and Tentzeris MM. Passive Wireless Frequency Doubling Antenna Sensor for Strain and Crack Sensing. IEEE Sensors Journal. 2016; 16(14): 5725-5733.

68. Daliri A, Galehdar A, Rowe WS, Ghorbani K, and John S. Utilising Microstrip Patch Antenna Strain Sensors for Structural Health Monitoring. Journal of Intelligent Material Systems and Structures. 2012; 23(2): 169-182.

69. Kim J, Wang Z, and Kim WS. Stretchable RFID for Wireless Strain Sensing with Silver Nano Ink. IEEE Sensors Journal. 2014; 14(12): 4395-44401.

70. Manzari S, Occhiuzzi C, Nawale S, Catini A, Natale CD, and Marrocco G. Humidity Sensing by Polymer-Loaded UHF RFID Antennas. IEEE Sensors Journal. 2012; 12(9): 2851-2858.

71. Virtanen J, Ukkonen L, Bjorninen T, Elsherbeni AZ, and Sydänheimo L. Inkjet-Printed Humidity Sensor for Passive UHF RFID Systems. IEEE Transactions on Instrumentation and Measurement. 2011; 60(8): 2768-2777.

72. Occhiuzzi C, Rida A, Marrocco G, and Tentzeris M. RFID Passive Gas Sensor Integrating Carbon Nanotubes. IEEE Transactions on Microwave Theory and Techniques. 2011; 59(10): 2674-2684.

73. Potyrailo RA, and Surman C. A Passive Radio-Frequency Identification (RFID) Gas Sensor with Self-Correction Against Fluctuations of Ambient Temperature. Sensors and Acutators B: Chemical. 2013; 185 587-593.

74. Girbau D, Ramos Á, Lazaro A, Rima S, and Villarino R. Passive Wireless Temperature Sensor Based on Time-Coded UWB Chipless RFID Tags. IEEE Transactions on Microwave Theory and Techniques. 2012; 60(11): 3623-3632.

75. Noor T, Habib A, Amin Y, Loo J, and Tenhunen H. High-Density Chipless RFID Tag for Temperature Sensing. Electronics Letters. 2016; 52(8): 620-622.

76. Burny F, Donkerwolcke M, and Moulart F. Concept, Design and Fabrication of Smart Orthopedic Implants. Medical Engineering & Physics. 2000; 22(7): 469–479.

77. Korduba LA, Grabowsky MB, Uhl RL, Hella MM, and Ledet EH. Radio Frequency Identification as A Testbed For Integration of Low Frequency Radio Frequency Sensors into Orthopedic Implants. Journal of Medical Devices. 2013; 7(1): 11008.

78. Burton AR, Sun P, and Lynch JP. Bio-Compatible Wireless Inductive Thin-Film Strain Sensor For Monitoring The Growth and Strain Response of Bone in Osseointegrated Prostheses. Structural Health Monitoring. 2019; 1475921719831452.

79. Wamba SF, Anand A, and Carter L. A Literature Review of RFEenabled Healthcare Applications and Issues. International Journal of Information Management. 2013; 33(5): 875-891.

80. Senyurek VY. Detection of Cuts and Impact Damage at The Aircraft Wing Slat by Using Lamb Wave Method. Measurement. 2015; 67 10-23.

81. An YK, and Sohn H. Integrated Impedance and GuidedWave Based Damage Detection. Mechanical Systems and Signal Processing. 2012; 28 50-62.

82. Aldrin JC, Medina EA, Lindgren EA, Buynak C, Steffes G, and Derriso M. Model-Assisted Probabilistic Reliability Assessment for Structural Health Monitoring Systems, Conf Proc AIP Conference. 2010; 1965-1972.

83. Monaco E, Boffa ND, Memmolo V, Ricci F, Testoni N, , Marchi LD, Marzani A, Hettler J, Tabatabaeipour M, Delrue S, and Koen VD. Methodologies for Guided Wave-Based SHM System Implementation on Composite Wing Panels: Results and Perspectives From SARISTU Scenario 5 Conf Proc Smart Intelligent Aircraft Structures (SARISTU) 2016; 495-527.

84. Rahmani M, and Todorovska MI. Structural hHealth Monitoring of A 54-Story Steel-Frame Building Using A Wave Method and Earthquake Records. Earthquake Spectra. 2015; 31(1): 501-525.

85. Todorovska MI, and Rahmani MT. System Identification of Buildings by Wave Travel Time Analysis and Layered Shear Beam Models—Spatial Resolution and Accuracy. Structural Control and Health Monitoring. 2013; 20(5): 686-702.

86. Vayron R, Nguyen VH, Bosc R, Naili S, and Haïat G. Finite Element Simulation of Ultrasonic Wave Propagation in A Dental Implant For Biomechanical Stability Assessment. Biomechanics and Modeling in Mechanobiology. 2015; 14(5): 1021-1032.

87. Vayron R, Mathieu V, Michel A, and Haïat G. Assessment of In Vitro Dental Implant Primary Stability Using An Ultrasonic Method. Ultrasound in Medicine & Biology. 2014; 40(12): 2885-2894.

88. Wang W, and Lynch JP. Application of Guided Wave Methods To Quantitatively Assess Healing in Osseointegrated Prostheses. Structural Health Monitoring. 2017; 17(6): 1377-1392.

89. Mitra M, and Gopalakrishnan S. Guided Wave Based Structural Health Monitoring: A Review. Smart Materials and Structures. 2016; 25(5): 053001.

90. Bogue R. Recent Developments in MEMS Sensors: A Review of Applications, Markets and Technologies. Sensor Review. 2013;

91. Bedon C, Bergamo E, Izzi M, and Noè S. Prototyping and Validation of MEMS Accelerometers for Structural Health Monitoring—The Case Study of The Pietratagliata Cable-Stayed Bridge. Journal of Sensor and Actuator Networks. 2018; 7(3): 30.

92. Cao L, Kim TS, Mantell SC, and Polla DL. Simulation and Fabrication of Piezoresistive Membrane Type MEMS Strain Sensors. Sensors and Actuators A: Physical. 2000; 80(3): 273-279.

93. Abeysinghe DC, Dasgupta S, Boyd JT, and Jackson HE. A Novel MEMS Pessure Sensor Fabricated on An Optical Fiber. IEEE Photonics Technology Letters. 2001; 13(9): 993-995.

94. Feng P. Development of MEMS-Based Corrosion Sensor. MS. Mechanical Engineering. University of Arkansas. Fayetteville. 2012.

95. Weinberg MS, Wall C, Robertsson J, O'Neil E, Sienko K, and Fields R. Tilt Determination in MEMS Inertial Vestibular Prosthesis. Transactions of the ASME. 2006; 128 943-956.

96. Hasenkamp W, Thevenaz N, Villard J, Bertsch A, Arami A, Aminian K, Terrier A, and Renaud P. Design and Test of A MEMS Strain-Sensing Device for Monitoring Artificial Knee Implants. Biomedical Microdevices. 2013; 15(5): 831-839.

97. Bhansali S, and Vasudev A. MEMS for Biomedical Applications. Elsevier;2012.

98. Loh KJ. Development of Multifunctional Carbon Nanotube Nanocomposite Sensors for Structural Health Monitoring. Ph.D. Civil Engineering. University of Michigan Ann Arbor. Ann Arbor, Michigan. 2008.

99. Bhushan B. Springer Handbook of Nanotechnology. Springer. 2017;

100. Tombler TW, Zhou C, Alexseyev L, Kong J, Dai H, Liu L, Jayanthi CS, Tang M, and Wu SY. Reversible Electromechanical Characteristics of Carbon Nanotubes Underlocal-Probe Manipulation. Nature. 2000; 405(6788): 769-772.

101. Smith AD, Niklaus F, Paussa A, Vaziri S, Fischer AC, Sterner M, Forsberg F, Delin A, Esseni D, Palestri P, and Ostling M. Electromechanical Piezoresistive Sensing in Suspended Graphene Membranes. Nano Letters. 2013; 13(7): 3237-3242.

102. Lee BM, and Loh KJ. Carbon Nanotube Thin Film Strain Sensors: Comparison Between Experimental Tests and Numerical Simulations. Nanotechnology. 2017; 28(15): 155502.

103. Pham GT, Park YB, Liang Z, Zhang C, and Wang B. Processing and Modeling of Conductive Thermoplastic/Carbon Nanotube Films for Strain Sensing. Composites Part B. 2008; 39 209-216.

104. Kong J, Franklin NR, Zhou C, Chapline MG, Peng S, Cho K, and Dai H. Nanotube Molecular Wires as Chemical Sensors. Science. 2000; 287(5453): 622-625.

105. Loh KJ, Kim JH, Lynch JP, Kam NWS, and Kotov NA. Multifunctional Layer-By-Layer Carbon Nanotube-Polyelectrolyte Thin Films For strain and corrosion sensing. Smart Materials and Structures. 2007; 16(2): 429-438.

106. Dinh-Trong N, Steitz J, Lei B, and Kanoun O. Influence of The Composition of MWCNTs Layers on The Properties of Strain Gauges, Conf Proc 9th IEEE Conference on Nanotechnology. 2009; 477-480.

107. Kang I, Lee JW, Choi GR, Jung JY, Hwang SH, Choi YS, Yoon KJ, and Schulz MJ. Structural Health Monitoring Based on Electrical Impedance of A Carbon Nanotube Neuron. Key Engineering Materials. 2006; 321-323 140-145.

108. Kang I, M. J. S, Kim JH, Shanov V, and Shi D. A Carbon Nanotube Strain Sensor For Structural Health Honitoring. Smart Materials and Structures. 2006; 15(3): 734-748.

109. Dharap P, Li Z, Nagarajaiah S, and Barrera EV. Nanotube Film Based on Single-Wall Carbon Nanotubes For Strain Sensing. Nantechnology. 2004; 15(3): 379-382.

110. Hou TC, Loh KJ, and Lynch JP. Spatial Conductivity Mapping of Carbon Nanotube Composite Thin Films by Electrical Impedance Tomography for Sensing Applications. Nanotechnology. 2007; 18(31): 315501/1-9.

111. Vauhkonen M. Electrical impedance tomography and prior information. Ph.D. . Natural and Environmental Sciences. University of Kuopio. Kuopio, Finland. 1997.

112. Barber D. Quantification in Impedance Imaging. Clinical Physics and Physiological Measurement. 1990; 11 45-56.

113. Dijkstra A, Brown B, Leathard A, Harris N, Barber D, and Edbrooke D. Review Clinical Applications of Electrical Impedance Tomography. Journal of Medical Engineering & Technology. 1993; 17 89-98.

114. Smallwood R, Mangnall Y, and Leathard A. Transport of Gastric Contents (Electric Impedance Imaging). Physiological Measurement. 1994; 15 A175-A188.

115. Harris N, Brown B, and Barber D. Continuous Monitoring of Lung Ventilation with Electrical Impedance Tomography, Conf Proc 14th Annual International Conference of the IEEE,. 1992; 1754-1755.

116. Brown B, Sinton A, Barber D, A. L, and McArdle F. Simultaneous Display of Lung Ventilation and Perfusion on a Real-Time EIT System, Conf Proc Engineering in Medicine and Biology Society, 14th Annual International Conference of the IEEE. 1992; 1710-1711.

117. Brown B, Barber D, Eyüboglu B, Harris N, and McArdle F. Electrical Impedance Imaging Developed to Image Cardiopulmonary Function, Conf Proc 9th International Conference of IEEE Engineering Medical Biological Society. 1987; 1200-1202.

118. Goharian. M. New Hardware and Software Design for Electrical Impedance Tomography. 2007.

119. Murphy D, Burton P, Coombs R, Tarassenko L, and Rolfe P. Impedance Imaging in the Newborn. Clinical Physics and Physiological Measurement. 1987; 8 131-140.

120. Newell JC, Edic PM, Ren X, Larson-Wiseman JL, and Danyleiko MD. Assessment of Acute Pulmonary Edema in Dogs by Electrical Impedance Imaging. IEEE Transactions on Biomedical Engineering. 1996; 43 133-138.

121. Zhang D, Ye L, Wang D, Tang Y, Mustapha S, and Chen Y. Assessment of Transverse Impact Damage in GF/EP Laminates of Conductive Nanoparticles Using Electrical Resistivity Tomography. Composites Part A: Applied Science and Manufacturing. 2012; 43 1587-1598.

122. Tallman T, Gungor S, Wang K, and Bakis C. Damage Detection and Conductivity Evolution in Carbon Nanofiber Epoxy Via Electrical Impedance Tomography. Smart Materials and Structures. 2014; 23(045034): 1-9.

123. M.Hallaji, Seppänen A, and Pour-Ghaz M. Electrical Impedance Tomography-Based Sensing Skin for Quantitative Imaging of Damage in Concrete. Smart Materials and Structures. 2014; 23((085001)): 1-13.

124. Hou TC, and Lynch JP. Electrical Impedance Tomographic Methods for Sensing Strain Fields and Crack Damage in Cementitious Structures. Journal of Intelligent Material Systems and Structures. 2008; (1-18):

125. Soleimani M. Nonlinear Inverse Finite Element Methodd in Electrical Tomography. Ph.D. School of Mathematics. University of Manchester. Manchester, UK. 2005.

126. Huang SM, Plaskowski AB, Xie CG, and Beck MS. Tomographic Imaging of Two-Component Flow Using Capacitance Sensors. Journal of Physics E: Scientific Instruments. 1989; 22(3): 173-177.

127. Yang WQ, Chondronasios A, Nattrass S, Nguyen VT, Betting M, Ismail I, and McCann H. Adaptive Calibration of A Capacitance Tomography System for Imaging Water Droplet Distribution. Flow Measurement and Instrumentation. 2004; 15(5-6): 249-258.

128. Jaworski AJ, and Dyakowski T. Application of Electrical Capacitance Tomography for Measurement of Gas-Solids Flow Characteristics in A Pneumatic Conveying System. Measurement Science and Technology. 2001; 12(8): 1109-1119.

129. Chaplin G, Pugsley T, Lee Lvd, Kantzas A, and Winters C. The Dynamic Calibration of An Electrical Capacitance Tomography Sensor Applied To The Fluidized Bed Drying of Pharmaceutical Granule. Measurement Science and Technology. 2005; 16(6): 1281-1290.

130. Waterfall RC, He R, White NB, and Beck CM. Combustion Imaging From Electrical Impedance Measurements. Measurement Science and Technology. 1996; 7(3): 369-374.

131. Dyakowski T, York T, Mikos M, Vlaev D, Mann R, Follows G, Boxman A, and Wilson M. Imaging Nylon Polymerisation Processes by Applying Electrical Tomography. Chemical Engineering Journal. 2000; 77(1-2): 105-109.

132. Gupta S, Fan G, and Loh KJ. Noninvasive Monitoring of Epoxy Curing. IEEE Sensors Letters. 2017; 1(5): 1-4.

133. Yin X, and Hutchins DA. Non-Destructive Evaluation of Composite Materials Using A Capacitive Imaging Technique. Composites Part B: Engineering 2012; 43(3): 1282-1292.

134. Gupta S, and Loh KJ. Characterization and Localization of Sub-Surface Structural Features Using Non-Contact Tomography, Conf Proc ASME 2016 Smart Materials, Adaptive Structures, and Intelligent Systems (SMASIS) Conference. 2016.

135. Ren Z, and Yang WQ. Visualisation of Tooth Surface by Electrical Capacitance Tomography. Biomedical Physics & Engineering Express 2017; 3(1): 1-12.

136. Taruno WP, Baidillah MR, Sulaiman RI, Ihsan MF, Fatmi SE, Muhtadi AH, Haryanto F, and Aljohani M. 4D Brain Activity ScannerUsing Electrical Capacitance Volume Tomography (ECVT), Conf Proc 10th International Symposium on Biomedical Imaging. 2013; 1006-1009.

137. Loyola BR. Distributed in Situ Health Monitoring of Conductive Self-Sensing Fiber-Reinforced Polymers Using Electrical Impedance Tomography. Ph.D. Department of Mechanical and Aerospace Engineering. University of California Davis. Davis, CA. 2012.

138. Cheng KS, Isaacson D, Newell J, and Gisser DG. Electrode Models for Electric Current Computed Tomography. IEEE Transactions on Biomedical Engineering. 1989; 36 928-924.

139. Sherina ES, and Starchenko AV. Finite Volume Schemes for the Electrical Impedance Tomography Problem. Vestnik Tomskogo Gosudarstvennogo Universiteta Matematika i Mekhanika. 2014; 25-38.

140. Lazarovitch R, Rittel D, and Bucher I. Experimental Crack Identification Using Electrical Impedance Tomography. NDT & E International. 2002; 35 301-316.

141. Fish J. and Belytschko T. A First Course in Finite Elements. John Wiley & Sons, 2007.

142. Yorkey TJ, and Webster JG. A Comparison of Impedance Tomographic Reconstruction Algorithms. Clinical Physics and Physiological Measurement. 1987; 8(55-62):

143. Brandstätter B, Holler G, and Watzenig D. Reconstruction of Inhomogeneities In Fluids by Means of Capacitance Tomography, Conf Proc COMPEL-The International Journal for Computation and Mathematics in Electrical and Electronic Engineering. 2003.

144. Soleimani M, and Lionheart WR. Nonlinear Image Reconstruction for Electrical Capacitance Tomography Using Experimental Data. Measurement Science and Technology. 2005; 16(10): 1987.

145. Jing L, Liu S, Zhihong L, and Meng S. An Image Reconstruction Algorithm Based on The Extended Tikhonov Regularization Method for Electrical Capacitance Tomography. Measurement. 2009; 42(3): 368-376.

146. Cheney M, Isaacson D, Newell JC, Simske S, and Goble J. NOSER: An Algorithm For Solving The Inverse Conductivity Problem. International Journal of Imaging Systems and Technology. 1990; 2 66-75.

147. Loyola BR, Briggs TM, Arronche L, Loh KJ, Saponara VL, O'Bryan G, and Skinner JL. Detection of Spatially Distributed Damage in Fiber-Reinforced Polymer Composites. Structural Health Monitoring. 2013; 12 225-239.

148. Adler A, Arnold JH, Bayford R, Borsic A, Brown B, Dixon P, Faes TJ, Frerichs I, Gagnon H, Gärber Y, and Grychtol B. GREIT: A Unified Approach To 2D Linear EIT Reconstruction of Lung Images. Physiological Measurement. 2009; 30(6): S35-S55.

149. Samsonov P. Nondestructive Inspection of Aging Aircraft, Conf Proc SPIE. 1993; 257-261.

150. I. International. Documentation for Greenhouse Gas Emission and Energy Factors Used in the Waste Reduction Model (Warm). vol. 3, 13 ed: Environmental Protection Agency, pp. 1-7, 2014.

151. *Highways*. Available: http://www.cement.org/think-harder-concrete-/paving/concrete/highways.

152. Concrete Information.Iin Types and Causes of Concrete Deterioration, ed: Portland Cemenet Association, pp. 1,4-5, 2002.

153. Transportation Research Circular. In Control of Cracking in Concrete State of the Art J. Correro, Ed., ed: Transportation Research Board of The National Academies, pp. 4-7,13-16,20-21, 2006.

154. Harries K. Structural Testing of Prestressed Concrete Girders from the Lake View Drive Bridge. Journal of Bridge Engineering. 2009; 14 78-92.

155. Hadzor TJ, Barnes RW, Ziehl PH, Xu J, and Schindler AK. Development of Acoustic Emission Evaluation Method for Repaired Prestressed Concrete Bridge Girders, Conf Proc Highway Research Center, Department of Civil Engineering. 2011.

156. Musbah A, Kabir S, and Salem A. Sub-Surface Concrete Structure Damage Quantifcation Using TIR and Visual Inspection Conf Proc Progress In Electromagnetics Research Symposium 2011; 781-784.

157. Verma SK, Bhadauria SS, and Akhtar S. Review of Nondestructive Testing Methods for Condition Monitoring of Concrete Structures. Journal of Construction Engineering. 2013; 2013

158. Sanchez F, and Sobolev K. Nanotechnology in Concrete – A Review. Construction and Building Materials. 2010; 24 2060-2071.

159. Pu-Woei C, and Chung DDL. Carbon Fiber Reinforced Concrete as an Intrinsically Smart Concrete for Damage Assessment During Static and Dynamic Loading. Materials Journal. 1996; 93

160. Ding Y, Han Z, Zhang Y, and Azevedo CM. Hybrid Use of Steel and Carbon-Fiber Reinforced Concrete for Monitoring of Crack Behavior, Conf Proc European Conference on Composite Materials (ECCM). 2012.

161. Han B, Yu X, and Kwon E. A Self-Sensing Carbon Nanotube/Cement Composite for Traffic Monitoring. Nanotechnology. 2009; 20 1-5.

162. Ou J, and Han B. Piezoresistive Cement-Based Strain Sensors and Self-Sensing Concrete Components. Journal of Intelligent Material Systems and Structures. 2009; 20 329-336.

163. Sui LL, and Liu TJ. State-of-the-Art Multifunctional and Smart Concrete. Key Engineering Materials. 2006; 302-303 424-431.

164. Wille K, and Loh KJ. Nano-Engineering Ultra-High Performance Concrete with Multi-Walled Carbon Nanotubes. Journal of the Transportation Research Board. 2010; 2142 119-126.

165. Xun Y. A Carbon Nanotube Cement Composite with Piezoresistive Properties. Smart Materials and Structures. 2009; 18 055010.

166. Han B, Yu X, Kwon E, and Ou J. Effects of CNT Concentration Level and Water/Cement Ratio on the Piezoresistivity of CNT/Cement Composites. Journal of Composite Materials. 2012; 46 19-25.

167. Baoguo H. Integration and Road Tests of a Self-Sensing CNT Concrete Pavement System for Traffic Detection. Smart Materials and Structures. 2013; 22 015020.

168. Wong I, Loh KJ, Wu R, and Garg N. Sensing Properties of Mortar Incorporating Ultra-Low Concentrations of Carbon-Based Conductive Additives, Conf Proc Proceedings of the 5th Asia-Pacific Workshop on Structural Health Monitoring. 2014; 1-10.

169. Nasibulina LI, Anoshkin IV, Shandakov SD, Nasibulin AG, Cwirzen A, and Mudimela PR. Direct Synthesis of Carbon Nanofibers on Cement Particles. Journal of the Transportation Research Board. 2010; 2142 96-101.

170. Hou TC, Chiou Y-H, Pan HH, and Chang CH. Electrical Resistivity Measurement of Cement-Based Binders Using Embedded Four-Terminal Probe Method, Conf Proc 4th ACF international conference. 2010; 1-4.

171. Wong I. Effects of Ultra-Low Concentrations of Nanomaterials on the Piezoresistivity of Cementitious Composites. MS. Civil & Environmental Engineering. University of California Davis. Davis, CA. 2015.

172. Mortensen LP, Ryu D, Zhao Y, and Loh KJ. Rapid Assembly of Multifunctional Thin Film Sensors for Wind Turbine Blade Monitoring. Key Engineering Materials. 2013; 569-570 515-522.

173. Loyola BR, Zhao Y, Loh KJ, and Saponara VL. The Electrical Response of Carbon Nanotube-Based Thin Films Subjected to Mechanical and Environmental Effects. Smart Materials and Structures. 2013; 22 1-11.

174. M. J. O'Donnell. Standards for Specifying Construction of Airports. Advisory Circular. 2011.

175. Standards for Specifying Construction of Airports. AC 150/5370-10G. Federal Aviation Administration, 2014.

176. ASTM C39/C39M - 15a : Standard Test Method for Compressive Strength of Cylindrical Concrete Specimens. West Conshohocken, Pa: ASTM International, 2015.

177. ASTM C617/C617M - 15 : Standard Practice for Capping Cylindrical Concrete Specimens. West Conshohocken, Pa: ASTM International, 2015.

178. ASTM C78/C78M - 15a : Standard Test Method for Flexural Strength of Concrete (Using Simple Beam with Third-Point Loading). West Conshohocken, Pa: ASTM International, 2015.

179. Cao J, and Chung DDL. Electric Polarization and Depolarization in Cement-Based Materials, Studied by Apparent Electrical Resistance Measurement. Cement and Concrete Research. 2004; 34 481-485.

180. Yu X, and Kwon E. A Carbon Nanotube/Cement Composite with Piezoresistive Properties. Smart Materials and Structures. 2009; 18(055010): 1-5.

181. Corydon L. F. Ready Mixed Concrete Industry Data Report. National Ready Mixed Concrete Association, 2012.

182. Hou TC, and Lynch JP. Electrical impedance tomographic methods for sensing strain fields and crack damage in cementitious structures. Journal of Intelligent Material Systems and Structures. 2009; 20(11): 1363-1379.

183. Kersey AD, Davis MA, Patrick HJ, Koo ML, Askins CG, Putnam MA, and Friebele EJ. Fiber grating sensors. Journal of Lightwave Technology 1997; 15(8): 1442-1463.

184. Li HN, Li DS, and Song GB. Recent Applications of Fiber Optic Sensors to Health Monitoring in Civil Engineering. Engineering Structures. 2004; 26(11): 1647-1657.

185. Glišić B, Yao Y, Tung S T, Wagner S, Sturm J C, and Verma N. Strain sensing sheets for structural health monitoring based on large-area electronics and integrated circuits. Proceedings of the IEEE. 2016; 104(8): 1513-1528.

186. Kharroub S, Laflamme S, Song C, Qiao D, Phares B, and Li J. Smart sensing skin for detection and localization of fatigue cracks. Smart Materials and Structures. 2015; 24(6): 1-16.

187. Tallman TN, Gungor S, Koo GM, and Bakis CE. On the inverse determination of stresses and strains in a carbon nanofiber/polyurethane nanocomposite from conductivity data obtained via electrical impedance tomography. Journal of Intelligent Material Systems and Structures. 2017; 28 2617-2629.

188. Soleimani M. Image and shape reconstruction methods in magnetic induction and electrical impedance tomography. Ph. D. University of Manchester. Manchester, England. 2005.

189. Gupta S, Gonzalez JG, and Loh KJ. Self-Sensing Concrete Enabled by Nano-Engineered Cement-Aggregate Interfaces. Struct Health Monit. 2016; 16(3): 309-323.

190. Chen X, Zheng X, Kim JK, Li X, and Lee DW. Investigation of Graphene Piezoresistors for Use as Strain Gauge Sensors. ournal of Vacuum Science & Technology B, Nanotechnology and Microelectronics: Materials, Processing, Measurement, and Phenomena. 2011; 29(6): 06FE01.

191. Bae SH, Lee Y, Sharma BK, Lee HJ, Kim JH, and Ahn JH. Graphene-based transparent strain sensor. Carbon. 2013; 51 236-242.

192. Liu Q, Chen J, Li Y, and Shi G. High-performance strain sensors with fish-scale-like graphene-sensing layers for full-range detection of human motions. ACS Nano. 2016; 10(8): 7901-7906.

193. Tian H, Shu Y, Cui Y, Mi W, Yang Y, Xie D, and Ren T. Scalable fabrication of high-performance and flexible graphene strain sensors. Nanoscale. 2013; 6 699-705.

194. Manna K, Hsieh CY, Lo SC, Li YS, Huang HN, and Chiang WH. Graphene and graphene-analogue nanosheets produced by efficient water-assisted liquid exfoliation of layered materials. Carbon. 2016; 105 551-555.

195. Manna K, Huang HN, Li WT, Ho YH, and Chiang WH. Toward understanding the efficient exfoliation of layered materials by water-assisted cosolvent liquid-phase exfoliation. Chemistry of Materials. 2016; 28(21): 7568-7593.

196. Hilding J, Grulke EA, Zhang G, and Lockwood F. Dispersion of Carbon Nanotubes in Liquids. Journal of Dispersion Science and Technology. 2003; 24(1): 1-41.

197. Loyola BR, Saponara VL, Loh KJ, Briggs TM, G. O'Bryan, and Skinner JL. Spatial sensing using electrical impedance tomography. IEEE Sensors (1530-437X). 2013; 13(6): 2357-2367.

198. Khemka A, Frossard L, Lord S, Bosley B, and Muderis MA. Osseointegrated Prosthetic Limb for Amputees: Over Hundred Cases, Conf Proc 6th International Conference Advances in Orthopaedic Osseointegration. 2015.

199. Love C, Marwin SE, and Palestro CJ. Nuclear Medicine and The Infected Joint Replacement. S. eminars in Nuclear Medicine. 2009; 39(1): 66-78.

200. Kwee TC, Kwee RM, and Alavi A. FDG-PET for Diagnosing Prosthetic Joint Infection: Systematic Review and Metaanalysis. European Journal of Nuclear Medicine and Molecular Imaging. 2008; 35(11): 2122-2132.

201. Marples RR, Downing DT, and Kligman AM. Control of Free Fatty Acids in Human Surface Lipids by Corynebacterium Acnes. . Journal of Investigative Dermatology. 1971; 56(2): 127-131.

202. Dumas R, Cheze L, and Frossard L. Loading Applied on Prosthetic Knee of Transfemoral Amputee: Comparison of Inverse Dynamics and Direct Measurements. Gait & Posture 30(4): 560-562.

203. Stephenson P, and Seedhom BB. Estimation of Forces at The Interface Between An Artificial Limb and An Implant Directly Fixed Into The Femur In Above-Knee Amputees. Journal of Orthopaedic Science. 2002; 7(3): 292-297.

204. Taylor SJG, and Walker PS. Forces and Moments Telemetered From Two Distal Femoral Replacements During Various Activities. Journal of Biomechanics. 2001; 34(7): 839-848.

205. Frossard L, Gow DL, Hagberg K, Cairns N, Contoyannis B, Gray S, Brånemark R, and Pearcy M. Apparatus For Monitoring Load Bearing Rehabilitation Exercises of A Transfemoral Amputee Fitted with An Osseointegrated Fixation: A Proof-Of-Concept Study. Gait & Posture. 2010; 31(2): 223-228.

206. Stenlund P, Trobos M, Lausmaa J, Brånemark R, Thomsen P, and Palmquist A. Effect of Load on The Bone Around Bone-Anchored Amputation Prostheses. Journal of Orthopaedic Research. 2017; 35(5): 1113-1122.

207. Koehler SR, Dhaher YY, and Hansen AH. Cross-Validation of A Portable, Six-Degree-of-Freedom Load Cell for Use In Lower-Limb Prosthetics Research. Journal of Biomechanics. 2014; 47(6): 1542-1547.

208. Lohmann CH, Rampal S, Lohrengel M, and Singh G. Imaging in Peri-Prosthetic Assessment: An Orthopaedic Perspective. EFORT Open Reviews. 2017; 2(5): 117-125.

209. Unger AC, Cabrera-Palacios H, Schulz AP, C. J, and Paech A. Acoustic Monitoring (RFM) of Total Hip Arthroplasty Results of A Cadaver Study. European Journal of Medical Research. 2009; 14(6): 264-271.

210. She C, Shi GL, Xu W, Zhou XZ, Li J, Tian Y, Li WH, Dong QR, and Ren PG. Effect of Low-Dose X-Ray Irradiation and Ti Particles on The Osseointegration of Prosthetic. Journal of Orthopaedic Research. 2016; 34(10): 1688-1696.

211. Konyushenko EN, Stejskal J, Šeděnková I, Trchová M, Sapurina I, Cieslar M, and Prokeš J. Polyaniline Nanotubes: Conditions of Formation. Polymer International. 2006; 55(1): 31-39.

212. Wang LP, Wang W, Di L, Lu YN, and Wang JY. Protein Adsorption Under Electrical Stimulation of Neural Probe Coated with Polyaniline. Colloids and Surfaces B: Biointerfaces. 2010; 80(1): 72-78.

213. Stejskal J, Sapurina I, and Trchová M. Polyaniline Nanostructures and The Role of Aniline Oligomers in Their Formation. rogress in Polymer Science. 2010; 35(12): 1420-1481.

214. Humpolicek P, Kasparkova V, Saha P, and Stejskal J. Biocompatibility of Polyaniline. Synthetic Metals. 2012; 162(7): 722-727.

215. Adhikari B, and Majumdar S. Polymers in Sensor Applications. Progress in Polymer Science. 2004; 29(7): 699-766.

216. Vandenberg A, and Loh KJ. Evaluating The pH Sensitivity of Carbon Nanotube-Polyaniline Thin Films With Different Dopants. Nano LIFE. 2012; 2(4): 1-12.

217. Wei HY, and Soleimani M. Theoretical and Experimental Evaluation of Rotational Magnetic Induction Tomography. IEEE Transaction on Instrumentation and Measurement. 2012; 61(12): 3324-3321.

218. Hosani EA, Zhang M, and Soleimani M. A Limited Region Electrical Capacitance Tomography for Detection of Deposits in Pipelines. IEEE Sensors Journal. 2015; 15(11): 6089-6099.

219. Su KB. Delamination Resistance of Stitched Thermoplastic Matrix Composite Laminates. Advances in Thermoplastic Matrix Composite Materials. 1989; 279-300.

220. Gholizadeh S. A Review of Nondestructive Testing Methods of Composite Materials. Procedia Structural Integrity. 2016; 1 50-57.

221. Gustafson CG, and Selden RB. Monitoring Fatigue Damage in CFRP using Acoustic Emission and Radiographic Techniques. Delamination and Debonding of Materials. 1985;

222. Imielińska K, Castaings M, Wojtyra R, Haras J, Clezio EL, and Hosten B. Air-Coupled Ultrasonic C-Scan Technique In Impact Response Testing of Carbon Fibre and Hybrid: Glass, Carbon and Kevlar/Epoxy Composites. Journal of Materials Processing Technology. 2004; 513-522 157-158.

223. Bhardwaj MC. Evolution of Piezoelectric Transducers To Full Scale Non-Contact Ultrasonic Analysis Mode, Conf Proc 16th World Conference on Nondestructive Testing. 2004.

224. Grimberg R, Premel D, Savin A, Bihan YL, and Placko D. Eddy Current Holography Evaluation of Delamination in Carbon-Epoxy Composites. Insight. 2001; 43(4): 260-264.

225. Kim KH, Klann RT, and Raju BB. Fast Neutron Radiography for Composite Materials Evaluation and Testing. Nuclear Instruments and Methods in Physics Research Section A: Accelerators, Spectrometers, Detectors and Associated Equipment. 1999; 422(1-3): 929-932.

226. Gupta S, and Loh KJ. Noncontact Electrical Permittivity Mapping and pH-Sensitive Films for Osseointegrated Prosthesis and Infection Monitoring. IEEE Transactions on Medical Imaging. 2017; 36(11): 2193-2203.

227. Hu X, and Yang W. Planar Capacitive Sensors–Designs and Applications. Sensor Review. 2010; 30(1): 24-39.